

**School of Chemical and Petroleum Engineering  
Department of Chemical Engineering**

**Effect of feed channel spacer geometry on hydrodynamics and mass  
transport in membrane modules**

**Asim Saeed**

**This thesis is presented for the Degree of  
Doctor of Philosophy  
of  
Curtin University**

**August 2012**

## Declaration

To the best of my knowledge and belief this thesis contains no material previously published by any other person except where due acknowledgment has been made.

This thesis contains no material which has been accepted for the award of any other degree or diploma in any university.

Signature:

A handwritten signature in blue ink, appearing to be 'S. A. Jones', written over a horizontal line.

Date:

09/01/2013

## Abstract

Among different types of membrane modules used for cross flow filtration processes, Spiral Wound Module (SWM) dominates in the area of Ultra Filtration (UF), Nano Filtration (NF) and RO (Reverse Osmosis) due to high packing density, moderate energy utilization, standardization, cost effectiveness and being readily available from different suppliers. Membrane operations are often confronted with challenges associated with periodic maintenance of membranes due to significant material build-up on the surfaces. Operational issues arising from scaling and fouling primarily include: increased membrane resistance, decreased permeate flow, increased energy requirement and decreased membrane life. These issues have been addressed by several researchers, in a limited way, by proposing better pre-treatment processes or by alternative membranes through experimental and modelling studies. However, there appears a need to change membrane secondary structures to alter the flow patterns associated with fluids within the membrane module.

In spiral wound modules, net-type spacers are introduced to develop feed channel, by keeping the membrane surfaces apart. Presence of feed spacers generate secondary flow patterns within the membrane module which may lead to enhance mass transport of the solute away from the membrane to minimize concentration polarization, which is a desirable feature for efficient membrane operations. However, the undesirable features associated with their use are increased pressure drop and development of fluid stagnant zones. Therefore, the efficiency of a membrane module depends largely on the efficacy of the spacers to increase mass transport away from the membrane surface into the bulk fluid at moderate pressure loss.

Literature review reveals that a number of experimental studies were conducted in past to shed light on the role of feed spacers in membrane modules. However, due to difficulty in applying flow visualization and measuring techniques in experimental studies, an in-depth understanding of the flow and concentration patterns generated within the modules was not possible. The flow visualization was made possible with the development of Computational Fluid Dynamics (CFD) techniques, but was restricted to two-dimensional analyses due to computational constraints and provided useful information regarding hydrodynamics prevailing in spacer filled narrow

channels. With the ongoing developments in CFD techniques and computational resources three-dimensional studies are being conducted, which can provide in-depth analysis of concentration patterns and hydrodynamics in membrane modules.

In this thesis three-dimensional modelling of flow through spacer filled narrow channels is carried out using CFD package ANSYS FLUENT to investigate the impact of feed spacer filament orientation on shear stress exerted on membrane surfaces and Power number. The impact of dimensionless filament spacing on mass transport, shear stress, pressure drop and friction factor is also investigated using a systematic approach by hooking a User Defined Function (UDF) to ANSYS FLUENT. The predicted results showed excellent agreement with the previous experimental and other numerical studies revealing that CFD predicts hydrodynamics and mass transport within feed channel of spacer obstructed membranes quite accurately. These investigations are new to membrane related studies which shed light on spacer impact on performance of RO operations.

Post processing of the results revealed the complex flow patterns generated within the spacer filled narrow channels and showed that the alignment of the feed spacers with the flow direction have great influence on the generation of secondary flow patterns through the spacer filled channels. Pressure drop and Power number in spacer filled SWM appears to depend largely on the filament orientation based on current investigations. Pressure drop and power number will be higher if the filaments are inclined more towards the channel axis and vice versa.

For ladder type spacers wall shear stress at the top membrane surface is always higher (approximately 3 to 8 times for the spacer arrangements considered in the study at  $Re_h=100$ ) than that for the bottom wall, but interestingly the mass transfer coefficient values for the two walls are not significantly different for spacer arrangement having low to moderate bottom filament spacing ( $L_2 = 2$  to  $4$ ). However, when the bottom filament spacing is further increased ( $L_2 = 6$ ), there is a sharp decline in the pressure drop but the area weighted mass transfer coefficient for the top membrane wall showed a sharp reduction compared to the bottom membrane wall suggesting high fouling propensity of the top membrane wall which is not a desirable feature in membrane operations.

Different spacer arrangements considered in this work are compared on the basis of Spacer Configuration Efficacy (SCE), which in this thesis is defined as the ratio of Sherwood number to Power number. Spacer having higher SEC values would lead to higher mass transport of the solute away from the membrane walls to the bulk of the solution at moderate pressure losses. It has been concluded by carrying out mass transfer simulations for different spacer arrangements that the spacer arrangement having top and bottom filament dimensionless ratio equal to 4 performs better than all the other considered arrangements for hydraulic Reynolds number up to 200.

The results emanated out of the current study are considered to be of practical significance and could potentially lead to the development of efficient membrane modules with optimum spacer arrangements for RO operations.

## Acknowledgements

I would like to acknowledge direct and indirect help and support of many people for the production of this thesis. I would like to express my sincere gratitude to my supervisor, Associate Professor Hari Vuthaluru for his patience, guidance and belief in my abilities which kept me motivated all the time and helped a lot to complete this task.

I would also like to thank my co-supervisor, Dr. Rupa Vuthaluru, for motivating and providing her invaluable suggestions regarding the computational aspects of this thesis and her guidance and suggestions in preparation of research articles.

I would like to acknowledge Australian Government for the “Australian Post Graduate Award” and Curtin University for the “Discretionary Scholarship” which catered for my family’s financial needs during the research period.

I would like to appreciate all my Post Graduate colleagues for the formal discussions we used to have regarding our projects and would like to extend my heartfelt appreciation to a very special friend, who prefers to remain anonymous due to some personal reasons, for helping me many times to get back on track.

I would like to thank my parents for their unconditional love and motivation they used to provide despite being far away and never let me realize that they are living on the other side of the world.

Last but not the least, I would like to thank my beloved wife, Dr. Qurat-ul-Ain, for her endless patience and everlasting support, my children, Zara and Ali, for their love and being a source of every day motivation for all the efforts I have put into this thesis.

## **Publications emanating from this thesis**

### **Journal Papers:**

**Saeed A**, Vuthaluru R, Vuthaluru HB. Effect of feed spacer arrangement on flow dynamics through spacer filled membranes. *Desalination* 2012, 285:163-169.

**Saeed A**, Vuthaluru R, Vuthaluru HB. Impact of feed spacer mesh spacing on flow dynamics of membrane surfaces in ladder type spacer obstructed narrow channels. Submitted to Chemical Engineering Journal, currently under review.

**Saeed A**, Vuthaluru R, Vuthaluru HB. CFD based investigations into mass transport and flow dynamics of spacer filled membrane modules. Article will be submitted soon to an appropriate Journal.

### **Conference presentations**

**Saeed A**, Vuthaluru R, Vuthaluru HB. Impact of feed side filament mesh spacing on wall shear stress and mass transfer coefficient in spacer filled narrow channels. Article accepted for presentation in CHEMECA 2012.

**Saeed A**, Vuthaluru R, Vuthaluru HB. Concept of Spacer configuration efficacy (SCE) applied to optimize ladder type feed spacer filament spacing in narrow channels. Abstract accepted for presentation in Indian Desalination Association Annual Congress-2013 (InDACON-2013).

## Table of Contents

Abstract .....	i
Acknowledgements .....	iv
Table of Contents .....	vi
List of Figures .....	xi
List of Tables.....	xvii
Chapter 1. Introduction .....	1
1.1 Introduction .....	1
1.2 Scope of research work .....	6
1.3 Organization of thesis.....	7
Chapter 2. Literature review .....	9
2.1 Types of membrane modules .....	10
2.1.1 Plate and frame module.....	10
2.1.2 Tubular membrane module .....	11
2.1.3 Hollow fiber module .....	12
2.1.4 Spiral Wound Module (SWM).....	13
2.2 Important parts of spiral wound membrane.....	17
2.2.1 Permeate collection tube .....	17
2.2.2 Permeate spacer.....	18
2.2.3 Feed spacer.....	19
2.2.4 Anti telescoping device (ATD) and Brine seal .....	22
2.2.5 Module interconnector .....	24
2.2.6 Pressure vessel .....	26
2.3 Module Characteristics .....	28
2.4 Basic definitions and concepts .....	29
2.4.1 Osmosis and Reverse Osmosis.....	29
2.4.2 Osmotic pressure.....	31

2.4.3	Recovery .....	32
2.4.4	Rejection, salt passage and Differential pressure.....	34
2.4.5	Flux, Permeability and Permeance.....	37
2.4.6	Concentration polarization.....	38
2.4.7	Fouling .....	40
2.4.8	Mass transfer coefficient.....	42
2.4.9	Energy losses and friction factor.....	44
2.4.10	Reynolds number .....	46
2.5	Techniques to reduce concentration polarization and fouling.....	46
2.5.1	Feed channel spacer .....	47
2.5.2	Periodic back-flushing .....	47
2.5.3	Gas sparging.....	47
2.5.4	Helical and rotating channel.....	48
2.5.5	Ultrasonic vibration.....	48
2.5.6	Electromagnetic field .....	48
2.5.7	Cyclic operations.....	49
2.6	Theoretical models for membranes .....	49
2.6.1	Film theory .....	49
2.6.2	Osmotic pressure model.....	51
2.6.3	Boundary layer resistance or Resistance in series model.....	52
2.6.4	Retained solute model.....	53
2.7	Experimental and theoretical Studies for prediction of mass transfer and concentration polarization.....	53
2.8	Simulation of spiral wound membrane modules.....	59
2.9	Flow and mass transfer modelling in plane channels using CFD .....	62
2.10	Studies focusing on feed spacer's impact on SWM performance .....	68
2.10.1	Experimental studies .....	68

2.10.2	Computational Fluid Dynamics (CFD) based studies.....	79
2.10.2.1	Two-Dimensional (2D) CFD studies.....	80
2.10.2.2	Three-Dimensional (3D) CFD studies.....	91
2.11	Research Objectives.....	110
	Nomenclature.....	111
Chapter 3.	Introduction to Computational Fluid Dynamics (CFD).....	114
3.1	Basic elements of a CFD code.....	115
3.1.1	Pre-processor.....	115
3.1.2	Solver.....	116
3.1.3	Post-processor.....	117
3.2	Transport equations.....	118
3.3	Finite volume method employed by ANSYS FLUENT.....	120
3.3.1	Solving the linear system.....	123
3.3.2	Spatial discretization.....	123
3.3.3	Temporal Discretization.....	124
3.4	Programming procedure.....	125
	Nomenclature.....	126
Chapter 4.	Feed spacer orientation and flow dynamics.....	127
4.1	Introduction.....	127
4.2	Geometric parameters for spacers.....	130
4.3	Hydraulic diameter and porosity of spacer filled channel.....	131
4.4	Modelling Procedure.....	134
4.4.1	Computational domain and boundary conditions.....	134
4.4.2	Grid refinement and independence.....	138
4.4.3	Governing equations, solution methods & controls.....	140
4.5	Simulation results and discussion.....	142
4.6	Conclusion.....	153

Nomenclature .....	154
Chapter 5. Mass transfer and flow dynamics .....	156
5.1 Geometric parameters of spacers.....	157
5.2 Hydraulic diameter and porosity of spacer filled channel.....	158
5.3 Modelling Procedure .....	159
5.3.1 Computational domain and boundary conditions .....	159
5.3.2 Grid refinement and independence .....	163
5.3.3 Governing equations, solution methods & controls.....	165
5.3.4 Incorporation of mass transfer coefficient in the model .....	168
5.3.4.1 Details of the User Defined Function (UDF).....	169
5.4 Part of the computational domain representing the SWM module .....	172
5.5 Discussion on results for Spacer SP44 .....	178
5.5.1 Top membrane surface .....	179
5.5.2 Bottom membrane surface .....	182
5.6 Effect of filament spacing .....	187
5.7 Comparison of present study with previous experimental and numerical studies.....	201
5.8 Comparison of spacers at different Reynolds number .....	205
5.9 Conclusions .....	210
Nomenclature .....	212
Chapter 6. Conclusions and future work.....	214
6.1 Conclusions .....	214
6.2 Recommendations for future research.....	218
References .....	220
A. Appendix-I .....	229
A.1. ANSYS FLUENT 13.0 .....	229
A.2. Boundary conditions .....	229
A.3. Equations solved .....	230

A.4. Executed on demand .....	230
A.5. Under-Relaxation Factors .....	230
A.6. Pressure-Velocity coupling .....	231
A.7. Spatial discretization Schemes .....	231
A.8. Solution limits .....	231
A.9. Material Properties .....	231
B. Appendix-II .....	239
C. Appendix-III .....	241

## List of Figures

Figure 2.1: Filtration spectrum showing separation techniques and particle size range (Source: Adapted from presentation of guest lecturer from HATCH QED at Curtin University.).	9
Figure 2.2: Plate and frame membrane module (source:[39]).	11
Figure 2.3: Tubular membrane module (source:[39]).	12
Figure 2.4: Hollow fiber module (source: [39]).	13
Figure 2.5: Hollow fiber module (source:[40]).	13
Figure 2.6: Flow paths for feed (a) and Permeate (b) in SWM (Source: Adapted from presentation of guest lecturer from HATCH QED at Curtin University.).	14
Figure 2.7: A single flat leaf of SWM in un wound state showing flow direction across the leaf.	16
Figure 2.8: Parts of spiral wound membrane in pressure vessel (Dow Water Solutions, 2007).	17
Figure 2.9: Geometric characterization of feed spacer.	21
Figure 2.10: Square (ladder-type) spacer arrangement.	21
Figure 2.11: Uniform telescoping (Source [42]).	22
Figure 2.12: Telescoping Protruding feed spacer (Source [42]).	22
Figure 2.13: Telescoping Protruding membrane and feed spacer (Source [42]).	23
Figure 2.14: ATD mounted with U-cupped shaped brine seal (Source [42]).	24
Figure 2.15: Placement of module interconnector adapter for standard ATD end caps (Source [42]).	24
Figure 2.16: Dow Water Solutions- FilmTec iLEC ATDs with integral O-Ring (Source [42]).	25
Figure 2.17: Using a strap wrench with iLEC membranes (Source [42]).	25
Figure 2.18: Six SWM housed in pressure vessel in series arrangement (Source [42]).	26
Figure 2.19: SWM in pressure vessel without pressure vessel end cap in place (Source [42]).	27
Figure 2.20: Pressure vessel with permeate effluent piping and end cap installed (Source [42]).	27

Figure 2.26: Characteristics of polyamide composite RO membranes (source: <a href="http://www.biologymad.com">http://www.biologymad.com</a> , 2004). .....	30
Figure 2.27: Osmosis and reverse osmosis (Source: [7] )......	31
Figure 2.28: Concentrate and instantaneous permeate concentration as function of recovery.....	34
Figure 2.29: Concentration polarisation, where $c_b$ is the bulk concentration and $c_s$ is the concentration at membrane surface. Source : [42].....	39
Figure 2.30: Concentration profile at membrane surface.....	50
Figure 2.31: Fluid flow streamlines in spacer filled flat channel [25]. .....	73
Figure 2.32: Zigzag spacer used by Schwinge et al. [131] .....	77
Figure 2.33: A3LS configuration proposed by Schwinge et al. [133] .....	78
Figure 2.34: Streamlines for zigzag (left) and cavity (right) configurations, presented by Kang and Chang [32]. .....	81
Figure 2.35: Schematics of different 2D spacer configurations.....	82
Figure 2.36: Rectangular feed channel with transverse filament adjacent (a) and opposite (b) to the membrane. Source [21]......	84
Figure 2.37: Stream lines distribution at $Re=200$ , $v_p= 2.5 \times 10^{-5}$ m/s, $L_f=3.8$ . Source [20]. .....	86
Figure 2.38: Entrance transition length for I. Rectangular spacer, II, cylindrical spacer, III, triangular spacer, source: [143].....	87
Figure 2.39: Cross section of spacer filaments. (a) Original spacer (b) Concave-square (c) V-shaped (d) Concave- $W/H = 4/3$ (e) Concave- $W/H= 3/4$ . Adapted from [153]......	94
Figure 2.40: Novel spacers investigated by Li et al. [160] .....	98
Figure 2.41: 3D spacers investigated by Fimbers-Weihs and Wiley [28] (a) $90^\circ$ orientation (b) $45^\circ$ orientation. ....	100
Figure 2.42: Schematics of 3D spacers investigated by Santos et al. [162].....	101
Figure 2.43: Principal spacers configurations investigated by Shakaib et al. [164] (a) Diamond type spacer (b) Parallel spacer.....	102
Figure 3.1: Control volume used to illustrate Discretization of a transport equation [167]......	121
Figure 4.1: Schematic diagram of SWM in partly unwound state, adapted from [29]. .....	129

Figure 4.2: Schematic of feed channel spacer and geometric characterization of feed spacer.....	131
Figure 4.3: Schematic of feed channel spacer and selected computational domain.....	135
Figure 4.4: Approach to get mass flow rate at a desired channel Reynolds number. ....	137
Figure 4.5: Computational grid (flow direction is along x-axis). ....	139
Figure 4.6: Quadratic profiles used in QUICK scheme. Source: [35]. ....	141
Figure 4.7: Shear stress distribution on bottom (a) and top (b) wall (Note:- Vertical lines indicate centre lines of bottom filaments). ....	144
Figure 4.8: X-Velocity contours at selected faces in the computational domain.....	146
Figure 4.9: X-Shear stress contours on bottom wall.....	146
Figure 4.10: Velocity vectors on a plane $0.05 * h_{ch}$ .....	147
Figure 4.11: X-Shear stress contours on top wall. ....	147
Figure 4.12: Velocity vectors at top surface. ....	148
Figure 4.13: Velocity vectors at $0.95 * h_{ch}$ .....	149
Figure 4.14: Pathlines of Velocity realising from the inlet (a) and (b) bottom view, (c) top view. ....	149
Figure 4.15: Velocity contours at (a) $0.25 * \text{channel height}$ (b) $0.75 * \text{channel height}$ . ....	152
Figure 5.1: Schematic of feed channel spacer and selected computational domain.....	158
Figure 5.2: Top wall shear stress vs number of meshed cells for SP22 at $Re_h=100$ . ....	164
Figure 5.3: Pressure drop vs number of meshed cells for SP22 at $Re_h=100$ .....	164
Figure 5.4: Mass transfer coefficient vs number of meshed cells for SP22 at $Re_h=100$ .....	165
Figure 5.5: Residuals of continuity, velocity components and solute mass fraction. ....	167
Figure 5.6: Monitoring points (MP1 & MP2) in computational domain.....	168
Figure 5.7: Number of iterations vs (a) solute mass fraction at MP2 (b) velocity magnitude at MP1. ....	168
Figure 5.8: Logic behind the User Defined Function (UDF).....	171
Figure 5.9: Total computational domain with Lines A & B on bottom and top wall respectively. ....	172

Figure 5.10: Shear stress and Mass transfer coefficient distribution on bottom wall for SP44 at $Re_h=100$ .....	173
Figure 5.11: Shear stress and Mass transfer coefficient distribution on top wall for SP44 at $Re_h=100$ . ....	173
Figure 5.12: Contours of bottom wall shear stress for SP44 at $Re_h=100$ between the selected and adjacent region of the computational domain. ....	175
Figure 5.13: Contours of mass transfer coefficient at bottom wall for SP44 at $Re_h=100$ between the selected and adjacent region of the computational domain. .	175
Figure 5.14: Contours of (a) top wall shear stress (b) mass transfer coefficient at top wall for SP44 at $Re_h=100$ between the selected and adjacent region of the computational domain.....	176
Figure 5.15: Contours of (a) wall shear stress and (b) mass transfer coefficient for different spacers at $Re_h=100$ between the selected and adjacent region of the computational domain.....	177
Figure 5.16: Contours of solute mass fraction and contours of velocity magnitude overlayed by the velocity vectors (fixed length) at different vertical planes for SP44 at $Re_h=100$ .....	179
Figure 5.17: Velocity vectors coloured by velocity magnitude (fixed length) at a plane very close to top membrane ( $Z=0.95\text{mm}$ ) for SP44 at $Re_h=100$ .....	180
Figure 5.18: (a) Selected computational domain with virtual lines on top membrane wall. (b-e) Mass transfer coefficient and shear stress distribution on top wall along virtual lines b-e respectively for SP44 at $Re_h=100$ . ....	181
Figure 5.19: Velocity vectors coloured by velocity magnitude at a plane in the vicinity of bottom membrane wall ( $Z=0.05\text{mm}$ ), showing flow reattachment and separation. ....	182
Figure 5.20: (a) Contours of velocity magnitude overlayed by the velocity vectors (fixed length) at vertical plane ( $y=0\text{ mm}$ ). (b) Shear stress and mass transfer coefficient distribution at plane $y=0\text{mm}$ , for SP44 at $Re_h=100$ . ....	183
Figure 5.21: (a) Selected computational domain with virtual lines on bottom membrane wall.(b-f) Mass transfer coefficient and shear stress distribution on bottom wall along virtual lines b-f respectively for SP44 at $Re_h=100$ .....	186
Figure 5.22: Velocity vectors coloured by velocity magnitude (fixed length) for different spacers at $Z=0.05h_{ch}$ and $Re_h=100$ . ....	188

Figure 5.23: Contours of mass transfer coefficient for (a) SP44 and (b) SP66 at $Re_h=100$ at bottom and top membrane surfaces.....	189
Figure 5.24: Velocity vectors (fixed length) overlaid by mass transfer coefficient contours at top & bottom membrane surfaces for different spacers at $Re_h=100$ . ....	192
Figure 5.25: Dimensionless filament spacing effect on pressure drop at $Re_h=100$ .	194
Figure 5.26: Dimensionless filament spacing effect on top wall average shear stress at $Re_h=100$ .....	195
Figure 5.27: Dimensionless filament spacing effect on bottom wall average shear stress at $Re_h=100$ .....	195
Figure 5.28: Dimensionless filament spacing effect on top wall average mass transfer coefficient at $Re_h=100$ .....	197
Figure 5.29: Dimensionless filament spacing effect on bottom wall average mass transfer coefficient at $Re_h=100$ . ....	197
Figure 5.30: Dimensionless filament spacing effect on top & bottom wall average mass transfer coefficient at $Re_h=100$ .....	198
Figure 5.31: Comparison of different spacer configurations at $Re_h=100$ . ....	201
Figure 5.32: Comparison of some spacer configurations with experimental and numerical study of Geraldles et al. [20] at $Re_h=100$ . ....	202
Figure 5.33: Comparison of wall shear stress for different spacer arrangements with Shakaib et al. [164] at $Re_h=100$ . ....	203
Figure 5.34: Comparison of pressure drop for different spacer arrangements with Shakaib et al. [164] at $Re_h=100$ . ....	204
Figure 5.35: Comparison average mass transfer coefficient values for different spacer arrangements with Shakaib et al. [165] at $Re_h=125$ .....	204
Figure 5.36: Comparison of Sherwood number for different spacer arrangement with previous experimental and numerical studies at $Sc=1350$ . ....	205
Figure 5.37: Hydraulic Reynolds number vs (a) Pressure drop and (b) Power number for few spacer arrangements. ....	206
Figure 5.38: Hydraulic Reynolds number vs SCE for few spacer arrangements.....	207
Figure 5.39: Velocity vectors in the vicinity of bottom membrane surface for SP44 at (a) $Re_h=75$ (b) $Re_h=100$ (c) $Re_h=125$ (d) $Re_h=150$ (e) $Re_h=200$ and for (f) SP63 at $Re_h=200$ .....	208
Figure 5.40: Power number versus Sherwood number for different spacer arrangements. ....	210

Figure A.1: Computational grid and console window of ANSYS FLUENT 13.0 ..	232
Figure A.2: Domain extents. ....	233
Figure A.3: Setting properties of the mixture. ....	233
Figure A.4: Setting mass flow rate at inlet for SP22 to achieve $Re_h=100$ . ....	234
Figure A.5: Setting solute mass fraction at inlet. ....	234
Figure A.6: Setting Boundary conditions at top (and bottom) membrane surface. .	235
Figure A.7: Defining solute mass fraction at top (and bottom) membrane surface.	235
Figure A.8: Boundary conditions at outlet. ....	236
Figure A.9: Solution methods, control, limits and equations. ....	236
Figure A.10: Defining Monitoring point in the domain. ....	237
Figure A.11: Selecting residuals of continuity, velocity components and solute mass fraction. ....	237
Figure A.12: Solution initialization. ....	238
Figure A.13: Reporting average values of the variables. ....	238
Figure A.14: Reporting average values of bottom wall shear stress for SP22 at $Re_h=100$ . ....	239

## List of Tables

Table 2.1: Materials for permeation collection tube (source: Dow Water Solutions, 2007) .....	18
Table 2.4: Characteristics of different modules (Source: Adapted from [39]) .....	28
Table 2.5: Concentration factor as a function of Recovery. ....	33
Table 2.6: General rejection capabilities of most polyamide composite membranes at room temperature (Source: [42]).....	36
Table 2.7: Recommended flux as a function of influent water source (Source: [42]). .....	37
Table 2.8: Summary of CFD based three dimensional studies. ....	106
Table 4.1: Geometric characteristics of spacer. ....	130
Table 4.2: Comparison of average shear stresses on walls and pressure drop at $Re_h=100$ with available data [135, 164].....	150
Table 4.3: Comparison of current and previous studies at flow attack angle of $45^0$ and $Re_h=100$ . ....	151
Table 4.4: Shear stress, pressure drop, dimensionless pressure drop and power number at flow attack angle $\theta_1=135^0$ and $\theta_2=0^0$ at $Re_h=100$ .....	152
Table 5.1: Spacer configurations considered in this section and corresponding results at $Re_h=100$ .....	199
Table 5.2: Comparison of selected spacer configurations at $Re_h=100$ .....	200
Table 5.3: Comparison of SP44 and SP63 at $Re_h=200$ . ....	209

# Chapter 1. Introduction

## 1.1 Introduction

The first recorded membrane study can be dated back to 1748, when a French priest Abbé Nollet discovered the phenomena of osmosis through natural membranes. He placed “spirits of wine” in a vessel and covered its mouth with animal bladder and immersed it in pure water. Since the bladder membrane was more permeable to water than to wine, it swelled and sometimes even burst. However, major membrane development and commercialization gained pace and attention after the invention of thin cellulose acetate membrane by Loeb and Sourirajan in late 1950s [1]. This invention gained the industrial interest in membrane technology and lead to the development and commercialisation of ultrafiltration membranes. Over the past decade membrane processes have become main stream industrial technologies due to their cost effectiveness and low energy consumption compared to their thermal counterpart separation technologies like distillation, and are being used in many large scale industrial separation applications: food, biotechnical, waste water treatment, pollution control, product recovery and in electronics [2].

In membrane base separation techniques a driving force is required for the separation process. For instance, temperature gradient for membrane based distillation operations, electric potential gradient for electrodialysis. But most of the large scale membrane based industrial processes are pressure driven.

The choice of the membrane process to be used depends primarily on the size of the particles that are needed to be separated from the feed stream. Microfiltration (MF) is used to separate suspended solids having a particle size range of 0.08 to 10  $\mu\text{m}$ . Hydraulic pressure range is about 1-2 bar for MF. Ultrafiltration (UF) is used to separate macromolecular solids in the particle range of 0.001-0.1  $\mu\text{m}$ . The hydraulic pressure requirement for UF is in the range of 1-7 bar. Nanofiltration (NF) process rejects the molecular solids and multivalent salts in the size range of 0.0005-0.007  $\mu\text{m}$  and requires an operating pressure of about 14 bar. Reverse Osmosis (RO) membranes are capable of rejecting molecular solids and salts (multivalent as well as monovalent) having the size range of 0.00025-0.003  $\mu\text{m}$  and requires an operating

pressure of 20-50 bar [3]. RO membrane separation process is used to separate or concentrate a substance in fluid solutions. A fluid mixture is allowed to flow under pressure through a porous membrane and permeate fluid stream is withdrawn generally at atmospheric pressure and surrounding temperature. The permeate or product stream is rich in one or more constituents of the mixture. The other stream often called the reject stream or retentate (at the upstream side of the membrane) is concentrated in the other constituents. This process does not need thermal energy as there is no heating/or phase change involved [4].

For industrial application, apart from the individual performance of the membranes, the membrane modules which house those membranes are also very important. Due to the similarities between heat and mass transfer phenomena, the modules used for membranes processes are analogous to the units used in the heat transfer operations. For example shell and tube heat exchanger is analogous to Spiral Wound Membrane (SWM) and Plate and frame heat exchanger is analogous to Hollow Fibre Membrane (HFM). For most of the industrial application involving membrane separation technologies SWM configuration is preferred over its counterpart ranging from RO to UF due to a good balance between ease of operation, packing density ( $< 1000\text{m}^2/\text{m}^3$ ), permeation rate and high mass transfer rate due to presence of feed spacers [5-7] and is the focus of the present work. RO membrane based separation technologies are amongst the most versatile water treatment technologies and is used for water recycling, producing potable water, process water and resource recovery [8-11] and the area of interest for this thesis.

But Reverse Osmosis operations are often confronted with challenges associated with periodic maintenance of membranes due to significant material build-up on the surfaces. Operational issues arising from scaling and fouling primarily include: increased membrane resistance, decreased permeate flow rate, increased energy requirement and decreased membrane life. Fouling in RO membrane is traditionally defined as decline in performance due to deposition of insoluble rejected material at the membrane surface [12-14].

During normal operation feed water passes through the SWM configuration under pressure and the permeate flows through the membrane and adapt a spiral path to reach the collection tube. As a result of the permeation process the concentration of

salts especially near the membrane wall surface increases and further increases in the flow direction. When maximum solubility limit of a species is reached it precipitates out of the solution and forms a salt layer at the membrane surface. Once that point is reached or exceeded the onset of scaling begins. The convective flux towards the membrane surface dominates the back diffusion to the bulk. This phenomenon is called concentration polarization because it results in a higher concentration of salt layer at the membrane surface as compared to bulk of the fluid.

The ions present in water which cause inorganic fouling (or scaling) are Calcium, Magnesium, Sulphate, Silica, Iron and Barium [15]. Inorganic fouling begins when the concentration of the sparingly soluble salts (divalent and multivalent) exceeds their solubility limit. During normal course of operation the concentration of those salts increase with increasing recovery and the risk of fouling is amplified. Eventually the salts crystallize out of the solution and get deposited on the membrane surface leading to the formation of a cake, a phenomena called cake formation. The extent of concentration polarisation depends on the membrane properties, solution chemistry, temperature, operating conditions and module geometry [7, 16]. Often the term adsorption is used in literature in a broader prospective for the interaction of solute and membrane, whereas the term aggregation is broadly used for solute/solute interaction and the phenomenon of gelation, polymerisation, flocculation, adhesion or coagulation comes under the umbrella of aggregation. The severity of these cake forming phenomenons depends upon local solute concentration and hence on the degree of polarisation [17].

Biological fouling is the term broadly used to describe the deposition of biomass (algae, fungi, bacteria, protozoa etc) on the membrane surface. Bio film formation of the membrane surface has three stages:- 1- Transport to the membrane surface, 2- Attachment to the surface, 3- Biofilm growth. It is hard to remove the biological fouling because the micro-organism is protected by a gel like covering layer. If this layer is removed by disinfectants the remaining dead mass still provides food and becomes responsible for the further biological regrowth. Biological fouling prevention techniques are usually employed in the pre-treatment section before the feed stream is introduced to the membrane modules [18].

Feed side and permeate side spacers present in SWM configuration has important roles to play. Permeate side spacers separate the membranes and bear pressure on them. The net spacer in the feed channel not only keep the membrane layers apart, hence providing passage for the flow, but also significantly affect the flow and concentration patterns in the feed channel. On one hand they are responsible for the pressure drop and limited flow zones (dead zones) creation, and on the other hand they are responsible to promote mixing between the fluid bulk and fluid elements adjacent to the membrane surface. In other words they are intended to keep the membranes clean by enhancing mass transfer and disrupting the solute concentration boundary layer. In past several experimental and theoretical studies were carried out to shed light on this phenomena and to optimize spacer configuration [19-24]. So it is quite understandable that the presence of these spacers promotes directional changes in the flow which reduces membrane fouling /or concentration polarization. Hence the efficiency of a membrane module depends heavily on the efficacy of the spacers to increase mass transport away from the membrane surface into the fluid bulk by increasing shear rate at the membrane surface [25].

Since spiral wound membranes have tightly wrapped structures which cannot be opened easily for chemical cleaning or cannot be back flushed by operating in reverse direction. So the fouling control methods for SWM are limited to hydrodynamics, pre-treatment of feed and operational controls [26]. The fouling issues can be addressed to a larger extent by varying the hydrodynamic conditions prevailing in spiral wound membrane. The feed spacers can be oriented to generate high cross flow velocities or secondary flow patterns which can develop higher scouring forces on the membrane surface to reduce fouling and concentration polarization. However this approach will need higher pumping energy to compensate losses within the membrane module. Hence the feed spacers must be optimized to reduce the build-up on the membrane surface with moderate energy loss, as some energy losses do not directly translate into enhancement of the mass transfer. Mass transfer to energy losses ratio depends on the configuration of the spacers present in the membrane module [27, 28].

In most of the cases the presence of spacers results in the enhancement of mass transfer (of solute from the membrane walls to the bulk of the fluid) which often outweighs the disadvantage caused by the energy losses. As a result, the use of

spacer filled channelled becomes more economically viable as compared to empty channels [25, 29, 30].

As already mentioned, the presence of spacers in the feed channel of membrane module give rise to secondary flow patterns, such as directing the flow towards the membranes walls and wall shear perpendicular to the main (bulk) flow direction [28, 31]. Specific spacer arrangement that promotes those flow effects without any significant increase in energy losses would bring economic improvements in membrane operations.

The traditional experimental techniques while taking measurements close to the membrane walls intrude or alter the flow field and bring in complexities for analysis. However, techniques such as flow visualization with dye [32], Particle Image Velocimetry (PIV) [33] and Direct Observation through the membrane (DOTM) [5, 34] which are less intrusive in nature are employed to study the mass distribution and flow patterns in a membrane cell. But often the limitation of these techniques is the lack of small scale resolution required to analyse mass transfer phenomena occurring within the boundary layer. Hence there is a need for another approach or technique which provides further understanding of the mass transfer aspects associated with the use of membrane operations, especially when the objective is to capture near membrane wall effects.

Computational techniques, possesses the powers to provide information regarding the flow anywhere in the selected domain without interfering with the flow itself and can lead to better understanding of the mass transfer aspects of the membrane operations. Experimental techniques require considerable financial investment such as equipment procurement, infrastructure construction, resources dedication, hiring and training of staff. Numerical modelling reduces dramatically the costs, time and risks involved in running the repeated experiments. Computational Fluid Dynamics (CFD) is one of the many numerical techniques used for simulating fluid flow [35] and the tool used in this thesis. CFD allows simulation and subsequent analysis of fluid systems by solving conservation equations for mass, energy and momentum using numerical methods.

Many researchers are utilizing CFD technique to gain insight of various phenomena taking place within the membrane modules to improve its performance or to provide

valuable information for the design process. Moreover, many research groups have shifted their focus to CFD making it widely used tool in the field of membrane science [36]. The advantage of CFD tool over the traditional experimental methods lies in the built-in flexibility to change operating conditions, fluid properties and geometric parameters of the flow channel. For instance, geometric parameters of the flow channel can be varied using an appropriate CFD software, and does not need the physical construction of the modified channel, to investigate the effects on parameters of interest. Similarly fluid properties and operating conditions can be varied to investigate their impact on the parameters of interest without experimentations. Another important and interesting feature of the CFD is that the data can be reported anywhere in the computational domain at any time during the simulation without obstructing the flow itself.

## **1.2 Scope of research work**

CFD tools are used in thesis to simulate flow through spacer filled narrow channels, such as those encountered in SWM module, and to generate data to analyse fluid dynamics and the associated mass transfer aspects. The flow domain including the spacers was created and meshed primarily in Gambit<sup>®</sup>. However ANSYS DesingModeler and ANSYS Meshing softwares were sparingly used as Gambit<sup>®</sup> was not available after 1 January, 2011. ANSYS FLUENT, integrated to ANSYS Workbench, was used to simulate the flow through the channels.

Following are the main aims of the research work carried out:

- Flow visualization, to understand complex flow patterns generated in spacer filled narrow channels, such as those encountered in SWM module, at various planes along channel heights.
- The effects on flow patterns, average wall shear stress, power number and pressure drop when the membrane secondary structures (feed spacer filaments) are set at various angles with the inlet flow i.e. by changing the flow attack angle.
- To study the impact of filament spacing and hydraulic Reynolds number on hydrodynamics and mass transfer aspects of spacer filled narrow channels.

- To achieve reliable conclusions and results that would lead to development of more efficient and economical spacer meshes.

### **1.3 Organization of thesis**

This thesis is divided into six chapters. The aim of the first chapter is to provide a snapshot of the challenges faced by cross-flow separation process involving membranes and the role played by the feed channel spacers, which are primarily meant to introduce directional changes to the fluid flow, to meet those challenges. This chapter also briefly discusses the superiority of computational techniques over normal experimental methods.

In chapter 2, different membrane modules used in membrane separation processes are described briefly. Among those modules spiral wound assembly is discussed in detail. This chapter also covers the important concepts, definitions, theories and relevant equations that are helpful to understand scaling and fouling tendencies within membrane modules. Extensive literature review is also presented in this chapter which covers experimental and numerical studies related to concentration polarization, modelling of Spiral Wound Modules and flow simulation and visualization through empty and spacer filled narrow channels. Some deficiencies in the previous studies are tabulated at the end of this chapter along with the objective of this thesis.

Chapter 3 provides a brief introduction to Computational Fluid Dynamics (CFD) and details the methodology used by ANSYS FLUENT to obtain converged solution of the Navier-Stokes transport equations.

Chapter 4 includes the details of simulations carried out using ANSYS FLUENT for different spacer configurations to investigate the impact of feed spacer orientation on flow dynamics and resulting impact on pressure drop, shear stress on membrane surfaces and power number.

Chapter 5 includes the details of User Defined Functioned (UDF) developed and hooked with ANSYS FLUENT to simulate mass transfer of a mono-valent solute by utilizing a dissolving wall assumption. This chapter also includes the comparison of the present model with other experimental and numerical studies. Different spacer

geometries were compared by altering the filament dimensionless distance in terms of mass transfer coefficient, Sherwood number and power number at same and different hydraulic Reynolds numbers.

Chapter 6 summarizes the conclusions drawn from the thesis and also provides recommendations for future research work.



## **2.1 Types of membrane modules**

Apart from the membranes, the modules that house those membranes also play a vital role in the performance of the equipment. Plate-and-frame and Tubular membrane modules were used extensively in the past, but due to the inefficiency, complications associated with their configuration and high cost they are replaced effectively by the hollow fibre (HF) and Spiral Wound Modules (SWM). These days both HF and SWM are commercially available, but the latter dominates in the area of UF, NF and RO. A brief description of the modules discussed above is given below.

### **2.1.1 Plate and frame module**

Design of these modules is principally based on conventional filter press. Plate and frame modules were amongst the earlier design and are now limited to small to moderate scale operations. Usually these modules consist of flat membrane sheets which sit on rectangular plates. The flow channels are made by inserting mesh like spacers. A number of plates are stacked in parallel or in series. To bear the pressure these modules are equipped with heavy duty end plates. The simplest design consists of several sets of alternating frames. These frames are meant to support the membranes on the permeate side and separate them at the feed side. The assembly is pressed between two end plates and held together with tie rods. Flow enters through one and exits at the other end as shown in Figure 2.2. Some alternations to the basic design are also available which use disc or elliptical plates instead of rectangular ones and feed flows radially or from one side of the elliptical disc to the other.

Design and construction of large Plate and frame membrane module is difficult as compared to that of a large plate and frame heat exchanger due to two reasons. Firstly, lack of adequate membrane support which limits its operation to low hydraulic pressure and/or requires nearly same pressure at both sides of the membranes, which indirectly means very precise and accurate process control and hence reduces the flexibility of the process. Secondly, due to low packing density it needs higher capital and operational cost [37]. In addition to that, leaks caused by a high amount of gaskets seals present limit the use of this module for small scale operations only. Replacement of the membranes has to be carried out sheet by sheet making the process labour intensive. These configurations are widely used in electrolytic membrane applications such as electro dialysis [38]. These modules are

replaced by SWM for large scale applications such as water treatment and dairy industry.

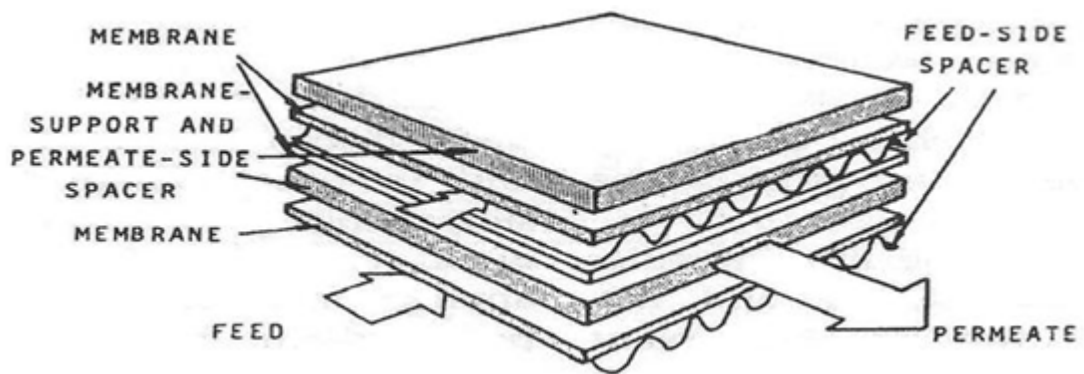


Figure 2.2: Plate and frame membrane module (source:[39]).

### 2.1.2 Tubular membrane module

These modules are similar to shell and tube heat exchangers, as shown in Figure 2.3, and are designed by casting membranes on porous supporting tubes having diameters in the range of 0.125 to 1.0 inch. These tubes must be strong enough to bear the feed stream pressure and usually made up of stainless steel, fibreglass, carbon, ceramics and porous plastics. These tubes are pressed against tube sheets at each end and are housed in a low pressure jacket. As the recovery per tube length is very low so the tubes are connected in series by external U-shaped connections in order to achieve desired recoveries.

High pressure feed is allowed to enter the tube bore and the permeate passes through the membrane and the porous support structure and enters the low pressure jacket from where it is removed through the permeate ports. The feed gets concentrated along the flow direction till the flow reaches the other end of the tube. Its direction is then reversed (while passing through the U-shaped connectors) and allowed to pass through additional tubes to get the required recovery.

The advantages of these modules are: they can be operated at high pressures, membranes can be removed and reformed, low fouling tendency, easy to clean, can achieve high flow velocities and large and well defined flow passage. In some membrane types (such as cellulose acetate), the fouling material forms a gel-like layer which floats loosely over the wet cellulose acetate surface and can easily be

removed by mechanical means. A method known as foam-ball cleaning procedure is developed to get rid of the fouling materials.

However the disadvantages are they are expensive to maintain and operate, such membranes are complex to produce, minimum choice of membrane materials and low membrane surface area to volume ratio restrict their use to moderate scale operations [40].

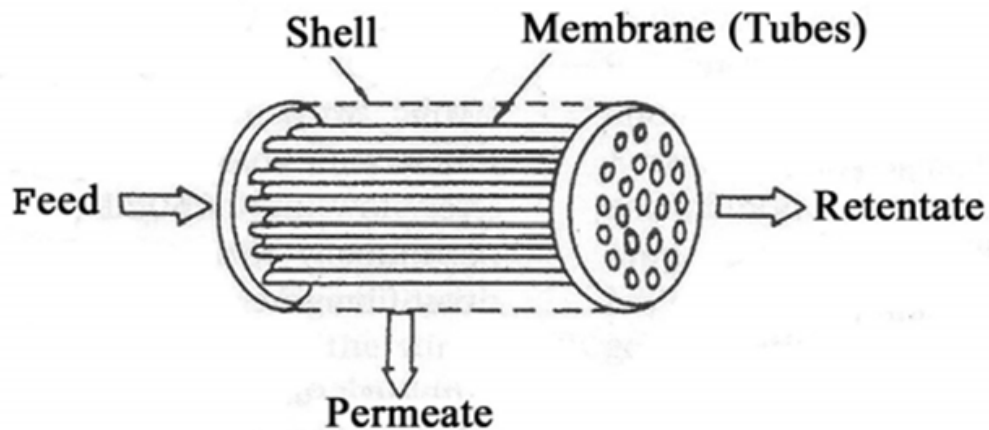


Figure 2.3: Tubular membrane module (source:[39]).

### 2.1.3 Hollow fiber module

The design of these modules is similar to Tubular shell and tube arrangement. Depending upon the fiber dimensions, support mechanism and membrane materials they can be operated with either shell side or lumen side feed.

The walls of the fibers need to withstand high pressure to avoid collapse or bursting, depending on the feed introduction mode or method. The outer diameters are usually in the range of 0.5 to 1.0mm, whereas the inner (lumen) diameters are in the range of 0.3 to 0.8mm. These modules contain thousands of fibers arranged in bundle and potted with special epoxy resins in an outer shell as shown in Figure 2.4.

The fibers are subjected to high external pressure in case of shell side feed arrangement and can withstand high pressure (10Mpa) required for seawater desalination utilizing reverse osmosis principle. However, in case of seawater desalination SWM has superseded the Hollow fiber membrane modules. In case of lumen side feed arrangements, the fibers are developed in the form of a composite having polyether sulphone support and polyamide inner skin and feed pressures up

to 2.7 Mpa have been reported making this arrangement suitable for NF and low pressure RO applications [39, 40].

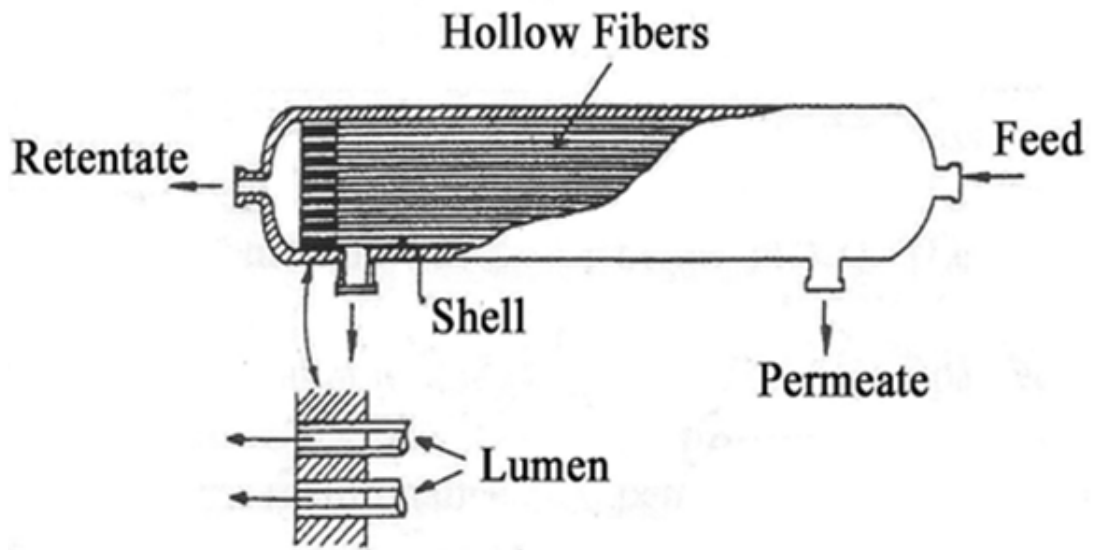


Figure 2.4: Hollow fiber module (source: [39]).

Figure 2.5 shows schematic of a hollow fiber membrane module. Pressurized feed is introduced in a central tube and flows radially outwards towards the outer structure of the fibers. Water permeates through the walls of the fibers and enters their bores and exits through a permeate port. The concentrated stream (brine) flows between the outside of the fiber bundle and inside of the shell to the brine port.

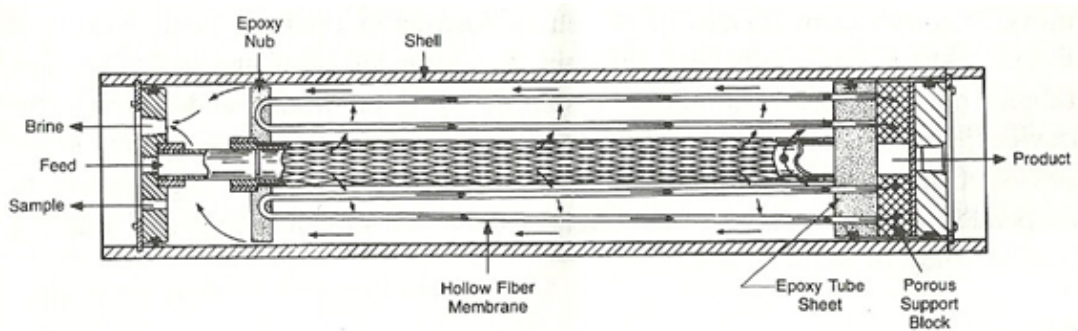
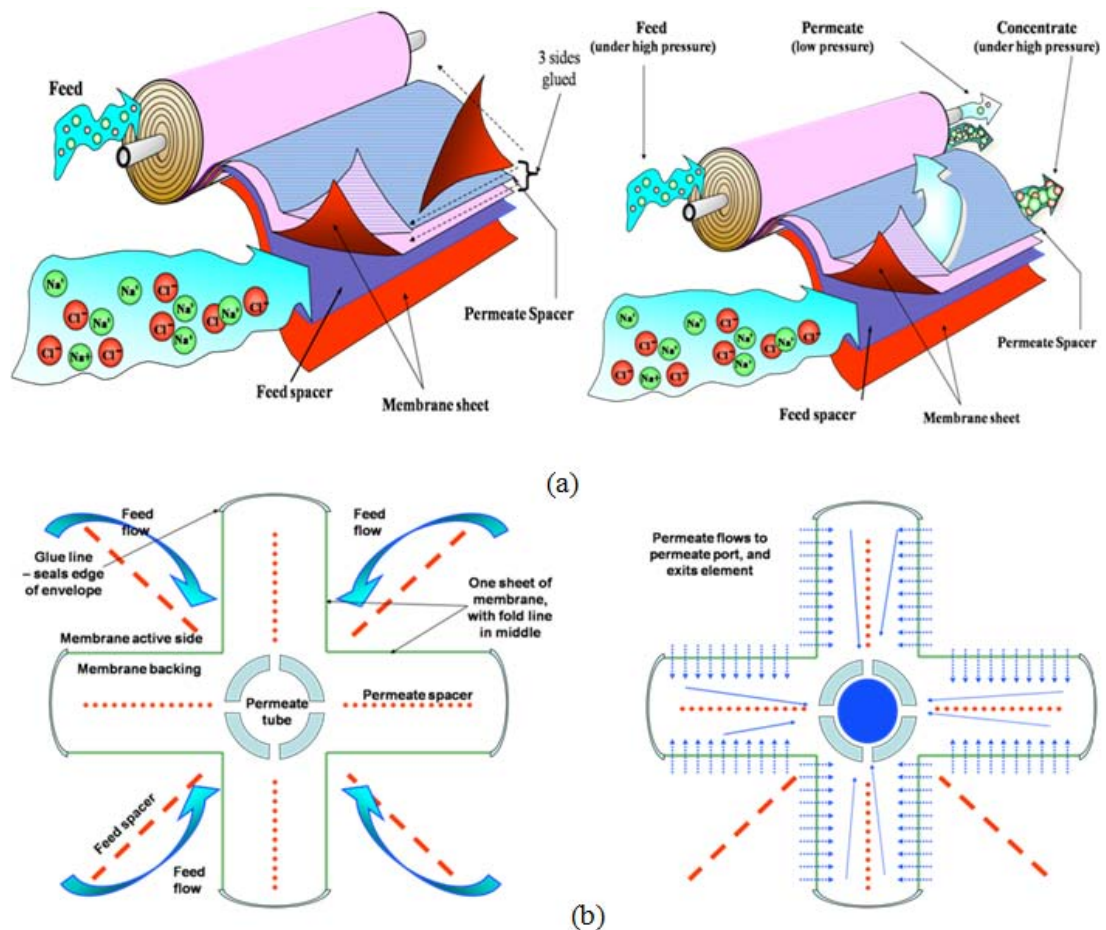


Figure 2.5: Hollow fiber module (source:[40]).

#### 2.1.4 Spiral Wound Module (SWM)

Spiral Wound configuration is one of the most popular modules commercially used due to moderate to large surface area per unit volume. They are made up of flat membrane sheets which are glued together at three sides and contains permeate

spacer between them. This arrangement referred to as membrane envelop is connected at the fourth open side to a central perforated tube called permeate collection tube. Between two consecutive membrane envelops feed spacer is inserted and the assembly is wound tightly around the central perforated permeate tube. This tight spiral coil is then housed in an outer casing. The function of the permeate spacer is to support the membranes without collapsing under high pressure and also to conduct permeate to the inner perforate central permeate tube. The feed spacer used between the membrane envelops provide the flow passage to the feed and hence define the channel height and also develops some secondary flow patterns at the feed side of the SWM which can be beneficial for the mass transfer of the solute away from the membrane surface back to the bulk flow [17, 39, 40].



**Figure 2.6: Flow paths for feed (a) and Permeate (b) in SWM (Source: Adapted from presentation of guest lecturer from HATCH QED at Curtin University.).**

Design and the flow path through a SWM are shown in Figure 2.6 (a & b). Figure 2.6 (a) shows the feed stream entering and permeate stream leaving the module in a

partial unwound state. It also shows the assembly of membrane envelop by gluing three sides of two flat sheet membranes.

Pressurised feed is allowed to pass through narrow feed spacer filled channels. Liquid permeating radially through the membrane surface enters the membrane envelop and guided by the permeate spacer to follow a spiral path to the central perforated permeate collection tube and eventually removed through a permeate port. Figure 2.6 (b) represents the end view of a SWM and shows the paths followed by the feed and permeate streams.

The axial pressure losses over the length of the leaf, due to the presence of feed side spacers and the radial pressure losses over the width of the leaf, due to the presence of permeate spacer produce a distribution of transmembrane pressure drop. SWM are available commercially in 2.5, 4 and 8 inch. These modules are fitted in standard pressure vessels which can connect several elements in series with O-ring seals in order to prevent feed to permeate flow and bypassing [39].

The individual geometry of a SWM is characterised by the number of leaves, length and width of the leaves. The feed and permeate channel heights are described by the individual feed side and permeate side spacers respectively. The filaments are further described by the porosity, hydraulic diameter, thickness, orientation with respect to each other and with the flow direction and also by the filament mesh and respective shapes.

Figure 2.7 represents a spiral wound membrane leaf before being wrapped around the central tube. Feed solution flowing along x-axis, enters at  $x = 0$  and exits at  $x = L$ . Permeate flows along y-axis. The closed end of the permeate channel is at  $y = 0$ . Permeate exits the permeate flow channel and enters the collection tube at  $y = W$ . The adjustable operating conditions are feed pressure, feed flow rate, feed concentration and permeate tube pressure.

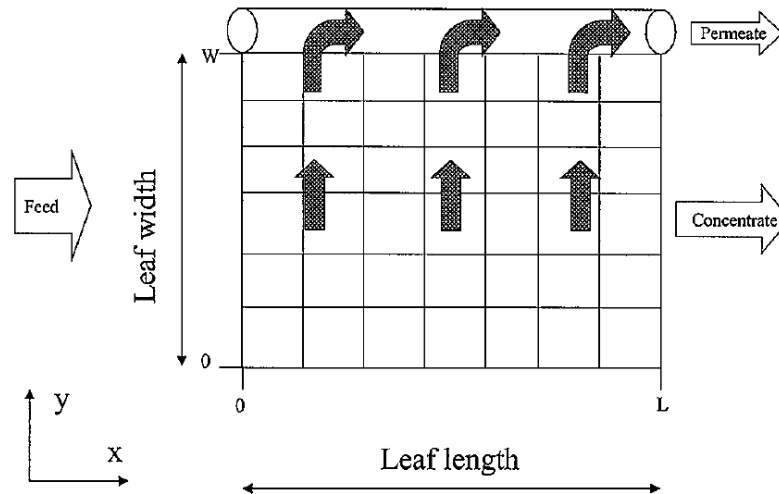


**Figure 2.7: A single flat leaf of SWM in un wound state showing flow direction across the leaf.**

Major challenges for SWM are concentration polarization, fouling and high pressure loss. The performance of SWM is affected by the following main factors [6]:

- The geometry of the membrane leaves wound spirally to the central tube. This may include the length, width and the number of leaves used.
- Feed side and permeate side channel heights, which is the direct representation of the feed and permeate side filament thickness
- Spacer's orientation, shape, dimensions and mesh. Since the feed spacer is meant to induce secondary flow patterns to enhance mass transport of the solute away from membrane walls, but at the same time may lead to higher pressure losses.
- Fouling tendency and cleaning ability
- Operating conditions, especially, feed concentration and pressure, percentage permeate recovery and nature of feed pre-treatment.

Individual spiral wound elements are connected in series and housed in a pressure vessel. As a result of this arrangement concentrated stream exiting one element becomes the feed stream for the next element. The individual permeate tubes of the elements are connected and the final permeate stream is a blend of permeate streams from all the individual elements. Desired system recovery and capacity is achieved by connecting the pressure vessels in parallel and by reject staging [40].

Following section covers the important parts of spiral wound membranes in pressure vessel.

## 2.2 Important parts of spiral wound membrane

The important parts of spiral wound membrane in pressure vessel are shown in Figure 2.8.

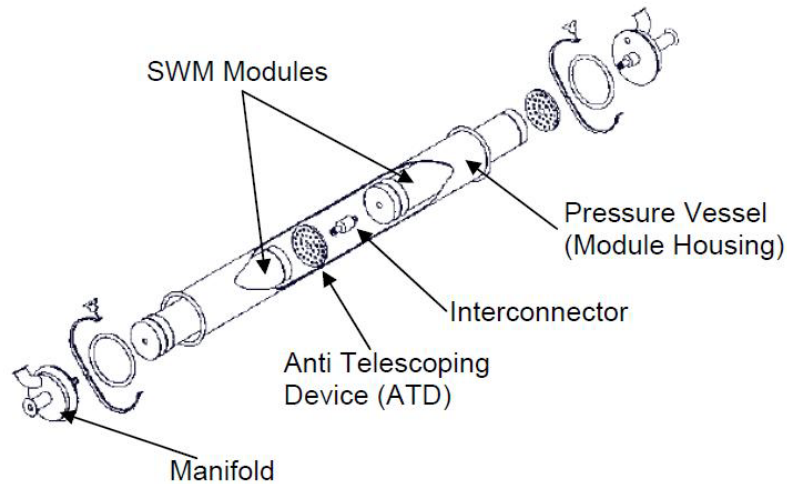


**Figure 2.8: Parts of spiral wound membrane in pressure vessel (Dow Water Solutions, 2007).**

### 2.2.1 Permeate collection tube

Permeate collection tube is the central part of the element with perforations. Membrane envelopes are connected to the tube at the fourth (unglued) side. The membrane envelopes having permeate side spacer inside and feed side spacers in between the consecutive envelopes are all wound spirally around this central tube. During the normal course of operation, the permeate flows through the membrane and adopts a spiral flow pattern due to the packing design and presence of permeate spacer, and get collected in this tube. Apart from collecting permeate it also provides structural strength to the element [39]. Common materials for construction of the permeate collection tube is shown in the following Table 2.1.

**Table 2.1: Materials for permeation collection tube (source: Dow Water Solutions, 2007)**

<b>Material</b>	<b>Application</b>
Noryl/ABS	Low pressure, ambient temperature environments with few Chemical compatibility problems.
PVC	High pressure seawater application. (Inexpensive)
Polysulfone	Wider temperature and pH range with chemical resistant required environment.
Aluminum	Extremely high pressure environment.
Stainless Steel	Extremely high pressure environment with chemical resistant required environment.

### **2.2.2 Permeate spacer**

Permeate spacer is inserted in the membrane envelop and faces the non-active (membrane backing) side of the membranes. They are meant to guide the permeate flow to the central perforated tube in a spiral pattern (due to being spirally wound) and also serves the purpose of bearing the operational pressure and prevent the membrane from collapsing and hence prevent blockage of the flow path. In other words their presence is necessary at the permeate side to minimize the membrane compaction. Under excessive forces and/or temperature membrane backing material tend to undergo plastic deformation when pressed against the permeate spacer, a phenomena called intrusion. As a result the pattern of the permeate spacer is imprinted on the membrane. The surface of the permeate spacer should be smooth to prevent this intrusion. Compaction and intrusion may occur simultaneously and hard to be distinguished from each other and are more likely to occur under high feed pressure, high temperature and water hammering (when the high pressure pump is started with air in the system). The result of membrane compaction is decrease in permeate flux. Compaction rate is directly proportional to the increase in temperature and pressure. Compaction of RO membrane occurs over time and hence requires higher feed pressure with time. That is the reason the feed pumps are designed keeping in view the operational requirements for the third operational year. In case of Cellulose Acetate membrane compaction occurs if they are operated at higher than normal pressures for extended hours. Whereas, Polyamide membranes having higher

structural strength can be operated at higher than normal pressures with little concern to compaction.

Thickness of permeate spacer normally used in SWM lies in the range of 0.2 to 0.4 mm, which is significantly lower than that for the feed spacer and the porosity is also on the lower side compared to feed spacer. Usually the permeate spacer is made up of tricot material, generally described as epoxy or melamine coated polyester that has been woven. This type of spacer is adequate for normal operating pressures, however for aggressive environments, high operating pressure or temperature various patterns of metallic web or net are suggested [41].

### **2.2.3 Feed spacer**

Spacer used in feed channel is a net-type sheet made up of low density polypropylene filaments. The arrangement of spacer is such that one set of parallel filaments are placed on the top of another set of parallel spacers. Usually the thickness of feed spacer is in the range of 28 mils to 34 mils (1000mils=1 inch). Filaments that constitute the feed spacer usually have thickness less than 1mm. The height of the feed channel is defined by the feed spacer thickness [39, 42]. The porosity for feed spacer is significantly higher than that of the permeate spacer.

The net spacer in the feed channel not only keep the membrane layers apart, hence providing passage for the flow, but also significantly affect the flow and concentration patterns in the feed channel. On one hand they are responsible for the pressure drop and limited flow zones (dead zones) creation, and on the other hand they are responsible to promote mixing between the fluid bulk and fluid elements adjacent to the membrane surface. In other words they are intended to keep the membranes clean by enhancing mass transfer and disrupting the solute concentration boundary layer. Several experimental and theoretical studies were carried out to shed light on these phenomena and to optimize spacer configuration [19-24]. So it is quite understandable that the presence of these spacers promotes directional changes in the flow which reduces membrane fouling and concentration polarization. Hence the efficiency of a membrane module depends heavily on the efficacy of the spacers to increase mass transport away from the membrane surface into the fluid bulk by increasing shear rate at the membrane surface[25].

Since spiral wound membranes have tightly wrapped structures which cannot be opened easily for chemical cleaning or cannot be back flushed by operating in reverse direction. So the fouling control methods for SWM are limited to hydrodynamics, pretreatment of the feed and operational controls [26]. The fouling issues can be addressed to a larger extent by varying the hydrodynamic conditions prevailing in spiral wound membrane. The feed spacers can be oriented to generate high cross flow velocities or secondary flow patterns which can develop higher scouring forces on the membrane surface to reduce fouling and concentration polarization. However this approach will require higher pumping energy to compensate losses within the membrane module. Hence the feed spacers must be optimized to reduce the buildup on the membrane surface with moderate energy loss.

Various types of feed spacer are being used by different manufacturers depending of the feed and operational conditions, such as: suspended solids, viscosity, temperature, presence of fouling species, precipitation or crystal formation propensity are a few to name. Generally, the spacers are available in diamond or ladder array with mesh size of 4 to 5 mm [39].

Geometry of spacers used in SWM can be characterized with the help of some important parameters shown in Figure 2.9. In the figure  $d_b$  and  $d_t$  represent diameters of bottom and top filaments, whereas  $l_b$  and  $l_t$  represents the mesh spacing of bottom and top filaments respectively. The flow attack angles that top and bottom filament makes with the y-axis are represented by  $\theta_1$  and  $\theta_2$  respectively. Whereas  $\alpha$  is angle between the top and bottom crossing filaments. It is evident from the geometry description that the available channel height  $h_{ch}$  is sum of the filaments diameters in top and bottom layers.

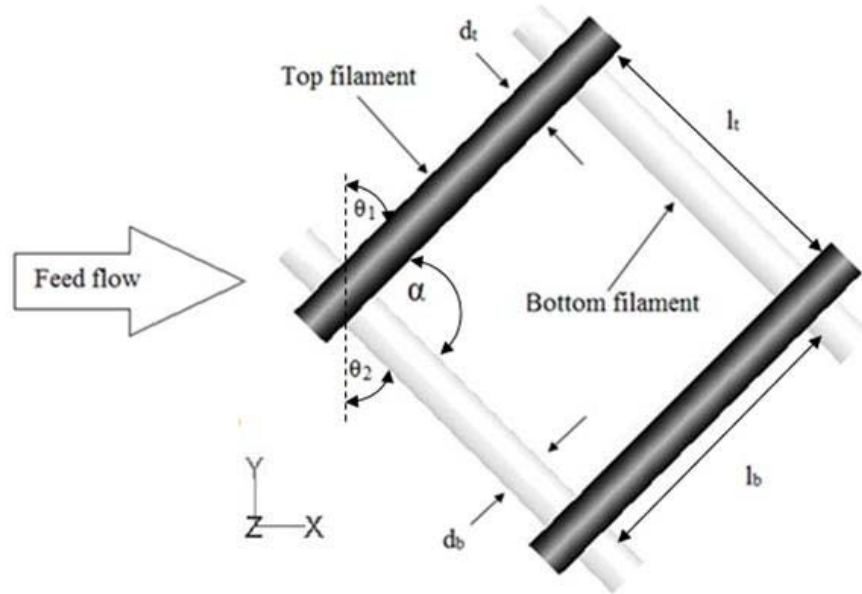


**Figure 2.9: Geometric characterization of feed spacer.**

Figure 2.10 shows the ladder (square) spacer arrangement in which the orientation of the bottom filament is transverse to the flow direction, whereas the top filaments are in axial direction to the flow hence making the flow attack angle (with Y-axis of flow direction) for the top and bottom filaments to be  $90^\circ$  and  $0^\circ$  respectively and the angle between top and bottom filaments is  $90^\circ$ .

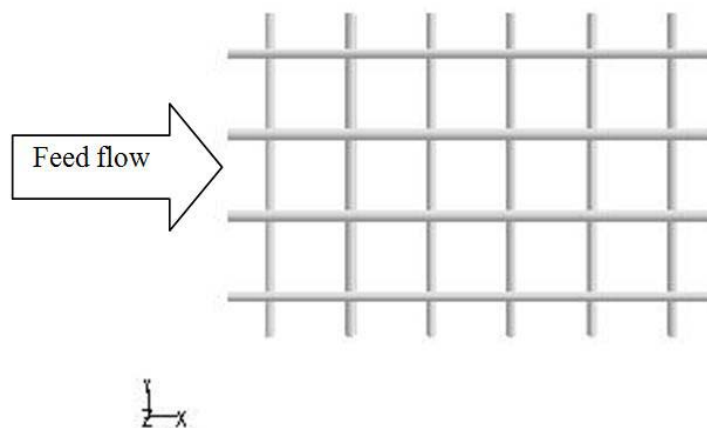


**Figure 2.10: Square (ladder-type) spacer arrangement.**

Literature review reveals that the spacer parameters are usually non-dimensionalized by using channel height ( $h_{ch}$ ). The ratio of filament diameter to the channel height

( $D = d/h_{ch}$ ) is referred to as dimensionless diameter whereas the ratio of filament mesh size to the channel height ( $L = l/h_{ch}$ ) is known as dimensionless filament spacing.

#### **2.2.4 Anti telescoping device (ATD) and Brine seal**

Telescoping or longitudinal unravelling of a spiral wound element is caused by excessive pressure differential between the feed and concentrate ends of the element and results in the extension of the membrane beyond the spacer material. This can cause damage to the outer wrapping and may allow water to flow on the outside of the element. Consequently, this will lead to reduction in the crossflow across the membrane and will facilitate fouling potential. Telescoping may also stress the glue line and in extreme cases may lead to glue line failure.

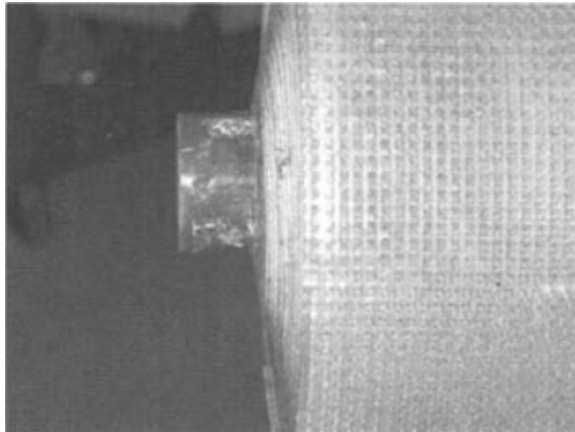


**Figure 2.11: Uniform telescoping (Source [42]).**

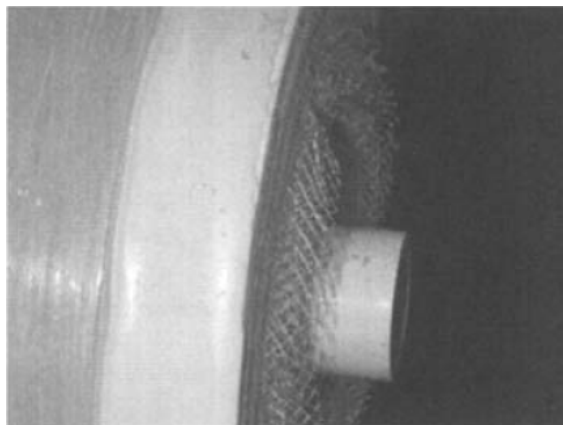


**Figure 2.12: Telescoping Protruding feed spacer (Source [42]).**

To prevent the telescoping potential of the elements, Anti telescoping devices are used at feed and concentrate end of the cartridge. They provide open flow path as well a structural sport to the cartridge.

Anti telescoping devices have two major roles to play. At the upstream side or feed end they are meant to carry the brine seal (hence they are also referred as seal carriers in literature) which prevent the feed to by-pass the membrane and at the downstream side or the concentrate end they are meant to support the back face of the element and prevent the membrane leaves to elongate longitudinally due to pressure differential across the element. Bartels et al. [43], has come up with an improved design for these devices which is also helpful to vent trapped air in the annular gap between the pressure vessel walls and outside of the elements.

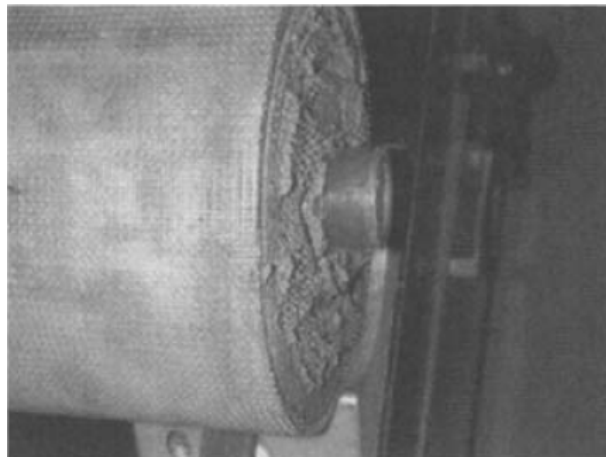


**Figure 2.13: Telescoping Protruding membrane and feed spacer (Source [42]).**

Despite the presence of the ATD telescoping may occur if the pressure drop is high enough for an extended period of time. Telescoping can be uniform as shown in Figure 2.11, it may involve the feed spacer as shown in Figure 2.12 or it can also involve the membrane and the feed spacer as shown in Figure 2.13.

Spiral wound membranes are also equipped with brine seal to prevent the feed water by-passing the membrane. Brine seal is U-cupped shaped gaskets material mounted on the ATD present on the inlet end of the membrane module. Figure 2.14 shows the ATD mounted with U-cupped shaped brine seal.

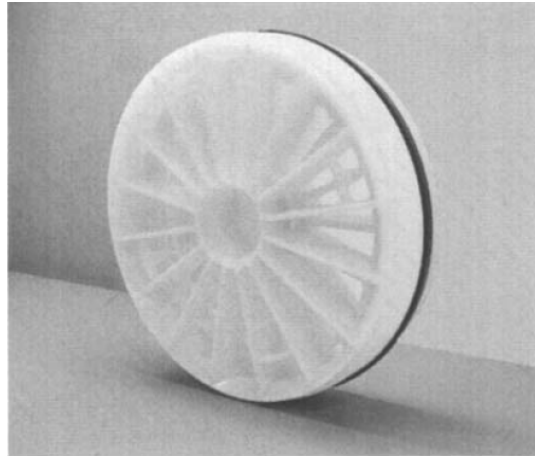


**Figure 2.14: ATD mounted with U-cupped shaped brine seal (Source [42]).**

### **2.2.5 Module interconnector**

Module interconnector or interconnector adapter are used to connect modules with each other. Figure 2.15 shows the module interconnector with O-ring. These interconnectors have O-rings at both the ends to ensure a tight seal with the module Anti Telescoping Devices (ATDs).

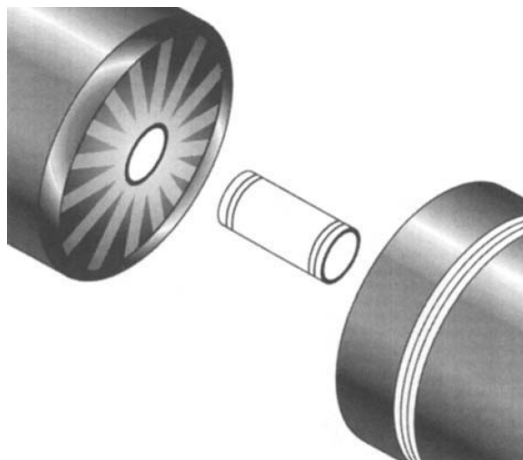


**Figure 2.15: Placement of module interconnector adapter for standard ATD end caps (Source [42]).**

While connecting the modules using standard ATD end caps having O-rings, there are chances that the O-rings may roll into the membrane module consequently allowing feed and permeate to mix and effecting the process adversely. So while connecting the modules great care must be exercised to prevent rolling of the O-Rings. At time lubrication may minimize the friction and rolling potential of the O-Rings.

Dow Chemical Company has introduced a new design of ATD for iLEC™ membrane module which does not rely on the separate interconnecting adapters. The ATD iLEC™ end cap comes with an integral O-ring which cannot be rolled or pinched during installation. They also claim that the water hammer cannot wear on the O-Ring as it does on conventional interconnector's O-Ring, which consequently minimize the feed water leakage propensity to the permeate [42]. Figure 2.16 shows Dow Water Solutions- FilmTec iLEC™ ATDs with integral O-Ring.

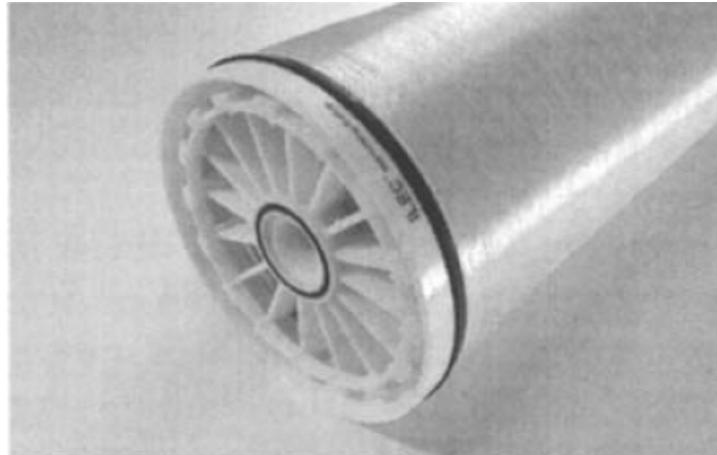


**Figure 2.16: Dow Water Solutions- FilmTec iLEC ATDs with integral O-Ring (Source [42]).**

To connect two iLEC modules a strap wrench is used to hold one module in place while the other iLEC module is twisted onto the first module as illustrated in Figure 2.17.

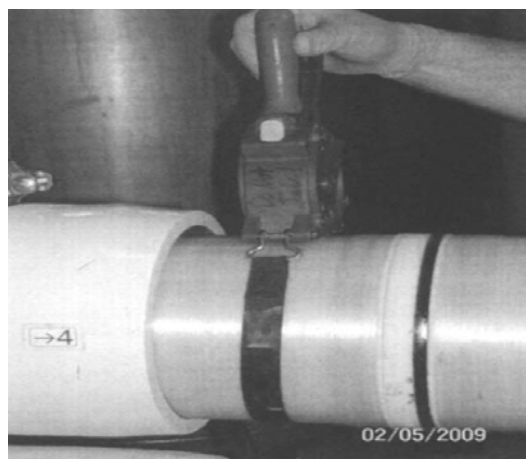


**Figure 2.17: Using a strap wrench with iLEC membranes (Source [42]).**

SWM are typically covered in fibreglass for mechanical strength and to protect the membrane leaves. Because of the adhesive used and the potential for annealing the membrane the maximum operating temperature is limited to 45<sup>0</sup>C [42].

### 2.2.6 Pressure vessel

SWM are connected in series and placed in external pressure vessel (also referred to as pressure housing in literature) for use. Depending upon the operational requirement they are available in various pressure ratings [42] :

- Water softening (Nanofiltration) : 50 psig to 150 psig
- Brackish water reverse osmosis : 300 psig to 600 psig
- Seawater reverse osmosis : 1000 psig to 1500psig

A variety of pressure vessels are available to accommodate 2.5 inch to 18 inch diameter industrial modules. Their length can be as short as to accommodate only one module and they can be as long to accommodate seven modules in series. Figure 2.18 shows a pressure vessel housing six SWM connected in series.

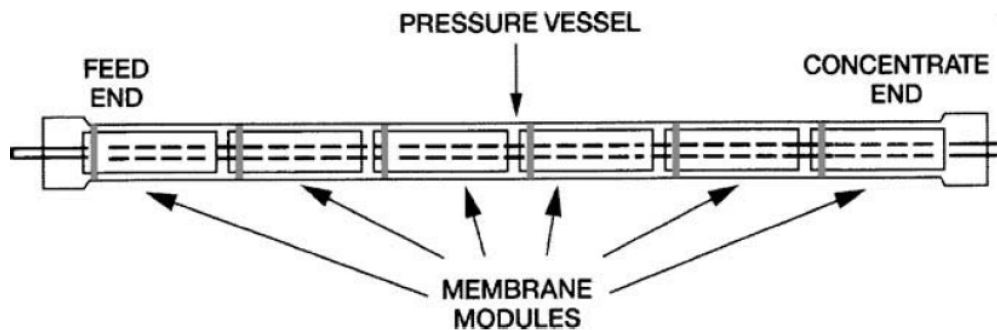
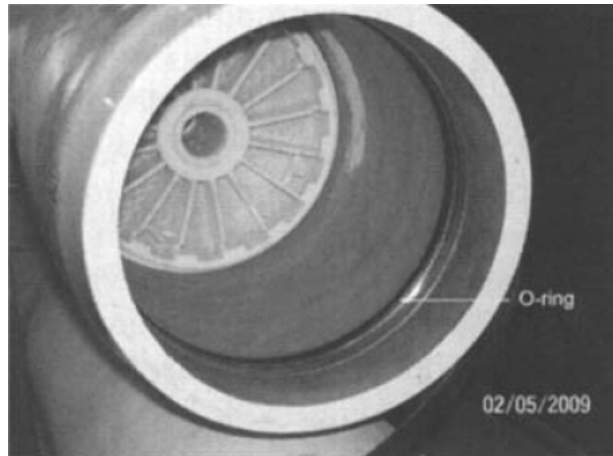


Figure 2.18: Six SWM housed in pressure vessel in series arrangement (Source [42]).

Figure 2.19 shows the end of a SWM in a pressure vessel without pressure vessel end caps where as Figure 2.20 shows a pressure vessel with end cap and permeate effluent piping installed.



**Figure 2.19: SWM in pressure vessel without pressure vessel end cap in place (Source [42]).**

To facilitate the module replacement in the pressure vessel, the vessels with side-entry and exit for feed and concentrate are preferred over end-entry configuration. This is because in the former case the amount of piping that has to be disconnected to facilitate module replacement is considerably minimized i.e., only the permeate piping has to be disconnected. In both configurations permeate exits through the end of the pressure vessel as shown in Figure 2.20 [42].



**Figure 2.20: Pressure vessel with permeate effluent piping and end cap installed (Source [42]).**

The sequence of loading or installing the membrane modules in the pressure vessel is very critical. The modules should be loaded in the direction of flow. That means to follow the following sequence [42]:

- Concentrate end of the first module (end without the brine seal) is inserted in the pressure vessel first. The O-Ring on the conventional module

interconnector and brine seal of the first module put in are lubricated with silicon, water or glycerine to facilitate installation.

- The feed end of the first module put in is then connected with the concentrate end of the second module put in and the arrangement is push in the flow direction by adding more modules in series in the similar fashion.
- The procedure described above is followed till the required number of modules (depending on the pressure vessel design) is installed in the pressure vessel. As a result of this arrangement, the module that was put in first in the pressure vessel becomes the last module of the series.

The modules are removed also in the flow direction. That means, the module that was put in first in the pressure vessel (last module of the series) will be the first one to be pulled out.

### 2.3 Module Characteristics

Different module designs have some advantages and disadvantages associated with them and before selecting a particular design for a given application its various characteristics must be probed in. Table 2.4 represents characteristics of different module designs.

**Table 2.2: Characteristics of different modules (Source: Adapted from [39])**

Characteristic	Plate & frame	Spiral wound	Tubular	Hollow fiber
Packing density (m <sup>2</sup> /m <sup>3</sup> )	Moderate (200-500)	High (500-1000)	Low-moderate (70-400)	High (500-5000)
Energy Usage	Low-moderate (Laminar)	Moderate (spacer-losses)	High (Turbulent)	Low (Laminar)
Fluid management & fouling control	Moderate	Good (no solids) Poor (solids)	Good	Moderate-good
Standardisation	No	Yes	No	No
Replacement	Sheet (or cartridge)	Element	Tubes (or element)	Element
Cleaning	Moderate	Can be difficult (solids)	Good-physical clean possible	Back flush possible
Ease of manufacture	Simple	Complex (automated)	Simple	Moderate
Limitation to specific types of membrane	No	No	No	Yes

As shown in table, hollow fiber modules have high packing density compared to SWM, but due to good and balanced mix of operational ease, fouling control, permeation rate, less limitations to specific types of membranes and packing density SWM is preferred over its counterpart for industrial applications. SWM are used commercially in industrial application ranging from UF to RO. They are used worldwide for water treatment, desalination, water reclamation, waste water treatment, pharmaceuticals and in dairy industry [44-48]. Another advantage of SWM is being Industrial standard which provides wide choice of membranes and opportunity to refurbish with alternative membranes. However, they are complex to manufacture, but commercially they are now produced on automatic or semi-automatic production facilities. They can also be used to treat dirty feeds, provided extensive and effective pre-treatment procedures are carried out before letting the feed stream to enter the modules.

Due to complexity and engineering involved SWM are moderately expensive, but cost per unit membrane area is relatively low. It is relatively difficult to clean SWM due to the development of dead pockets within module where the high velocity fluid cannot scour the membrane surface and also cleaning solutions do not mix well to remove the debris. High quality modules manufactured on automated facilities have higher packing density ( $\text{m}^2$  membrane/ $\text{m}^3$  module volume) due to precise glue line application on membrane leaves and hence are cost effective. For example, if automated manufacturing is employed a module having 8 inches diameter and 40 inches length can hold up to  $400 \text{ ft}^2$  of membrane area [42].

## **2.4 Basic definitions and concepts**

In the following sections some important definitions and concepts are presented which have been used extensively in the published literature and research regarding membrane systems and SWM modules. Also, for understanding the work presented and conclusion drawn in this thesis these terms will be helpful.

### **2.4.1 Osmosis and Reverse Osmosis**

Osmosis is the movement of water molecules, through a semi-permeable membrane, from an area of low solute concentration to an area of higher solute concentration

until the concentration on both sides of the membrane becomes equal. The membrane separating the two solutions is permeable to water molecules and impermeable to solute molecules. This phenomenon will also take place if the pressure on both sides of the membrane is different, as long as the pressure difference  $\Delta P$  between the concentrated side and the dilute side is not larger than a certain value that depends on the difference of the respective concentrations and is called Osmotic Pressure difference ( $\Delta \pi$ ). If the pressure differential  $\Delta P$  is larger than  $\Delta \pi$ , direction of flow will be reversed and it will start flowing from an area of higher solute concentration to an area of lower solute concentration. This philosophy is used in Reverse Osmosis (RO) operations. In desalination the feed water has higher salt content as compared to that of the permeate (having negligible solute concentration) and hence will have a greater osmotic pressure than that of the permeate side. If feed side is operated under elevated pressure flow of water through the membrane will be observed (from feed to permeate) as long as the differential pressure is greater than the osmotic pressure of the feed side. The major energy required for desalinating (using membrane module) is for pressurizing the sea feed water. There is no heating or phase change requirement associated with the process. Figure 2.26 represents the schematic representation of osmosis whereas Figure 2.27 refers to osmosis and reverse osmosis.

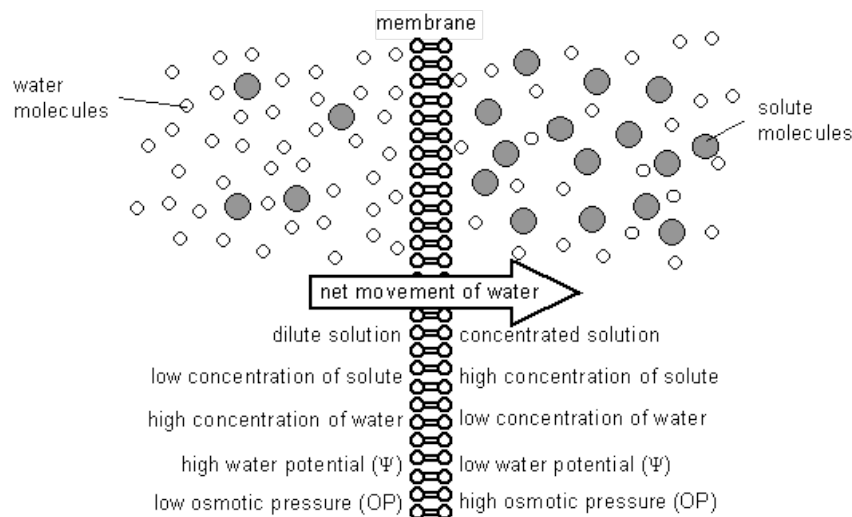


**Figure 2.21: Characteristics of polyamide composite RO membranes (source: <http://www.biologymad.com>, 2004).**

In Reverse Osmosis (RO) an external pressure in excess of the osmotic pressure of the feed water is applied. As a result, the natural direction of flow of water through a semi-permeable membrane is reversed. The Retentate (reject stream) left behind has a higher salt concentration as compared to permeate (product stream). The major energy intensive part in seawater RO process is the high pressure pump used to create a pressure of 60 to 80 Bar. However the pressure requirement to treat brackish water is considerably on a lower side (about 15 bars) compared to that required in desalination of seawater [7].

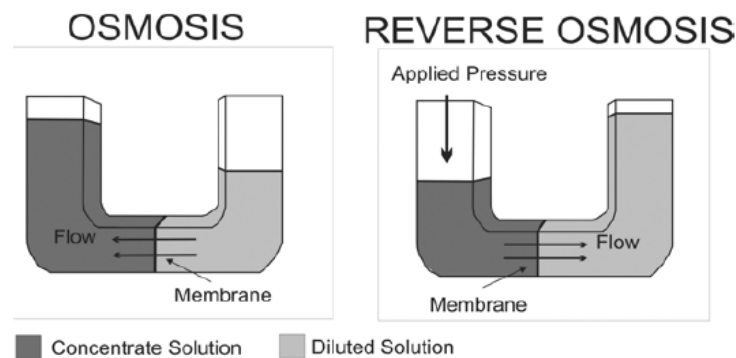


Figure 2.22: Osmosis and reverse osmosis (Source: [7] ).

## 2.4.2 Osmotic pressure

Osmotic pressure of a solution depends on the solute concentration, ionic species present and temperature. As a rule of thumb the osmotic pressure of a solution having predominantly sodium chloride at ambient temperature is 10 psi (0.7 atm) per 1000 mg/l concentration [7]. Osmotic pressure ( $\pi$ ) for a dilute solution can be approximated by van't Hoff equation [1]:

$$\pi = v_i c_i R T \quad (2.4.2 - 1)$$

In the above equation,  $\pi$  represents Osmotic pressure,  $c_i$  is the solute molar concentration,  $v_i$  represents number of ions formed on solute dissociation (for instance, 2 for NaCl and 3 for BaCl<sub>2</sub>), R is the universal gas constant and T represents absolute temperature.

For concentrated solutions a coefficient called “osmotic coefficient” is introduced in the above equation which can be obtained from vapour pressure data or freezing point depression of the solution [49]. For brackish water Van't Hoff equation can be

used. In case of seawater experimental osmotic pressure data obtained for seawater solutions may be used [4].

Due to added resistance of the membrane in a RO system the required to achieve reverse osmosis is significantly higher than the osmotic pressure. For instance, in case of brackish water having 1500 TDS (Total Dissolved solids) the operating pressure is in the range of 150 to 400 psi and for seawater having 35000 TDS the operating pressure as high as 1500 psi may be required [42].

### 2.4.3 Recovery

Reverse Osmosis systems are rated on the basis of product flow rate. For instance, a unit having a rating of 1000 gpm (gallons per minute) means it is designed to generate 1000 gallons of permeate per minute at defined feed conditions. Recovery in context of RO system is defined as the volume percent of influent water recovered as permeate. For instance, a RO system having a recovery of 75% means for every 100 gpm of influent water 75 gpm is recovered in the form of permeate stream and 25 gpm is rejected in the form of concentrate stream. Generally, the recovery for RO system lies between the range of 50 to 85% and the recovery for individual SWM modules are in the range of 10 to 15%. Majority of RO systems are designed at 75 % recovery [42]. Recovery is calculated using the following equation:

$$\% Recovery = \frac{\text{Permeate flow}}{\text{Feed flow}} \times 100 \quad (2.4.3 - 1)$$

Let's assume a system having a recovery of 75%. It means that the three-fourth of the total influent volume permeates through the membrane leaving behind one-fourth of the total permeate volume at the concentrate side. If it is further assumed that the all the dissolved solids are retained by the membrane then one-fourth of the total influent volume at the concentrate side will have concentration of dissolved solids 4 times that of the influent stream. This is known as concentration factor (since all the dissolved solids are not retained by the membrane, it is just an approximation). Similarly, In case of 50% recovery concentrate volume will be one-half of the influent volume and the concentration of dissolved solids will increase by a factor of 2. Table 2.5 summarize the concentration factor as a function of recovery. A higher recovery calls for smaller volume of rejected water to be disposed off. But at the

same time it will concentrate the feed side of the membrane enhancing the fouling potential and it will also lead to low-purity permeate.

**Table 2.3: Concentration factor as a function of Recovery.**

Recovery (%)	Concentration factor
50	2
66	~ 3
75	4
80	5
83	6
87.5	8

The discussion in the previous paragraph can be explained with the help of Figure 2.28. Consider a membrane that allows 2% of the total dissolved solids (TDS) to pass through it. Let at the influent end of the membrane the concentration of TDS is 100 ppm and recovery is 0%. Permeate right at that particular spot will have a concentration of 2 ppm. As the influent water passes across more and more membrane area, more water is recovered as permeate. Since the concentration factor is 2 at 50% so the influent water will have a concentration of 2 ppm and that for the permeate at that particular spot will be 4 ppm. Similarly at 75% recovery, the concentration of the influent water will be 400 ppm (as the concentration factor is 4 at 75% recovery) and at that particular spot the concentration of the permeate will increase to 8 ppm. Hence it may be concluded that higher recovery results in higher concentration of TDS at the concentrate side of the membrane and also effect adversely the purity of permeate.

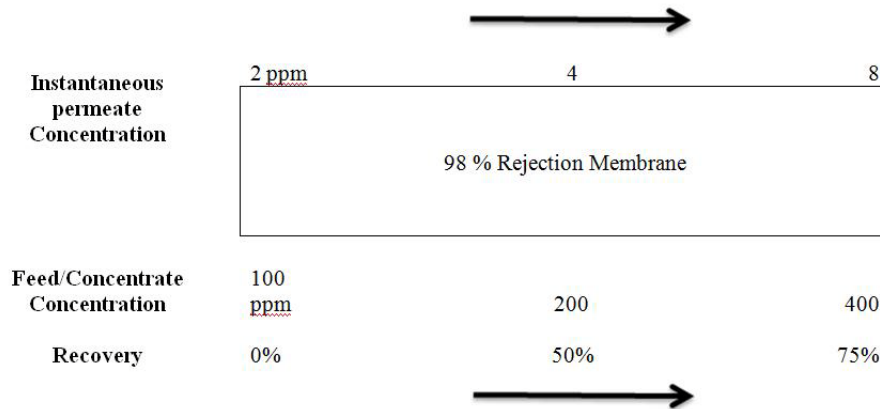


**Figure 2.23: Concentrate and instantaneous permeate concentration as function of recovery.**

In practice, a control valve is installed at the concentrate stream of RO system to control the recovery. Throttling the control valve results in higher operating pressure forcing more water through membrane as opposed to down along the feed/concentrate side of the membrane and hence results in high recovery.

Recovery of a RO system is set by the system designer. Exceeding the optimum recovery will result in less water with higher concentration of dissolved solids on the concentration end which indirectly means more TDS and less water to scour the membrane surface at the concentrate side which eventually leads to accelerated fouling and scaling. However operating the system at lower recovery will not have an adverse effect on membrane scaling or fouling, but it will lead to higher volume of waste or rejected water through the RO system.

#### **2.4.4 Rejection, salt passage and Differential pressure**

The term rejection means what percentage of a particular species present in the influent will be retained by the membrane [42]. For instance a membrane having 98% rejection of silica will allow 2% of the influent silica to pass through it (also referred to as salt passage) and will retain 98% of the influent silica. Rejection is defined by the following equation:

$$\% \text{ Rejection} = \frac{C_{f,i} - C_{p,i}}{C_{f,i}} \times 100 \quad (2.4.4 - 1)$$

Where:

$C_{f,i}$  = influent concentration of a specific component

$C_{p,i}$  = permeate concentration of a specific component

It is important to note that for exact calculations, instead of using feed concentration at a point in time an average value for feed concentration that accounts for both feed and concentrate concentration should be used for rejection calculation.

Salt passage is defined by the following equation and is just the opposite of rejection.

$$\% \text{ Salt Passage} = 100 - \% \text{ Rejection} \quad (2.4.4 - 2)$$

$$\% \text{ Salt Passage} = \frac{C_{p,i}}{C_{f,i}} \times 100 \quad (2.4.4 - 3)$$

Rejection is property of a particular membrane and a particular species present in the feed water. General rejection capabilities of most polyamide composite membranes are shown in Table 2.6.

Ionic charge on the species plays an important role in rejection by RO membranes. Generally the rejection rate of multi-valent ions is greater than that for mono-valent ions. In addition to the ionic charge rejection also depends on the following characteristics of the species [42]:

- Degree of dissociation: Generally, higher rejection is noticed for species have higher degree of dissociation. For instance, weak acids at higher pH are rejected better.
- Molecular weight: Generally, species having higher molecular weights have higher rejections than those with lower Molecular weights. For instance, rejection of Calcium is marginally better than that of Magnesium as apparent from Table 2.6.
- Polarity: Generally, rejection of species having low polarity is usually higher. For instance, organics are rejected better than water.
- Degree of hydration: Generally, rejection of species having higher degree of hydration is usually higher. For instance, rejection of chloride is better than nitrate
- Degree of molecular branching: Generally, species having higher degree of molecular branching are usually rejected better than those with lower degree

of molecular branching. For instance, rejection of isopropanol is better than normal propanol.

**Table 2.4: General rejection capabilities of most polyamide composite membranes at room temperature (Source: [42]).**

Species	Rejection (%)
Sodium	92 - 98
Calcium	93 - 99+
Magnesium	93 - 98
Potassium	92 - 96
Iron	96 - 98
Manganese	96 - 98
Aluminum	96 - 98
Ammonium*	80 - 90
Copper	96 - 99
Nickel	96 - 99
Zinc	96 - 98
Silver	93 - 96
Mercury	94 - 97
Chloride	92 - 98
Bicarbonate	96 - 99
Sulfate	96 - 99+
Fluoride	92 - 95
Silicate	92 - 95
Phosphate	96 - 98
Bromide	90 - 95
Borate	30 - 50
Chromate	85 - 95
Cyanide	90 - 99+

\* Below pH 7.8. Above this pH, ammonia exists as a gas that is not rejected by RO membranes

Differential pressure drop ( $\Delta p_d$ ) is defined as the difference between the feed pressure ( $p_f$ ) and the concentrate pressure ( $p_c$ ) and is represented by the following equation:

$$\Delta p_d = p_f - p_c \quad (2.4.4 - 4)$$

A significant rise in the differential pressure (normally 15% of the specified value), reduction in salt rejection and reduced recovery are the symptoms of poor performance and need immediate attention to rectify the cause(s).

### 2.4.5 Flux, Permeability and Permeance

In the context of RO, flux is defined as the volumetric flow rate of water per unit membrane area. Flux through RO membrane is directly proportional to the net pressure driving force applied to water and can be expressed by the following equation [42]:

$$J = \bar{P}_m (\Delta P - \Delta \pi) \quad (2.4.5 - 1)$$

In the above equation:

$J$  = volumetric water flux

$\bar{P}_m$  = water transport coefficient or Permeance = permeability / thickness of the membrane active layer

$\Delta P$  = pressure difference across the membrane

$\Delta \pi$  = osmotic pressure difference across the membrane

Recommended or designed flux for a RO system is a function of influent water source and Silt Density Index (SDI), where SDI is the measure of membrane fouling tendency of the water. As already described, higher flux enhances the fouling potential of the membrane. So, for inferior influent water qualities lower fluxes are used to minimize the chances of rapid fouling.

**Table 2.5: Recommended flux as a function of influent water source (Source: [42]).**

Feed Water Source	SDI	Recommended flux, gfd *
RO Permeate	< 1	21 - 25
Well Water	< 3	14 - 16
Surface Supply	< 3	12 - 14
Surface Supply	< 5	10 - 12
Secondary Municipal Effluent -Microfiltration Pre-treatment**	< 3	10 - 14
Secondary Municipal Effluent - Conventional Pre-treatment	< 5	8 - 12

\* For 8-inch diameter, brackish water membrane modules

\*\* Microfiltration pore size < 0.5 microns.

Table 2.7 represents recommended flux as a function of influent water source (an indirect measure of water quality) and Silt density index (SDI). When in doubt a default flux of 14 gallons of water per square foot of membrane area per day (gfd) is recommended [42].

To compare the performance of one membrane with another a term called “Specific flux” or membrane permeability is used [42]. Specific flux is approximated by dividing the overall system flux with applied driving pressure:

$$\text{Specific flux} = \text{Flux} / \text{Applied pressure} \quad (2.4.5 - 2)$$

For membrane performance comparison, higher the specific flux (or membrane permeability) lower will be the required driving pressure for the RO system operation.

#### **2.4.6 Concentration polarization**

Concentration polarization refers to the accumulation of solute at the membrane surface resulting in high concentration of solute near the surface of membrane as compared to that in the bulk of solution.

During normal course of membrane filtration operations, solute and solvent are brought to the membrane surface by convective transport mechanism. Solutes which are larger than the membrane’s molecular weight cut-off are not allowed to pass and retained on the membrane surface, while solvent and smaller solute make their way through the membrane barrier and forms permeate. Rejected solutes concentrate at the membrane surface and in the concentration boundary layer up to a level where the diffusive back transport balances the convection transport of solutes to the membrane [50]. Hence, concentration polarization is reversible build-up of rejected solute near and at the membrane surface which leads to the development of concentration boundary layer as shown in Figure 2.29.

Concentration polarization depends on feed velocity, feed concentration, membrane structure and transmembrane pressure (TMP) [45, 46, 51]. It adversely affects the membrane performance and reduces the membrane throughput in three different ways:

- It tends to reduce the water flux as it acts as hydraulic resistance to water flow through membrane.

- Due to solute build-up it enhances the osmotic pressure in the concentration boundary layer which reduces the effective driving force which enables water to flow through membrane.
- It leads to higher solute passage to the permeate resulting in inferior quality of permeate as compared to what was actually predicted by the feed water concentration and membrane rejection. To understand this point, assume a feed water stream having 10 ppm of silica and the membrane used for the separation process has 98% salt rejection. So from the feed water and membrane information we can assume the resulting permeate to have 0.2 ppm of silica.

Since concentration polarization is inevitable in filtration processes lets further assume that the silica concentration at the membrane reaches a value of 11.5 ppm. Since the rejection of the membrane depends on the concentration of the species present at its surface so in this case permeate will have 0.23 ppm of silica in it ( $11.5 \times 0.02$ ). It is important to know that still the membrane has an actual rejection of 98% but the apparent rejection has fallen to 97.7%.

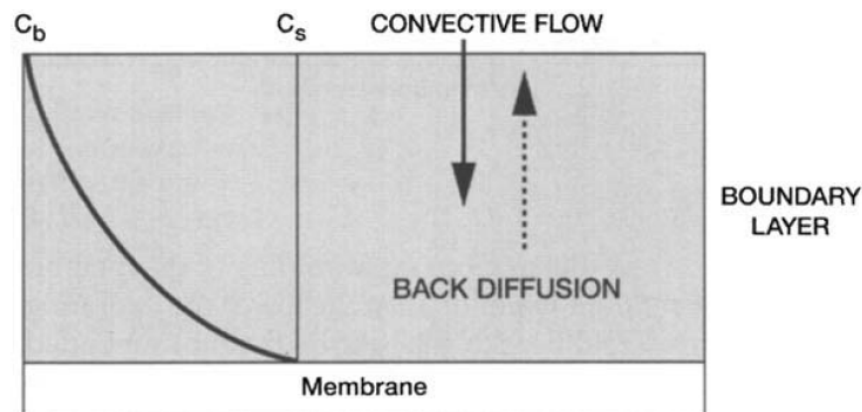


**Figure 2.24: Concentration polarisation, where  $c_b$  is the bulk concentration and  $c_s$  is the concentration at membrane surface. Source : [42].**

Concentration polarization affects almost all the membrane separation processes. In case of RO operations, development of a solute concentrated layer at the membrane surface results in higher osmotic pressure as compared to the rest of the bulk, which

consequently needs higher operating pressure to overcome the raised osmotic pressure [52, 53]. In case of Ultrafiltration macromolecular solutes and colloidal species have an insignificant osmotic pressure. In this case the concentration at the membrane surface may exceed to a point where a gel like precipitation layer is formed which results in decline of permeate flux. Thus, it is important to control or minimize concentration polarisation to have higher permeate flux at moderate energy consumption.

Concentration polarization is considered to be reversible and can be controlled in the membrane module by various means, such as : Velocity adjustment, pulsation, by an ultrasonic or electric field [51].

Concentration polarisation factor also as referred “Beta” in literature is a way of quantifying concentration polarisation and is defined as a ratio of a species concentration at membrane surface to that in the bulk solution [51] . Since higher Beta number refers to relatively higher concentration of a species at the membrane surface as compared to that in the bulk, further if the species concentration at the membrane surface reaches the saturation limit scale formation will be inevitable. Hence, higher Beta number increases the membrane fouling or scaling potential. To minimize scale formation maximum acceptable Beta typically ranges from about 1.0 to 1.2.

#### **2.4.7 Fouling**

Concentration polarization also leads to fouling, which is an irreversible loss of membrane permeability due to deposition of rejected solute, suspended solids and organics on membrane surface or into membrane pores. Fouling leads to decrease in membrane productivity, salt rejection capability and decrease the usable life span of the membrane.

Potential for a membrane to foul increases in case of higher flux requirement and low cross flow velocity i.e., for both conditions that leads to concentration polarization. In case of higher flux requirement, water is recovered by the membrane at a higher rate which leads to higher amount of rejected solutes and suspended solids in relatively lower volume of water in the concentration polarization boundary layer at the feed or concentrate side of the membrane. If resident time is long enough

these solids and rejected solutes (which may precipitates out if saturation is reached, also referred to as scaling in literature) get deposited permanently on the membrane surface and membrane pores. In case of lower cross flow velocity the thickness of the concentration polarization boundary layer increases accommodating more solids and rejected solutes in it for a longer period of time and eventually increase the fouling potential.

A fouled membrane has three major performance issues

- Higher than normal operating pressure: Since the foulants makes an additional barrier on the membrane surface through which water has to permeate. So it needs higher than normal net driving forces to facilitate water transport through the membrane to maintain the same productivity, which reflects in a higher than normal operating pressure demand for the process.
- Higher pressure drop: The foulant layer leads to an increased resistance to cross flow which translates into higher than normal pressure drop. Higher pressure drop may lead to axial pressure on the membrane module and in severe case can lead to membrane and spacer telescoping and damage to outer module casing (explained in detail in section 2.2.4).
- Lower salt rejection: If the concentration of the rejected solute(s) or any species is higher at the membrane surface than the normal bulk (concentration polarization) it will lead to lower salt rejection and more solute will pass through the membrane and will adversely affect the permeate purity (explained in detail in section 2.4.6)

In a RO system, since the concentration of salts is highest in the last stages, fouling due to salt build-up (also called scaling) will be higher in those stages. Fouling due to microbes (microbial fouling) can be anywhere in the RO system where favourable growth conditions are available. Apart from the two mentioned fouling types, the lead module (which comes in contact with feed first) of a RO system is more prone to fouling due to other species present in the feed.

A membrane can never retrieve its original flux once fouled. During normal course of operation there is continuous decrease in flux due to foulant build-up on membrane surface or in membrane pores [45, 46, 54].

Fouling of RO membranes can be reduced significantly by using appropriate feed pre-treatment methods (by using anti-scalant and biocides) and by selecting appropriate membrane material. Apart from these methods, it can be minimized by modifying hydrodynamics, especially in the feed channels and adopting other means that lead to reduced concentration polarization [51].

### 2.4.8 Mass transfer coefficient

Mass transfer coefficient parameter usually correlates mass transfer rates, contact area and concentration differences. It may be defined in different ways (local, average, global etc). Mass flux of a solute (mass transfer per unit area per unit time) is related to mass fraction gradient by Fick's law [55], and is given as:

$$J_{slt} = -\rho D \frac{dY}{dy} \quad (2.4.8 - 1)$$

Where  $J_{slt}$  is the solute mass flux,  $\rho$  and  $D$  represents density and mass diffusivity respectively and  $\frac{dY}{dy}$  is the mass fraction gradient of the solute along a particular direction (y-direction). However it is important to note that the mass fraction gradient is local one and it may present large variations within a flow field. So it is more practical to relate solute mass flux with concentration or mass fraction difference between the bulk flow and a surface, for instance membrane surface (or membrane wall). Hence for solute mass transfer at interface of solid and liquid the relation can be given as:

$$J_{slt} = \rho k_l (Y_w - Y_b) \quad (2.4.8 - 2)$$

Where  $k_l$ ,  $Y_w$ ,  $Y_b$  in the above equation represents local mass transfer coefficient, solute mass fraction at the membrane wall and solute mass fraction in the bulk respectively. By combining the above pair of equation, following relation for local mass transfer coefficient can be realized:

$$k_l = \frac{D}{Y_b - Y_w} \left[ \frac{\partial Y}{\partial n} \right]_w \quad (2.4.8 - 3)$$

In the above equation  $\left[ \frac{\partial Y}{\partial n} \right]_w$  represents the mass fraction gradient at the wall (or membrane surface). Above relation is useful to find out local mass transfer

coefficient ( $k_l$ ) if mass fraction of the solute at the membrane surface and in the bulk and mass fraction gradient at the membrane surface is known. To find out the average value of mass transfer coefficient the area-averaged value over the mass transfer area ( $A_t$ ) is given by:

$$k_{av} = \frac{1}{A_t} \int_{A_t} k_l dA \quad (2.4.8 - 4)$$

There may be instances when the local mass fraction values are not readily available for every point on the mass transfer surface which makes it difficult to calculate the local mass transfer coefficient at every point, hence average mass transfer coefficient cannot be calculated. In such cases mean-logarithmic concentration difference is proposed to find out global mass transfer coefficient. Log-mean concentration (mass fraction) difference is defined as:

$$\Delta Y_{LM} = \frac{(Y_{w2} - Y_{b2}) - (Y_{w1} - Y_{b1})}{\ln \left[ \frac{Y_{w2} - Y_{b2}}{Y_{w1} - Y_{b1}} \right]} \quad (2.4.8 - 5)$$

In the above expression  $\Delta Y_{LM}$  is the log-mean mass fraction difference and the global mass transfer coefficient based on  $\Delta Y_{LM}$  is defined by the following relation:

$$J_{st,avg} = \rho k_{glob} \Delta Y_{LM} \quad (2.4.8 - 6)$$

As seen from the respective equations for global and area-averaged mass transfer coefficients, the two are not necessarily the same but they are fairly close to one and other. Hence global mass transfer coefficient may provide a suitable approximation for area-averaged mass transfer coefficient where local mass fractions of solute cannot be calculated at each point at the mass transfer area (membrane area). However some researchers prefer to use arithmetic-mean concentration difference instead of using log-mean concentration difference to define mass transfer coefficient. The arithmetic-mean concentration difference is defined as:

$$\Delta Y_{AM} = \frac{(Y_{w2} - Y_{b2}) + (Y_{w1} - Y_{b1})}{2} \quad (2.4.8 - 7)$$

$\Delta Y_{AM}$  can be used reasonably when the difference in the concentrations (wall - bulk) varies just slightly over the channel length, for example, short channel lengths with

low relative permeation compared with the bulk flow. In case of higher concentration differences, use of  $\Delta Y_{AM}$  will yield lower mass transfer coefficient as compared to that obtained by the use of  $\Delta Y_{LM}$ . Both types of mass transfer coefficients appear in literature for various flows and geometric configurations [56-58].

Usually, correlations for mass transfer coefficient are expressed as the dependence of Sherwood number (Sh) with the flow conditions in the form of Reynolds number (Re), Schmidt numbers (Sc) and other geometric parameter of the flow channel. A commonly used correlation is given as:

$$Sh = \frac{\text{Mass transfer coefficient} * \text{Characteristic dimension}}{\text{Mass diffusivity}} = A Re^B Sc^C \quad (2.4.8 - 8)$$

Values of  $A$  and  $B$  incorporates the conditions at the membrane surface and the geometry of the particular flow channel under consideration [46, 59]. Whereas the value of  $C$  is set 0.33 which is constant for laminar and developing turbulent flow regimes [46, 55].

#### 2.4.9 Energy losses and friction factor

From the discussion in the previous sections, it appears that in order to enhance the mass transport of solute away from the membrane surface increase in Reynolds number (and hence fluid velocity) could be one possible solution. But increase in Reynolds number also results in increased pressure drop across the channel. The pumping energy ( $W_s$ ) for a fluid at volumetric flow rate ( $Q$ ) and having a channel pressure drop ( $\Delta p_{ch}$ ) is given as [60]:

$$W_s = Q \Delta p_{ch} \quad (2.4.9 - 1)$$

Dimensionless Fanning friction factor is normally used to report pressure drop in channel flow, and for conduits without obstacles is defined by the following relation [55]:

$$f = \frac{d_h \Delta p_{ch}}{2\rho u_{avg}^2 L} \quad (2.4.9 - 2)$$

However, the above equation is modified for flow with obstacles, like spacer filled narrow channels and the fanning friction factor is related to hydraulic diameter,

effective velocity, channel length and pressure drop across the membrane by the following relation:

$$f = \frac{d_h \Delta p_{ch}}{2\rho u_{eff}^2 L} \quad (2.4.9 - 3)$$

Thus the pressure drop per unit length may be calculated by the following relation:

$$\frac{\Delta p_{ch}}{L} = \frac{2f\rho u_{eff}^2}{d_h} = \frac{2\mu^2}{\rho d_h^3} Re_h^2 f \quad (2.4.9 - 4)$$

Usually, the mass transfer enhancement techniques (for instance, changing feed spacer geometric characteristics) are compared on the same Reynolds number preferably when the energy losses are not significant [61]. But some researchers prefer to compare the mass transfer enhancement on same pressure drop and same pumping power [62] especially when the energy losses are significant. Thus, In order to have same pressure drop per unit length for a particular fluid under two different flow conditions following condition must hold good:

$$\frac{Re_{h1}^2 f_1}{d_{h1}^3} = \frac{Re_{h2}^2 f_2}{d_{h2}^3} \quad (2.4.9 - 5)$$

From the above relations, it may be concluded that for the same hydraulic diameter, flow of same fluid will have same pressure drop per unit length for different flow conditions if the dimensionless factor ( $Re_h^2 f$ ) is same.

Required pumping power per unit length can be calculated by the following relation:

$$\frac{W_s}{L} = \frac{Q \Delta p_{ch}}{L} = \frac{2f A_T \varepsilon \rho u_{eff}^3}{d_h} = \frac{2 A_T \varepsilon \mu^3}{\rho^2 d_h^4} Re_h^3 f \quad (2.4.9 - 6)$$

In order to have same power requirement per unit length for a same fluid under two different flow conditions, following relation must hold good:

$$\frac{Re_{h1}^3 f_1 \varepsilon_1 A_{T1}}{d_{h1}^4} = \frac{Re_{h2}^3 f_2 \varepsilon_2 A_{T2}}{d_{h2}^4} \quad (2.4.9 - 7)$$

From the above relations it may be concluded that, for same hydraulic diameter, porosity and cross sectional area. Energy loss per unit length will be same for a given

fluid in different flow conditions provided the dimensionless factor ( $Re_h^3 f$ ) is the same. This dimensionless group ( $Re_h^3 f$ ) is termed as Power number by various researchers [63]. However, a modified friction factor is used by some researchers which is proportional to the cubic root of this dimensionless group [64].

#### 2.4.10 Reynolds number

Classical definition of Reynolds number is the ratio of inertial forces to viscous forces in fluid flow. In literature regarding flow through spacer-filled narrow channels different definitions of Reynolds number can be cited, depending on use of different characteristic dimension and fluid velocity, which may lead to confusion, since values of Reynolds number obtained using definitions are not equivalent. For instance some researchers [28, 61] use effective velocity ( $u_{eff}$ ) and hydraulic diameter ( $d_h$ ) to calculate Reynolds number and terms it as hydraulic Reynolds number ( $Re_h$ ). Some use filament diameter ( $d_f$ ) and average velocity ( $u_{avg}$ ) to calculate cylinder Reynolds number ( $Re_{cyl}$ ) [65, 66]. Similarly, some researchers [32] have used channel Reynolds number ( $Re_{ch}$ ) dependant on channel height ( $h_{ch}$ ) and average velocity ( $u_{avg}$ ). However, above mentioned three types of Reynolds number are related as:

$$\frac{\varepsilon}{d_h} Re_h = \frac{1}{d_f} Re_{cyl} = \frac{1}{h_{ch}} Re_{ch} \quad (2.4.10 - 1)$$

It is also important to note that some researchers have used different Reynolds numbers interchangeably, so before comparison of results it is quite important to see the definition they have used to define Reynolds number.

### 2.5 Techniques to reduce concentration polarization and fouling

Efficiency of a membrane module may be enhanced by reducing its potential to foul. This can be done in number of ways as discussed in the previous sections (2.4.6 and 2.4.7). This section deals with the possible ways or methods to alter or modify hydrodynamics in membrane modules that minimizes the solute concentration in the concentration boundary layer adjacent to the membrane surface and eventually leads to minimize the fouling propensity of the membrane. Some techniques that are

commonly used to modify hydrodynamics in membrane modules as described below briefly.

### **2.5.1 Feed channel spacer**

The net type spacer in the feed channel not only keeps the membrane layers apart, hence providing passage for the flow, but also significantly affects the flow and concentration patterns in the feed channel. Presence of these spacers promotes directional changes in the flow which reduces membrane fouling and concentration polarization. Hence the efficiency of a membrane module depends heavily on the efficacy of the spacers to increase mass transport away from the membrane surface into the fluid bulk by increasing shear rate at the membrane surface [25]. The fouling issues can be addressed to a larger extent by varying the hydrodynamic conditions prevailing in spiral wound membrane. The feed spacers can be oriented to generate high cross flow velocities or secondary flow patterns which can develop higher scouring forces on the membrane surface to reduce fouling and concentration polarization. However this approach will need higher pumping energy to compensate losses within the membrane module. Hence the feed spacers must be optimized to reduce the build-up on the membrane surface with moderate energy loss.

### **2.5.2 Periodic back-flushing**

This technique is mainly used to back-flush periodically MF and UF membranes. In this approach permeate is caused to flow in reverse direction through the membrane by applying reverse transmembrane pressure. In some applications compressed air is also used as the cleaning agent instead of permeate. Back-flushing causes the foulant layer to expand, de-clog and eventually forces it to move away from the surface of the membrane [67].

### **2.5.3 Gas sparging**

In this technique air bubbles are injected in the main feed stream. The secondary flow around the bubbles causes enhanced local mixing which results in the transport of solute away from the membrane surface back into the bulk solution and hence reduces the thickness of concentration polarization layer. The efficiency of this

method is largely on the bubble size, frequency, type of membrane operation and fluid pressure [68].

#### **2.5.4 Helical and rotating channel**

Dean and Taylor vortices are harnessed in membrane separation processes by using helical and rotating feed channels respectively. As a result of these vortices secondary flow patterns are generated within the membrane module and limit concentration polarization boundary layer growth. The downside of those channels is high power consumption, complex channel design and higher capital cost [67].

#### **2.5.5 Ultrasonic vibration**

Ultrasonic waves promote vigorous mixing within the system and generate strong convective currents (also known as acoustic streaming) and increasing turbulence which causes bulk water movement towards and away from the membrane surface. These irradiations also help to generate micro mixing by implosive collapse of cavitation bubbles near the membrane surface which leads to formation of liquid microjets helpful to score membrane surface. It is also reported that these waves can agglomerate fine particles reducing the potential of membrane pore blocking and cake compaction. Ultrasonic irradiation also supply sufficient mechanical vibrational energy to the system that help keeping the particles partly suspended rather than allowing them to adhere to membrane surface and hence resist membrane fouling. Efficiency of this technique depends on several factors, like power intensity, ultrasonic frequency, feed characterises, membrane properties, pressure and temperature [69-71]

#### **2.5.6 Electromagnetic field**

This technique involves the use of electric coils in circular pattern embedded in the pressure vessel containing the membrane modules. These coils are energized by alternating current and induce electromagnetic field (EMF) in the feed solution. The induced electric field alternates in a circular fashion between clockwise and anticlockwise direction (about 2000 times per second) depending on the momentary direction of magnetic field. Since the anions and cations present in the feed solution bear opposite charges so they tend to move tangentially along the membrane surface

in opposite directions. The movement of cations and anions in the opposite interferes with development of concentration polarization boundary layer at the surface of the membrane and reduces the chances of scale formation and fouling potential at the membrane surface. EMF field also physically moves particles away from the membrane surface and hence they can be swept away by the bulk fluid motion. The effect of EMF on permeate flux has been investigated by researchers and they have reported that it leads to enhanced and more stable permeate flux and mitigate fouling phenomena [72-74].

### **2.5.7 Cyclic operations**

Cyclic operations as compared to steady-state operations generate flow instabilities which results in disrupting the fouling layer on the membrane surface and may lead to, if optimized properly, enhanced permeate rate and quality [67, 75]. However to have a precise control over the cyclic fluctuation of a key parameter such as pressure or flow rate additional sophisticated devices and instrumentation such as pulsation generator, oscillating pistons, pneumatic valves etc are needed.

## **2.6 Theoretical models for membranes**

Four most commonly used models to describe permeate flux through membrane and concentration at membrane surface are described in the following sections. They are namely: Film theory model, osmotic pressure model, boundary layer resistance model and retained solute model.

### **2.6.1 Film theory**

Film theory is based on solute mass balance near the membrane surface and is commonly used due to its simplicity and reasonable prediction of mass transfer coefficient and solute concentration at the membrane surface. In the beginning of any filtration process, solute is rejected at the membrane surface which increases solute concentration at the membrane surface. Later, stable condition is achieved when the convective transport of the solute to the membrane becomes equal to the solute transport through the membrane plus the back diffusion from the membrane surface to the bulk of the solution. Figure 2.30 represent the terms necessary for solute balance in membrane operation at stable conditions.

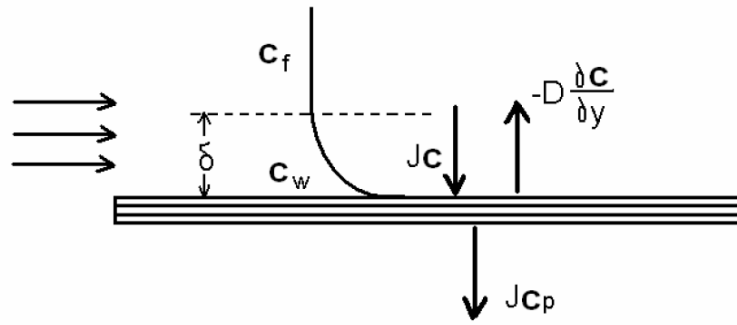


Figure 2.25: Concentration profile at membrane surface.

To write down solute balance across a membrane (as shown in the figure), let's assume  $J$  is permeate velocity (or volumetric permeate flux),  $C$  is the concentration. The term  $J.C$  represents the convective flow of solute towards the membrane (mass flux). If  $c_p$  represents the concentration of solute in permeate, then the term  $J.c_p$  represents the passage through the membrane and the term  $D \frac{dc}{dy}$  represents the back diffusion of solute in the bulk of solution, where  $D$  represents mass diffusivity and  $\frac{dc}{dy}$  represents concentration gradient in  $y$  direction. The flux balance is given by the following equation:

$$JC + D \frac{dC}{dy} = J c_p \quad (2.6.1 - 1)$$

Above equation can be integrated using the following boundary conditions:

$$y = 0 \quad C = c_w$$

$$y = \delta \quad C = c_f$$

Where  $c_w, c_f$  and  $\delta$  represents concentration at membrane wall, concentration of feed and boundary layer thickness respectively. Using the above boundary conditions equation 2.6.1-1 can be integrated to the following equation:

$$J \frac{\delta}{D} = \ln \frac{c_w - c_p}{c_f - c_p} \quad (2.6.1 - 2)$$

Since the ratio of mass diffusivity and boundary layer thickness is defined as Mass transfer coefficient “ $k_f$ ”, i.e.

$$k_f = \frac{D}{\delta} \quad (2.6.1 - 3)$$

So equation 2.6.1-2 can be rewritten as:

$$J = k_f \ln \frac{c_w - c_p}{c_f - c_p} \quad (2.6.1 - 4)$$

If the concentration of solute in permeate is negligible ( $c_p \sim 0$ ) i.e., all of the solute has been retained by the membrane, then equation 2.6.1-4 reduces to :

$$J = k_f \ln \frac{c_w}{c_f} \quad (2.6.1 - 5)$$

Many researchers have found that the applicability of film theory is justified in RO systems under operating conditions of low permeate flux and high cross flow velocity, which usually prevail in most practical applications [76].

## 2.6.2 Osmotic pressure model

Osmotic pressure model is defined by and is represented by equation 2.6.2-1 [77]. According to this model if the applied pressure is in excess of the solution’s osmotic pressure the solvent will permeate through the membrane surface and forms a dilute solution (permeate) on the other side of the membrane. However if the pressure applied is less or equal to the solution’s osmotic pressure no permeate will occur.

$$J = L_p (\Delta P_{TM} - \sigma \Delta \pi) \quad (2.6.2 - 1)$$

$\sigma$  is the reflection coefficient, having values in the range of 0 to 1.  $\sigma = 0$  means no solute rejection and  $\sigma = 1$  means complete solute rejection.  $L_p$  is the hydraulic permeability coefficient of the membrane,  $\Delta P_{TM}$  is the transmembrane pressure (TMP) defined, in case of minute difference between the feed and concentrate end pressures, as the difference in feed ( $p_f$ ) and permeate pressures ( $p_p$ ).

$$\Delta P_{TM} = p_f - p_p \quad (2.6.2 - 2)$$

$\Delta\pi$  represents osmotic pressure difference between membrane surface ( $\pi_w$ ) and the permeate ( $\pi_p$ ). Osmotic pressure depends on the solute type and its concentration as explained in section 2.4.2.

$$\Delta\pi = \pi_w - \pi_p \quad (2.6.2 - 3)$$

It is evident from the above set of equations that on increasing the feed pressure the solute concentration on the membrane surface will increase resulting in higher osmotic pressure. As a result the net available driving force that causes permeation to take place will decrease and will lead to low permeation flux.

### 2.6.3 Boundary layer resistance or Resistance in series model

In this model total resistance offered to the permeate flux is sum of the membrane resistance ( $R_m$ ) and resistance offered by the concentration boundary layer ( $R_{bl}$ ) and is defined by the following equation [45, 78]:

$$J = \frac{(\Delta P - \sigma \Delta\pi)}{(R_m + R_{bl}) \mu} \quad (2.6.3 - 1)$$

Boundary layer resistance is further subdivided into resistance due to pore plugging  $R_u$ , resistance due to deposits on membrane surface  $R_d$ , Resistance due to gelation  $R_g$  and resistance due to concentration polarization  $R_{cp}$  [79] and is given by the sum of all mentioned resistances by the following equation:

$$R_{bl} = R_u + R_d + R_g + R_{cp} \quad (2.6.3 - 2)$$

Resistance offered by the boundary layer ( $R_{bl}$ ) depends mainly on the molecular weight of the species present in the boundary layer. In case of UF operations the macromolecular solutes are present in the boundary layer and hence  $R_{bl}$  is significant. However in case of RO operations low molecular weight solute are present in boundary layer and hence this resistance is small and this model becomes equivalent to Osmotic pressure model for negligible  $R_{bl}$ .

#### 2.6.4 Retained solute model

This model was introduced by Song and Elimelech [80] and it describes concentration polarization in two dimensions. This model describes the local variation of solvent permeation and concentration polarization along cross flow direction. The concentration of retained solute in the concentration polarization layer at steady state satisfies the following relation:

$$J_x c + D \frac{\partial c}{\partial y} = 0 \quad (2.6.4 - 1)$$

Where  $c$  is concentration of retained solute,  $x$  and  $y$  are the longitudinal and transverse coordinates respectively.  $D$  is the mass diffusivity and  $J_x$  represents the permeate velocity (or volume flux). According to this model the relationship between  $J_x$  and concentration at membrane surface (or wall)  $c_w$  is given by the following relationship:

$$c_w = \frac{\Delta P - \frac{J_x}{L_p} + \phi (1 - \sigma) c_f}{\phi} \quad (2.6.4 - 2)$$

Where  $\phi$  is the osmotic coefficient. This model is appropriate to predict UF flux of nano-particle suspensions. But not appropriate to estimate concentration polarization in RO systems [76].

### 2.7 Experimental and theoretical Studies for prediction of mass transfer and concentration polarization

As established in previous sections that concentration polarization reduces the permeate flux and effect adversely the permeate quality. In the past several studies, both experimental and theoretical, were carried out to predict the effect of operating conditions, such as: Feed concentration, driving pressure, cross flow velocities etc on concentration polarization and permeate (or product) rate and quality. One of the studies includes the experimental work of Wijmans et al. [81] in which they compared osmotic pressure model with boundary layer resistance model and found the two models to be essentially equivalent. They showed that concentration boundary layer effects could be presented either by a reduction in driving force (as

depicted by the osmotic pressure model) or by an increase in total resistance (as depicted by the boundary layer resistance model). They studied the effect of feed velocity and operating pressure on permeate flux through UF membrane system. Their study showed that the product (or permeate) flux tends to decline as a result of increased bulk concentration and decreased cross-flow velocity. Whereas, product flow increases with increase in operating pressure, but the gradient of the increasing flux tends to drop with increase in pressure due to increased osmotic pressure and higher resistance of concentration polarization boundary layer.

In another experimental and theoretical study conducted by De and Bhattacharya [82] various correlations for Sherwood number in laminar flow regime for different membrane arrangement (rectangular, tubular and radial cell) were obtained. Those correlations were used to predict mass transfer coefficient and in turn permeate flux by coupling it with osmotic pressure model. In another study Bhattacharya and Hwang [83] came up with an expression that provides the relationship between average modified Peclet number ( $Pe$ ), separation factor ( $\alpha$ ) and concentration polarization index ( $I$ ) and is described as follows:

$$Pe = \left[ \left[ \frac{\alpha}{1-I} \right] \ln \left[ \frac{I-\alpha}{1-\alpha} \right] \right] - 1 \quad (2.7 - 1)$$

In the study it was concluded that the extent of polarization depends on many factors, namely: permeability of membrane, solute rejection (or separation factor), membrane thickness, boundary layer mass transfer coefficient and Henry's constant. The theoretical model presented was in reasonable agreement with the experimental data for pervaporative separation of dilute solutions of VOC (volatile organic compounds) and dissolved gases and for the UF of proteins and carbowax.

Miranda and campos [84] studied mass transport for higher Peclet number flows in a parallel channel with suction in laminar regime. It was shown that the suction perturbs the flow in a narrow region very close to the permeable wall and extension of this region depends on Reynolds number. It was also shown that inside mass boundary layer normal diffusive flux and normal convective flux are not equal.

Jonsson [85] conducted experimental study by using dextran and whey solutions. He showed experimentally, using coloured macromolecules, that during UF dissipative

structure were formed on the membrane surface and also showed that there will be no uniform boundary layer present during UF and concluded that for macromolecules, gel-layer model do not present a realistic pressure gradient across a gel layer of given thickness.

Van Oers et al. [86] studied unsteady-state flux behaviour in relation to a gel layer. They carried out experiments for dextran and silica solutions. Their results for dextran solution confirms that there was no gel layer formed during filtration and the only layer formed was the polarization layer, where as in case of silica solution a gel layer was also produced. They confirmed that the flux behaviour for the two solutions were completely different. It took less than a minute to form a polarization layer for the dextran solution, where as in case of silica solution it took hours for the build-up of gel layer. They also showed that for the dextran case, mass transfer coefficient can be predicted accurately by combining osmotic pressure model and film model.

Rautenbach and Helmus [87] studied material transport resistance through asymmetric membranes and showed that concentration polarization at the feed side of the membrane is just one of the several transport resistances and must be regarded relative to transport resistance of the membrane itself. They explained that the net filtration resistance in those membranes is combined effect of the concentration polarization boundary layer, membrane resistance (active layer) and resistance offered by the membrane porous support layer (back layer).

McDonogh et al. [88] used two different direct observation methods to visualize concentration polarization layer during filtration of Dextran Blue and bovine serum albumin (BSA) and showed that it coincides with the qualitative descriptions given in literature. In the first technique mentioned in their research article they make use of a radioisotope to measure the overall build-up of concentration polarization layer. The second technique involved the measurement of infrared adsorption of species present in the polarization layer by a micro-array of semiconductor photosites.

Karode [89] in an article discuss unique flux-pressure profiles for three types of solute (Dextran, silica and BSA) used commonly for membrane ultrafiltration processes. In the article he describes that a step change in transmembrane pressure transforms into unsteady-state permeate flux response and the pressure-flux profile is

unique for different solutes used in the study. The three solutes used in the study were (1) Dextran : a solute which do not form gel, but exerts an osmotic pressure; (2) Silica: a solute that do form a gel, but do not exert an Osmotic pressure; (3) Bovine serum albumin (BSA): a solute that form a gel and also exert osmotic pressure. His study predicted the performance of UF membrane performance using above mentioned three types of solute and resulted in unique flux- pressure profiles for the each of the three solutes.

Song and Elimelech [80] developed a novel theory to predict concentration polarization in cross-flow filtration systems for non-interacting particles. According to their theory the extent of concentration polarization and permeate flux behaviour is characterized by a dimensionless filtration number. They also show that for a given suspension and operational conditions there is a critical value for the filtration number. If the filtration number is lesser than the critical values there exists a polarization layer next to the membrane surface. At higher filtration number a cake-like layer of the retained particles is formed between the membrane surface and the polarization layer. They also produced mathematical models for both the cases and derived analytical solution for permeate flux. They also showed that if the filtration number is less than 15, which is typical for RO systems, there only exists a concentration polarization layer next to membrane wall and when filtration number is greater than 15, which is typical for UF systems, cake formation also occurs between membrane wall and concentration polarization layer.

Baker and Strathmann [90] studied ultrafiltration of macromolecular solutions with high flux membranes using batch and recirculation cells. Their experiments revealed that during ultrafiltration of macromolecular solutions at lower pressure the solvent flux was almost equivalent to that of the flux of the pure solvent. The solvent flux showed a direct dependence on the pressure and increased with an increase in pressure, but at higher pressure the solvent flux reaches a maximum value and then becomes constant and does not increase with further increase in pressure. However, they found the dependence of maximum solvent flux on other variable and showed that it increases with an increase in temperature and agitation, but it decreases as a result of increased solute concentration. They explained this behaviour by the formation of a gel-like layer next to the membrane surface which functions as a barrier to the passage of the solvent and low molecular weight solutes. They further

concluded that the formation of gel-like layer next to the membrane surface was the characteristic of UF membrane separation processes and NF and RO processes do not facilitate the formation of gel layer.

Murthy and Gupta [77] calculated mass transfer coefficient by combining concentration polarization models with membrane transport models and concluded that when reflective coefficient is much less than unity, Spiegler-Kedem model in combination with film theory model predicts mass transfer coefficient more accurately as compared to solution-diffusion model coupled with film theory model. Gupta et al. [91] used different dilute salt solutions in their experiments to determine concentration polarization parameter, reflection coefficient and solute permeability for RO and NF systems. They related product flux, solute permeability and pressure drop using combination of Spiegler-Kedem and film theory model. Their model indicated that the true salt rejection (intrinsic salt rejection) of a membrane is a unique function of total volumetric flux through the membrane.

Khayet and Mengual [92] studied transport of monovalent and divalent inorganic salts through polyamide thin film composite membranes. It was concluded that the solute transport parameter for salts having divalent ions was lower as compared to salts with monovalent ions. Secondly, it was also concluded that for inorganic salts having higher diffusion coefficients also shows higher mass transfer coefficients.

Sutzkover et al. [93] in their research paper describes a simple technique to calculate mass transfer coefficient and the level of concentration polarization in RO membranes. The core of the technique is to evaluate permeate flux decline by allowing salt water solution to pass through the membrane which was initially subjected to the passage of salt free or pure water. As the osmotic pressure is increased near the membrane wall due to increased solute concentration which decreases the net driving force causing permeation through the membrane and hence a decline in permeate flux is realized and its magnitude enables evaluation of concentration at the membrane surface and eventually leads to evaluation of mass transfer coefficient using the following equation:

$$k_f = \frac{J}{\ln \left\{ \frac{\Delta p_{TM}}{\pi_b - \pi_p} \left( 1 - \frac{J}{J_{pure}} \right) \right\}} \quad (2.7 - 2)$$

In the above equation  $k_f$  is the mass transfer coefficient,  $\pi_b$  and  $\pi_p$  represents osmotic pressure at solution bulk and permeate concentration respectively.  $J$  and  $J_{pure}$  represents the permeate volumetric flux (or simply velocity) of salt solution and pure water passing through the membrane respectively. The proposed relation was also verified experimentally using tubular RO system under turbulent flow conditions. They also obtained following mass transfer correlation for their experimental work which covers the Reynolds number range of 2,600 to 10,000:

$$Sh = 0.020 Re^{0.91} Sc^{0.25} \quad (2.7 - 3)$$

Song and Yu [94] developed a model for cross flow RO process in which they considered local solute wall concentration variation along feed flow direction (i.e. variation of solute concentration at the membrane surface in bulk flow direction) and coupling between the permeate flux and concentration polarization was investigated. Their model showed that the concentration of solute at the membrane wall influences salt rejection, mass diffusivity, shear rate and permeate flux. The model made it possible to predict concentration values at different product fluxes and operating pressures.

Song [95] developed a model to predict limiting flux in UF systems. The occurrence of limiting flux was explained by the formation/existence of a cake or gel-layer at the membrane surface which is an essential condition for the occurrence of limiting flux. Their model represents a complex dependence of feed concentration on limiting flux. In other studies Song et al. [96, 97] examined the mechanisms that control the overall performance of full scale reverse osmosis system under various operating conditions. They show that in case of a full scale RO system thermodynamic restriction is a limiting factor and it arises when the osmotic pressure at the feed side of the membrane, which keeps on increasing along the flow direction due to increase in salt concentration, becomes equal to the transmembrane pressure and at that critical point there will be no permeation of solvent across the membrane will occur beyond that portion of membrane channel and hence the permeate flux will vanish.

## 2.8 Simulation of spiral wound membrane modules

Spiral wound configuration is one of the most popular modules commercially used due to moderate to large surface area per unit volume and have found application ranging from MF to RO. The performance of SWM is affected by the following main factors [6]:

- The geometry of the membrane leaves wound spirally to the central tube. This may include the length, width and the number of leaves used.
- Feed side and permeate side channel heights, which is the direct representation of the feed and permeate side spacer filaments thickness.
- Spacer's orientation, shape, dimensions and mesh. Since the feed spacer is meant to induce secondary flow patterns to enhance mass transport of the solute away from membrane walls, but at the same time may lead to higher pressure losses.
- Fouling tendency and cleaning ability
- Operating conditions, especially, feed concentration and pressure, percentage permeate recovery and nature of feed pre-treatment.

Several studies have been conducted to model the separation performance of spiral wound membrane module in relation to operating conditions (such as feed concentration and flow rate, feed pressure, %age recovery etc) and geometry parameters (such as number of leaves, leaf length and width, feed and permeate channel height etc). Productivity of a module ( $\xi$ ) is related to the permeation rate ( $Q_p$ ), module volume ( $V_{mod}$ ) and feed entrance pressure ( $p_f$ ) by the following relation [98, 99] :

$$\xi = \frac{Q_p}{V_{mod} \cdot p_f} \quad (2.8 - 1)$$

In the past, selectivity analyses were carried out by varying only one parameter and studying its effect on the module productivity. The optimum feed channel height was found to be in the range of 0.6 – 1.5 mm [98, 100-103]. At constant module diameter and volume, for the feed channel height below 0.6 mm, a high pressure loss along the feed channel is the cause to reduce the effective driving force (Transmembrane pressure) which results in low productivity of the module. Furthermore, the

reduction in productivity (caused by the increased pressure drop along the feed channel) cannot be counteracted by the increase in the packing density of the module (achieved by the reduction in the feed channel thickness). For the modules having feed channel height above 1.5 mm, decreases the pressure loss along the feed channel (compared to 0.6 mm channel height) but at the same time reduces the packing density and hence results in low module productivity. However, the pressure loss characteristics associated with the presence of feed channel spacer has a strong effect on the optimum channel height. Hence for maximum module productivity, thin feed channel spacers with less pressure drop and high mass transfer effect would be an ideal case scenario, since it will decrease the feed channel height and will increase the packing density.

The optimal permeate channel height for maximum productivity was found in the range of 0.25 to 0.5 mm depending of the width of the membrane leaf [98, 99]. At a constant module volume and diameter, for permeate channel height below 0.25 will lead to higher pressure loss in the permeate channel and will result in low module productivity, even though there will be an increase in the packing density. For modules having permeate channel height above 0.5mm, there will be a decrease in productivity due to decrease in packing density. Wider leaves requires a permeate channel of higher height in order to reduce the pressure loss developed by large amount of permeate flowing along the permeate channel towards the central collection permeate tube. For the modules in which smaller width membrane leaves having smaller permeate channel height are used, the number of membrane leaves is increased.

For the optimized productivity, apart from considering the individual feed channel and permeate channel heights, their ratio should also be considered. The optimized permeate channel height to feed channel height ratio is between the range of 0.5 - 1. Above or below this optimum ratio, either feed or permeate channel pressure loss increases and results in lower module productivity [99].

Boudinar et al. [98] developed a computer simulation programme, for spiral wound membranes, based on Finite Difference Method (FDM) which took into account the geometry of the spiral wound module and the physical phenomena taking place inside the module. The programme solved differential equations for transport

numerically using finite difference method and enabled the prediction of concentration, pressure and flow rate at any point in the feed and permeate channel. Based on their analysis they claimed that the optimal number of leaves to be 3 to 5, based on membrane length/membrane width ratio of 0.8. The model was also capable to predict product flux and concentration at different feed velocities and operating pressures.

Schwinge et al. [6] reviewed different techniques to analysis and optimize the performance of spiral wound modules. They also analysed different configurations in which individual spiral wound modules can be connected. The outcome of the study was that different factors such as: feed solution concentration, fouling tendency of the feed solution, required separation efficiency, fluid volume to be processed, available space and available pump head has a direct impact on the favourable configurations in which the individual modules should be connected to get optimized performance. In another research paper Schwinge et al. [104] simulated the development of colloidal fouling across membrane leaf of SWM. The model also predicts the variation of membrane resistance and permeate flux across the membrane leaf. It was shown from the simulations that the fouling was distributed unevenly over the membrane leaf and the results were confirmed by real life membrane autopsies.

Avlonitis et al. [100] determined the performance of spiral wound module, both analytically and experimentally at different operating flow rates and pressures, using three key parameters, namely: (1) brine friction parameter; (2) permeate friction parameter and ; (3) water permeability coefficient. The analytical solution presented in their work was further used to predict feed velocity, permeate velocity and effective pressure at different locations. In a follow up research article by the same group [101] they presented a five parameter model as compared to the previous three parameter model. The two additional parameters used in the study were mass transfer coefficient and solute permeability coefficient. Using this model the performance of spiral wound module was predicted, at different cross-flow velocities and feed concentrations, in terms of concentration polarization and product flux.

Zhou et al. [105] developed a mathematical model to predict the performance of a spiral wound module channel with spacer. The effectiveness of the spacer is

quantified by the magnitude of a specific parameter “hydraulic dispersion coefficient” in the model. Higher values of this parameter indicated that the spacer promote mixing which results in lower degree of concentration polarization, whereas lower value of the parameter was an indication of higher degree of concentration polarization due to lower or inadequate back mixing. The presented model was also capable of predicting product flux and recovery at different driving pressures, feed velocities and membrane resistances. The results obtained from their study motivated researchers to focus and investigate the flow patterns associated with spacer presence in the feed channel which enhances mixing and reduce concentration polarization and fouling.

## **2.9 Flow and mass transfer modelling in plane channels using CFD**

The traditional experimental techniques while taking measurements close to the membrane walls intrude or alter the flow field and bring in complexities for analysis. However, techniques such as flow visualization with dye [32], Particle Image Velocimetry (PIV) [33] and Direct Observation through the membrane (DOTM) [5, 34] which are less intrusive in nature are employed to study the mass distribution and flow patterns in a membrane cell. But often the limitation of these techniques is the lack of small scale resolution required to analyse mass transfer phenomena occurring within the boundary layer. Hence there is a need for another approach or technique which provides further understanding of the mass transfer aspects associated with the use of membrane operations, especially when the objective is to capture near membrane wall effects.

Computational techniques, possess the powers to provide information regarding the flow anywhere in the selected domain without interfering with the flow itself and can lead to better understanding of the mass transfer aspects of the membrane operations. Experimental techniques require considerable financial investment such as equipment procurement, infrastructure construction, resources dedication, hiring and training of staff. Numerical modelling reduces dramatically the costs, time and risks involved in running the repeated experiments. Computational Fluid Dynamics (CFD) is one of the many numerical techniques used for simulating fluid flow [35] and the tool used in this thesis. CFD allows simulation and subsequent analysis of fluid

systems by solving conservation equations for mass, energy and momentum using numerical methods.

Many researchers are utilizing CFD technique to gain insight of various phenomena taking place within the membrane modules to improve its performance or to provide valuable information for the design process. Moreover, many research groups have shifted their focus to CFD making it widely used tool in the field of membrane science [36]. The advantage of CFD tool over the traditional experimental methods lies in the built-in flexibility to change operating conditions, fluid properties and geometric parameters of the flow channel. For instance, geometric parameters of the flow channel can be varied using an appropriate CFD software, and does not need the physical construction of the modified channel, to investigate the effects on the parameters of interest. Similarly fluid properties and operating conditions can be varied to investigate their impact on the parameters of interest without experimentations. Another important and interesting feature of the CFD is that the data can be reported anywhere in the computational domain at any time during the simulation without obstructing the flow itself.

CFD techniques are being widely used in the field of membrane science to get insight of the complex flow and concentration patterns generated inside the module during the normal course of operation. CFD tools have lead to better understanding of the membrane separation processes and have proven to be cost effective and time saving, compared to the experimental approach, and also provide accurate results provided adequate computational power is available depending on the nature of problem [36]. Today, CFD is being used as a widely accepted tool to propose new and effective module design within time and budget constraints.

To study flow and mass transfer in membrane modules using CFD tools, there are several studies that have used the simplified model of narrow parallel channel to visualize flow and mass transfer within the module. A brief description of the relevant studies is presented in this section. These studies focus on flow through plain membrane channels either under constant or variable suction velocity. However those studies do not incorporate the flow and concentration changes associated with the presence of spacer in the feed channel of the module.

Pellerin et al. [106] performed simulations using a grid size of 35x26 cells, which was proven adequate to reproduce the results of the analytical models. They simulated flow through flat plain membrane channel with varying the permeation velocity from  $1.5 \times 10^{-7}$  to  $5.0 \times 10^{-4}$  and studied the velocity and concentration patterns in the flat membrane channel. Their study revealed that the effect of permeation velocity up to  $1.0 \times 10^{-4}$  m/s was negligible on the flow profiles.

Geraldes et al. [107] came up with a numerical model to predict hydrodynamics and concentration polarization in the entrance region of membrane feed channel and validated it experimentally. It was shown in their study that the boundary layer development in the entrance region was independent of the permeation velocity in the range of interest for NF and depends only on the circulating Reynolds number ( $Re$ ), which they calculated by using inlet uniform velocity and total channel height as the characteristic dimension along with the density and dynamic viscosity of the salt solution. They developed a mass transfer correlation which relates permeation Stanton number ( $St_p$ ), Permeate Reynolds number ( $Re_p$ ), Channel half height ( $h$ ), spatial direction ( $x$ ) and circulation Reynolds number ( $Re$ ) and is represented below:

$$St_p = 1 + 3.68 \times 10^{-4} \left(\frac{x}{h}\right)^{-1.11} Re^{0.95} Re_p^{-1.79} \quad (2.9 - 1)$$

Geraldes et al. [108] by taking into account the interaction between solute, solvent and membrane wall tried to define the performance of NF systems in terms of permeate flux and rejection coefficient. They simulated fluid flow through a slit using two dimensional steady state laminar flow conditions. They defined the membrane wall as semi-permeable in their model. They reached to the conclusion in their study that the development of hydrodynamic boundary layer is not dependant on the Schmidt number and permeation velocity. But the concentration boundary layer depends heavily on both of them. As a continuation of their study Geraldes et al. [109] developed another numerical model to predict hydrodynamics and mass transfer of various aqueous solutions in feed channel of spiral wound and plate and frame systems and validated it experimentally. In their study they compared, numerically and experimentally, the permeate flux and rejection coefficients of different solutions and found excellent agreement between them. They developed the following correlation for concentration boundary layer thickness ( $\delta$ ) in terms of the

channel height ( $h_{ch}$ ), channel length ( $L$ ), Schmidt Number ( $Sc$ ), circulation Reynolds number ( $Re$ ) and Permeate Reynolds number ( $Re_p$ ):

$$\frac{\delta}{h_{ch}} = 15.5 \left( \frac{L}{h_{ch}} \right)^{0.4} Re^{-0.4} Sc^{-0.63} Re_p^{-0.04} [1 - 186 Sc^{-1.0} - Re_p^{-0.21}] \quad (2.9 - 2)$$

In another research article Gerald et al. [110] developed a numerical model to predict concentration polarization for different operating conditions and membrane characteristics. In the study, they also shed light on accuracy of the results versus different discretization schemes. It was presented that the use of upwind discretization scheme resulted in inaccurate results. However the exponential and hybrid schemes yielded the results with same level of numerical accuracy. But it was also presented that CPU time required for a converged solution, in case of exponential scheme, was at least 37% more than that for the hybrid scheme. Hence it was concluded that, in cases when the flow is aligned with the grid orientation hybrid scheme is the most appropriate to discretise transport equations.

Darcovich et al. [111] designed a thin channel cross-flow module. The feed of the module comes from a number of small tubes attached to the channel. The objective of the study was to design a thin channel cross-flow module having minimum pressure drop over the permeating area and minimum flow non-uniformity, and the method used was finite difference technique to model the flow. The operating variables considered in the study were cross-flow velocity and the inlet pressure. The design variables considered were the channel length, width and height, plenum diameter, number of the inlets on the plenum, their distribution and their diameter. Initially, in their study they make use of two level factorial design to screen the design variables. Later, with reduced set of design variables, a refined three level factorial design was utilized to find optimum values of the geometric parameters of the module.

Ahmad et al. [112] made use of commercial CFD package FLUENT to predict concentration polarization, wall shear stress and mass transfer coefficient in empty narrow membrane channels. Their study revealed that the concentration polarization decrease with the increased feed Reynolds number and it increases with a decrease in shear stress at the membrane surface. The simulated results agreed reasonably with already published data. In another study by Ahmad and Lau [113] the variation of

the fluid properties and permeation velocity along the flow direction was considered in the simulations. The permeate flux determined computationally reasonably agreed with the one obtained experimentally for various solutions.

Karode [114] evaluated pressure drop in flow channel with constant and varying permeation velocity at the membrane surface. It was shown that the pressure drop was smaller if the constant permeation velocity assumption is followed in the simulation and greater if the variable permeation velocity assumption is used.

Alexiadis et al. [115] studied the effect of disturbances in three operating parameters on the performance of RO system. These three parameters studied were inlet velocity, inlet concentration and transmembrane pressure. It was observed that the permeate flux was disturbed from its steady state value even for a small duration of disturbing pulses for inlet velocity, inlet concentration and transmembrane pressure and requires sufficient long time to revert back to normal steady state value after these pulses. For instance in case of a sudden increase in inlet velocity momentarily, there will be an increased scouring of the membrane surface which results in the de-attachment of solute build-up on the membrane wall. This will lead to reduced local osmotic pressure and eventually lead to enhanced permeate flux. With passage of time more and more solvent will pass through the membrane surface at a higher rate resulting in re-accumulation of solute on the membrane surface till it reaches the initial concentration (before the change in inlet velocity) and will bring the permeate flux back to the steady state value. Same author, in a different study [116], modelled the flow of sodium chloride solution in permeate and feed channels of a RO membrane. It was shown that the salt concentration increases in the flow direction on the membrane surface at both feed and permeate sides. Moreover the salt concentration on the membrane surface increases with an increase in the operating pressure.

Pinho et al. [117] used the experimental data (permeate flux and solute concentration in the permeate), obtained from a NF membrane separation system of neutral solute solutions, as the boundary conditions in CFD simulations to predict the solute concentration on the feed side of the membrane. This approach leads to the evaluation of the intrinsic salt rejection as a function of transmembrane pressure. For the membrane used in their experimental work, an average pore radius of 50 nm was

determined. Magueijo et al. [118] used Computational Fluid Dynamics and experimental studies to investigate ultrafiltration of lysozyme solution at different ionic strengths. It was concluded in the study that there was a slight decrease in the rejection coefficient of lysozyme with an increase in the solution ionic strength.

Lyster and Cohen [119] used COMSOL (a finite element code) to investigate concentration polarization in rectangular RO membrane channel and in a plate-and-frame RO membrane channel using three different solute i.e., calcium chloride, sodium chloride and sodium sulphate. They showed in their study that for the rectangular channel concentration polarization factor (ratio of solute concentration at the membrane surface to that in the bulk of the fluid, referred as concentration polarization modulus in their paper) increases continuously along the flow direction. But in the case of plate-and-frame channel there were local peaks of concentration polarization factor due to presence of stagnant flow zones. For the plate-and-frame reverse osmosis membrane channel, they showed the similarities between the concentration polarization profiles predicted by their model with an optical image, published in another study. In that study [120] similar membrane was used and was scaled with gypsum (calcium sulphate anhydride) as a result of desalting synthetic brackish water solution having a concentration of calcium sulphate above its saturation limit after 24 hours of operation. They showed that the particular zones that were having high scale density in optical image coincided with the zone with high concentration polarization predicted by their model and proved the reliability of their model.

Wiley and Fletcher [121] developed a general purpose CFD model to investigate flow patterns and concentration polarization in the feed and permeate channels of pressure driven membrane separation processes. In their study, they tested and validated the model by comparing their results with the already published results in the literature. In another research paper, by the same authors [122], they used CFX and showed the effect of changes in rejection, solution properties and permeation rates on velocity and concentration profiles in empty channels. They also validated their presented model with a number of existing semi-analytical solutions. Fletcher and Wiley [123] investigated the buoyancy effects on salt separation mechanism using a salt-water system and a flat sheet reverse osmosis membrane. They showed

in their study that the gravity effects are only significant when the following two operating conditions prevail:

- (i) Under low flow rate conditions, resulting in the accumulation of the salt at the membrane surface. They further defined the flow rate in terms of Channels Reynolds number and concluded that for salt-water system, the gravity effects would be significant if the channel Reynolds number is less than 20.
- (ii) When the flow is aligned along the direction of the gravity, such as flow in a vertical channel.

However when the main flow direction is aligned normal to gravity, there results showed no effect of gravity. This important outcome of their study is used extensively by many researchers conducting studies in the membrane separation area to simplify their model and save computational time.

## **2.10 Studies focusing on feed spacer's impact on SWM performance**

The previous section described the studies that were carried out to understand the fundamentals of concentration polarization and flow patterns in empty channels. This section will focus on the studies carried out to understand the flow behaviour and concentration patterns generated within spiral wound membrane module having spacer present in the feed channel. This section is broadly divided in two main sections, the first section deals the experimental studies, and in the second section different studies will be presented which make use of CFD tools and further divided into two subsections, one dealing with the 2 dimensional (2D) studies and the second dealing with three dimensional (3D) studies. At the end a summary of 3D studies is presented, as the thesis involves 3D study to understand the flow patterns and mass transfer characteristics associated with presence of spacer in the feed side of a membrane housed in narrow channel, just like RO membranes.

### **2.10.1 Experimental studies**

The net spacer in the feed channel not only keep the membrane layers apart, hence providing passage for the flow, but also significantly affect the flow and concentration patterns in the feed channel. On one hand they are responsible for the

pressure drop and limited flow zones (dead zones) creation, and on the other hand they are responsible to promote mixing between the fluid bulk and fluid elements adjacent to the membrane surface. In other words they are intended to keep the membranes clean by enhancing mass transfer and disrupting the solute concentration boundary layer. In past several experimental and theoretical studies were carried out to shed light on this phenomena and to optimize spacer configuration. So it is quite understandable that the presence of these spacers promotes directional changes in the flow which reduces membrane fouling and concentration polarization. Hence the efficiency of a membrane module depends heavily on the efficacy of the spacers to increase mass transport away from the membrane surface into the fluid bulk by increasing shear rate at the membrane surface.

Importance of spacer in spiral wound modules can be realized by fact that in past many experimental studies were conducted to understand the role spacer plays in the feed and permeate channels of a SWM and how do they effect the performance of the module. One of the most important experimental studies, which formed the basis for many other studies was the work carried out by Schock and Miquel [61]. In the experimental study they compared the pressure drop in FilmTec spiral wound membrane and compared the results with spacer filled flat channel and revealed that pressure drop for the two systems were approximately the same. This investigation led to fact the hydrodynamics and fouling tendency prevailing in spiral wound modules can be approximated by a flat channel fitted with spacers. Further, the expenses and evaluation time required to conduct studies for spacer filled flat channel is comparatively lower than that for spiral wound modules. They also studied the mass transport in empty flat channels and in spacer filled channels and showed that the Sherwood number for the latter case was significantly higher. In their study they also indicated that the optimal number of leaves in a spiral wound membrane module is 3 to 5. In their work they used a modified definition for hydraulic diameter ( $d_h$ ) for spacer filled channel. Same concept of hydraulic diameter has been used in this research thesis. For a feed channel, having porosity  $\varepsilon$ , channel height  $h_{ch}$  and width  $b$ , hydraulic diameter ( $d_h$ ) can be defined as [61] :

$$d_h = \frac{4 \varepsilon}{\frac{2(h_{ch} + b)}{h_{ch} \times b} + S_{V,sp} (1 - \varepsilon)} \quad (2.10.1 - 1)$$

In the above equation  $S_{V,sp}$  is “Specific surface of the spacer” and is defined by the ratio of wetted surface of the spacer ( $S_{sp}$ ) to spacer volume ( $V_{sp}$ ). The porosity of the feed channel  $\varepsilon$  is defined by the ratio of available volume for flow to that of the total volume of the channel

$$\varepsilon = \frac{V_T - V_{sp}}{V_T} \quad (2.10.1 - 2)$$

In the above relation  $V_T$  and  $V_{sp}$  represent total channel volume and volume of the spacer respectively.

For a spacer filled narrow channel, the channel height ( $h_{ch}$ ) is negligible as compared to channel width ( $b$ ) so the equation 2.10.1-1 can be reduced to the following form for the condition  $b \gg h_{ch}$  :

$$d_h = \frac{4 \varepsilon}{\frac{2}{h_{ch}} + S_{V,sp} (1 - \varepsilon)} \quad (2.10.1 - 3)$$

The above equation is used to calculate the hydraulic diameter of the spacer filled narrow channels, which inturns is used to provide the Reynolds number to understand the flow regime inside the channel. Above equation can lead to two extreme situations, for instance in case of empty channels with no spacers or spacers having very high porosity,  $\varepsilon$  tends to unity and the above equation reduces to:

$$d_h = 2 \times h_{ch} \quad (2.10.1 - 4)$$

Equation 2.10.1-4 is used to calculate the hydraulic diameter of a narrow channel without spacers. For the second extreme condition as in pack beds, when the channel height ( $h_{ch}$ ) tends to infinity, equation 2.10.1-3 yields the definition of hydraulic diameter in a packed tower and reveals that the hydraulic diameter only depends on the geometric characteristics ( $\varepsilon$  and  $S_{V,sp}$ ) of the spacer. Since the flow in the spacer filled narrow channels is in between those two extreme conditions, so equation 2.10.1-3 must be used to evaluate hydraulic diameter of spacer filled narrow channels. Also, in chapter 4 of this thesis equation 2.10.1-3 is used to calculate the hydraulic diameter of the narrow channel filled with spacer and further used to

calculate the Reynolds number for the flow in the channel for comparison purposes. Since the presence of the spacer in the channel reduces the empty volume and as a result the effective velocity inside the channel increases and the following relations are used to calculate the effective velocity ( $u_{eff}$ ) if the channel width, porosity and channel height are known:

$$u_{eff} = \frac{\text{volumetric flow rate}}{\text{Effective Area}} \quad (2.10.1 - 5)$$

The effective area available for the flow in the presence of spacer is given by the following relation:

$$\text{Effective Area} = b \times h_{ch} \times \varepsilon \quad (2.10.1 - 6)$$

The above two equations (2.10.1-5 and 2.10.1-6) are used to calculate effective velocity within the spacer filled channel to calculate the prevailing Reynolds number in the channel, using hydraulic diameter as the characteristic dimension:

$$Re_h = \frac{d_h u_{eff} \rho}{\mu} \quad (2.10.1 - 7)$$

In the above equation  $\rho$  and  $\mu$  represent the density and dynamic viscosity of the fluid flowing in the channel.

The friction factor can be obtained by using effective velocity as characteristic velocity and hydraulic diameter as characteristic length, and is given as:

$$f = \frac{d_h \Delta p_{ch}}{2 \rho u_{eff}^2 L} \quad (2.10.1 - 8)$$

An important thing to be made clear regarding the above equation is that, the above equation represents fanning friction factor whereas in their study [61] they have used the definition of moody friction factor. Moody friction factor is equivalent to four times the fanning friction factor and the two are directly proportional and conversion from one definition to the other is trivial. In their study they found that pressure drop characteristics of all the spacer tested (in terms of fanning friction factor), despite being different in terms of geometry, can be presented by the following correlation within the Reynolds number range of 100 to 1000:

$$f = \frac{6.23}{4} Re_h^{-0.3} = 1.5575 Re_h^{-0.3} \quad (2.10.1 - 9)$$

It has to be noted that the above equation is divided by 4 to convert the reported Moody friction factor in their work to Fanning friction factor.

Levy and Earle [124] investigated the effect of spacer height on the performance of Ultrafiltration system and concluded that the feed spacers present at the feed side channel of the membrane disrupts concentration polarization boundary layer and increase the permeate flux through the membrane. For the feed solution tested in their work, channel height (equivalent to feed spacer height) of 0.8 mm was found optimal. They showed that small channel height can improve the system performance for low viscosity and dilute flows and a large channel height would be beneficial for the overall system performance for concentrated and viscous flows.

The experimental work of Polyakov and Karelin [125] was aimed to find a suitable spacer for the feed channel in RO membrane which provides maximum permeate flux and requires minimum power. They tested five different spacers, using sodium chloride solution and reverse osmosis membrane as separation medium. They showed that spacer with the spacing of 3mm found to have minimum power to permeate flux ratio.

Winograd et al. [126], in electrochemical systems, focused on the impact of net spacers on mass transfer in narrow spacer filled channels. The model presented in their work shows that the average boundary layer thickness is inversely proportional to the square root of the Peclet number and the model reasonably predicts the dependence of mass transfer rate on flow velocity and Schmidt number.

Farkova [19] investigated pressure drop in empty channels and channels filled with different spacers at different Reynolds number. It was shown that the presence of spacer effects the pressure drop and friction factor values and the impact further intensifies at higher Reynolds number. They also developed correlations for friction factor and Reynolds number for the spacers considered in their work. It was suggested in the study that the pressure drop results can be used for further improvement and optimization of the membrane module design.

Da Costa et al. [25] investigated pressure drop, concentration polarization and permeate flux for Dextran T 500 solution filtration through UF membrane using different spacers and revealed that the permeate flux system is 3 to 5 times greater as compared to flux through empty channels and the pressure drop increase from 5 to 160 times. The study also showed that, at lower flow rate concentration polarization coefficients (ratio of solute concentration at membrane surface and bulk solute concentration) were similar for all the spacers investigated. But at higher flow rates the concentration polarization coefficient values varied significantly for different spacers. They established a correlation between Schmidt number, Reynolds number and Sherwood number and obtained the values of the constants a, b, c and d experimentally for the different types of spacers considered in their work:

$$Sh = c Re_h^a Sc^b \left[ \frac{d_h}{L} \right]^d \quad (2.10.1 - 10)$$

In their study they also confirmed the importance of spacer angle on the mass transfer and pressure drop. Their visualization experiments revealed that the fluid flowing through the spacer filled narrow channels can be broadly divided into two portions. One portion follows the spacer filament and forms a zigzag flow pattern as shown in the following figure (Figure 2.31) and the other fluid portion follows the axial flow direction. Spacers having smaller porosity are responsible for higher pressure drop, turbulence and enhanced mass transfer. They also showed that increasing the porosity from 70 to 90% will reduce the pressure drop to 34%.

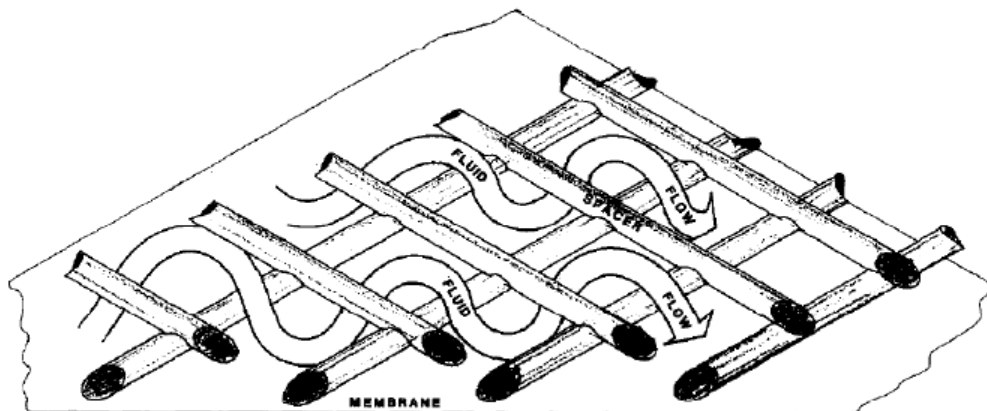


Figure 2.26: Fluid flow streamlines in spacer filled flat channel [25].

In another study Da Costa et al. [127] investigated the effect of spacer on membrane fouling and concluded that the spacer did not stop fouling but reduces concentration polarization and reduces fouling rate on the membrane surface. In another study, Da Costa et al. [128] developed a pressure drop model and concluded that the frictional losses at the membrane wall and on the surface of the spacer are very small. Pressure loss in spacer filled narrow channel is dominated by form drag on spacer strands and kinetic losses due to directional changes in the fluid flow. When the spacer filaments are in transverse and axial direction with respect to the flow, Grober equation is adequate to predict mass transfer. However a correction factor is need for the Grober equation when the filaments are inclined to the channel axis. It was further concluded that mass transfer can be enhanced by increasing the cross flow velocities by keeping the optimal hydrodynamic angle from  $70^{\circ}$  to  $90^{\circ}$  and porosity between 60 to 70%.

Da Costa and Fane [27] in their experimental study concluded that the effect of transverse filament is much more important than changing the flow direction. They showed that, when the transverse filament was set at  $90^{\circ}$  to the flow direction, it could generate 50% higher flux compared to the flow changing direction by  $90^{\circ}$ . They also showed the impact of filament thickness on the flux was significant. When the transverse filament thickness was increased from 0.76 mm to 1.07 mm there was 9% increase in flux reported. They further concluded in that study that the mass transfer mechanism in spacer filled channels depends on two mechanisms. The first mechanism involves the generation of viscous friction as a result of mixing fluid streams crossing each other at an angle. The second mechanism involves viscous friction generated, as a result of wake formation when the fluid past over transverse filaments.

Zimmerer and Kottke [23] investigated the mixing behaviour of different types of spacers. They observed two distinct flow patterns prevailing in spacer filled rectangular ducts. The first pattern was referred to as the channel flow in which the flow followed the channel made by two neighbouring filaments. The second type was referred to as the corkscrew flow, which was the flow passed over the spacer following the channel axis. It was shown that the proper selection of spacer filament wavelength ratio and spacer angle could lead to a mixed flow pattern of the two

distinct patterns mentioned earlier and could improve spacer performance in terms of mass transfer.

Eriksson and Escondido [129] compared the performance of two membrane elements one having diamond spacer and the other having parallel spacer. In case of diamond spacers the top and bottom set of the filaments make an angle with each other and touch the membrane surface, whereas in case of the parallel spacers there are thick longitudinal filaments and thin filaments in cross directions. The thin filaments do not touch the membrane surface, but they are connected off-centered to the thick filaments. It was found that the membrane element with parallel spacer was fouled with calcium carbonate and particulate fouling in short period of time as compared to the membrane element having diamond spacer. The reason for the fast fouling in parallel spacer filled membrane element was attributed to the fact that the parallel spacer promotes less mixing, as compared to diamond spacer, which leads to higher degree of concentration polarization and hence increases the fouling tendency.

Sablani et al. [103] investigated the effect of spacer thickness on the salinity and product flow by conducting experiments on spiral wound membranes for RO system. A thickness of 0.071cm was reported as the optimal thickness for the spacer for maximum product flow.

Li et al. [34] conducted a study using direct observation through the membrane (DOTM) technique to investigate the deposition of particles on the membrane surface during microfiltration. Their research work demonstrated that DOTM is a powerful technique to investigate the particle deposition phenomena on the membrane surface and the interaction between particles and the membrane. In their work, imposed flux mode was used so that the flux can be maintained at, below or above the critical flux. It was observed that below the critical flux the deposition of the particles was not obvious or negligible, near the critical flux there was significant particle deposition. Above the critical flux, particles tend to form layers on the membrane surface. They also investigated the impact of cross-flow velocity on the size of the particles deposited on the membrane surface. It was concluded that smaller particles tend to deposit on the membrane surface with an increase in the cross flow velocity. Another interesting conclusion drawn was that, particles are more likely to get deposited on the membrane surface when other particles have

already been deposited there. In another research article Li et al. [130] determined critical flux experimentally for cross-flow microfiltration process for different particle sizes using DOTM technique and compared the experimentally obtained critical flux values with the values predicted by two different theoretical models, i.e., by shear induced diffusion (SID) model and Inertial lift (IL) model. It was shown that SID model predicts the critical flux values that agreed with the experimental investigations for smaller particles, but it over predicted the critical flux for larger particles. While, IL model under predicted critical flux for all the cases investigated in their work.

Neal et al. [5] used DOTM technique to investigate the effect of presence of spacer and spacer orientation on the critical flux. It was shown that the critical flux for empty channel was significantly lower than that for the spacer filled channels. The reason given in their study for this was that, the presence of spacer generates high shear zones near the surface of the membrane which reduces the deposition tendency of the particles at the membrane surface. It was also shown in the study that the particle deposition pattern on the membrane surface is greatly impacted by the orientation of the feed spacer. They described the particle deposition pattern for  $90^{\circ}$ ,  $0^{\circ}$  and  $45^{\circ}$  spacer orientation with the flow.

Schwinge et al. [131] investigated the effect of a zigzag spacer, in a thin channel under UF conditions, on flux enhancement and pressure drop. The UF experiment was conducted in a flat channel having width of 25mm, total length was 285mm and active membrane length was 203mm. The channel height was 3.2mm. The zigzag spacer used in the experimental study is shown in the following figure (Figure 2.32) and had length, width and height 203mm, 25mm and 3.2mm respectively. On top of the spacer the width between peaks represented by  $r$  in the following figure was 0.8mm. The axial length between the bends represented by  $q$  in the figure below was 10.6mm.

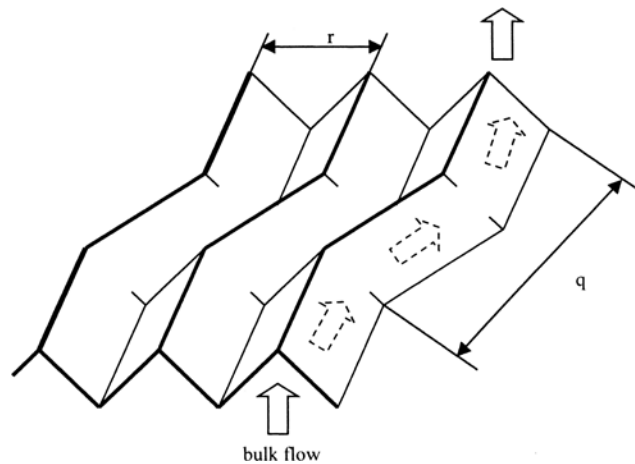


**Figure 2.27: Zigzag spacer used by Schwinge et al. [131]**

It was concluded the presence of Zigzag spacer promoted turbulence and enhanced the fluxes of silica and dextran significantly during ultrafiltration membrane separation process. But there was not a significant flux enhancement reported for whey proteins during UF using zigzag spacer. The biggest advantage of the Zigzag type spacer lies in the fact that they have no obstruction to block the flow path. As a result the flow path cannot be blocked easily by the feed solution which may have big molecules, particles or dirt. So this type of spacer is suitable for non-fouling feed solutions as well as feed solutions containing particles. The flexibility the use of this kind of spacer may bring in, is the removal of pre-filtration step upstream the membrane separation process as the particles in the feed do not obstruct the flow path and do not have a marked negative impact on the flux and permeate quality. In other studies focusing on the development of novel spacers Schwinge et al. [132, 133] compared flux and pressure loss of conventional 2-layer spacers and a proposed novel spacer which they call “advance 3-layer spacer” (A3LS). It was shown that for the case of conventional 2-layer spacer the permeate flux first increases with the reduction in the spacer filament spacing. But beyond optimal filament spacing the flux reduces with further reduction in the filament spacing which is attributed to the reduction in the membrane effective area resulting from increased area of the membrane surface covered by the filaments. However it was concluded that the pressure drop in case of conventional 2-layer spacers increases with reduction in the filament spacing. They also showed that A3LS had less fouling propensity and superior mass transfer characteristics compared to conventional 2-layer spacers. However the pressure drop in case of A3LS was greater as compared to 2-layer

spacers, due to additional flow resistance caused by an extra layer of middle transverse filaments. But at the same time A3LS improved the flux through the membrane compared to 2-layer spacers (at identical mesh length and hydraulic diameter) as they do not cover additional membrane surface area but produce more turbulence and directional changes. However the A3LS are complicated to manufacture due to three layer assembly and the difficulty involved in embedding the middle layer into top and bottom layers. Schematic of the novel spacer configuration is presented in Figure 2.33.

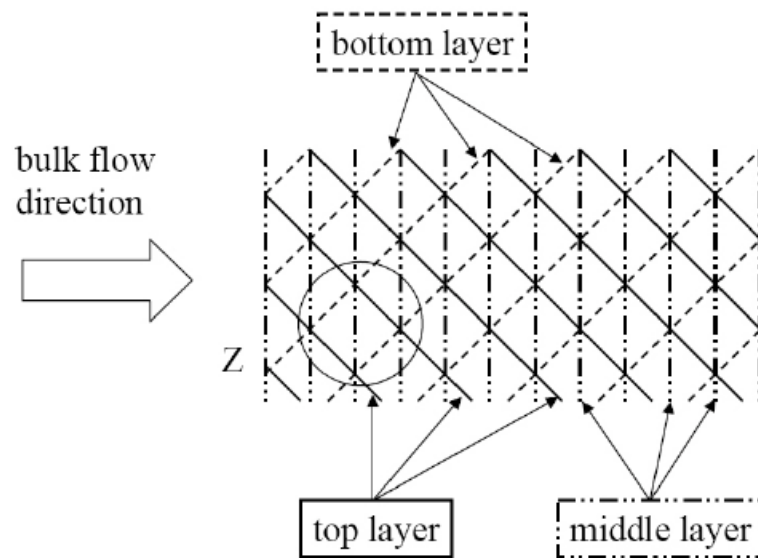


**Figure 2.28: A3LS configuration proposed by Schwinge et al. [133]**

Yang et al. [134] performed theoretical and experimental study to predict concentration polarization in spiral wound nanofiltration element using Polyethylene glycol solution. It was found that there was significant change in the solute concentration over the membrane surface along the cross flow direction. However, the degree of concentration polarization was significantly reduced by the feed side spacer. For instance, the degree of concentration polarization can be less than 1.02 for a filament spacing of 3mm, applied pressure of 1.0 MPa and wall shear rate of  $1000 \text{ s}^{-1}$ .

Li et al. [135] tested a number of woven and non-woven spacers commercially available and confirmed experimentally that the spacer geometric parameters has a considerable impact on mass transfer at a given cross-flow power number. They also

found that the entry length in a spacer filled channel is equivalent to 3 to 5 repeated flow cells in the bulk flow direction, since this length is way shorter than that in empty channels so they suggested that the entry effect in feed channels filled with net-type spacers can be neglected. They also showed in the study that the performance of woven and non-woven commercial spacers is almost similar.

Bartels et al. [43] indicated improvements in the design of seal carrier and presented an improved design which is also helpful to vent trapped air in the annular gap between the pressure vessel walls and outside of the elements. They also mentioned the advancement in the feed spacer of the spiral wound module. In the context of the feed spacer improvements, they pointed out that narrow feed spacers are a good option for the systems having adequate pre-treatment process. However, in case of poor water quality having high fouling tendency the use of narrow feed spacer is not recommended as it may plug the flow channel and hence a thicker feed spacer is more adequate for this sort of applications. They have also reported that Hydranautics, Inc has manufactured membrane with greater spacer thickness and unique geometry which results in lesser pressure drop and claim it to be suitable for treatment of poor quality water.

### **2.10.2 Computational Fluid Dynamics (CFD) based studies**

It is established in the previous sections, that the presence of spacer promotes directional changes in the flow which reduces membrane fouling and concentration polarization. Hence the efficiency of a membrane module depends heavily on the efficacy of the spacers to increase mass transport away from the membrane surface into the fluid bulk by increasing shear rate at the membrane surface. However it is not possible to get the detailed insight of the spacer effect by deploying ordinary experimental methods due to complexities involved in flow and concentration patterns visualization in narrow channels. Due to this fact a number of researchers in the field of membrane science are either using CFD tools or have shifted their focus from experimental methods to CFD tools to investigate mass transfer and hydrodynamics in spacer-filled narrow channels. Following two sub-sections will deal with studies involving CFD tools and exploring the effect of feed spacer geometric characteristics on the performance of membrane module.

### **2.10.2.1 Two-Dimensional (2D) CFD studies**

It is quite evident that the flow conditions prevailing in the real-world spiral wound module are of three dimensional nature, however numerous two dimensional (2D) CFD studies have provided adequate understanding of effect of filament thickness, filament spacing and spacer type on the performance of spiral wound membrane. In case of 2D modelling, the filaments of the feed spacer are positioned normal to the flow direction.

Kang and Chang [32] carried out numerical studies to investigate mass transfer and flow pattern between two parallel plates having rectangular obstruction making zigzag and cavity type arrangement. They concluded that the mass transfer is enhanced as the obstructions give rise to recirculating zones which enhances the convective mass transfer and results in increase in the wall shear stress. It was concluded from their visual and numerical study that for both types of obstruction, there were two fluid recirculation regions, one being larger in size develops at downstream and the other being smaller in size develops upstream of the obstruction. The effect of increase in Reynolds number was also investigated in their study for zigzag and cavity obstruction. It was shown that in case of zigzag obstruction the size of the upstream recirculation zone increase with an increase in Reynolds number and also the centre of the particular recirculating fluid zone shifts along the fluid flow direction with increase in the Reynolds number. Whereas, in case of cavity obstruction the downstream recirculating zone grew in size with the increase in Reynolds number till it occupied whole of the cavity region eliminating the upstream eddy. The eddy size predicted by the numerical study was in line with the visualization experiments carried out. Figure 2.34 shows the streamline distribution for zigzag and cavity geometry studied by Kang and Chang [32].

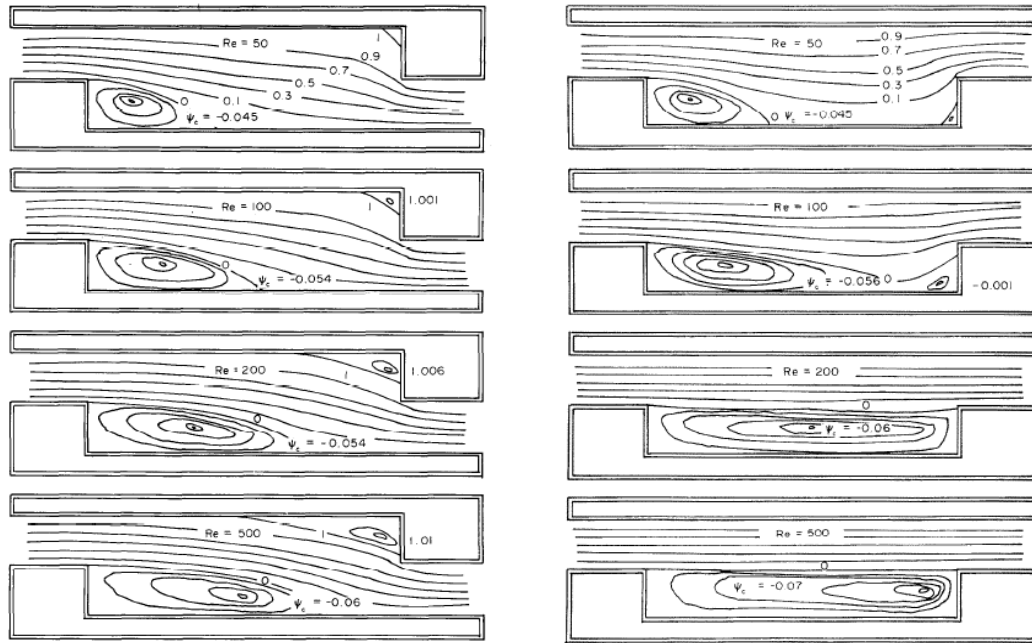


**Figure 2.29: Streamlines for zigzag (left) and cavity (right) configurations, presented by Kang and Chang [32].**

Cao et al. [136] simulated flow through narrow spacer filled channels using CFD commercial code FLUENT. In the study three different type of configuration were considered by changing the respective position of the cylindrical filament in relation to membrane surface. The three configurations (presented in Figure 2.35), namely: Zigzag, cavity and submerged were investigated for flow patterns, velocity distribution and turbulent kinetic energy distribution. It was found that the mass transfer rate was equal on the top and bottom membrane surface when the filaments touch alternatively the top and bottom membrane wall (Zigzag configuration) and when they are positioned in the centre of the channel (submerged configuration). However it was shown from the comparison of simulations results, for the three different configurations, that the submerged configuration overall yielded better results. Their simulation results also suggested that the high shear stress regions, velocity fluctuations and eddy formation is due to the presence of spacer in the channel and the mass transfer mechanism is directly related to the high shear stress zones, velocity fluctuations and eddy formation. It was also concluded that eddies are generally formed before and after the cylindrical filament, whereas peak shear stress zones are repeated after each cylindrical filament. Thus it was concluded that if the filament spacing is reduced the distance between two consecutive shear stress peak on the membrane surface may be reduced which will benefit mass transfer, but

at the same time the reduction in the inter filament spacing will lead to increased pressure loss. So it was concluded in their study that optimal spacer design is a trade-off between these factors.

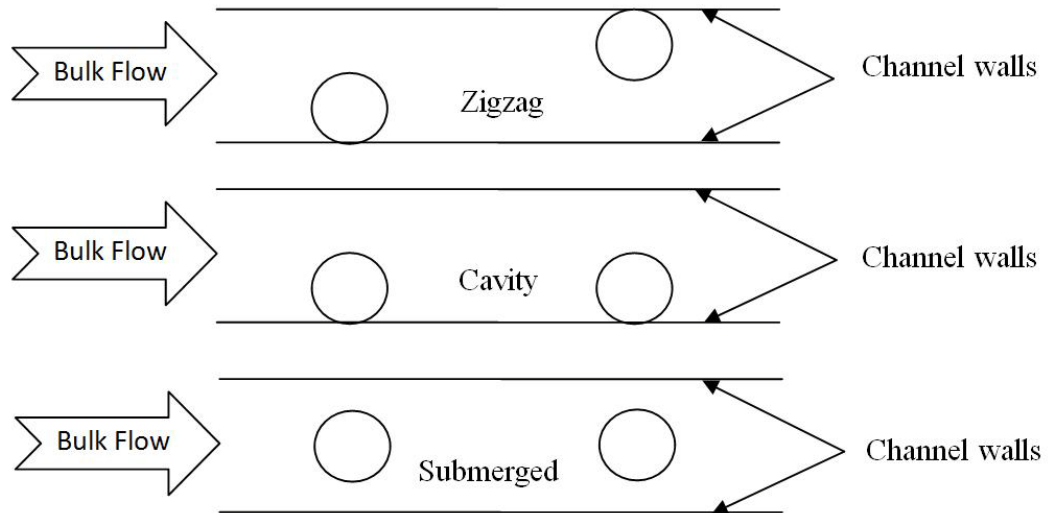


**Figure 2.30: Schematics of different 2D spacer configurations.**

Schwinge et al. [137-140] presented two dimensional analyses of spacer filled narrow channels using CFD tools. They extended the work of Cao et al. [136] and considered similar three spacer configurations as shown in the above figure and studied the effect of filament spacing, filament type, filament thickness on hydrodynamics and mass transfer aspects of the channels using transient and steady state simulations. They concluded that, under steady state laminar flow conditions zigzag configuration performed better than their two counterparts, when both pressure loss and mass transfer enhancement characteristics are taken into consideration. They showed that, for submerged configuration the onset of vortex shedding occurred at hydraulic Reynolds number between 200 and 400, and for zigzag and cavity geometries onset of vortex shedding occurs at hydraulic Reynolds number of 400 and 800. Their conclusion was inline line with the results obtained by Kang and Chang [32], who showed that for zigzag and cavity configurations flow becomes unsteady at hydraulic Reynolds number between 455 and 545. It was also shown that under unsteady flow conditions vortex shedding occurs behind the cylindrical filament and the shed vortices scour the membrane wall on their way to the next downstream filament resulting in increase in the wall shear stress and

disturbing the concentration boundary layer. For the different spacer arrangements different vortex shedding patterns were recorded in their study.

The efforts of Geraldés and co workers regarding investigation of concentration polarization phenomena and membrane characteristics by simulating flow through empty channels are described in section 2.9 [107-110]. They extended their work and included square spacer filaments in the feed channel and investigated the resulting changes in concentration and flow patterns [20-22, 141]. Their model also included the semi-permeable characteristic of the membrane as one of the boundary condition to account for the loss of fluid through permeation. In all the studies they have defined the upper membrane layer as impermeable wall and the bottom membrane as semi-permeable.

Figure 2.36 shows two distinct cases investigated by them [21, 141] by changing the relative position of spacer filaments with respect to the semi-permeable membrane. They concluded that average concentration polarization at the membrane wall in case of channels having transverse filaments adjacent to the membrane is independent of the distance from the inlet, because in that case the concentration polarization boundary layer is periodically disrupted due to the presence of spacer filaments adjacent to the membrane surface, whereas average concentration polarization increases with the distance along the channel when the transverse filaments are positioned opposite to the membrane surface due to continuous growth of concentration boundary layer along flow direction. They concluded that spacer plays a vital role in disruption of concentration boundary layer which results in enhanced mass transfer. So they proposed to position spacers adjacent to both top and bottom membrane surfaces to increase mass transfer within narrow channels spacers. Their model also predicted the apparent rejection coefficient of NaCl which agreed reasonably with the experimental results.

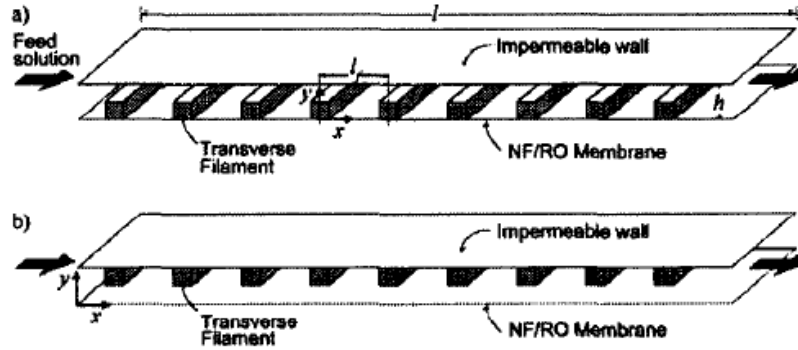


**Figure 2.31: Rectangular feed channel with transverse filament adjacent (a) and opposite (b) to the membrane. Source [21].**

In another work [20] they varied the distance between the filaments and investigated the corresponding effect on the critical Reynolds number i.e. onset of transition of flow regime from laminar to turbulent. They utilized tracer injection method and validated their findings with CFD simulations making use of streamline distribution at various Reynolds numbers for different geometric arrangements of ladder type spacers present in narrow channel. They concluded that the inter filament distance has a marked impact on the critical Reynolds number and on increasing the inter filament distance the Critical Reynolds number decreases. They summarized their finding by concluding that the critical Reynolds number for narrow channels filled with ladder-type filament, having a filament thickness to channel height ratio of 0.5, is in the range of 150 to 300 and is significantly lower than critical Reynolds number for empty narrow channel (usually greater than 1000). Since spacers are responsible to generate turbulence in the channel. Therefore, for the same Reynolds number, the mass transfer process in ladder type spacer filled thin channels is efficient as compared to the empty channels. In the same paper they also investigated the effect of the dimensionless transverse filament height (ratio of filament height to channel height, as described by  $p_f$  in the Figure 2.37) on the flow patterns generated. They concluded that with the increase in dimensionless filament height the length of the recirculation zone increase and on further increase a secondary recirculation zone in generated close to the next downstream filament, within the primary recirculation region. The flow direction of the fluid near the membrane wall at that particular area and the flow direction in that secondary recirculating flow zone are opposite in direction which causes scouring on the membrane surface and reduces the concentration layer thickness in that area and promotes mass transfer away from the

membrane surface. Figure 2.37 represents the impact of increase in dimensionless filament height at Reynolds number of 200 (defined by average inlet velocity and channel height as characteristic velocity and characteristic length in their study), permeation velocity =  $2.5 \times 10^{-5}$  m/s and dimensionless filament spacing of 3.8 (ratio of inter filament size to channel height, represented by  $L_f$  in the following figure). They indicated three different flow patterns, in their study, prevailing in narrow channels filled with ladder type spacers:

- At low Reynolds number and low dimensionless filament height but higher dimensionless inter filament distance the recirculation region developed downstream of the first filament does not reach the next filament in the flow direction. As a result of this flow pattern two solute concentration boundary layers are developed in different directions with maximum solute concentration near the upstream and downstream filament.
- At higher Reynolds number and higher dimensionless filament height but lower dimensionless inter filament spacing the recirculation region developed downstream of the first filament extends to the next filament in the downstream direction. As a result of this flow pattern a single concentration boundary layer is developed from downstream to the upstream filament and has the maximum solute concentration near the last filament.
- The third flow pattern is depicted in the following figure for special case when the dimensionless filament height is equal to 0.75, in addition to the primary recirculation region developed downstream the first filament, a secondary recirculation region is also developed within the primary recirculation region which disrupts the potential growth of concentration boundary layer from downstream filament to upstream filament and results in decrease of solute concentration at the membrane surface at that particular region.

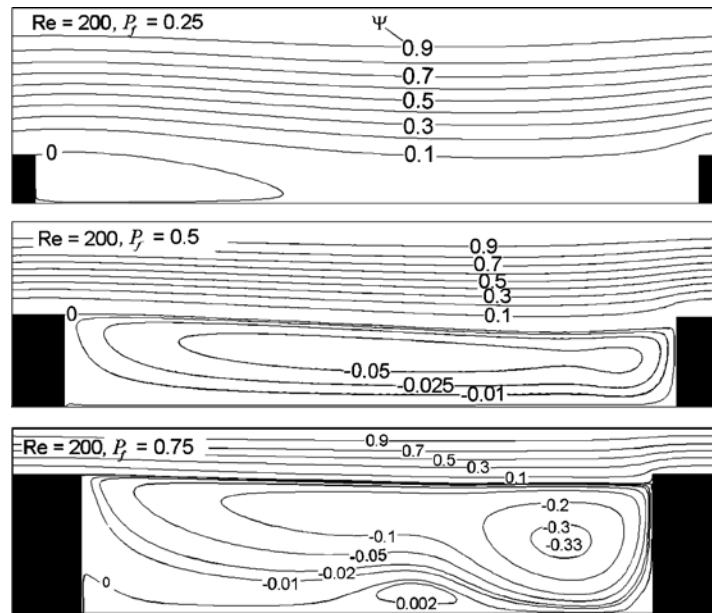
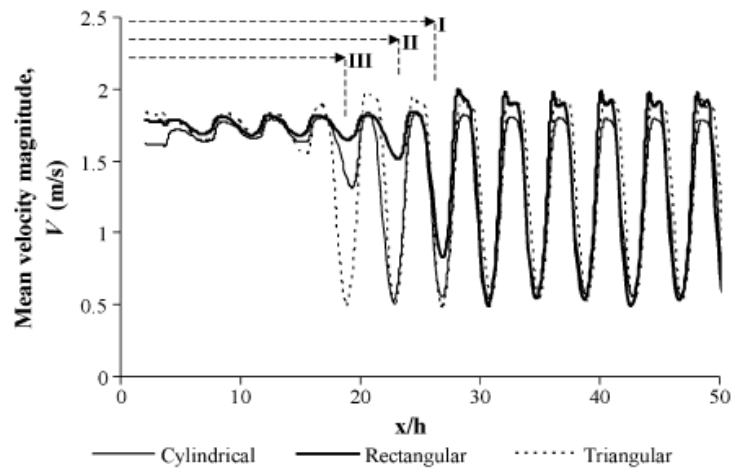


Figure 2.32: Stream lines distribution at  $Re=200$ ,  $v_p=2.5 \times 10^{-5}$  m/s,  $L_f=3.8$ . Source [20].

Since these three distinct flow patterns have different implications on the development of concentration boundary layer patterns and as a result the magnitude of concentration polarization depends on the dominant flow pattern prevailing in the narrow channel filled with ladder type spacer.

Ahmad et al. [142] used commercial CFD code FLUENT 6 to simulate two dimensional flow and permeation through narrow channels filled with spacer filament. They compared the performance of spacers having three different geometric shapes i.e., cylindrical, triangular and square in terms of pressure drop and reduction in concentration polarization. They concluded that feed Reynolds number (using feed velocity and channel height as characteristic velocity and dimension respectively) should be used as the criteria for optimum spacer geometry. Based on this conclusion they suggested the use of cylindrical spacer at the feed side of the membrane channel for the filtration processes involving higher flow rates for energy minimization. They recommended the use of triangular and squares shaped spacers in the feed channel for low flow rate filtration systems as those geometries were proved to provide a better mix of concentration polarization reduction, energy requirement and head loss. In another study by Ahmad and Lau [143], they investigated the impact of different spacer filament geometry on unsteady hydrodynamics and concentration polarization in spacer filled channel. With the aid of velocity counter plots at different time they showed the development, movement

and dissipation of unsteady vortices in different directions within the channel having cylindrical, rectangular and triangular spacers. They also showed the unsteady hydrodynamics occurs in channel after certain transition distance from the inlet referred as “transition length”, which depends on the geometry of the spacer with which the channel is filled. It was shown that transition length was shortest for triangular spacers and longest for the rectangular spacer and that for the cylindrical spacer lies between the two extremes. Figure 2.38 illustrates the transition length evaluated for the three different spacer studied in their work with the aid of a plot between mean velocity magnitude and dimensionless distance from the inlet ( $x/h$ , in the following plot). The mean velocity changed drastically till certain length from the inlet of the channel due and then after that distance (transition length) it started to vary in a periodic manner. They also showed that cylindrical and triangular spacers demonstrated unsteady vortices at feed Reynolds number of 200, whereas for those unsteady vortices were shown for rectangular spacers at feed Reynolds number of 300.



**Figure 2.33: Entrance transition length for I. Rectangular spacer, II, cylindrical spacer, III, triangular spacer, source: [143].**

Estimation of solute concentration at the membrane surface of a RO membrane is vital to investigate the degree concentration polarization in the system. In many models the assumption of constant permeate velocity at the membrane surface is made to get wall concentration profiles. Ma et al. [144] investigated the accuracy of this assumption under different flow conditions for empty and spacer filled narrow channels. They concluded that the assumption of constant permeate velocity may

yield acceptable results (with an error  $< 10\%$ ) for average wall concentration. But this assumption leads to over estimation of maximum wall concentration. It was shown in their study for cases when the membrane wall do not touch the transverse filament (as in case of empty channels, submerged configuration or for the case when the semi permeable membrane is opposite to the transverse filament such as in the cavity configuration) this assumption leads to evaluation of maximum wall concentration within an error of 20%. For the cases when the membrane wall touches the transverse filaments, the assumption of constant permeate velocity can lead to a very large error in evaluation of maximum wall concentration. This error could be as high as 120%.

Ma and co-workers [145-147] used two dimensional streamline upwind Petrov/Galerkin finite element model to investigate the impact of spacer type (zigzag, cavity and submerged) and filament spacing on permeate flux and concentration patterns developed in RO membrane channels. It was shown that compared to empty channels, spacer filled channels alleviate concentration polarization at considerable portion of the membrane, however there were few regions, such as immediately in front and behind the filaments, where the salt concentration was increased. For the three types of spacers tested, it was found that the permeate flux was dependant on the filament spacing. For submerged configuration, permeate flux continuously increased with decrease in filament spacing. It was found that in case of zigzag and cavity configuration the optimal filament spacing depended on the salinity of the feed.

Subramani et al. [148] considered short channel section with only one permeable wall to simulate flow through open and spacer filled channels using a finite element model. As suggested in their research paper, the presence of feed spacers enhance the shear stress rate at the membrane wall which reduces the concentration polarization, but at the same time the presence of spacers give rise to stagnant flow regions, especially, in front and behind of the spacers which may contribute to enhanced local concentration polarization in those particular areas. It was concluded in their study that the selection of non-optimal spacer configuration may lead to generation of such areas having local peaks of concentration polarization and may adversely affect the performance of the membrane module. Within different flow

conditions simulated in their work they concluded that the cavity and submerged spacer performed better than the zigzag spacers.

Fimbers-Weihs et al. [31] conducted numerical study, using a commercial CFD code ANSYS CFX (version 10.0), to investigate two dimensional unsteady flows and mass transport in narrow channels filled with cylindrical spacers having zigzag configuration. Mass transfer was incorporated in the model by using a dissolving wall boundary condition. The dimensionless filament thickness and filament spacing was considered 0.5 and 4 respectively in their study. For the particular spacer geometry it was found that the flow became unsteady at the hydraulic Reynolds number (using effective velocity and hydraulic diameter as characteristic velocity and dimension respectively) between 526- 841. They also concluded that mass transfer is enhanced in the regions showing two distinct behaviours:

- Regions having high wall shear rate
- Regions where the direction of fluid flow is towards the membrane walls i.e. inflow of fluid from low concentration region to concentration boundary layer (higher concentration zone).

It was concluded that for the filtration of sodium chloride solution, using the spacer characteristic as demonstrated, out of the two main causes described, the later dominated the enhancement of unsteady mass transfer.

Gimmelshtein (Modek) and Semiat [33, 149] investigated flow through narrow channel having submerged spacer configuration. The numerical study was conducted using FemLab software and the experimental study was based on particle image velocimetry (PIV). It was shown in the study that with an increase in spacer thickness the vorticity values above and below the spacer significantly increased. The velocity values predicted by the numerical model agreed reasonably with the experimental results obtained from the PIV images.

Koutsou et al. [65] used a commercial CFD code FLUENT to simulate two dimensional fluid flow through a narrow channel filled with periodic array of submerged cylindrical filaments. They made use of periodic boundary conditions in the model to reduce the size of computational domain which could adequately represent the whole process. They identified various flow features and regions in the

computational domain such as the development and separation of boundary layers, recirculation regions and regions of high shear stress. They also studied the effect of Reynolds number on wall shear and pressure drop. Their study showed that when the cylindrical Reynolds number (defined by taking average fluid velocity and filament diameter as characteristic velocity and dimension respectively) exceeded the values of 60 the flow became destabilized. The recirculation eddies, behind the filament became asymmetric and oscillated periodically. With further increase of cylinder Reynolds number the instabilities developed got further intensified and led to a chaotic state.

A similar study was carried out by Santos et al. [150]. They used finite volume based CFD software package OpenFOAM to model flow and concentration patterns in narrow channels filled with ladder type spacers. To support their model they also carried out experimental study, by visualization of tracer flow patterns, and validated the results obtained from the numerical model. They varied the Reynolds number (based on channel height and superficial velocity) in the range of 60 to 548 and discussed its impact on the flow features and concentration patterns. They concluded that for low Reynolds number, steady flows are obtained with recirculation regions after the upstream and before the downstream filaments. When the Reynolds number was increased beyond a critical value the flow became unstable and vortex shedding was observed which broke the recirculation regions and had a sweeping effect on the membrane surface and reduced the concentration polarization.

Li and Tung [151] investigated the impact of curvature in spiral wound membrane on flow behaviour of channels filled with different types of spacers, namely: cavity, zigzag and submerged configurations, with dimensionless filament diameter and spacing equal to 0.5 and 4 respectively. It was concluded for the spacer configuration studied in their work that the curvature of the feed channels had some minor impact on the hydrodynamics, but those impacts were not significant on the shear rate and velocity profiles for the spacer tested in their study. This fact was evident by the comparison of numerical values of shear stress given for the inner and outer wall for different values of dimensionless radius of curvature for different spacers and by the comparison of the velocity profiles for different values of dimensionless radius of curvature and spacer arrangements in their study.

### **2.10.2.2 Three-Dimensional (3D) CFD studies**

In case of 2D studies only one set of spacer filaments which are aligned normal to the flow direction are considered and these studies completely neglect the effect of the other set of spacer filaments. However in case of 3D studies both sets of spacer filaments are considered and provides a true representation of flow inside a SWM module which in fact is three dimensional by nature. Memory and time requirements for 3D calculations to produce results with same accuracy as their counterpart 2D calculation are significantly higher. This is because 3D flow brings along with it extra computational burden as it incorporates an extra dimension as compared to 2D flow. Due to this reason the initial 3D studies were restricted to low spatial resolution and they did not include mass transport.

Hydrodynamics involved in the real life SWM modules are very complex in nature and there are few three dimensional studies available which investigate the impact of geometric characteristics of the feed spacers on flow patterns as compared to 2D studies. This section deals with the 3D studies aimed to investigate the flow and concentration patterns developed in SWM module under the influence of different feed spacer configurations.

One of the initial three dimensional flow visualization attempts using CFD was made by Karode and Kumar [152] utilizing CFD packages PHONICS. Their study did not consider the mass transfer aspect and involved simulation of steady state, laminar fluid flow through channel filled with non woven net type spacers in a test cell. The geometric characteristics of the spacers, such as the inter filament angle, flow attack angle, mesh length and filament diameter etc, were taken from the commercially available spacers for the feed channel of the membrane modules. They modelled the entire test cell by defining a flat velocity profile at the inlet and constant pressure at the outlet. They compared different spacers in terms of velocity profiles generated along the channel height, shear rates exerted at the top and bottom walls and total drag coefficient (to incorporate total pressure drop in the channel). They also plotted total drag coefficient as a function of hydraulic Reynolds number for different spacers and came up with correlations between the two parameters for individual spacers by curve fitting. The characteristic constant ( $A$ ) and Reynolds exponent ( $n$ ) in the correlations, for the most of the spacers, had reasonable agreement with those experimentally determined by Da Costa et al. [128]. It was concluded in their study

that the ratio between inter filament distance to filament diameter influences the bulk flow pattern. For spacers having higher inter filament distance to filament diameter ratio, bulk of the fluid changes direction at each mesh length and follows a zigzag path but maintain its primary direction along the channel axis. This conclusion was in accordance with the experimental observation of Da Costa et al. [128]. However, for the spacers having equal top and bottom filament diameter and lower ratio of inter filament distance to diameter it was concluded that the bulk of the fluid flows parallel to the spacer filaments in their vicinity (fluid flow direction in the zones near bottom wall was parallel to bottom filaments and the fluid flow direction in the regions near the top membrane was parallel to the top filaments) and the directional changes were only visualized when the fluid reaches the lateral wall of the test cell. For such cases they found that the major contributor towards the total pressure drop was the sudden directional change in the velocity vectors at a transition plane where the top and bottom layer of the crossing spacer filaments intersect or simply put, it was attributed to the shear between bottom and top layers of fluid moving in different directions. They also concluded for the spacers having same top and bottom filament diameter (symmetric spacers) and similar relative angle with the channel axis develop same shear rate at top and bottom membrane surfaces. However, in case of asymmetric spacers larger portion of the bulk fluid flows along the thicker filament and contributes higher shear rate values at the particular membrane wall which is attached with thicker set of filaments. They also reported that pressure drop in case of symmetric spacers was higher as compared to that of asymmetric spacers for an identical thin channel. Out of all the spacers considered in their work, one (NALTEX-51-2) with the relatively low total drag coefficient coupled with high average shear rate (average of shear rates at top and bottom membrane surfaces) under different flow conditions was termed as the most effective spacer.

Their work [152] was an excellent initial effort to link experimental results with CFD based 3D investigations, but there were some disagreement found and are described below:

1. The characterization constant (A) and Reynolds exponent (n) evaluated by curve fitting by plotting total drag coefficient as a function of hydraulic Reynolds number (defined by effective velocity and hydraulic diameter of the channel as characteristic velocity and dimension respectively) although

agreed reasonably with those found experimentally by Da Costa et al. [128] for most of the spacers. But characterization constant (A) values especially in case of NATLEDX-129, Conwed-1 and Conwed-2 spacers were significantly under predicted. Similarly the Reynolds exponent (n) for NATLEDX-129 and Conwed-1 spacers were under predicted significantly. There was also disagreement between their calculated pressure drop and experimentally determined pressure drop by Da Costa et al. [128] for Conwed-1 spacer, especially, at higher inlet velocities. They attributed this discrepancy to two possible reasons:

- a) Errors in determining the pressure drop experimentally.
  - b) Real spacers (used in the experimental work of Da Costa et al. [128]) have undulating filaments which may allow some of the fluid to flow between them and the membrane wall. Whereas in the work of Karode and Kumar [152] idealized spacers were used which do not allow such flows.
2. They concluded that the thicker filament will result in higher shear rate values at the membrane surface to which they are attached. Almost all the spacer presented in the study follow that conclusion except NATLEX- 51-2 which has thin top filaments (table 1 of their manuscript) as compared to the bottom filaments but at the same time delivers higher shear rate value at the top membrane surface (figure 12 of their manuscript).
  3. Karode and Kumar [152] indicated NALTEX-51-2 spacer as the best performer based on relatively low total drag coefficient (which results in lower pressure drop in the channel) coupled with high average shear rate. However by comparing Figure 2 and 13 of their manuscript NALTEX-56 appears to be the best performer because it exhibits relatively higher average shear rates for most values of inlet velocities considered and relatively lower total drag coefficient for all values of hydraulic Reynolds number considered in their work.

In their study [152] the geometric characteristics of the spacers were altered in an unsystematic manner (the reason being, they only considered the commercially available spacers) so conclusive results regarding the geometric variation of the spacer filaments cannot be drawn.

Since the work of Karode and Kumar [152] was based only on feed spacers available commercially. Their work was further extended by a co-worker of their research team. Dendukuri et al. [153] considered new spacer design that were not commercially available and had non-circular cross sections. They make use of CFD commercial packages FLUENT and used SIMPLE algorithm to solve conservation equations, however mass transfer aspect was not considered in this work too. In the work they consider three basic commercially available spacers (Conwed-1, UF2 and NALTEX- 56) and changed the original design resulting in four distinct geometric shapes for each commercial spacer chosen. The change in design of the commercial spacers was basically from convex to concave shape and further it was based on either varying the width to height ratio or modification of the concave section into “v” type shape. Figure 2.39 illustrates the four different configurations investigate for each type of commercially available spacers.

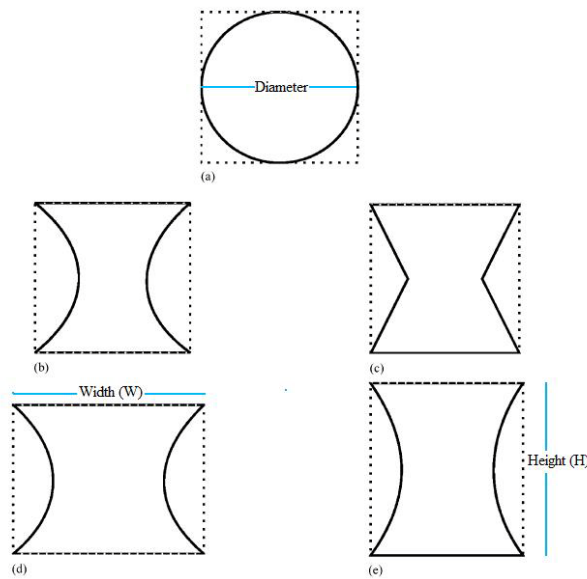


**Figure 2.34: Cross section of spacer filaments. (a) Original spacer (b) Concave-square (c) V-shaped (d) Concave- $W/H = 4/3$  (e) Concave-  $W/H= 3/4$ . Adapted from [153].**

For all the four different shapes considered in their study it was made sure that the curvature depth was always greater than one third of the original filament diameter. It was concluded that compared to their original counterparts some of the new designed spacers resulted in less pressure drop across the channel while exhibiting nearly same strain rate near the membrane surfaces. With this study [153] they further reinforced their conclusion drawn in the previous work [152], that the

pressure drop in the spacer filled channels depends on the inter filament distance to filament diameter ratio for the original as well as the altered spacers. They also showed for Conwed-1 altered spacer design i.e. V-shaped conwed-1 (Figure 2.39 c) that the velocity vectors at planes near top and bottom membranes were along direction away from the membrane surface (which was not in the case for the original Conwed-1) which may reduce the propensity of solute or suspended particles build-up at the membrane surfaces. However, the new designs seem to be difficult to manufacture and since the new design reduce the curvature thickness of the filament which will lead to decline in the physical strength of the spacers. Physical strength of the filament to tolerate flow conditions prevailing in spacer filled channels is questionable and needs to be tested by putting them in real life membrane operations.

Researchers in the field of membrane science using CFD tools for flow visualization through membrane module normally make the assumption that the flow through a spacer filled rectangular channel is a good representation of the flow in case of spiral wound membrane modules having similar spacer in the feed channel. This assumption was first validated experimentally by Schock and Miquel [61] and later by Ranade and Kumar [154, 155] using a periodic unit cell approach. They validated the unit periodic cell approach by showing the contours of pressure and wall shear stress and predicted velocity profiles along the channel height for computational domain consisting of one and four periodic unit cell were identical [155]. They showed that the hydrodynamics of rectangular and curvilinear spacer filled channels are not significantly different and curvature does not have a significant effect on the fluid behaviour. To support their conclusion they plotted pressure drop against Reynolds number (based on superficial velocity and hydraulic diameter) for rectangular and curvilinear channel filled with same type of spacer and obtained almost the similar results. Moreover, they also showed that the velocity fields at mid plane parallel to the membrane surfaces and contours of wall shear stress for both arrangements were almost similar [154, 155]. Based on the investigations they concluded that the results obtained by the rectangular channels can be conveniently used to determine the performance of spiral wound membranes having spacers in the feed channel. However, their conclusion regarding lack of influence of curvature on fluid patterns is restricted to spacer filled membrane modules only. As the literature

review reveals that the curvature has significant effect on flow patterns and enhances membrane performance by generating secondary flow patterns, such as Dean vortices, in conduits without spacers [67, 156-158]. This discrepancy is due to the presence of spacer and can be explained by considering the fact that the influence of spacers on flow patterns is greater than the effect of secondary flow developed by curvature effects [61, 155]. Moreover, they extended the previous studies [152, 153] and evaluated the performance of the original Conwed-1 and other spacers having different curvatures based on a conclusive plot between strain rate and power dissipation per unit mass. The basis of the idea was that an ideal spacer would have least pressure drop across the channel and maximum wall shear rate per unit mass of power dissipation and the major contribution of the pressure drop should come from the viscous drag (and not from the form drag). This is because viscous drag increases the shear rates at the membrane wall, whereas form drag leads to power dissipation without any beneficial impact on the membrane performance.

Li et al. [63, 159] included mass transfer aspect in their model by considering a solute having Schmidt number of 1728 using CFD commercial code CFX-4.3. Their computation domain consisted of a periodic unit cell to which periodic boundary conditions were applied to simulate laminar steady and unsteady flow through spacer filled flat narrow channels. However, in the research paper they did not specify the method used for the implementation of periodic boundary condition for solute transport. They considered symmetric spacers (same diameter for top and bottom filaments) having equal mesh lengths for top and bottom filaments. They compared the performance of different spacers on the basis of mass transfer enhancement and mechanical power dissipation for hydraulic Reynolds number range of 90 to 465. Instead of using directly mass transfer coefficient and power dissipation they plotted average Sherwood number against dimensionless power number for different spacer arrangement (by varying the mesh length and attack angle). They showed that for symmetric spacers (same diameter for top and bottom layer filaments) having same mesh length for both top and bottom filaments the optimum configuration, resulting in maximum average Sherwood number with minimum mechanical energy dissipation, is when the flow attack angle and the inter filament angle is set at  $30^\circ$  and  $120^\circ$  respectively and dimensionless inter filament to channel height ratio is set at 4.

In another research work Li et al. [160] used the same model developed in the previous work [63, 159] to assess the performance of conventional and novel spacers by the comparison of power number and average Sherwood number and compared it with the performance of the non-woven spacer declared optimum in their previous work [63, 159]. Based on analogy between heat and mass transfer they proposed that an optimal spacer configuration should generate longitudinal and transverse vortices near the membrane wall to enhance mass transfer of the solute from the membrane to the bulk of the solution, and at the same time it must require minimum cross-flow power consumption in the middle of the channel. They utilized the same model developed in the previous work [63, 159] to investigate the performance of modified spacers (MF) (with helical bar wound around the cylindrical filament) and spacers with twisted plates (TT) and compared the numerical results with those gained by experiments. They concluded that due to complex shape of the spacer configuration CFD simulation (using CFX-4) predicted higher performance than the experimental results. At the same time the experimental results showed that the performance of those two types were inferior to the optimal non-woven spacer concluded in their previous work [63, 159]. They further investigated the performance of more complex multi-layered spacers, having twisted tapes (MLTT) and normal filaments (MLNF) in the central portion of the flow domain, using experimental technique (limiting current method). Figure 2.40 shows the four different configurations investigated in their work. They further optimized the multi-layer spacer with twisted tape and found its performance more promising than the already optimized non-woven spacer in their previous work [63, 159]. At the same cross-flow power number the average Sherwood number for the optimized multi-layered spacer was found to be 30% higher than the optimized non-woven spacer in their previous work and the same average Sherwood number the cross-flow power consumption of the optimized multi-layer spacer was only 40% of that of the optimized non-woven spacer in their previous work [63, 159].

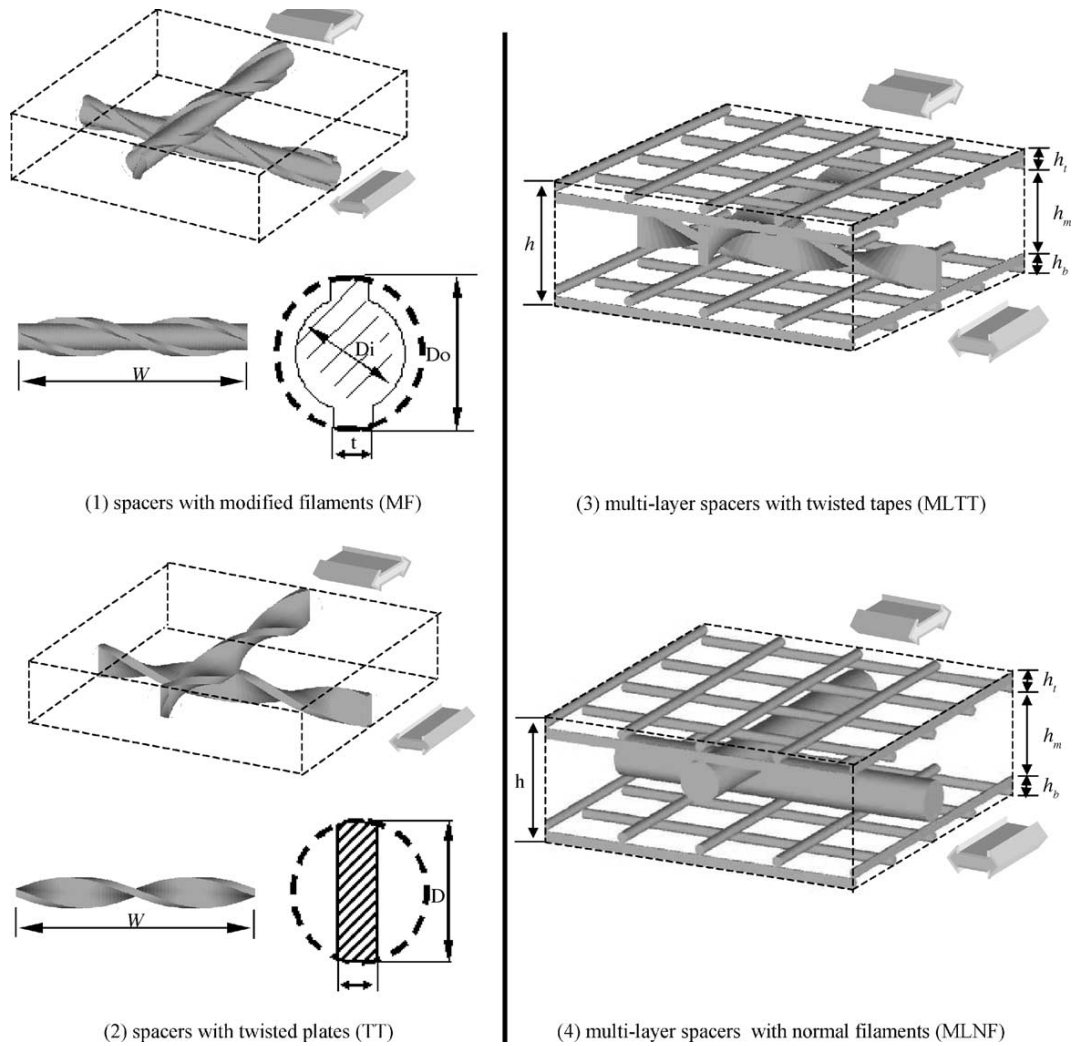


**Figure 2.35: Novel spacers investigated by Li et al. [160]**

Koutsou et al. [66] performed 3D Direct Numerical Simulations for various spacer arrangements in narrow channels. They studied various spacer configurations by varying the spacer mesh to filament diameter ratio, flow attack angle and inter filament angle. However the filament diameter, mesh length and flow attack angles were set to be same for top and bottom filaments for all the cases. They applied spatially- periodic boundary conditions to the flow domain and varied the cylinder Reynolds number (based on cylinder diameter and average velocity) from 35 to approximately 300 to investigate spacer performance in both steady and transient flow regimes. In their study spacer parameters were non-dimensionalized by using spacer filament diameter. They concluded that the pressure drop depends on filament mesh length to filament diameter ratio ( $L/D$ ) and also on the angle between top and bottom filaments. They showed by comparisons of different spacer arrangements that pressure drop tends to increase for smaller  $L/D$  ratios and increase with increase

in inter filament angle. The numerical results obtained for pressure drop for various spacer configurations found reasonable agreement with the experimental results. In their study they showed the difference between fluid flow patterns in earlier 2D and their 3D study. In the previous 2D studies from various researchers it was shown that fluid flows in stream lines whereas Koutsou et al. [66] showed that in case of 3D flows, for all the spacer configurations considered, the fluid flows in spiral manner along the spacer filament. They concluded that the vortices attached to the filament interact with a central free vortex, generated within the computational domain, and resulted in development of closed recirculation regions. It was also reported that the critical Reynolds number which reflects the transition of flow from steady to unsteady was in the range of 35 to 45 (based on filament diameter and average velocity) for the spacer configurations considered in their study. In a latter study Koutsou et al. [161] incorporated mass transport in the numerical model by treating the membrane walls impermeable and defining a constant solute concentration on the membrane walls. In this study they attempted to correlate Sherwood number by varying Reynolds number and Schmidt number for different spacer geometric configurations. They reported that the exponent of Sherwood number dependence on Schmidt number was nearly 0.4 in case of numerical simulations and validated the same conclusion by conducting a series of experiments.

Fimbers-Weihs and Wiley [28] used commercial CFD code ANSYS CFX-10.0 to simulate steady state laminar flow conditions (hydraulic Reynolds number up to 200 for 3D and up to 500 for 2D flows) through spacer filled narrow channels having dimensionless filament mesh length to channel height ratio of 4 and filament diameter to channel height ratio of 0.6. They incorporated mass transport in the numerical model by assigning a constant concentration of solute (having Schmidt number of 600) at the membrane walls. For 3D study they considered spacers configurations in which the filaments were oriented at an angle of  $45^{\circ}$  and  $90^{\circ}$  with the flow direction. The two 3D spacer configurations are shown in Figure 2.41. They applied periodic unit cell approach and fully developed mass fraction profile was utilized as boundary condition for the solute. It was concluded that when the pair of filaments were oriented at  $45^{\circ}$  with the flow direction promoted mass transfer to a greater extend (resulting in higher Sherwood number averaged over both top and

bottom wall as shown in figure 13 of their manuscript) as compared to the case when the filaments pair were oriented in parallel and transverse direction to flow.

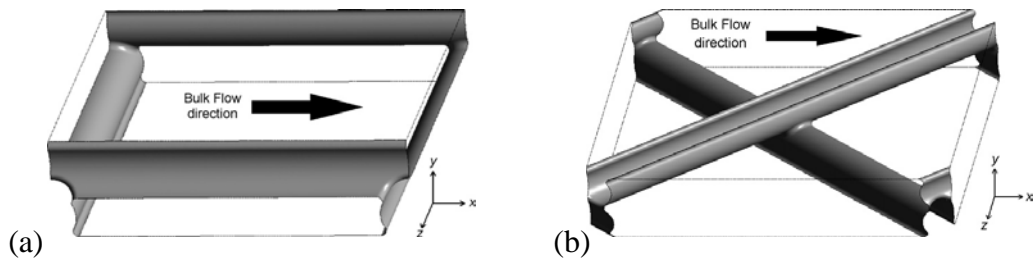


**Figure 2.36: 3D spacers investigated by Fimmers-Weihs and Wiley [28] (a)  $90^{\circ}$  orientation (b)  $45^{\circ}$  orientation.**

They also reported that the 3D geometries modelled in their study presented greater mass transfer enhancement when compared to their 2D counterparts. In their study an attempt was made to calculate the percentage of total energy loss due to form drag and viscous drag for various 3D and 2D spacer configurations at different hydraulic Reynolds numbers. It was concluded in their work that within hydraulic Reynolds number range encountered in daily life SWM operations major portion of energy loss is due to form drag and recommended to use spacer configuration which exhibit lower pressure drop and promotes higher share of viscous drag over form drag in total energy loss. Because increase in viscous drag promotes mass transfer by reducing the boundary layer thickness and directly reduces the resistance to mass transfer.

Santos et al. [162] used open-source OpenFOAM CFD software package to simulate Laminar steady and unsteady 3D flow conditions through channels filled with rectangular spacers. They studied different cases by altering the inter filament distances. Different spacer arrangement used in their study is presented in Figure 2.42. They also introduced a modified friction factor for the membrane walls which takes into account average shear stress at the walls, and claimed that it may be used to select best spacer arrangement in terms of mass transfer efficiency. It was concluded in their study that the effect of longitudinal filament spacing on flow profile, critical Reynolds number and on modified friction factor was not significant at all, but these factors depends significantly on the transversal filament spacing. They also investigated the impact of transversal filament spacing on mass transfer (in terms of Sherwood number) for three spacers arrangements without having axial filament namely: S1L0, S2L0 and S3L0. Moreover, plots of power number against

Sherwood number for top and bottom walls and also against Sherwood number averaged over top and bottom walls were also presented for the three spacers mentioned above. It can be seen from Figure 2.42 that they have considered few cylindrical filaments along the flow direction ( also not incorporated periodic boundary conditions) so the concentration patterns obtained in their study must have suffered from entrance effect. Their results can be assumed accurate for the entrance region only and thus cannot represent the average conditions sustained in membrane modules.

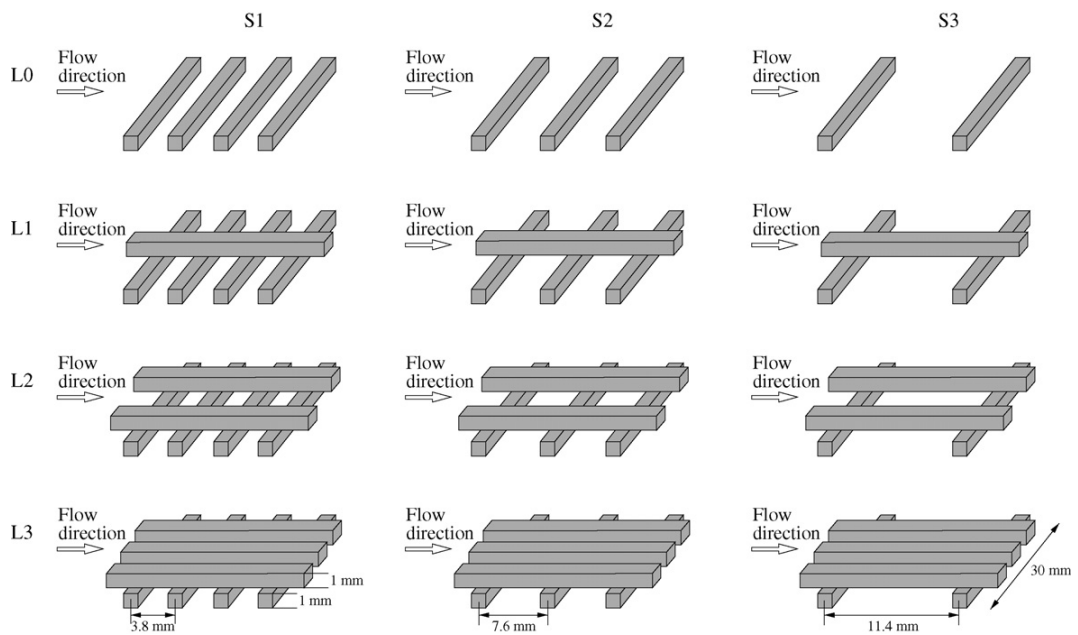


**Figure 2.37: Schematics of 3D spacers investigated by Santos et al. [162]**

Lau et al. [163] utilized CFD commercial package FLUENT V6 to simulate laminar steady and unsteady flow through narrow channels filled with cylindrical filaments by varying internal filament and flow attack angle. They made use of periodic unit cell approach along with developing wall concentration. The membrane walls were considered permeable in their numerical model. They fixed the filament mesh ratio to 3 and varied inter filament angle from  $30^{\circ}$  to  $120^{\circ}$  and flow attack angle was varied from  $0^{\circ}$  to  $60^{\circ}$ . The numerical predictions for channel pressure drop per unit length at different feed Reynolds numbers (defined by channel height and feed velocity) and permeate flux predictions at different transmembrane pressures agreed reasonably with their experimental values. It was found that the spacer arrangement having inter filament spacing of  $120^{\circ}$  and flow attack angle of  $30^{\circ}$  produced unsteady hydrodynamics (beneficial for disrupting solute concentration boundary layer) at

feed Reynolds number as low as 100 and also generated highest mean velocity magnitude and highest Root-mean-square (RMS) of velocity magnitude fluctuation for the range of feed Reynolds number considered in their work. Since the velocity within spacer filled channels ranges from 0.05 to 0.5 m/s and pressure drop above 1bar/m is not desirable [140, 163], so in their study they investigated spacer performance based on specific power consumption ( $SPC = \frac{\Delta p_{ch}}{L} \times velocity$ ) in the range of 2000 to 50000. Also the above mentioned spacer configuration resulted in highest wall shear stress at top and bottom membrane walls for a practical range of specific power consumption (between 2000 to 5000 Pa/s) and was reported to be the most efficient of all the spacers considered in their work.

Shakaib et al. [164] used commercial CFD code FLUENT (Version 6.2.16) to simulate laminar steady flow through narrow channels filled with principally two different types of spacer arrangement, namely: Diamond spacers and parallel spacers. In the first type the total channel height is defined by the sum of top and bottom filament thickness and the two set of filaments exist in two different planes at different orientations. One set of filament overlay upon the second filament set. In the second type the channel height is equal to the thickness of the axial filaments only and the thin transversal filaments are connected to the thick axial filaments. The two principal types of filaments configurations investigated in their study are presented in Figure 2.43.

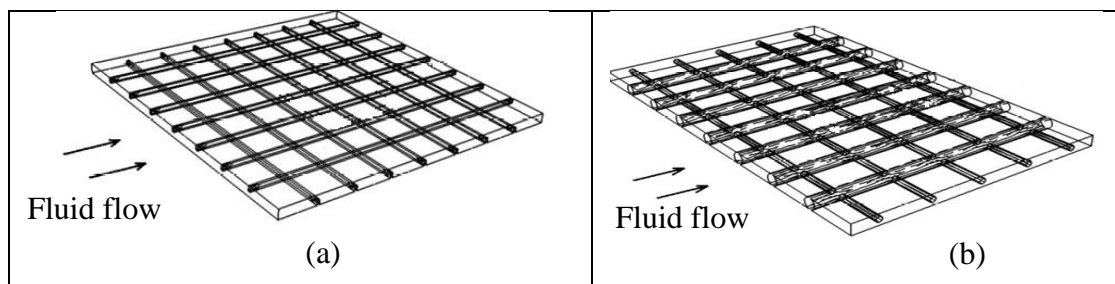


**Figure 2.38: Principal spacers configurations investigated by Shakaib et al. [164] (a) Diamond type spacer (b) Parallel spacer.**

In their model the both top and bottom membrane walls were considered to be impermeable and no slip conditions were defined at both the membrane walls. The simulated fluid was water having constant properties. Periodic unit cell approach was used in their study considering one pair of transversal and axial filament each. Two pairs of periodic zones for the four vertical faces of the domain were defined for the

diamond arrangement. In case of Parallel spacers only one pair of periodic boundary condition was defined for the two vertical faces perpendicular to the flow direction. Further the geometric characteristics of the spacers were non-dimensionlized using channel height. In their study they showed that the flow patterns are of quite complex and 3D in nature through spacer filled narrow channels and inter filament spacing have strong impact of the flow patterns generated within the channels which directly impact the pressure drop and average shear stress on the top and bottom membrane surfaces. They showed that the average shear stress values at the top and bottom walls are different due to difference in the flow patterns in the vicinity of the two membranes in case of the diamond spacer. However for diamond spacer having same filament thickness, spacing and flow attack angle the two values as almost equal. In case of parallel spacers the shear stress values at the top and bottom membrane surfaces were found to be equal. They also made an attempt to investigate the impact of transverse filament thickness on the hydrodynamics and concluded that thicker transverse filaments generate higher pressure drop and tend to develop significantly different shear stress distribution on top and bottom walls which is definitely an undesirable feature and must be avoided for better membrane performance.

In a latter study by Shakaib et al. [165] incorporated mass transport in their numerical model by defining a constant solute concentration on the membrane walls. Their computational domain consisted of six bottom and one top filament. It was found that the flow was fully developed and became periodic after first 3-4 transverse filaments and the region between the last two transverse filaments was the true representative of flow and mass transfer patterns in spiral wound membrane modules and was free from any entrance or exit effects. It was further shown that that for spacer configuration having bottom filaments aligned perpendicular to the flow direction and top filaments aligned parallel to the flow direction represented identical regions of high shear stress and high mass transfer coefficient at the top wall. But for the bottom membrane surface the areas of high mass transfer coefficients and high shear stress were different. This difference was explained due to different flow patterns generated in the vicinity of bottom wall due to fluid reattachment and recirculation. The impact of transverse filament thickness was also investigates and it was found that the diamond spacers with thicker transverse

filament were responsible for generating local peaks of mass transfer coefficient and resulted in non uniform distribution of the same.

Shakaib et al. [165] investigated the spacers configuration in past, but the methodology for grading the spacer did not look adequate as they used the ratio of average mass transfer coefficient and scaled value of pressure drop (which is again corresponding value of mass transfer coefficient assuming a linear relation). Following two equations were used in their study:

$$SP = \frac{k_{av}}{\Delta P^*} \quad (2.10.2.2 - 1)$$

$$\Delta P^* = k_{min} + \frac{(k_{max} - k_{min})}{(\Delta P_{max} - \Delta P_{min})} (\Delta P - \Delta P_{min}) \quad (2.10.2.2 - 2)$$

Where,

SP=Spacer performance

$k_{av}$  = Average mass transfer coefficient

$\Delta P$ = Pressure drop

$\Delta P^*$  = Scaled value of pressure drop

$k_{min}$ ,  $k_{max}$ ,  $\Delta P_{min}$  and  $\Delta P_{max}$  are the minimum and maximum values for the mass transfer coefficient and pressure drop for a particular spacer configuration present in the set of configurations studied in their research work.

It is quite evident from the above two relations that the value of spacer performance (SP) largely depends on the set of configurations chosen. Whenever, a different set of configurations is selected the values for SP will change dramatically. Additionally they have reported the mass transfer coefficient values to be approximately equal for both the membrane surfaces for ladder type spacer, which is not the case based on the investigations reported in the current study (Chapter 5). It has been established in the thesis that for ladder type spacers, having top filament and bottom filaments oriented axially and transversely with the main flow direction, the flow patterns are quite different in the vicinity of top and bottom membrane walls. Near the top membrane surface bulk of the fluid follows the main flow direction and near the

bottom membrane surface flow separation and reversal is quite evident. This distinct nature of flow near the two membrane surface yields different values for mass transfer coefficient for the two membrane surfaces. This leads to the conclusion that for all spacer configurations a single value of mass transfer coefficient ( $k_{av}$ ) cannot be used for grading purposes until and unless the two values are quite close to one another.

To grade the spacers I have used a different methodical approach and termed it as “Spacer configuration efficacy” (SCE) which is defined as the ratio of Sherwood number to Power number. In the previous studies no one has used this ratio to categorize spacer arrangement in terms of their performance.

Moreover, none of the previous studies reported any difference between the mass transfer coefficients between the top and bottom membrane walls which could be due to insufficient mesh sizing. Whereas, in the present study the grid independence has been studied and the simulations show that the mass transfer coefficient for the two walls are not identical for all of the ladder type spacer configurations and could lead to preferential fouling tendencies for the two walls, which is not at all a desirable feature for any membrane operation. Optimum filament spacing was concluded based on higher SEC values and almost equal mass transfer coefficient values for the two walls. This methodology has never been reported in the previous studies to grade the spacers.

The other important aspect of this thesis is that I have used a User Defined Functioned (UDF) to calculate local and average mass transfer coefficient values whereas the work conducted by Shakaib et al. [165] do not report how they have calculated those values.

Table 2.8 represents the summary of important three dimensional numerical studies which used CFD as working tool.

**Table 2.6: Summary of CFD based three dimensional studies.**

Researcher	Salient features of the study and limitations
Karode and Kumar [152]	<ul style="list-style-type: none"> <li>• Steady laminar fluid flow analysis channel having commercial feed spacers but without mass transfer aspects.</li> <li>• Investigate the impact of inter filament distance and filament diameter ratio on flow patterns and resulting pressure loss (in terms of total drag coefficient).</li> <li>• Indicated a superior spacer out of many studied in their work based on relatively less total drag coefficient and relatively higher shear rate at membrane walls. But the conclusion does not seem in line with figure 2 and figure 13 of their manuscript.</li> <li>• Since they studied commercially available spacers only, so the impact of variation in filament geometric characteristics on flow feature cannot be drawn precisely.</li> </ul>
Dendukuri et al. [153]	<ul style="list-style-type: none"> <li>• Laminar and unsteady flow conditions were assumed for simulating flow through new designed concave spacers.</li> <li>• A few of the newly designed spacers showed lower pressure drop than their original counterparts and at the same time presented nearly the same strain rate near membrane walls.</li> <li>• One of the altered design for Conwed-1 showed directional changes in flow near the membrane surfaces towards the main body of the channel</li> <li>• New concave designs are complex and costly to produce.</li> <li>• Physical strength of the spacers having new design is questionable.</li> </ul>
Ranade and Kumar [154, 155]	<ul style="list-style-type: none"> <li>• Laminar steady and turbulent (using <math>k - \epsilon</math> turbulence model) flow conditions were simulated through flat and curvilinear spacer filled channels without incorporation of mass transfer.</li> <li>• Results obtained from flat channels filled with spacers can be used to estimate performance of curvilinear channels having</li> </ul>

	<p>same spacer type.</p> <ul style="list-style-type: none"> <li>• An ideal spacer should produce lower pressure drop across the channel and viscous drag (not the form drag) should be the major contributor towards total pressure drop. Moreover it should exhibit maximum wall shear rate for minimum power dissipation per unit mass.</li> <li>• Compared original Conwed-1 spacer with new designed concave spacers. The later predicted higher shear rate at membrane surface with lower power dissipation per unit mass.</li> <li>• New spacer geometry is complex and costly from manufacturing point of view and their strength is questionable for actual use.</li> </ul>
<p>Li et al. [63, 159]</p>	<ul style="list-style-type: none"> <li>• Laminar steady and unsteady flow conditions were simulated through periodic unit cell filled with symmetric spacers having same mesh length using CFX-4.3. Also included solute transport in the model.</li> <li>• Used average Sherwood number vs dimensionless power number plot to arrive at optimum spacer geometric characteristics. However their study did not incorporate the impact of spacer geometric characteristics on local mass transfer.</li> <li>• Have not mentioned how they implemented the periodic boundary condition for solute transport in the model.</li> </ul>
<p>Li et al. [160]</p>	<ul style="list-style-type: none"> <li>• Laminar steady and unsteady flow conditions were simulated through periodic unit cell filled with novel spacers using CFX-4.3. For complex spacers geometries CFD simulations provided unreliable results (they did not report the spatial and time resolution information) and only experimental results were quoted and used for comparison.</li> <li>• The performance of optimized multi-layer spacer with twisted tape was found more promising than the already declared</li> </ul>

	<p>optimized non-woven spacer in their previous work [63, 159].</p> <ul style="list-style-type: none"> <li>• New spacer geometry is complex and costly from manufacturing point of view.</li> </ul>
Koutsou et al. [66]	<ul style="list-style-type: none"> <li>• Used CFD commercial code FLUENT to simulate steady and unsteady laminar flow conditions through spacer filled narrow channels by varying inter filament angle, flow attack angle and spacer mesh length to diameter ratio. Periodic unit cell approach was used without incorporating mass transfer aspect.</li> <li>• Pressure drop was numerically and experimentally calculated for different spacer arrangements and found reasonable agreement.</li> <li>• Critical cylindrical Reynolds number was found in the range of 35 to 45 for all the spacer configurations examined.</li> <li>• Reported generic 3D flow features, vortices generation and their mutual interaction along with generation of recirculation zones.</li> <li>• Did not report the insight into the effect of spacer geometry on flow patterns and wall shear stress.</li> </ul>
Fimbers-Weihs and Wiley [28]	<ul style="list-style-type: none"> <li>• Used CFD commercial code CFX-10.0 to simulate laminar steady 3D flow through spacers having filaments orientation <math>45^{\circ}</math> and <math>90^{\circ}</math> with the flow. Utilized periodic unit cell approach and fully developed mass fraction profile was used as boundary condition for the solute. Constant solute concentration was defined at the membrane walls.</li> <li>• Effect of viscous drag and form drag on mass transfer enhancement. Also attempted to analyse the relation between mass transfer enhancement and 3D flow features.</li> <li>• Did not include filament thickness and filament spacing impact on mass transfer.</li> </ul>

Santos et al. [162]	<ul style="list-style-type: none"> <li>• Used OpenFOAM CFD software package to simulate Laminar steady and unsteady 3D flow conditions through channels filled with rectangular spacers. Introduced a modified friction factor.</li> <li>• Varied axial and transverse filament mesh length to study the spacer performance.</li> <li>• Mass transfer simulations do not represent the average conditions prevailing in membrane modules due to less number of filaments considered in the flow direction (mass transfer periodic wrapping was not utilized). Moreover those simulations were carried out in the absence of top or axial filament.</li> <li>• Have not studied the impact of flow attack angle and filament thickness on their results.</li> </ul>
Lau et al. [163]	<ul style="list-style-type: none"> <li>• Simulated steady and unsteady laminar flow through spacer filled channel by varying inter filament and flow attack angle.</li> <li>• Made an attempt to find optimum spacer configuration based on SPC, wall shear stress and concentration polarization factor.</li> <li>• Questionable periodic boundary conditions specially for the velocity profiles.</li> </ul>
Shakaib et al. [164]	<ul style="list-style-type: none"> <li>• Simulated steady laminar flow through diamond and parallel spacer using CFD commercial code FLUENT6. Periodic unit cell approach was used with one and two pairs of periodic zones for diamond and parallel spacers respectively.</li> <li>• Investigated the impact of spacer spacing on wall shear stress and pressure drop</li> <li>• Their numerical model did not include mass transport as water was used as the working fluid.</li> </ul>
Shakaib et al. [165]	<ul style="list-style-type: none"> <li>• Incorporated solute transport to the numerical model and assumed constant solute concentration at the two membrane</li> </ul>

	<p>walls. Flow domain consisted of six bottom and one top filament to get rid of the entrance and exit effects</p> <ul style="list-style-type: none"> <li>• Investigated different diamond and parallel spacers in terms of flow patterns and their impact on local and average wall shear stresses and mass transfer coefficients.</li> </ul>
--	--

## 2.11 Research Objectives

The previous sections deal with the experimental, mathematical and CFD based numerical 2D and 3D studies. From the literature cited it can be seen that the number of 2D studies available to understand the spacer geometrical impact on flow and concentration patterns are more as compared to 3D studies which can be attributed to higher computational demands for 3D investigations. Memory and time requirements for 3D calculations to produce results with same accuracy as their counterpart 2D calculation are significantly higher. This is because 3D flow brings along with it extra computational burden as it incorporates an extra dimension as compared to 2D flow. Due to this reason the initial 3D studies were restricted to low spatial resolution and they did not include mass transport. But with the advancement in computer technology and CFD tools, 3D CFD based numerical modelling have gained the attention of many research group. Hydrodynamics involved in the real life SWM modules are very complex and three dimensional in nature and there are few three dimensional studies available which investigate the impact of geometric characteristics of the feed spacers on flow and concentration patterns as compared to 2D studies. Moreover, 3D CFD based investigations summarized in Table 2.8 shows that those studies have some associated limitations or gaps which are partially due to selection of questionable periodic boundary conditions for solute transport or velocity profiles or due to lack of systematic analysis of spacer geometric configuration's impact on flow and concentration patterns.

Keeping in view the evident limitations and gaps in the literature cited the main objectives of the research thesis are as follows:

- To visualize flow patterns at various planes for instance along channel height, main flow direction and direction transverse to the main flow. Since the flow

through spacer filled narrow channels is of complex nature therefore the flow visualization at various planes facilitates to understand those complex phenomena prevailing in such flow channels.

- To have a detailed understanding of fluid flow and concentrations patterns generated within SWM and their impact on resulting average and local wall shear stress and solute transport away from top and bottom membrane surfaces into the bulk of the solution (in terms of mass transfer coefficient).
- To study the impact of flow attack angle on flow patterns generated, average and local wall shear stress, power number and pressure drop by altering the feed spacer filament's angle with the main flow direction.
- To compare hydrodynamics and mass transport in narrow channels filled with spacers having different mesh lengths and indicate better spacer configurations which mitigate the fouling potential by enhancing mass transport of the solute away from the membrane walls and maintain lower pressure drop across the membrane at the same time.
- To arrive at reliable conclusions and results that could lead to development of more efficient spacer arrangements for RO operations.

## Nomenclature

Symbols	Description	Units
$A_T$	Cross-sectional area	$m^2$
$A_t$	Mass transfer area	$m^2$
$b$	Channel width	m
$C$	Concentration	g/l
$C_{f,i}$	Concentration of component i in influent stream	g/l
$C_{p,i}$	Concentration of component i in permeate	g/l
$c_f$	Feed concentration	g/l
$c_i$	Solute molar concentration	mol/l
$c_p$	Product concentration	g/l
$c_w$	Concentration at membrane wall	g/L
$D$	Mass diffusivity	$m^2/s$
$d_h$	Hydraulic diameter	m
$f$	Dimensionless fanning friction factor	-
$h_{ch}$	Channel height	m

$J$	Volumetric water Flux or permeate velocity	$\text{m}^3/\text{m}^2 \cdot \text{s}$ or $\text{m}/\text{s}$
$J_{pure}$	Volumetric pure water Flux or permeate velocity of pure water	$\text{m}^3/\text{m}^2 \cdot \text{s}$ or $\text{m}/\text{s}$
$J_{slt}$	Solute mass flux	$\text{Kg}/\text{m}^2 \cdot \text{s}$
$J_x$	Permeate velocity or volumetric flux in cross-flow direction	$\text{m}^3/\text{m}^2 \cdot \text{s}$ or $\text{m}/\text{s}$
$k_{av}$	Average mass transfer coefficient	$\text{m}/\text{s}$
$k_f$	Mass transfer coefficient	$\text{m}/\text{s}$
$k_{glob}$	Global mass transfer coefficient	$\text{m}^2/\text{s}$
$k_l$	Local mass transfer coefficient	$\text{m}/\text{s}$
$L$	Channel length	$\text{m}$
$L_p$	Hydraulic permeability coefficient	$\text{m}/\text{s} \cdot \text{Pa}$
$P$	Pressure	$\text{Pa}$
$\bar{P}_m$	Permeance	$\text{m}^3/\text{m}^2 \cdot \text{pa} \cdot \text{s}$
$\Delta P_{TM}$	Trans membrane pressure	$\text{Pa}$
$p_f$	Feed entrance pressure	$\text{Pa}$
$\Delta p_{ch}$	Channel pressure drop	$\text{Pa}$
$Q$	Volumetric flow rate	$\text{m}^3/\text{s}$
$Q_p$	Permeation rate	$\text{m}^3/\text{s}$
$R$	Universal gas constant	$\text{J}/\text{mol} \cdot \text{K}$
$R_i$	Hydrodynamic resistance, subscripts (i) are specified in section 2.6.3	$1/\text{m}$
$Re$	Reynolds number	-
$Re_{ch} = \frac{h_{ch} u_{avg} \rho}{\mu}$	Channel Reynolds number	-
$Re_{cyl} = \frac{h_f u_{avg} \rho}{\mu}$	Cylinder Reynolds number	-
$Re_h = \frac{d_h u_{eff} \rho}{\mu}$	Hydraulic Reynolds number	-
$Sc$	Schmidt number	-
$Sh$	Sherwood number	-
SPC	Specific power consumption	$\text{Pa}/\text{s}$
$St_p$	Permeation Stanton number	-
$S_{fc}$	Wetted surface of flat channel	$\text{m}^2$
$S_{sp}$	Wetted surface of spacer	$\text{m}^2$
$S_{v,sp}$	Specific surface of the spacer	$\text{m}^{-1}$
$T$	Absolute temperature	$\text{K}$
$u_{eff} = u_{avg}/\varepsilon$	Effective velocity	$\text{m}/\text{s}$
$V_{mod}$	Module volume	$\text{m}^3$
$V_{sp}$	Spacer volume	$\text{m}^3$
$V_T$	Total volume	$\text{m}^3$
$W_s$	Pumping energy	$\text{W}$
$Y$	Solute mass fraction	-
$Y_b$	Bulk mass fraction	-
$Y_w$	Mass fraction at wall	-

$\left[\frac{\partial Y}{\partial n}\right]_w$	Gradient of mass fraction at membrane wall (surface)	1/m
$\pi$	Osmotic pressure	Pa
$\delta$	Boundary layer thickness	m
$\sigma$	Reflection coefficient	-
$\Delta\pi$	Osmotic pressure difference	Pa
$\mu$	Dynamic viscosity	Pa s
$\phi$	Osmotic coefficient	Pa . l/g
$\rho$	Density of fluid	kg/m <sup>3</sup>
$\varepsilon$	Porosity	-
$\pi_b$	Bulk osmotic pressure	bar
$\pi_p$	Product osmotic pressure	bar
$\xi$	SWM productivity	m <sup>3</sup> / (m <sup>3</sup> . Pa. s)
$k - \epsilon$	Turbulent model, kinetic energy & dissipation rate.	turbulent m <sup>2</sup> /s <sup>2</sup> & m <sup>2</sup> /s <sup>3</sup> )

# Chapter 3. Introduction to Computational Fluid Dynamics (CFD)

Experimental techniques require considerable financial investment such as equipment procurement, infrastructure construction, resources dedication, hiring and training of staff. Numerical modelling reduces dramatically the costs, time and risks involved in running the repeated experiments. Computational Fluid Dynamics (CFD) is one of the many numerical techniques used for simulating fluid flow [35] and the tool used in this thesis. CFD allows computer-based simulations and subsequent analysis of fluid systems by solving conservation equations for mass, energy and momentum using numerical methods. Moreover computational techniques, possess the powers to provide information regarding the flow anywhere in the selected domain without interfering with the flow itself and can lead to better understanding of the mass transfer aspects of the membrane operations.

Many researchers are utilizing CFD technique to gain insight of various phenomena taking place within the membrane modules to improve its performance or to provide valuable information for the design process. Moreover, many research groups have shifted their focus to CFD making it widely used tool in the field of membrane science [36]. The advantage of CFD tool over the traditional experimental methods lies in the built-in flexibility to change operating conditions, fluid properties and geometric parameters of the flow channel. For instance, geometric parameters of the flow channel can be varied using an appropriate CFD software, and does not need the physical construction of the modified channel, to investigate the effects on parameters of interest. Similarly fluid properties and operating conditions can be varied to investigate their impact on the parameters of interest without experimentations. Another important and interesting feature of the CFD is that the data can be reported anywhere in the computational domain at any time during the simulation without obstructing the flow itself.

In this thesis basic data are generated by using Computational fluid dynamics (CFD) tools. It is therefore necessary to understand the basic concepts behind CFD. This

chapter covers the fundamental concepts of CFD and it also explains how the partial differential equations, describing fluid flow, are converted to algebraic equations for numerical solution.

### **3.1 Basic elements of a CFD code**

Fluid flow problems are tackled in every CFD code by means of numerical algorithms. The access to the solving powers of those algorithms is provided by means of user friendly interfaces in CFD codes. Those interfaces are used to provide problem specific input data and are also used to examine the results. Following are the three major elements of every CFD code [35]:

- Pre-processor
- Solver
- Post processor

#### **3.1.1 Pre-processor**

Function of a pre-processor is to provide flow problem inputs to CFD program by means of user-friendly interface and to convert the input provided in a form suitable to be used by the solver. At the stage of pre-processing following user activities are involved [35]:

- Defining computational domain i.e., geometry creation of specific region of interest
- Grid generation or meshing, by dividing the main computational domain into a number of smaller and non-overlapping sub-domains by means of a grid of cells. This yield small control volumes or elements
- Selecting chemical and physical phenomena that are needed to be modelled.
- Defining fluid properties
- Defining or specifying appropriate boundary conditions at the cells coinciding with domain boundary

In CFD the solution of the flow problem is defined at nodes inside each cell. The accuracy of the solution depends on the number of cells in the grid. Generally speaking, solution will be more accurate for grids involving larger number of cells.

The accuracy of the solution along with the computational cost (in terms of necessary computer hardware and computational time) both largely depends on the grid fineness. To reduce computational cost without having an adverse impact on the accuracy of the solution often non-uniform grids are used. These grids are finer in the regions where the variations are higher from point to point and coarser in the area where the variations are on a relatively lower side. To date no CFD commercial code is equipped with robust self-adapting meshing capabilities, although efforts are being made in this direction. Hence it solely relies on the CFD user to develop an optimal grid which provides a suitable compromise between solution accuracy and computational cost. In an industrial CFD project more than 50% of the total time is devoted to the computational domain generation and its meshing [35]. Most of the modern CFD codes either provides CAD-style interface or provides the facility to import data from other pre-processors.

### **3.1.2 Solver**

Commercially available CFD codes use different numerical solution techniques. For instance, CFD codes including ANSYS FLUENT, CFX, PHOENICS and STAR-CD make use of finite volume method to solve fluid flow problems. Generally, the numerical algorithm follows the following three steps:

- Governing equations of fluid flow are integrated over all the finite control volumes of the domain
- The resulting integral equations are converted to a system of algebraic equations, this step is also referred to as discretization
- An iterative method is employed to solve the algebraic equations

Control volume integration results in the conservation of relevant properties for each finite size cell. The most interesting aspect of finite volume method is the clear linkage between the numerical algorithm and physical conservation principles making it conveniently understandable by engineers and in this regard provides its superiority over other methods including finite element and spectral methods. Following equation represents conservation of a flow variable  $\phi$  within a finite control volume:

$$\left( \begin{array}{c} \text{Rate of change} \\ \text{of } \phi \\ \text{in control volume} \\ \text{w.r.t time} \end{array} \right) = \left( \begin{array}{c} \text{Net rate of increase} \\ \text{of } \phi \\ \text{due to convection} \\ \text{into the control volume} \end{array} \right) + \left( \begin{array}{c} \text{Net rate of increase} \\ \text{of } \phi \\ \text{due to diffusion} \\ \text{into the control volume} \end{array} \right) + \left( \begin{array}{c} \text{Net rate of creation} \\ \text{of } \phi \\ \text{inside control volume} \end{array} \right)$$

CFD codes are equipped with discretization techniques for the treatment of relevant transport phenomena (convection/or diffusion), source term (generation or destruction of  $\phi$ ) and for the rate of change with time. The underlying physical phenomena are quite complex and non-linear in nature and thus needs an iterative approach for the solution. The approach employed by ANSYS FLUENT for that matter is described in detail in section 3.3.1.

### 3.1.3 Post-processor

Most of the leading commercial CFD packages are equipped with powerful data visualization and export tools, for instance:

- Display of domain geometry and grid. The facility of generating different surfaces at different areas of interest
- Plotting vectors at various surfaces of interest
- Contour plots
- Two-dimensional and three-dimensional surface plots
- Particle tracking
- Manipulate the view (rotate, translate, scale etc)
- Animation for dynamic result display
- Data export facility to analyse the generated data outside the code

The reliability of the fluid flow problem results generated by the CFD codes depend on the proper embedment of physical laws and also on the skills of the user. The important decisions that the user has to make at an early stage is whether to model a flow problem in 2D or 3D, to include or exclude the effect of ambient temperature, assume constant density for the working fluid or incorporate the effect of pressure variations on the fluid density etc. The appropriateness of assumptions made by the user at this stage (to simplify the model) partly determines the quality of the results generated by the code.

To have successful simulation results defining the appropriate domain geometry and optimal grid generation are also important tasks for the user at the input stage. The

usual criteria for successful results are convergence and grid independence. It has been established earlier that the solution of the fluid flow problem using CFD codes is iterative in nature, which means that for a converged solution the residuals (measure of overall conservation of flow properties) should be very small. This aim can be met by appropriate selection of relaxation factors. The grid independent solution can be obtained by successive refinement of an initially coarse grid till the point when the key results do not change with further grid refinement.

### 3.2 Transport equations

A set of equations derived from mass momentum and energy balances are used to describe transport processes. These equations are generally known as Navier-stokes equations. These equations are partial differential equations (PDE) and have analytical solution for simple cases only. Numerical methods are employed to solve Navier-stokes equations for general flows which involve complex geometries and boundary conditions. CFD technique is employed for numerical solution of PDE of continuity, momentum, energy and species transport. Following equation represents general form of transport equation for any property  $\phi$  [35]:

$$\frac{\partial(\rho \phi)}{\partial t} + \text{div}(\rho \phi \mathbf{v}) = \text{div}(\Gamma_{\phi} \text{grad } \phi) + S_{\phi} \quad (3.2 - 1)$$

In the above equation  $\phi$  represents any transported quantity which could be a scalar, a vector or a second order tensor.  $\mathbf{v}$  and  $\Gamma_{\phi}$  are the velocity vector and diffusion coefficient of  $\phi$ . The term  $S_{\phi}$  represents generation or consumption of  $\phi$  by a source or a sink respectively. The first term in the above equation represents accumulation of  $\phi$ , second and third term represent transport of  $\phi$  due to convection (due to fluid velocity) and diffusion respectively. The above equation can be represented in a different manner with  $\nabla$  operator as:

$$\frac{\partial(\rho \phi)}{\partial t} + \nabla \cdot (\rho \phi \mathbf{v}) = \nabla \cdot (\Gamma_{\phi} \nabla \phi) + S_{\phi} \quad (3.2 - 2)$$

As it is evident from the literature review that for fluid flow in spacer filled narrow channels there is no significant effect of gravity and density variation on solution obtained by CFD simulations [121, 122]. Hence for that reason constant density was

employed for all the simulations carried in the thesis and the gravitational effect was also neglected. Moreover the working fluid was assumed to be Newtonian and isothermal having constant properties.

In most of real life cases, flow through spacer filled modules do fall in the Reynolds number category which is below the transition to turbulent flow regime [28]. However, in these types of membrane arrangements unsteady flow conditions are not uncommon. But for those cases the encountered time variations in flow are still laminar in nature as they do not represent chaotic variations which are signatures of turbulence [140, 166]. It can be concluded from the above discussion that steady and unsteady flow conditions through spacer filled membrane modules can be simulated by directly solving the transport equations without the need of incorporating any turbulence model.

For constant density fluids, continuity equation is defined as [35]:

$$\nabla \cdot \mathbf{v} = 0 \quad (3.2 - 3)$$

For incompressible Newtonian fluid neglecting the gravitational effects, momentum transport equation is defined as [167]:

$$\frac{\partial(\rho \mathbf{v})}{\partial t} + \nabla \cdot (\rho \mathbf{v} \mathbf{v}) = - \nabla P + \nabla \cdot [\mu (\nabla \mathbf{v} + \nabla \mathbf{v}^T)] + \mathbf{F} \quad (3.2 - 4)$$

In the above equations  $\mathbf{v}$ ,  $\rho$ ,  $P$ ,  $\mu$ ,  $t$  and  $\mathbf{F}$  represent Velocity vector, density, pressure, dynamic viscosity, time and external body forces vector respectively.

The species transport equation is defined as [55]:

$$\frac{\partial(\rho Y)}{\partial t} + \nabla \cdot (\rho Y \mathbf{v}) = \nabla \cdot (\rho D \nabla Y) + S \quad (3.2 - 5)$$

In the above equation  $Y$ ,  $D$  and  $S$  represents mass fraction of the species, mass diffusivity and source of the species in the fluid.

The above equations (3.2-3 to 3.2-5) are valid at every point in the fluid flow field and require problem specific boundary conditions for solution. The set of PDEs can be solved by a number of available numerical methods including finite element, finite volume, finite difference and spectral methods [35]. Basic philosophy of every

numerical method involves transformation of the PDEs to a system of algebraic equations which are later solved iteratively by numerical methods. Most of the CFD codes, including FLUENT, use finite volume method [35, 167] for the solution of PDEs. Steps followed by the numerical algorithm in case of finite volume method are explained in section 3.1.2.

In order to simulate flow of an incompressible Newtonian fluid, the governing equations for laminar, steady and three dimensional flow acquire the following form [55, 165] :

$$\text{Continuity} \quad \frac{\partial u}{\partial x} + \frac{\partial v}{\partial y} + \frac{\partial w}{\partial z} = 0 \quad (3.2 - 6)$$

$$x - \text{momentum: } u \frac{\partial u}{\partial x} + v \frac{\partial u}{\partial y} + w \frac{\partial u}{\partial z} = -\frac{1}{\rho} \frac{\partial P}{\partial x} + \nu \left[ \frac{\partial^2 u}{\partial x^2} + \frac{\partial^2 u}{\partial y^2} + \frac{\partial^2 u}{\partial z^2} \right] \quad (3.2 - 7)$$

$$y - \text{momentum: } u \frac{\partial v}{\partial x} + v \frac{\partial v}{\partial y} + w \frac{\partial v}{\partial z} = -\frac{1}{\rho} \frac{\partial P}{\partial y} + \nu \left[ \frac{\partial^2 v}{\partial x^2} + \frac{\partial^2 v}{\partial y^2} + \frac{\partial^2 v}{\partial z^2} \right] \quad (3.2 - 8)$$

$$z - \text{momentum: } u \frac{\partial w}{\partial x} + v \frac{\partial w}{\partial y} + w \frac{\partial w}{\partial z} = -\frac{1}{\rho} \frac{\partial P}{\partial z} + \nu \left[ \frac{\partial^2 w}{\partial x^2} + \frac{\partial^2 w}{\partial y^2} + \frac{\partial^2 w}{\partial z^2} \right] \quad (3.2 - 9)$$

$$\text{Concentration: } u \frac{\partial Y}{\partial x} + v \frac{\partial Y}{\partial y} + w \frac{\partial Y}{\partial z} = D \left[ \frac{\partial^2 Y}{\partial x^2} + \frac{\partial^2 Y}{\partial y^2} + \frac{\partial^2 Y}{\partial z^2} \right] \quad (3.2 - 10)$$

In the above equations  $u$ ,  $v$  and  $w$  represents the x, y and z components of velocity.

### 3.3 Finite volume method employed by ANSYS FLUENT

As already mentioned ANSYS FLUENT is used as the CFD tool to simulate flow through spacer filled narrow channel in this thesis and it employs finite volume method for the solution of Navier-Stokes equation [167]. This section addresses application of Finite volume method employed by ANSYS FLUENT in particular, for solution of fluid flow problems. The aim of this section is to provide an overview of the methodology followed by ANSYS FLUENT for discretization of transport equations.

General transport equation (3.2-2) for a scalar  $\phi$  can be integrated over a control volume ( $V$ ) as:

$$\int_V \frac{\partial(\rho \phi)}{\partial t} dV + \int_V \nabla \cdot (\rho \phi \mathbf{v}) dV = \int_V \nabla \cdot (\Gamma_\phi \nabla \phi) dV + \int_V S_\phi dV \quad (3.3 - 1)$$

According to Gauss's divergence theorem, volume integral of divergence of a vector over a control volume is equal to the surface integral of that particular vector over the area enclosing the control volume [168]. In the light of Gauss's theorem second and third terms of the above equation acquire the following form:

$$\int_V \nabla \cdot (\rho \phi \mathbf{v}) dV = \oint (\rho \phi \mathbf{v}) \cdot d\mathbf{A} \quad (3.3 - 2)$$

$$\int_V \nabla \cdot (\Gamma_\phi \nabla \phi) dV = \oint (\Gamma_\phi \nabla \phi) \cdot d\mathbf{A} \quad (3.3 - 3)$$

Equation (3.3-1) can be re-written in the following form:

$$\int_V \frac{\partial(\rho \phi)}{\partial t} dV + \oint (\rho \phi \mathbf{v}) \cdot d\mathbf{A} = \oint (\Gamma_\phi \nabla \phi) \cdot d\mathbf{A} + \int_V S_\phi dV \quad (3.3 - 4)$$

Above equation holds good for every control volume or cell present in the flow domain under Finite volume method. Each term in the above equation needs to be discretised to convert the set of PDEs to a system to algebraic equations.

A triangular control volume or cell, in two-dimensional form is presented in the Figure 3.1.

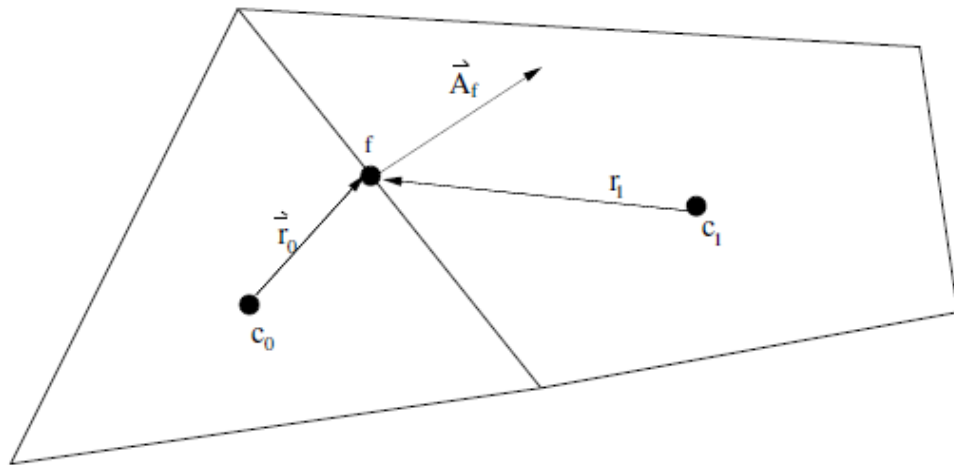


**Figure 3.1: Control volume used to illustrate Discretization of a transport equation [167].**

Discretization of equation (3.3-4) on a given cell can yield to the following expression [167]:

$$\frac{\partial(\rho \phi)}{\partial t} V + \sum_f^{N_{faces}} (\rho_f \phi_f \mathbf{v}_f) \cdot \mathbf{A}_f = \sum_f^{N_{faces}} (\Gamma_\phi \nabla \phi_f) \cdot \mathbf{A}_f + S_\phi V \quad (3.3 - 5)$$

In the above equation:

- $N_{faces}$  = Number of faces enclosing the cell
- $\phi_f$  = Value of  $\phi$  convected through face  $f$
- $(\rho_f \mathbf{v}_f) \cdot \mathbf{A}_f$  = Mass flux through the face
- $\mathbf{A}_f$  = Area of face  $f$
- $\nabla \phi_f$  = Gradient of  $\phi$  at face  $f$
- $V$  = Cell volume

The temporal discretization of the first term in above equation is discussed separately in section 3.3.3. In ANSYS FLUENT, the value of  $\phi$  and its diffusion coefficients are stored at cell centres. This results in a co-located or non-staggered grid layout because values of all the variables (pressure, velocity components, Reynolds stress components, and all scalars) are stored at the centre of the control volume or cell. Since both velocity and pressure values are stored at the same location (cell centre) which leads to the “checkerboard” pressure field [35, 167]. To prevent checker boarding of pressure ANSYS FLUENT employs a procedure similar to one proposed by Rhie and Chow [169] to find face value of velocity (value of velocity at face between cells C0 and C1 in Figure 3.1) required in equation (3.3-5).

The equations presented above, in addition to the transport of a scalar  $\phi$ , are also valid for Cartesian components of vectors or elements of a higher order tensor which are scalars.

### 3.3.1 Solving the linear system

In the previous section the discretised scalar equation (3.3-5) contains unknown scalar variable  $\phi$  at the cell centre; also the values are unknown at the neighbouring cells. This equation will be non-linear with respect to these variables. Following equation represents a linearized form of the equation (3.3-5) [167]:

$$a_p \phi = \sum_{nb} a_{nb} \phi_{nb} + b \quad (3.3.1 - 1)$$

In the above expression  $a_p$  and  $a_{nb}$  represents the linearized coefficients for  $\phi$  and  $\phi_{nb}$  respectively and the subscript nb stands for the neighbour cells. The number of neighbour cells for each particular cell depends on the topology of the mesh and, apart from the boundary cells, typically equal to number of faces that enclose the particular cell.

For each cell present in the mesh similar equation can be written which results in a set of algebraic equations. ANSYS FLUENT employs a point implicit linear equation solver (Gauss-Seidel) along with an algebraic multigrid (AMG) method to solve the linear system of the scalar equations.

### 3.3.2 Spatial discretization

Discrete values of the scalar  $\phi$  are stored, by ANSYS FLUENT, at the cell centre of the cells, for instance at  $C_0$  and  $C_1$  in Figure 3.1. Whereas the face values  $\phi_f$ , required by the convective terms in equation (3.3-5) are interpolated from the cell centre values by employing an upwind scheme.

The term Upwinding means that the face value  $\phi_f$  is obtained from the quantities in the cell upstream or upwind relative to the normal velocity. In ANSYS FLUENT different upwind schemes are present, for example:- First-order upwind, second-order upwind, power law, QUICK (Quadratic upstream interpolation for convection kinetics) etc. The user has the choice to choose from the those upwind schemes depending on the problem complexity and experience.

In this thesis QUICK and Power law upwind schemes are used to discretize momentum and concentration equations respectively and are discussed in chapter 4

and 5 along with the governing equation for the flow through spacer filled narrow channels. The diffusion terms in equation (3.3-5) are central-differenced and always second order accurate [167].

### 3.3.3 Temporal Discretization

In case of transient simulations, the governing equations have to be discretized in both time and space. For time-dependant equations, spatial discretization is same as that for steady-state cases. But for Temporal discretization every term involved in the differential equation has to be integrated over a time step  $\Delta t$ .

Time evolution of a variable  $\phi$  is represented by the following generic expression [167]:

$$\frac{\partial \phi}{\partial t} = F(\phi) \quad (3.3.3 - 1)$$

In the above expression function  $F$  incorporates any spatial discretization. Considering the time derivative is discretized using backward differences, first-order accurate temporal discretization is presented as:

$$\frac{\phi^{n+1} - \phi^n}{\Delta t} = F(\phi) \quad (3.3.3 - 2)$$

And the second-order temporal discretization can be represented as [167]:

$$\frac{3\phi^{n+1} - 4\phi^n + \phi^{n-1}}{2\Delta t} = F(\phi) \quad (3.3.3 - 3)$$

In the above equations:

- $n$  = Value at the current time level,  $t$
- $n+1$  = Value at next time level,  $t + \Delta t$
- $n-1$  = Value at previous time level,  $t - \Delta t$
- $\phi$  = A scalar quantity

For pressure base solver ANSYS FLUENT provides only the choice of using Implicit time integration to evaluate  $F(\phi)$  at future time level as:

$$\frac{\phi^{n+1} - \phi^n}{\Delta t} = F(\phi^{n+1}) \quad (3.3.3 - 4)$$

$\phi^{n+1}$  in a particular cell is related to  $\phi^{n+1}$  in the neighbouring cell through  $F(\phi^{n+1})$  as:

$$\phi^{n+1} = \phi^n + \Delta t F(\phi^{n+1}) \quad (3.3.3 - 5)$$

The above implicit equation can be iteratively solved at each time step before moving to next time step. The beauty of the above equation is that, it is unconditionally stable with respect to the size of the time step.

### 3.4 Programming procedure

In the thesis mainly GAMBIT<sup>®</sup> is used as a pre-processor and ANSYS FLUENT is used as a solver which allows importing the meshed computational domain developed in GAMBIT<sup>®</sup>. After reading the mesh file in FLUENT physical model, fluid and material properties are defined in FLUENT. Boundary conditions that were earlier defined in GAMBIT<sup>®</sup> can be varied (or kept same) to describe the nature of the problem in FLUENT. These user inputs along with the grid information are stored in a case file. A case file is a record of all the informations provided to the solver (FLUENT) pertaining to a specific fluid flow problem. All the calculation performed by FLUENT and post processing activities can be saved in a data file.

In this thesis the information generated by ANSYS FLUENT is compared with the experimental and numerical studies. Since the geometries of the spacers considered in the experimental studies are not identical to those considered in this thesis therefore quantitative comparison of results obtained from this work is made with experimental studies involving closely matching spacer configurations and numerical studies having identical spacer configurations. Among the variables considered for comparison purpose are wall shear stresses on membrane surfaces, linear pressure drop, Power number, dimensionless pressure drop and mass transfer coefficient.

## Nomenclature

Symbol	Description	Units
<b>A</b>	Surface area vector	$m^2$
$a_p$ and $a_{nb}$ in equation (3.3.1-1)	Linearized coefficients for $\phi$ and $\phi_{nb}$	
$C_0$ and $C_1$	Cells, having centres $C_0$ and $C_1$ respectively.	
$D$	Mass diffusivity	$m^2/s$
<b>F</b>	Force vector	N
$P$	Pressure	Pa
$S$	Source of species in fluid	$kg/m^3 s$
$S_\phi$	Source of transported property	
$t$	time	s
$u$	x-component of velocity	m/s
<b>v</b>	Velocity vector	m/s
$v$	y-component of velocity	m/s
$w$	z-component of velocity	m/s
$x$	x-coordinate	m
$Y$	Mass fraction of species	
$y$	y-coordinate	m
$z$	z-coordinate	m
$\phi$	Transported property	
$\Gamma_\phi$	Diffusion coefficient of $\phi$	$m^2/s$
$\mu$	dynamic viscosity	Pa s
<b>v</b>	kinematic viscosity	$m^2/s$
$\rho$	density	$kg/m^3$

# Chapter 4. Feed spacer orientation and flow dynamics

Literature review carried out in chapter 2 of the thesis revealed that concentration polarization is one of the main problem encountered in pressure driven membrane operations which adversely effect the membrane performance by increasing the chances of fouling at the membrane surface. Further, flow and concentration patterns generated in spacer filled membrane modules depend significantly on the geometrical characteristics of the spacer filaments. In this chapter the effect of feed spacer orientation on the resulting flow dynamics is investigated by varying the flow attack angle of both top and bottom filaments.

## 4.1 Introduction

Operational issues arising from scaling and fouling of membranes are addressed by pre-treatment processes and alternative membrane or membrane secondary structures. In the present work the flow patterns associated with fluids within the membrane module are investigated using Computational Fluid Dynamics (CFD) tools. The effects on flow patterns through a spacer filled Reverse Osmosis (RO) membrane with the secondary structure of the membranes (feed spacer filaments) at various angles with the inlet flow are analysed. The presence of the feed spacers in membrane module appear to generate secondary flow patterns enhancing the prospects for self induced backwashing increasing the allowable operational time and membrane efficiency. The flow visualization in the present study is useful in understanding the complex flow patterns generated in spacer filled RO membrane modules and could possibly lead to developing a new RO membrane which is more efficient, economical and appears to be a practically viable solution to reduce costs associated with the maintenance of RO membranes.

Reverse Osmosis operations are often confronted with challenges associated with periodic maintenance of membranes due to significant material build-up on the surfaces. Operational issues arising from scaling and fouling primarily include:

increased membrane resistance, decreased permeate flow, increased energy requirement and decreased membrane life. These issues have been addressed by several researchers, in a limited way, by proposing better pre-treatment processes. However, there appears a need to change membrane or membrane secondary structures to alter the flow patterns associated with fluids within the membrane module. To visualize flow through RO membranes Computational Fluid Dynamics (CFD) tools have been used extensively by various researchers. Literature review reveals that CFD tools have been used quite accurately to predict the flow behaviour through RO membranes [36, 135, 152, 163].

Spiral wound membrane module (SWM) is regarded as one of the most commonly used assemblies for water treatment using membrane separation processes. Figure 4.1 represents a SWM in partly unwound state. In case of Spiral Wound Module (SWM) a number of flat membrane sheets are glued together, in pair arrangement, on three sides forming a pocket and a permeate spacer is introduced between the membranes pocket. The fourth open end of the membrane pocket is connected to a common permeate collector tube. The membrane pockets are rolled around the tube with feed spacers between each pocket [7, 170]. As a result of the design alternating feed and permeate channels are developed. Feed enters through one side of the module and is forced through the membrane. Retentate leaves the module from the opposite side of the feed inlet, whereas permeate is collected in the common permeate tube.

The net spacer in the feed channel not only keep the membrane layers apart, thus providing passage for the flow, but also significantly affects the flow and concentration patterns in the feed channel. Spacers are not only responsible for the pressure drop and limited flow zones (dead zones) creation but also promote mixing between the fluid bulk and fluid elements adjacent to the membrane surface. In other words they are intended to keep the membranes clean by enhancing mass transfer and disrupting the solute concentration boundary layer. In the past several experimental and theoretical studies were carried out to shed light on these phenomena and to optimize spacer configuration [19-24]. So it is quite understandable that the presence of these spacers promote directional changes in the flow which reduces membrane fouling and concentration polarization. Hence the efficiency of a membrane module depends heavily on the efficacy of the spacers to

increase mass transport away from the membrane surface into the bulk fluid by increasing shear rate at the membrane surface [25].

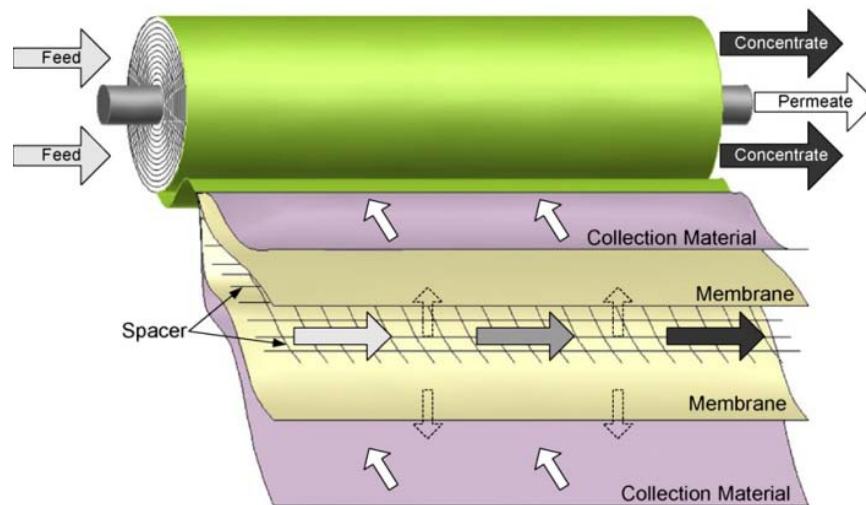


**Figure 4.1: Schematic diagram of SWM in partly unwound state, adapted from [29].**

Spiral wound membranes have tightly wrapped structures which cannot be opened easily for chemical cleaning or cannot be back flushed by operating in reverse direction. For these reasons, the fouling control methods for SWM are limited to hydrodynamics, pre-treatment of the feed and operational controls [26]. The fouling issues can be addressed to a large extent by varying the hydrodynamic conditions prevailing in spiral wound membrane. The feed spacers can be oriented to generate high cross flow velocities or secondary flow patterns which can develop higher scouring forces on the membrane surface to reduce fouling and concentration polarization. However, this approach will need higher pumping energy to compensate losses within the membrane module. Hence the feed spacers must be optimized to reduce the build-up on the membrane surface with moderate energy loss.

Literature review to date reveals that for the same type of spacers, spacer-filled flat channels and SWM channels show similar flow characteristics [61, 155]. Ranade and Kumar [154] in another study concluded that the transition from laminar to turbulent flow regime for most of the spacer-filled channels occurs at Reynolds numbers of 300-400 (based on hydraulic diameter) as reported for packed beds. In the present study we have used laminar flow, steady-state model as hydraulic Reynolds number ( $Re_h$ ) which was kept between 100 to 125 for all the cases. In most of the real life

cases flow through spacer filled modules do fall in the Reynolds number category where the flow is steady and laminar [28] and justifies our choice of steady-state and laminar flow regime.

In the present work, an attempt has been made to study the effect on flow patterns through a spacer filled RO membrane when the secondary structures of the membranes (feed spacer filaments) are set at various angles with the inlet flow. Three cases were analysed to investigate the effect of feed spacer orientation, with respect to the inlet flow, on wall shear stress, pressure drop and power number.

## 4.2 Geometric parameters for spacers

Geometry of spacers used in SWM can be characterized with the help of some important parameters shown in Figure 4.2. In the figure  $d_b$  and  $d_t$  represent diameters of bottom and top filaments, whereas  $l_b$  and  $l_t$  represents the mesh size of bottom and top filaments respectively. The flow attack angles that top and bottom filament makes with the y-axis are represented by  $\theta_1$  and  $\theta_2$  respectively. Whereas  $\alpha$  is angle between the top and bottom crossing filaments. It is evident from the geometry description that the available channel height  $h_{ch}$  is sum of the filaments diameters in top and bottom layers. In the current study we have considered symmetric spacers having same diameter and mesh size for both top and bottom filaments, i.e.  $d = d_b = d_t$  and  $l = l_b = l_t$ . Spacer parameters are non-dimensionalized by using channel height ( $h_{ch}$ ). The ratio of filament diameter to the channel height ( $D = d/h_{ch}$ ) is set at 0.5 whereas for filament mesh size to the channel height ( $L = l/h_{ch}$ ) is kept at 3.6. Angle between the top and bottom filaments ( $\alpha$ ) was kept at  $90^\circ$  for the first two cases and  $45^\circ$  for the third case study. Table 4.1 shows the important spacer geometric characteristics considered for the three different case studies.

**Table 4.1: Geometric characteristics of spacer.**

Case study	L	D	$\alpha$	$\theta_1$	$\theta_2$
1	3.6	0.5	$90^\circ$	$90^\circ$	$0^\circ$
2	3.6	0.5	$90^\circ$	$45^\circ$	$45^\circ$
3	3.6	0.5	$45^\circ$	$135^\circ$	$0^\circ$

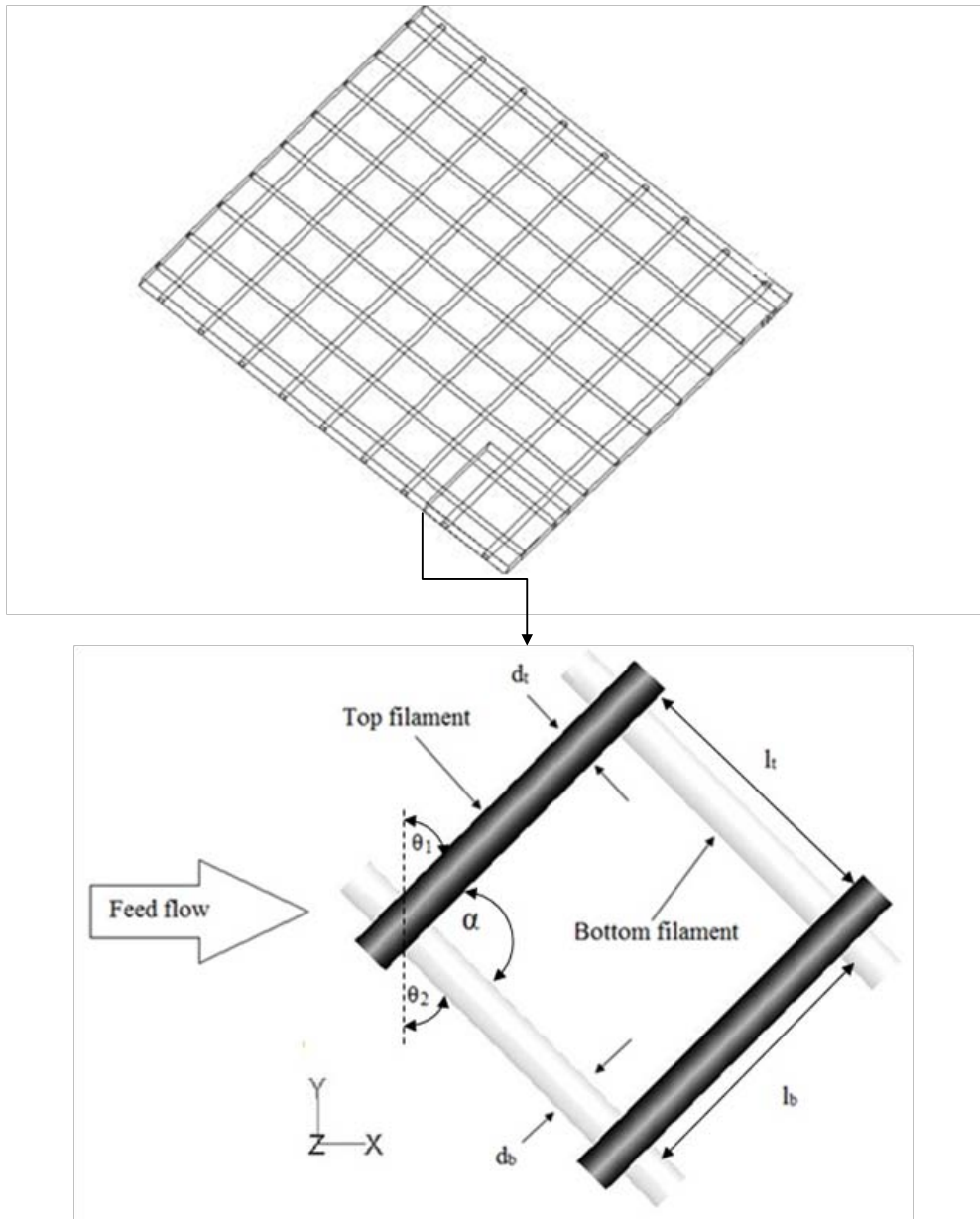


Figure 4.2: Schematic of feed channel spacer and geometric characterization of feed spacer.

### 4.3 Hydraulic diameter and porosity of spacer filled channel

Schock and Miquel [61] used a modified definition for hydraulic diameter ( $d_h$ ) for spacer filled channel. Same concept of hydraulic diameter has been used in this research thesis, so it is important to derive some useful relations which will be helpful to define the hydraulic diameter of a spacer filled narrow channel. The basic definition of hydraulic diameter for non-circular channel is:

$$d_h = \frac{4 \times \text{cross - section of the flow channel}}{\text{wetted circumference}} \quad (4.3 - 1)$$

Due to the presence of spacer at feed side of the membrane channel, there is a periodic variation in the cross section of such spacer filled channel, the above equation can be generalized for the such case as:

$$d_h = \frac{4 \times \text{Volume of the flow channel}}{\text{wetted surface}} \quad (4.3 - 2)$$

If the  $V_T$  represents the total volume of the channel,  $V_{sp}$  represents the spacer volume,  $S_{fc}$  represents the wetted surface of the flat channel and  $S_{sp}$  represents wetted surface of the spacer, above equation can be written in the form:

$$d_h = \frac{4(V_T - V_{sp})}{S_{fc} + S_{sp}} \quad (4.3 - 3)$$

Porosity ( $\varepsilon$ ) of the feed channel can be defined by the following equation:

$$\varepsilon = 1 - \frac{V_{sp}}{V_T} \quad (4.3 - 4)$$

On rearranging the above equation, we get the equation in the form:

$$\varepsilon = \frac{V_T - V_{sp}}{V_T} \quad (4.3 - 5)$$

Or

$$V_T - V_{sp} = \varepsilon V_T \quad (4.3 - 6)$$

On further rearrangement, above equation may be written as:

$$V_{sp} = V_T (1 - \varepsilon) \quad (4.3 - 7)$$

Equations 4.3-6 and 4.3-3 lead to the following relationship

$$d_h = \frac{4(\varepsilon V_T)}{S_{fc} + S_{sp}} \quad (4.3 - 8)$$

Above equation, on rearranging acquires the following form:

$$d_h = \frac{4 \varepsilon}{\frac{S_{fc}}{V_T} + \frac{S_{sp}}{V_T}} \quad (4.3 - 9)$$

If the two ratios in the denominator of the above equation ( $\frac{S_{fc}}{V_T}$  and  $\frac{S_{sp}}{V_T}$ ) are known, we can find the hydraulic diameter of the spacer filled channel.

Now if the “Specific surface of the spacer” ( $S_{v,sp}$ ) is defined by the following relation:

$$S_{v,sp} = \frac{S_{sp}}{V_{sp}} \quad (4.3 - 10)$$

Combining equations 4.3-7 and 4.3-10, we get the following relation:

$$S_{v,sp} = \frac{S_{sp}}{V_T (1 - \varepsilon)} \quad (4.3 - 11)$$

On re-arranging the above equation:

$$\frac{S_{sp}}{V_T} = S_{v,sp} (1 - \varepsilon) \quad (4.3 - 12)$$

If the height, width and length of the channel is represented by the  $h_{ch}$ ,  $b$  and  $L$  respectively, then wetted surface of the flat channel ( $S_{fc}$ ) can be represented by the following equation:

$$S_{fc} = 2(h_{ch} + b)L \quad (4.3 - 13)$$

Total volume of the channel ( $V_T$ ) can be represented by the following equation:

$$V_T = h_{ch} \times b \times L \quad (4.3 - 14)$$

Dividing equation 4.3-13 by 4.3-14, we get:

$$\frac{S_{fc}}{V_T} = \frac{2(h_{ch} + b)}{h_{ch} \times b} \quad (4.3 - 15)$$

Inserting equation 4.3-12 and 4.3-15 in equation 4.3-9 we get:

$$d_h = \frac{4 \varepsilon}{\frac{2(h_{ch} + b)}{h_{ch} \times b} + S_{V,sp} (1 - \varepsilon)} \quad (4.3 - 16)$$

For a spacer filled narrow channel, the channel height ( $h_{ch}$ ) is negligible as compared to channel width ( $b$ ) so the above equation can be reduced to the following form for the condition  $b \gg h_{ch}$  :

$$d_h = \frac{4 \varepsilon}{\frac{2}{h_{ch}} + S_{V,sp} (1 - \varepsilon)} \quad (4.3 - 17)$$

## 4.4 Modelling Procedure

### 4.4.1 Computational domain and boundary conditions

The arrangement of spacer in feed channel of SWM is such that one set of parallel filaments are placed on the top of another set of parallel spacers and the thickness of top and bottom filaments together defines the total height of the feed channel ( $h_{ch}$ ).

Computational domain comprising of six bottom and four top filaments was created using bottom up approach in Gambit<sup>®</sup>. Boolean operations (unite, subtract and intersect) and split functions were used extensively for that purpose. The geometry was further decomposed into several volumes to have a structured mesh. Figure 4.3 shows the spacers arrangement in which the orientation of the bottom filament is transverse to the flow direction, whereas the top filaments are in axial direction to the flow hence making the flow attack angle (with Y-axis ) for the top and bottom filaments to be  $90^\circ$  and  $0^\circ$  respectively.

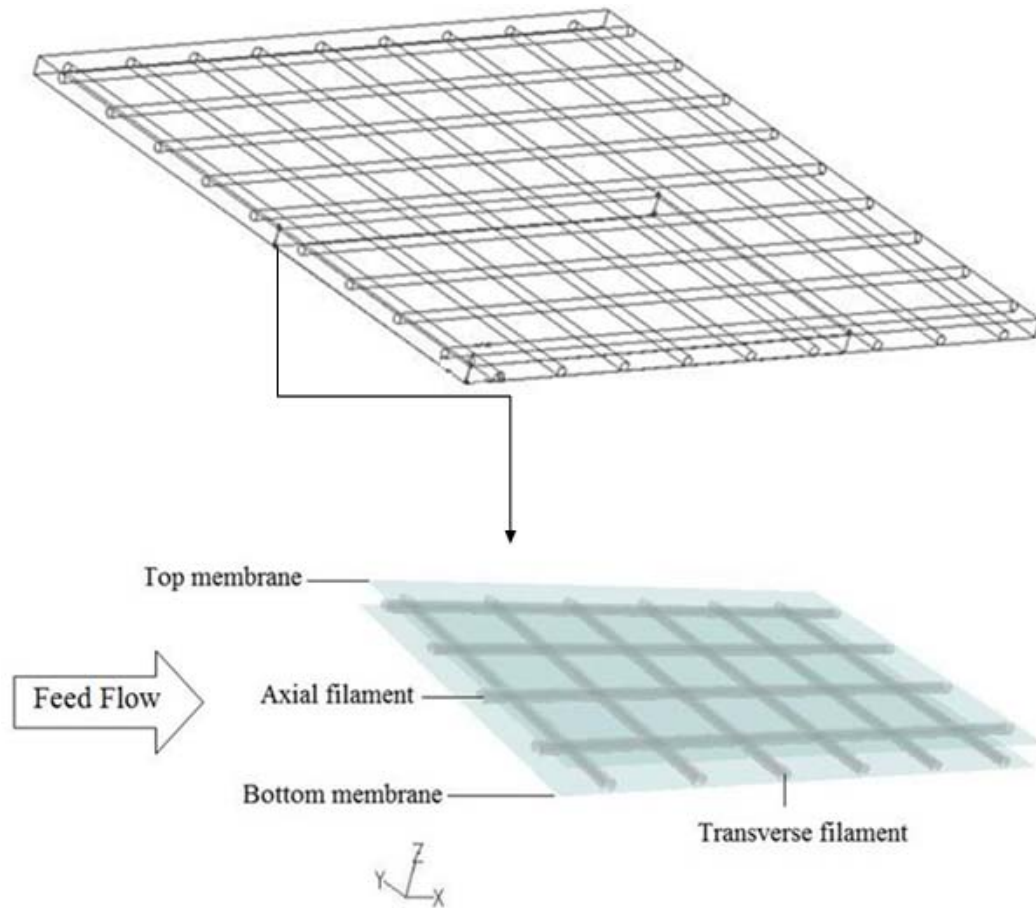


**Figure 4.3: Schematic of feed channel spacer and selected computational domain.**

Following boundary conditions are used for the computational domain:

- The two opposite vertical faces perpendicular to the flow direction (x-direction) are defined as Mass flow inlet and pressure outlet. Mass flow rate is specified in flow direction and varied to get the desired hydraulic Reynolds number ( $Re_h$ ).
- Translational periodic boundary conditions are defined for the two vertical surfaces parallel to top filaments.
- The filament surfaces are defined as walls.
- Since for most of the membrane processes the feed velocity is 3 - 4 times higher than the permeation velocity, the membrane walls are assumed to be impermeable walls with no-slip conditions [164, 165].

For all the cases  $Re_h$  was kept below the defined range of critical Reynolds number for spacer filled channels to enable laminar flow model to simulate flow through the computational domain. Water is used as working fluid and is assumed to be

incompressible, isothermal and having constant density (998.2 Kg/m<sup>3</sup>), viscosity (0.001 Kg/(ms)) and solute diffusivity (1.54 x 10<sup>-9</sup> m<sup>2</sup>/s). The filament surfaces are defined as walls. Since cross flow filtration processes tend to recover only 10 to 15 % of the feed (per module) as product and also have large surface area. Large surface area coupled with low recovery rates yields very low permeation velocities compared with feed velocity, hence the assumption of impermeable walls for both top and bottom membrane surfaces of the computational domain is justified [164, 165]. Due to low permeation rate through the membranes the variation of local concentration along the flow direction is neglected and hence top and bottom membrane walls are set to be at higher fixed values of concentration than at the inlet [165].

In the present study hydraulic Reynolds number defined earlier by Schock and Miquel [61] is used and presented in Eq. (4.4.1-1).

$$Re_h = \frac{d_h u_{eff}}{\nu} \quad (4.4.1 - 1)$$

In equation 4.4.1-1  $u_{eff}$ ,  $d_h$  and  $\nu$  represents the effective velocity (or average) in the computational domain, hydraulic diameter of the channel and kinematic viscosity respectively. An expression for the hydraulic diameter has been derived in the previous section which is defined by the following equation for a spacer-filled channel:

$$d_h = \frac{4 \varepsilon}{\frac{2}{h_{ch}} + S_{v,sp} (1 - \varepsilon)} \quad (4.4.1 - 2)$$

Where  $h_{ch}$  is the channel height,  $\varepsilon$  is the porosity of the spacer represented by eq. (4.4.1-3) and  $S_{v,sp}$  represents specific surface of the spacer represented by eq. (4.4.1-4). These two equations are described in detail in the previous section.

$$\varepsilon = 1 - \frac{\text{Spacer volume}}{\text{Total volume}} \quad (4.4.1 - 3)$$

$$S_{v,sp} = \frac{\text{Wetted surface of spacer}}{\text{Volume of spacer}} \quad (4.4.1 - 4)$$

In order to define mass flow rate ( $m$ ) at the inlet of the computational domain first of all the effective velocity is determined at a specific hydraulic Reynolds number using eq. (4.4.1-1) then the following equation is used to determine the mass flow rate ( $m$ ):

$$m = u_{eff} A_{eff} \rho \quad (4.4.1 - 5)$$

In the above equation  $A_{eff}$  and  $\rho$  represents the effective cross-sectional area and density respectively. For a channel filled with spacer having width  $b$  (along  $y$ -direction), channel height  $h_{ch}$  and porosity  $\varepsilon$ ,  $A_{eff}$  is defined by the following equation:

$$A_{eff} = h_{ch} b \varepsilon \quad (4.4.1 - 6)$$

Figure 4.4 shows the systematic approach to find out the mass flow rate which is defined as the boundary condition at the inlet of the computational domain at a specific hydraulic Reynolds number.

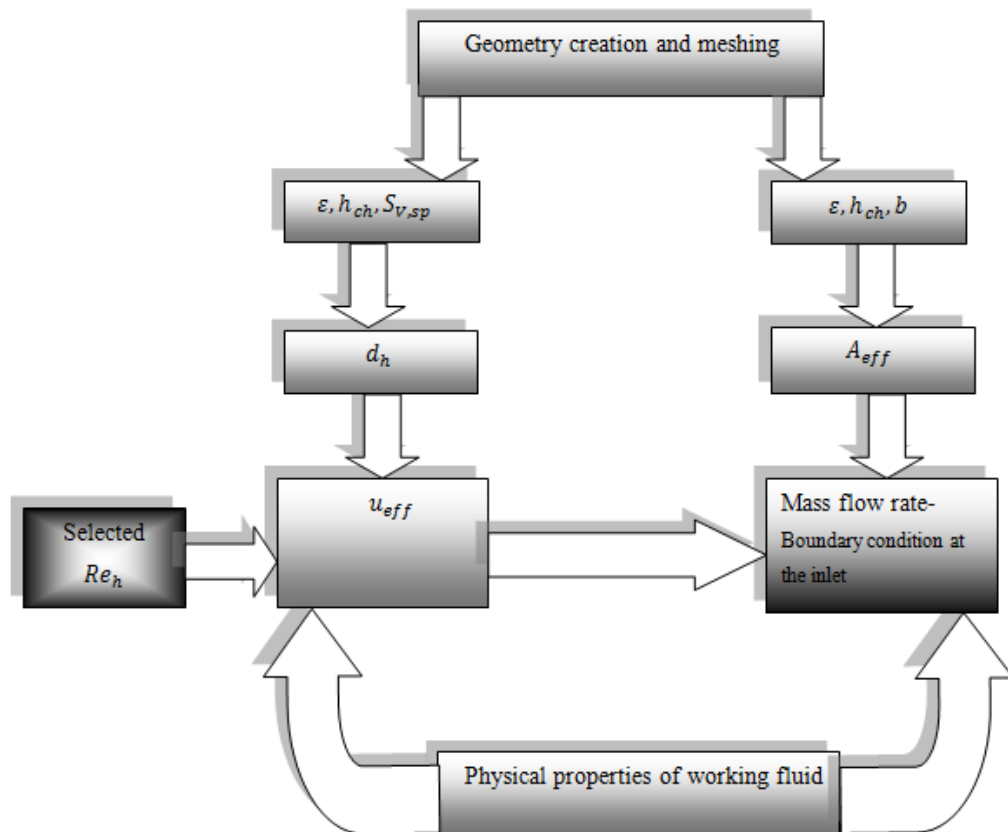


**Figure 4.4: Approach to get mass flow rate at a desired channel Reynolds number.**

In membrane systems, cost associated with pumping the fluid is one of the most important factors. Power number, which relates resistance force to inertia force, is evaluated to compare the results of the present study with the data available in literature. Earlier Li et al. [135] defined dimensionless power number ( $P_n$ ) to compare energy consumption of different spacer, used later by Skakaib et al. [164] in their study. The same definition is used for the present study and represented by the following equation:-

$$P_n = SPC \left( \frac{\rho^2 h_{ch}^4}{\mu^3} \right) \quad (4.4.1 - 7)$$

In the above equation SPC is the specific power consumption. Pressure drop cannot be avoided in spacer filled channels and it reduces the overall transmembrane pressure acting on the membrane surface. To compensate for the pressure loss higher pumping energy is required. The term SPC reflects the mechanical power consumption dissipated per unit volume of the flow channel [163]. Degree of SPC in spiral wound membrane channels depends on the spacer configuration and on  $Re_n$ . Specific power consumption (*SPC*) is given by the following relation

$$SPC \left[ \frac{u_{eff} \Delta P A}{L_c A} \right] = \frac{\Delta P}{L_c} u_{eff} \quad (4.4.1 - 8)$$

In the above expressions,  $L_c$  and  $\Delta P$  are the channel length and pressure drop over the channel respectively, whereas  $u_{eff}$ ,  $\mu$ ,  $\rho$  and  $A$  are the effective velocity, dynamic viscosity, density and channel cross-section area respectively. Dimensionless pressure drop is calculated by using the following relation and the results are compared to those published by Koutsou et al. [66] and Skakaib et al. [164].

$$\Delta P^* = \frac{\Delta P}{L_c} \left( \frac{d^3}{Re_{cyl}^2 \rho v^2} \right) \quad (4.4.1 - 9)$$

#### 4.4.2 Grid refinement and independence

The computational domain shown in Figure 4.5 was constructed and meshed in geometry construction and grid generation pre-processor software Gambit<sup>®</sup>. The grid generated consisted of a number of finite hexahedral volumes. On comparing results

obtained by successive grid refinement it was found that 600,000 cells were sufficient to have results independent of grid density. Further, due to enhanced computational time and burden with grid refinement, another confirmatory check was done by considering a smaller computational domain. For instance in case of case study 1, when the bottom and the top filaments were perpendicular and parallel to the flow directions respectively the computed ratio of shear stress at top and bottom membrane walls was found to be 5 with 600,000 cells. For the same spacer filament orientation and same boundary conditions, considering one top and six bottom filaments (thus dividing the computational domain to one-fourth) the ratio obtained was 5.02 with the same number of cells indicating an error less than 0.5%. Further the results obtained for top and bottom wall shear stress, pressure drop and power number for different cases studied in this chapter are compared with already published literature and an excellent agreement was found, which further justifies that the grid size chosen for the simulation was adequate. Figure 4.5 shows the computational grid generated for case study 1.

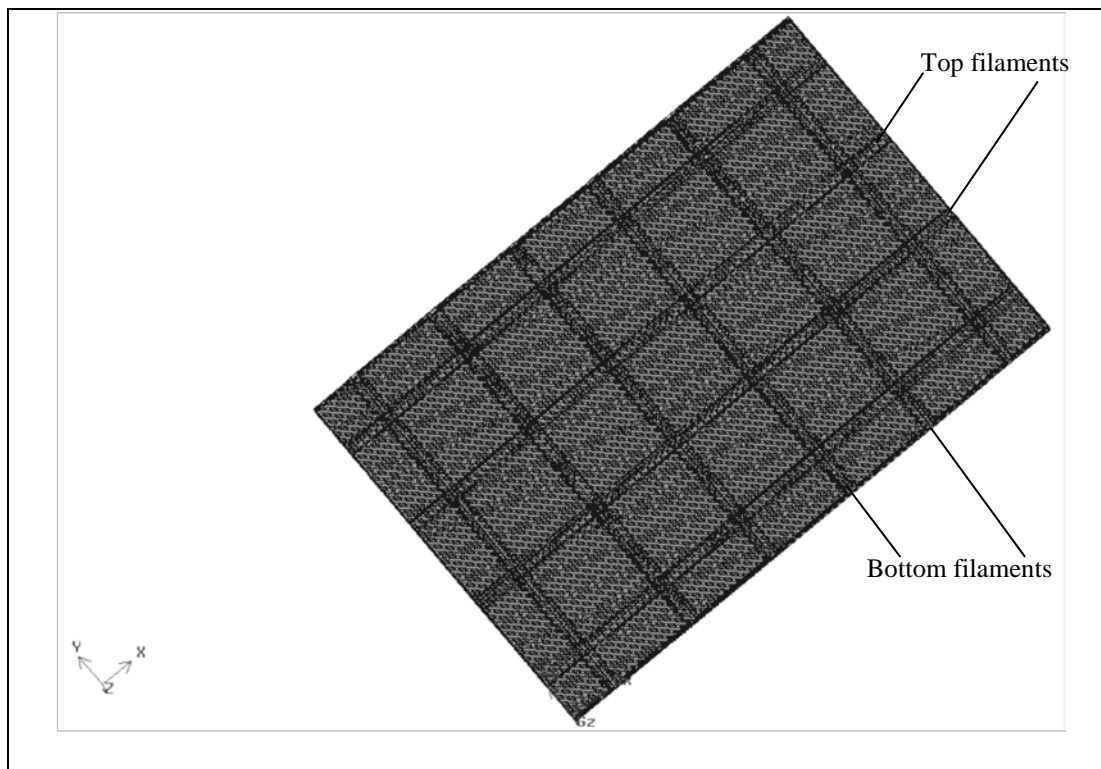


**Figure 4.5: Computational grid (flow direction is along x-axis).**

### 4.4.3 Governing equations, solution methods & controls

Continuity and three momentum equations (x, y and z momentum) are the four governing equations (Navier-Stokes equations) which are represented below for steady, laminar and incompressible flow in three-dimensional form [55, 165] and are described in chapter 3 of this thesis:

$$\frac{\partial u}{\partial x} + \frac{\partial v}{\partial y} + \frac{\partial w}{\partial z} = 0 \quad (4.4.3 - 1)$$

$$u \frac{\partial u}{\partial x} + v \frac{\partial u}{\partial y} + w \frac{\partial u}{\partial z} = -\frac{1}{\rho} \frac{\partial P}{\partial x} + \nu \left[ \frac{\partial^2 u}{\partial x^2} + \frac{\partial^2 u}{\partial y^2} + \frac{\partial^2 u}{\partial z^2} \right] \quad (4.4.3 - 2)$$

$$u \frac{\partial v}{\partial x} + v \frac{\partial v}{\partial y} + w \frac{\partial v}{\partial z} = -\frac{1}{\rho} \frac{\partial P}{\partial y} + \nu \left[ \frac{\partial^2 v}{\partial x^2} + \frac{\partial^2 v}{\partial y^2} + \frac{\partial^2 v}{\partial z^2} \right] \quad (4.4.3 - 3)$$

$$u \frac{\partial w}{\partial x} + v \frac{\partial w}{\partial y} + w \frac{\partial w}{\partial z} = -\frac{1}{\rho} \frac{\partial P}{\partial z} + \nu \left[ \frac{\partial^2 w}{\partial x^2} + \frac{\partial^2 w}{\partial y^2} + \frac{\partial^2 w}{\partial z^2} \right] \quad (4.4.3 - 4)$$

CFD commercial code ANSYS FLUENT which uses finite-volume based techniques for the solution is used in the study to solve the governing equations. Since the working fluid is considered to be incompressible hence pressure based solver which uses segregated algorithm is used for all the simulations in the thesis. Pressure based segregated solver segregates and solves the governing equations in a sequential manner, one after the other. In this approach pressure continuity and momentum equations are manipulated to get pressure correction equation which yields the pressure field. QUICK( Quadratic Upstream Interpolation for convective Kinetics) scheme is used for discretising momentum equations, whereas SIMPLEC (Semi-Implicit Method for Pressure linked Equations, Consistent) algorithm is used for pressure velocity coupling [35, 165, 167]. For solution control values of 0.3 and 0.7 were set respectively as under-relaxation factors for pressure and momentum.

QUICK is a three-point interpolation scheme used to determine the cell face values by a quadratic function passing through two neighbouring nodes present at each side of the face and one upstream node.

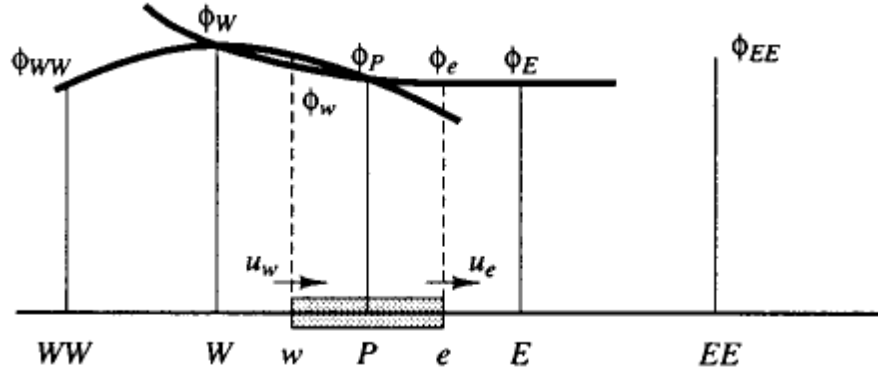


Figure 4.6: Quadratic profiles used in QUICK scheme. Source: [35].

In the Figure 4.6,  $\Phi$  represents value of any property and the subscripts represent the corresponding cells. It can be seen from the figure that for cases when  $u_w$  and  $u_e$  are greater than zero QUICK scheme make use of a quadratic fit through the two neighbouring cells (W & P) and one upstream cell (WW) to evaluate  $\Phi_w$ . Similarly to evaluate  $\Phi_e$ , a quadratic fit through P, E and W is used. For the cases when  $u_w$  and  $u_e$  are negative, values of  $\Phi$  at P, W and E are used to evaluate  $\Phi_w$ , and to evaluate  $\Phi_e$  values of  $\Phi$  at P, E and EE are used.

The general form of QUICK scheme, valid for both positive and negative flow directions, is presented by the following equation [35]:

$$a_P \Phi_P = a_W \Phi_W + a_E \Phi_E + a_{WW} \Phi_{WW} + a_{EE} \Phi_{EE} \quad (4.4.3 - 5)$$

In the above equation  $\Phi_P, \Phi_W, \Phi_E, \Phi_{WW}$  and  $\Phi_{EE}$  represents the values of any particular property at a particular cell “p”, neighbouring cell in west, neighbouring cell in east, upstream cell ( in case of positive flows) and upstream cell (in case of negative flows) respectively. Whereas  $a_P, a_W, a_E, a_{WW}$  and  $a_{EE}$  are the respective coefficients.

SIMPLEC (SIMPLE-Consistent) algorithm is used for pressure velocity coupling which is a variant of traditional SIMPLE (Semi-Implicit Method for Pressure linked Equations) algorithm and like SIMPLE algorithm uses the staggered grid for velocity components for calculation purposes. The two algorithms follow the same steps, with the main difference that momentum equations are manipulated in a way that velocity correction equations in SIMPLEC omit less significant terms than those in

SIMPLE algorithm [35]. In case of SIMPLEC algorithm, following equations is used to determine the face flux [167]:

$$J_f = J_f^* + J_f' \quad (4.4.3 - 6)$$

In the above equation  $J_f'$  represents the correction flux as the difference between corrected flux ( $J_f$ ) and guessed flux ( $J_f^*$ ) at any cell face. The corrected flux is further defined as the following equation:

$$J_f' = d_f (p'_{co} - p'_{cl}) \quad (4.4.3 - 7)$$

In the above equation the term  $d_f$  is a function of ( $a_p - \sum a_{nb}$ ) and called the d-term of pressure correction equation. Whereas  $p'_{co}$  and  $p'_{cl}$  represent the pressure corrections at adjacent cells and the terms  $a_p$  and  $a_{nb}$  are coefficients in discretised momentum equations.

The convergence criterion for the scaled residuals of continuity, x, y and z components of velocity was set to 1e-06. Moreover the convergence was further confirmed by stable values of average wall shear rates and velocities at different monitoring points in the computational domain.

## 4.5 Simulation results and discussion

Three case studies were carried out to investigate the effect of feed spacer orientation (with respect to the inlet flow) on shear stress, power number and pressure drop by changing the flow attack angles ( $\theta_1$  and  $\theta_2$ ) and angle between the crossing filaments ( $\alpha$ ). The results of first two case studies and comparison with previous studies are presented in Table 4.2 and Table 4.3.

In the third case study angle between the crossing filaments was set to  $45^0$  and the flow attack angles  $\theta_1$  and  $\theta_2$  were set as  $135^0$  and  $0^0$  respectively. The results are shown in Table 4.4.

In the first case study the orientation of the top and bottom filament with the flow direction was set in such a manner that top filaments were in axial direction whereas the bottom filaments were in transverse direction, that is  $\theta_1=90^0$  and  $\theta_2=0^0$ .

Variation in shear stress values on bottom and top membrane wall along the flow direction are shown in Figure 4.7 a & b respectively. Since the shear stress distribution is mainly dependent on the velocity field, so for the bottom membrane wall it is zero near the bottom filaments and reaches a maximum values close to the centre of the two consecutive bottom filaments along the flow direction. When the fluid flows through narrow space above the bottom filaments it is accelerated and hence the peak value for shear stress on the top membrane is observed just above the bottom filaments and it reaches its lowest value at the centre of the two consecutive bottom filaments.

In the present work the dimensionless filament spacing ( $L$ ) was set to 3.6. The shear stress distribution on walls can be explained by Figure 4.10 which represents velocity vectors on a plane in the vicinity of bottom wall. Two distinct flow regions are prominent near the bottom wall. In the first region, extending from the centre of the two consecutive transverse filaments to the next bottom filament in the normal flow direction, flow appears to reattach to the bottom surface and accelerates in the normal flow direction in a diverging manner. Whereas in the second region which extends from the centre to next transverse filament (in opposite flow direction) the flow tends to reverse and recirculate.

Similar flow behaviour and shear stress distribution has been reported by Shakaib et al. [165] in their study. Their computational domain comprised of six bottom and one top filament. Their study reflects the effect of dimensionless filament spacing on velocity, pressure and shear stress. However, they carried out the simulations at integer values ( $L=2, 3, 4$  and  $6$ ) for the dimensionless filament spacing and reported that there is considerable change in fluid flow behaviour when the spacing is changed from 3 to 4, especially for the bottom filaments as they are present in transverse direction to the normal flow. According to their study when  $L$  is set to 3 for the transverse filaments the portion of the flow striking the bottom filament shows complete recirculation without flow reattachment. But when the spacing is increased to 4 two distinct regions (flow reattachment and recirculation) appear near the bottom wall.

Shear stress distribution in Figure 4.7 a & b indicates that the shear stress values at the membrane walls are not equal for the first few filaments but then tend to become

equal for succeeding filaments revealing the signature of fully developed and periodic flow. Similar results were reported by Yuan et al. [171] in their research work and showed that the flow and heat transfer in channels with periodic cross-section becomes periodic and fully-developed after few cells. Later Li et al. [63] validated its use for non-woven net spacers. Our results are also in fair accordance with their findings as can be seen from the shear stress distribution trends. Furthermore profiles observed in the current study for shear stress are found to be similar to previous two-dimensional CFD studies by Cao et al. [136] and the three-dimensional CFD studies by Shakaib et al. [165].

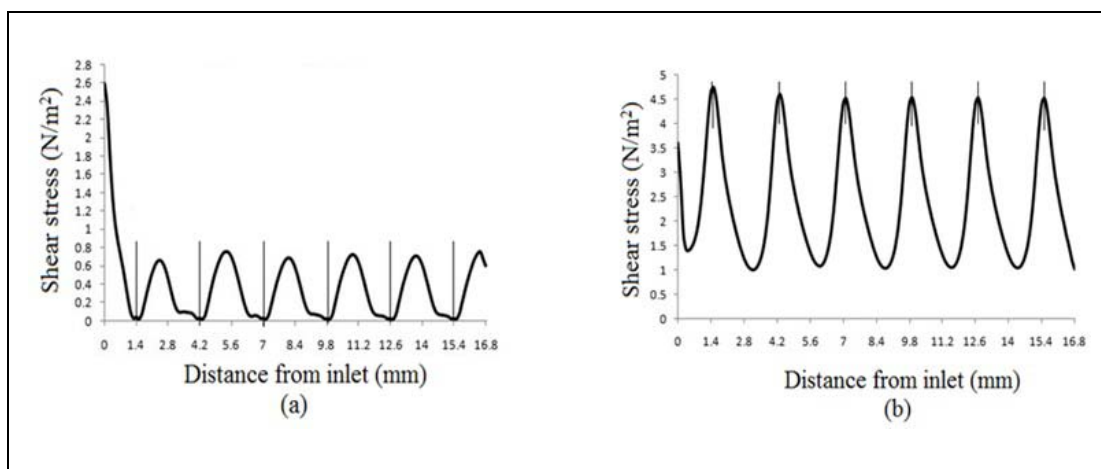


**Figure 4.7: Shear stress distribution on bottom (a) and top (b) wall (Note:- Vertical lines indicate centre lines of bottom filaments).**

Figure 4.8 represents the x-velocity contours of the fluid flowing through the membrane. It is quite evident from the figure that the fluid is accelerated at the narrow space available above the transverse filament. Moreover, it also shows the areas behind the bottom filaments where the velocity is opposite to the normal flow direction (negative values) which essentially means the flow reversal and recirculation. It is also evident that a portion of the fluid after striking the bottom filaments changes its direction and tends to accelerate in the direction opposite to that of the normal flow and reaches a maximum negative velocity (direction opposite to normal flow) somewhere in the middle of the two consecutive transverse filaments. As a result of this flow pattern the highest local negative shear stress values at the bottom wall towards the central portion of the two consecutive transverse filaments can be seen in Figure 4.9. Two distinct regions of high positive shear stress are also apparent just before the transverse filaments and in the vicinity of the crossing of transverse and axial filaments. Development of those regions can

be explained by Figure 4.10 representing the velocity vectors on a plane just above the bottom membrane at  $0.05 h_{ch}$ . The flow is seen to be accelerated in normal flow direction in a diverging manner thus explaining the generation of those distinct zones of higher positive shear stress. In addition to that, another region of peak negative shear stress is also evident just beneath the axial filament. It is evident from Figure 4.8 that the fluid is accelerated as a result of narrow space availability over the bottom filaments and therefore consequently results in shear stress peaks on the top wall above bottom transverse filaments as evident in Figure 4.11.

The selected computational domain also comprises of flow entry region where the flow is not fully developed. Further, it is shown that the flow becomes fully developed after passing over 2-3 transverse filaments in the flow direction. This part of the computational domain is not the true representative of the hydrodynamics prevailing in the major part of the SWM. Due to this reason the part of the computational domain between last three filaments which demonstrates fully developed flow is selected for the quantitative comparison of results with published literature, as it truly represents the hydrodynamics in major part of SWM. Further, it can be seen from Figures 4.7-4.14 that the contours of wall shear stress and velocity vectors and Pathlines are identical between 4<sup>th</sup> and 5<sup>th</sup> & 5<sup>th</sup> and 6<sup>th</sup> transverse filament, which further validates the selection of the region as true representative of flow conditions in the major part of the feed channel of SWM.

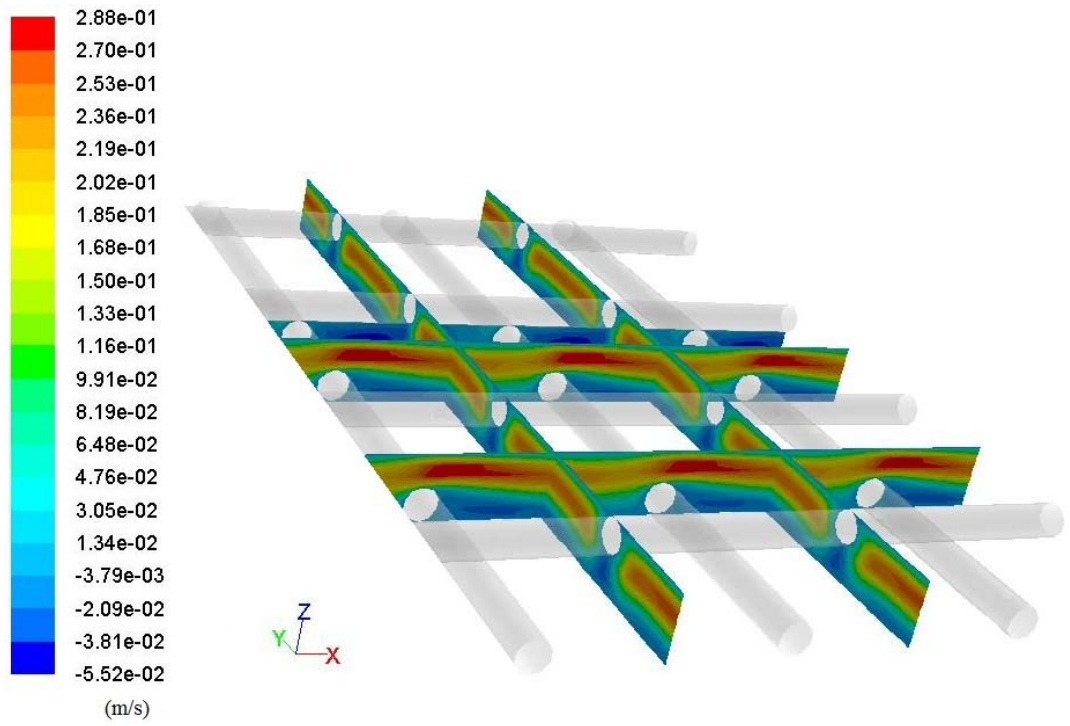


Figure 4.8: X-Velocity contours at selected faces in the computational domain.

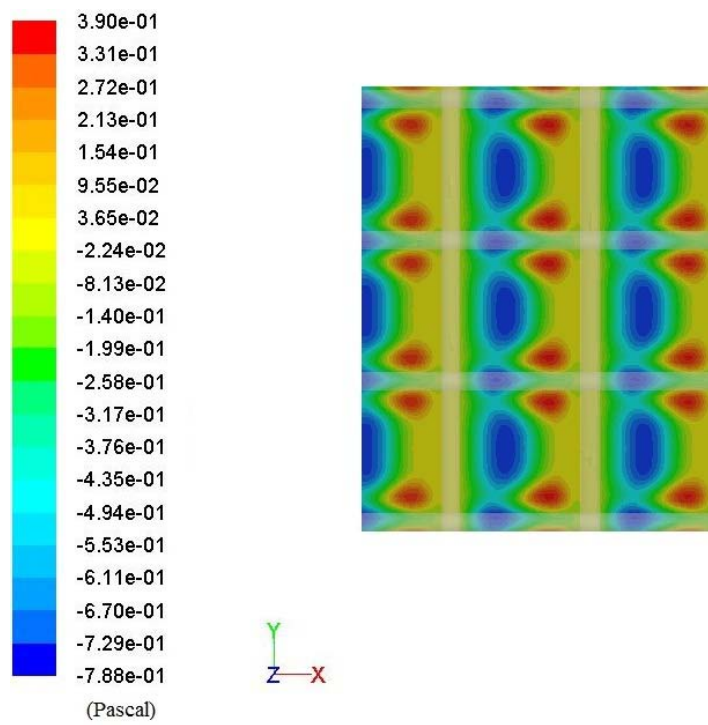


Figure 4.9: X-Shear stress contours on bottom wall.

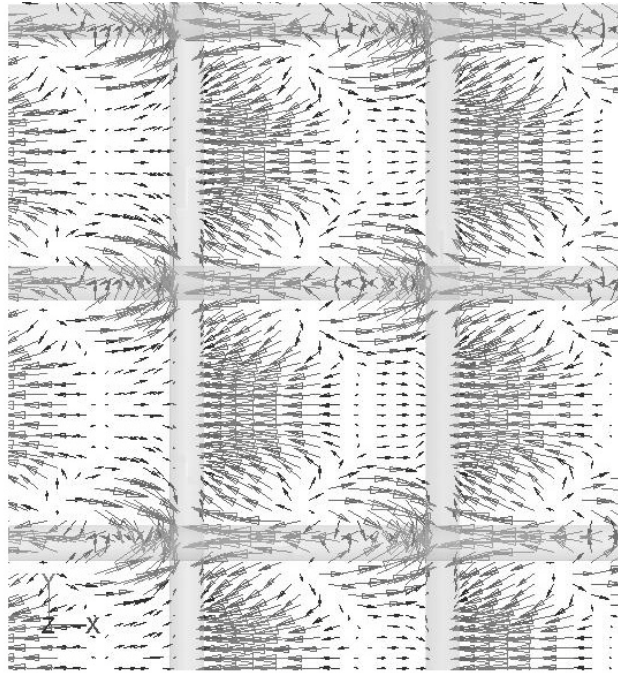


Figure 4.10: Velocity vectors on a plane  $0.05 * h_{ch}$ .

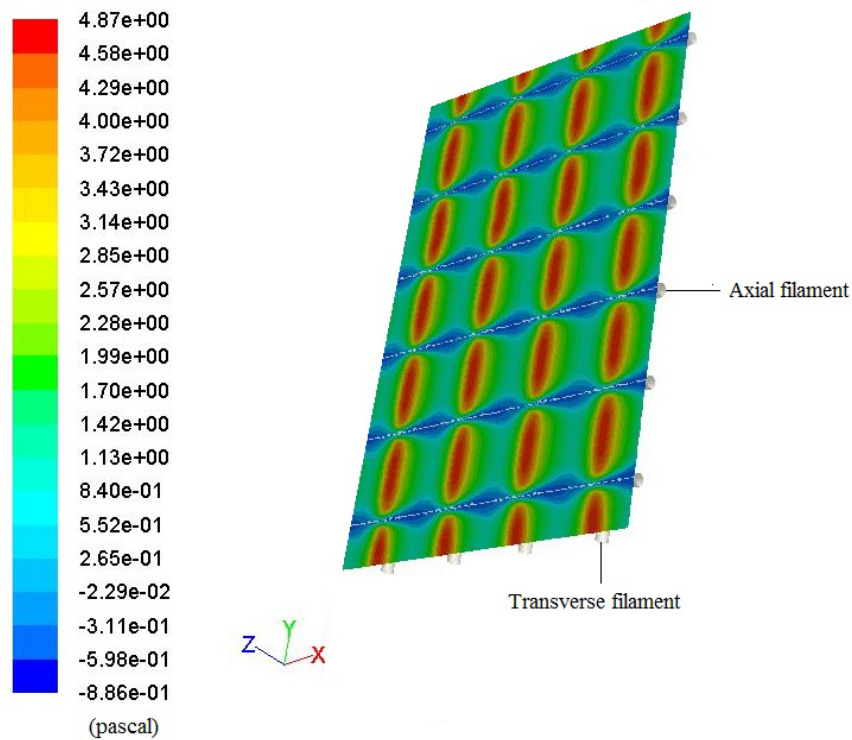
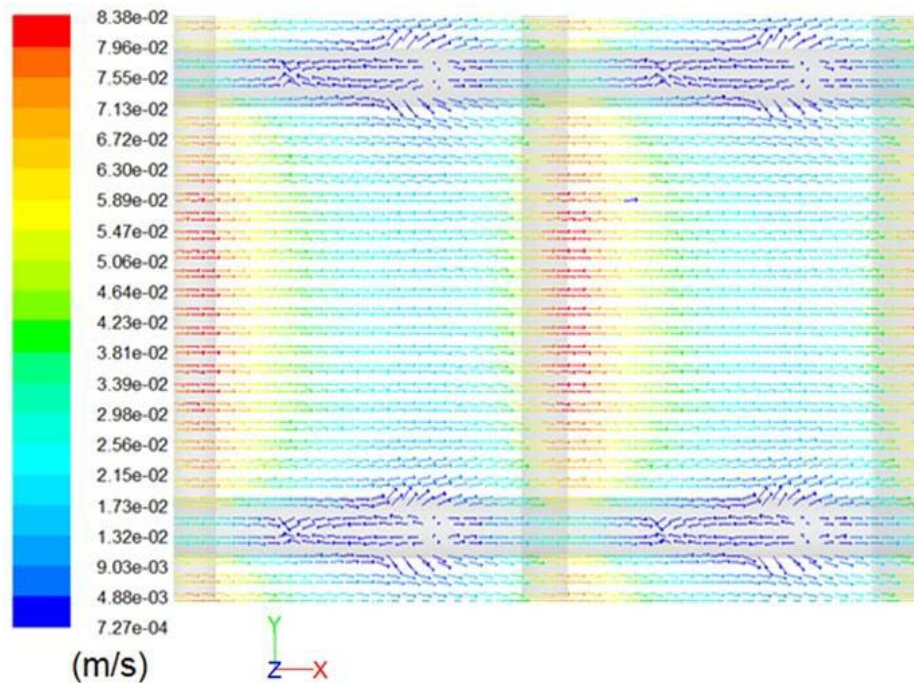


Figure 4.11: X-Shear stress contours on top wall.

From the literature review [164, 165] it is quite evident that major portion of the fluid flows in main flow direction (x-direction) in case of spacer filled SWM. However, the presence of net spacers give rise to strong three-dimensional effects.

Two separate zones are defined near the top wall where the flow patterns are influenced by the presence of axial filament. Flow tends to shift towards the top filament in the vicinity of top and bottom filament intersection and gets diverted away from the top filament somewhere in the middle of two consecutive transverse filaments. The two distinct zones, namely, flow attachment and separation are quite evident in Figure 4.12 and Figure 4.13. Figure 4.12 represents the velocity vectors at top wall showing the two distinct zones, whereas Figure 4.13 represents the contours of velocity over-layed by the velocity magnitude at a plane surface very close to the top wall. Since it is reported in literature that for large transverse filament dimensionless spacing ( $L=4$ ), high fluid velocity and shear stress is observed near the top wall right above the transverse filament and the values decrease considerably near the centre of two consecutive transverse filaments. All flow patterns, shear stress and velocity distribution represented in this study are in fair accordance with results available in literature [164, 165].



**Figure 4.12: Velocity vectors at top surface.**

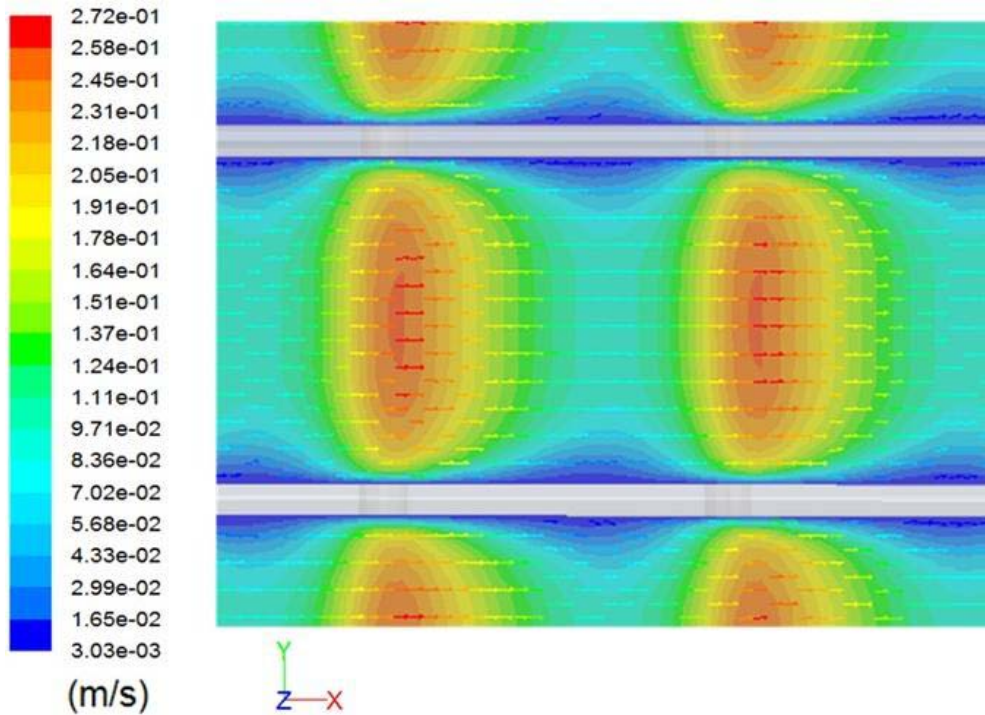


Figure 4.13: Velocity vectors at  $0.95 \cdot h_{ch}$

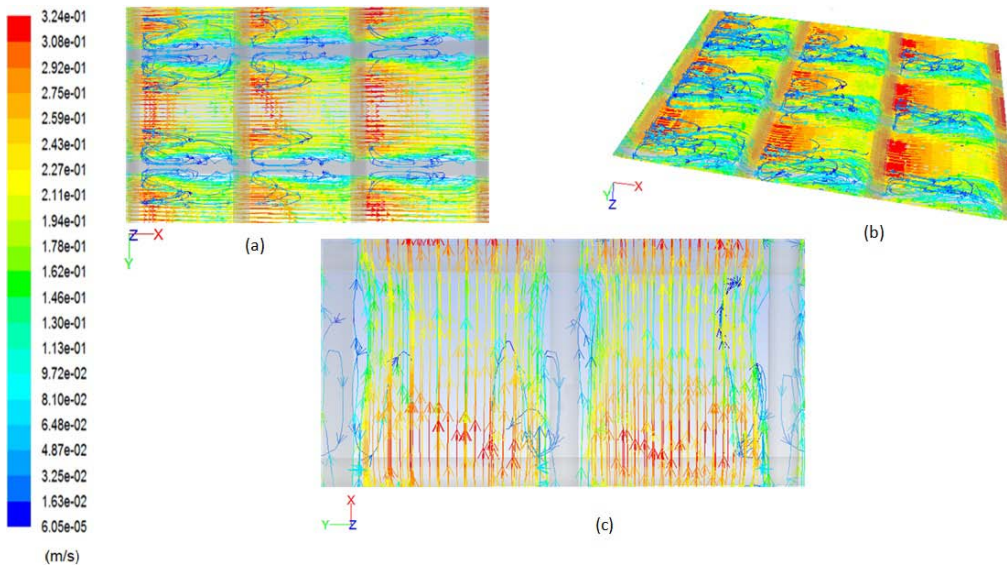


Figure 4.14: Pathlines of Velocity realising from the inlet (a) and (b) bottom view, (c) top view.

Figure 4.14 (a & b) represents different views of path lines of velocity releasing from the inlet. The figure shows the bottom view of the flow domain. It can be clearly seen from the figure that flow tends to recirculate in the region near the vicinity of the bottom membrane in the direction opposite to that of the normal flow and tends to reattach to the bottom surface somewhere in the middle. However the severity of recirculation dampens along flow direction. Figure 4.14 (c) represents the top view

of the domain where the flow tends to move towards the top filament at the intersection of the two filaments (flow reattachment) and shifts away from the top filament as it moves ahead in the normal flow direction (flow separation). Our study further reveals that for this type of spacer and flow conditions ( $L=3.6$ ,  $D=0.5$ ,  $\theta_1=90^\circ$ ,  $\theta_2=0^\circ$ ,  $Re_h=125$ ) the average value of shear stress on top wall is nearly 5 times high than that at the bottom wall. The ratio was further cross checked by making a very finely meshed geometry comprising of six bottom and one top filament. The total number of the meshed cells was kept nearly the same (which leads to highly refined grid resolution) and the boundary conditions were kept exactly the same. The ratio obtained, as discussed above, was 5.02 which indicate an error less than 0.5%. Moreover, the individual average values for shear stress at top and bottom wall did not show any significant change. The average shear stress value for the top and bottom walls were respectively 1.8 and 0.32  $N/m^2$ .

To compare our values with those reported in literature [135, 164], simulation was carried out at  $Re_h=100$ . Table 4.2 shows the comparison of the results neglecting the entrance and exit effects. Our reported values are in fair agreement with the reported ones.

**Table 4.2: Comparison of average shear stresses on walls and pressure drop at  $Re_h=100$  with available data [135, 164].**

Parameters	* Shakaib et al. [164]	**Li et al. [135]	Present study
Average Shear stress on top wall (Pa)	1	-	1.15
Shear stress on bottom wall (Pa)	0.16	-	0.20
Pressure drop* $10^{-3}$ (Pa/m)	5	-	6.29
Power number * $10^{-5}$	-	1.7	1.80
Dimensionless pressure drop	-	-	0.32

\* interpolated value from the plot between filament spacing vs avg shear stress on walls and linear pressure drop.

\*\* values reported for  $L=4$

In the second case study the filaments were oriented at an angle with the inlet flow instead of being axial or transverse. Flow attack angles that top and bottom filament makes with y-axis and represented by  $\theta_1$  and  $\theta_2$  in Figure 4.2 were set to  $45^\circ$ .

However the ratio of filament diameter to the channel height ( $D= d/h_{ch}$ ) was kept 0.5 and that for filament mesh size to the channel height ( $L=l/h_{ch}$ ) was also kept 3.6. However, hydraulic Reynolds number was set to 100 to compare our results with already available in literature [66, 135, 164]. Numerically obtained pressure drop value in the study is further used to calculate Power number defined by Eq. (4.4.1.7) and dimensionless pressure drop defined by Eq. (4.4.1.9). The results of the study show reasonable agreement with those available in literature and are reported in Table 4.3.

**Table 4.3: Comparison of current and previous studies at flow attack angle of  $45^0$  and  $Re_h=100$ .**

Parameters	*Shakaib et al. [164]	**Koutsou et al. [66]	**Li et al. [135]	Present work
Average shear stress on walls (Pa)	0.70	-	-	0.69
Pressure drop $\times 10^{-3}$ (Pa/m)	5.20	-	-	6.46
Dimensionless pressure drop	0.32	0.35	-	0.33
Power Number $\times 10^{-5}$	2.60	2.0	2.40	1.91

\* Interpolated value from the plot between filament spacing vs avg shear stress, linear pressure drop, dimensionless pressure drop at  $\theta_1= \theta_2 45^0$

\*\*Values reported at  $L=4$

In the third case study the angle between the top and bottom filaments ( $\alpha$ ) was changed to  $45^0$  and the flow attack angles  $\theta_1$  and  $\theta_2$  were set  $135^0$  and  $0^0$  respectively. In this case the bottom filaments are again in transverse direction however the top filaments are inclined towards the channel axis. It should be noted that flow through such configuration has never been investigated in previous studies and no results are available in literature.

Figure 4.15(a) represents the contours of velocity at plane close to the bottom membrane, whereas Figure 4.15(b) represents the contours of velocity at a plane close to the top membrane. It is evident from Figure 4.15(a & b) that the fluid tends to accelerate at the narrow space available below the top filament in the vicinity of the bottom wall; whereas the fluid velocity in the vicinity of the top membrane is on higher side above the bottom filaments.

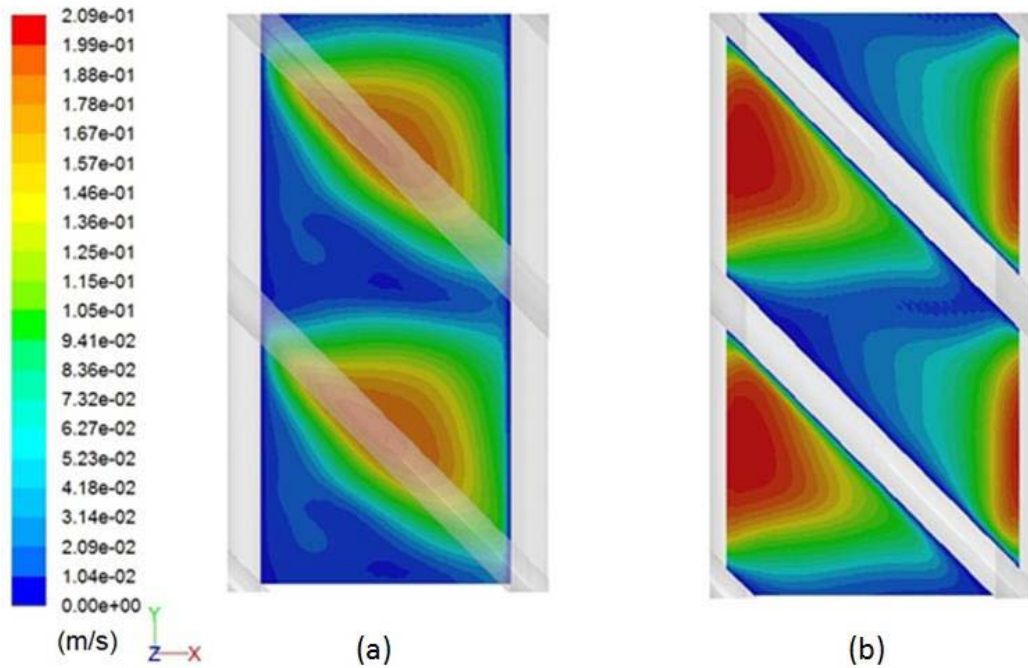


**Figure 4.15: Velocity contours at (a) 0.25\*channel height (b) 0.75\*channel height.**

The values for average shear stress on top and bottom wall, pressure drop and Power number are listed in Table 4.4.

**Table 4.4: Shear stress, pressure drop, dimensionless pressure drop and power number at flow attack angle  $\theta_1=135^\circ$  and  $\theta_2=0^\circ$  at  $Re_h=100$ .**

Average shear stress on top wall (Pa)	0.9
Average shear stress on bottom wall (Pa)	0.7
Pressure drop $\times 10^{-3}$ (Pa/m)	11.84
Dimensionless pressure drop	0.605
Power Number $\times 10^{-5}$	3.36

Pressure drop in spacer filled modules depends on the resistance offered by the filaments to flow, which in turn depends on the flow attack angles. Pressure drop will be at the higher side when the flow will hit more filaments in an upright fashion. It can be seen that when the flow attack angle  $\theta_1$  and  $\theta_2$  were set at  $90^\circ$  and  $0^\circ$  respectively the bottom filaments were perpendicular to the flow direction providing maximum resistance to flow whereas the top filaments were along the flow direction

and hence provide quite less resistance. When the flow attack angles  $\theta_1$  and  $\theta_2$  was set to 45 degree the bottom filaments were moved outwards the channel axis ( providing less resistance than the previous case) and the top filaments were moved inwards to the channel axis (hence providing more resistance as compared to the previous case). As a result pressure drop for the two filament arrangements do not differ to a large extent. However when the flow attack angle  $\theta_1$  and  $\theta_2$  was set to 135<sup>0</sup> and 0<sup>0</sup> degree, the bottom filaments are in perpendicular direction to the flow where as the top filaments were moved further inwards to the channel axis and hence providing maximum pressure drop and maximum power number for the arrangement.

#### **4.6 Conclusion**

In the present work, an attempt has been made to study the effect on flow patterns through a spacer filled RO membrane when the secondary structures of the membranes (feed spacer filaments) are set at various angles with the inlet flow. Due to the presence of feed spacers secondary flow patterns are developed in spacer filled membrane modules and can be helpful for self sustaining backwashing and hence increasing membrane efficiency. Post processing revealed that the alignment of the feed spacers with the flow direction have great influence on the generation of secondary flow patterns through the spacer filled channels. Optimization of the feed spacer's orientation can lead to desirable flow patterns generation within the membrane module eventually leading to enhanced membrane performance.

Shear stress values were found to be not equal for the first few filaments but tend to become equal for the succeeding filaments (after 2-3 filaments) in flow direction revealing the signature of fully developed and periodic flows. Spacer having filaments oriented in transverse and axial direction ( $\theta_1=90^\circ$ ,  $\theta_2=0^\circ$ ) induce high shear stress on the top wall than on the bottom wall. Fluid flow is of more complex nature in the vicinity of bottom wall where two distinct zones (flow reversal and reattachment) are apparent. However near the top membrane flow tends to shift towards the top filament at the vicinity of top and bottom filament intersection and divert away from the top filament as it progress in the normal flow direction somewhere in the middle of transverse filaments.

Pressure drop in spacer filled SWM appears to depend largely on the filament orientation based on current investigations. Pressure drop and power number will be higher if the filaments are inclined more towards the channel axis. Pressure drop and power number for the first two cases did not differ significantly, whereas in the third case study the bottom filaments are perpendicular to the flow direction and the top filaments were further moved inwards to the channel axis resulting in maximum pressure drop and power number.

To the best of author's knowledge, flow through spacer filled narrow channels having  $\theta_1$ ,  $\theta_2$  and  $\alpha$  set as  $135^\circ$ ,  $0^\circ$  and  $45^\circ$  respectively has never been investigated in previous studies and no results are available in the literature apart from the outcomes of current work.

Flow visualizations carried out in the current study appears to be very valuable in understanding the complex flow patterns generated in spacer filled RO membrane modules which could potentially lead to the development of efficient membrane modules with optimum spacer arrangements.

## Nomenclature

<b>Symbol</b>	<b>Description</b>	<b>Units</b>
$b$	Channel width (in y-direction)	m
$D$	Dimensionless filament thickness	-
$d$	Filament thickness	m
$d_b$	Bottom filament thickness	m
$d_h$	Hydraulic diameter	m
$d_t$	Top filament thickness	m
$h_{ch}$	Channel height	m
$L$	Dimensionless filament spacing	-
$L_c$	Channel length	m
$l_b$	Bottom filament spacing	m
$l_t$	Top filament spacing	m
$P$	Pressure	Pa
$P_n$	Power number	-
$\Delta P$	Pressure drop	Pa
$\Delta P^*$	Dimensionless pressure drop	-
$Re_{cyl}$	Cylinder Reynolds number	-
$Re_h$	Hydraulic Reynolds number	-
$SPC$	Specific Power Consumption	Pa/s
$S_{fc}$	Wetted surface of flat channel	$m^2$

$S_{sp}$	Wetted surface of spacer	$m^2$
$S_{v,sp}$	Specific surface of the spacer	$m^{-1}$
$u_{av}$	Average feed velocity or superficial velocity	$m/s$
$u_{eff} = u_{av}/\varepsilon$	Effective velocity or average velocity in domain	$m/s$
$u$	x-component of velocity	$m/s$
$V_{sp}$	Spacer volume	$m^3$
$V_T$	Total volume	$m^3$
$v$	y-component of velocity	$m/s$
$w$	z-component of velocity	$m/s$
$x$	x-coordinate	$m$
$y$	y-coordinate	$m$
$z$	z-coordinate	$m$
$\varepsilon$	Porosity	-
$\alpha$	angle between the crossing filaments	$(^\circ)$
$\theta_1$	Angle between top filament and y-axis (flow attack angle)	$(^\circ)$
$\theta_2$	Angle between bottom filament and y-axis (flow attack angle)	$(^\circ)$
$\mu$	Dynamic viscosity	$Pa \cdot s$
$\nu$	kinematic viscosity	$m^2/s$
$\rho$	Density	$kg/m^3$

## Chapter 5. Mass transfer and flow dynamics

In spacer filled narrow channels used for water treatment, such as reverse osmosis membrane modules, water is allowed to enter tangentially into the feed channel. The feed channel is equipped with feed spacer which provides the flow path for water by separating the two membrane layers apart. Due to directional changes induced by the feed spacers they are responsible to enhance the back mixing of the fluid element adjacent to the membrane walls to the bulk of the fluid and thus are responsible to reduce concentration polarization and membrane fouling. Additionally, feed spacers are also responsible for the pressure drop and limited flow zones (dead zones) creation. In other words, they are intended to keep the membranes clean by enhancing mass transfer and disrupting the solute concentration boundary layer. At the same time their presence increases pressure drop and dead zones creation which are not beneficial for the membrane separation process. An optimal spacer design will provide maximum mass transport of the solute, accumulated on the membrane surface during the separation process, away from the membrane surface towards the bulk solution as well as minimum pressure drop to reduce the associated pumping costs.

Chapter 4 of this thesis dealt with the flow dynamics associated with spacer filled narrow channels and provided an insight on the impact of feed spacer filament orientation on flow patterns, pressure drop, power number and wall shear stress. In this chapter the mass transfer effects are also added by including concentration equation to the model. It will be shown later in the chapter that concentration spatial distribution does not solely depend on the shear stress distribution but also depends on the entire flow structure within the feed channel of a SWM. This fact will be explained by comparing the contours of mass transfer coefficient and shear stress along with the flow patterns generated during normal course of operation of a spacer filled narrow channel.

As already described in chapter 4, the geometry of the spacer filled channel is of repeating nature and comprises of a large number of cells. There is a periodic variation in the cross section of such spacer filled channel. Flow entering through

one cell in the feed channel is identical to the flow entering the next adjacent cell in the span wise direction (y-direction in Figure 5.1). Moreover, in the flow direction there is translational periodicity i.e. along the flow direction (x-direction in Figure 5.1) the flow patterns repeat itself after periodic intervals. It has been shown in previous chapter that the entrance effects are eliminated after few filaments (3-4) and the flow becomes fully developed after few filaments in the flow direction. Moreover, if translational periodic boundary conditions are implemented at the two faces perpendicular to the flow direction then we can restrict the computational domain to six bottom and one top filament only. However, in order to eliminate the exit effects sufficient exit length is provided to avoid the interference of the outlet conditions with the recirculation regions after the last bottom filament. Hence, entrance effects are eliminated by considering six bottom filaments and performing all the calculations at the cell between the last two bottom filaments in the flow direction. The exit effects are eliminated by considering sufficient exit length along the flow direction after the last bottom filament. Figure 5.1 shows the schematic of feed channel spacer and selected computational domain. The boundary conditions used are also labelled on the figure.

## 5.1 Geometric parameters of spacers

As detailed in the previous chapter, height of the channel, which refers to the sum of the top and bottom filament diameter or thickness, is used to non-dimensionalize spacer geometric parameters. Channel height ( $h_{ch}$ ) is kept as 1mm for all simulations in this chapter for the sake of convenience. Top and bottom filament diameters are represented as  $d_1$  and  $d_2$  respectively and the mesh length for the top and bottom filaments are represented as  $l_1$  and  $l_2$  respectively. The non-dimensionalized diameters ( $D_1$  and  $D_2$ ) and filament spacing or mesh length ( $L_1$  and  $L_2$ ) are defined for top and bottom filaments by the following equations:

$$D_1 = \frac{d_1}{h_{ch}} , \quad D_2 = \frac{d_2}{h_{ch}} , \quad L_1 = \frac{l_1}{h_{ch}} , \quad L_2 = \frac{l_2}{h_{ch}}$$

In the above expressions the subscripts 1 and 2 are used for top and bottom filaments respectively. In this chapter ladder type spacer arrangement having symmetric filaments ( $D_1 = D_2$ ) are considered.

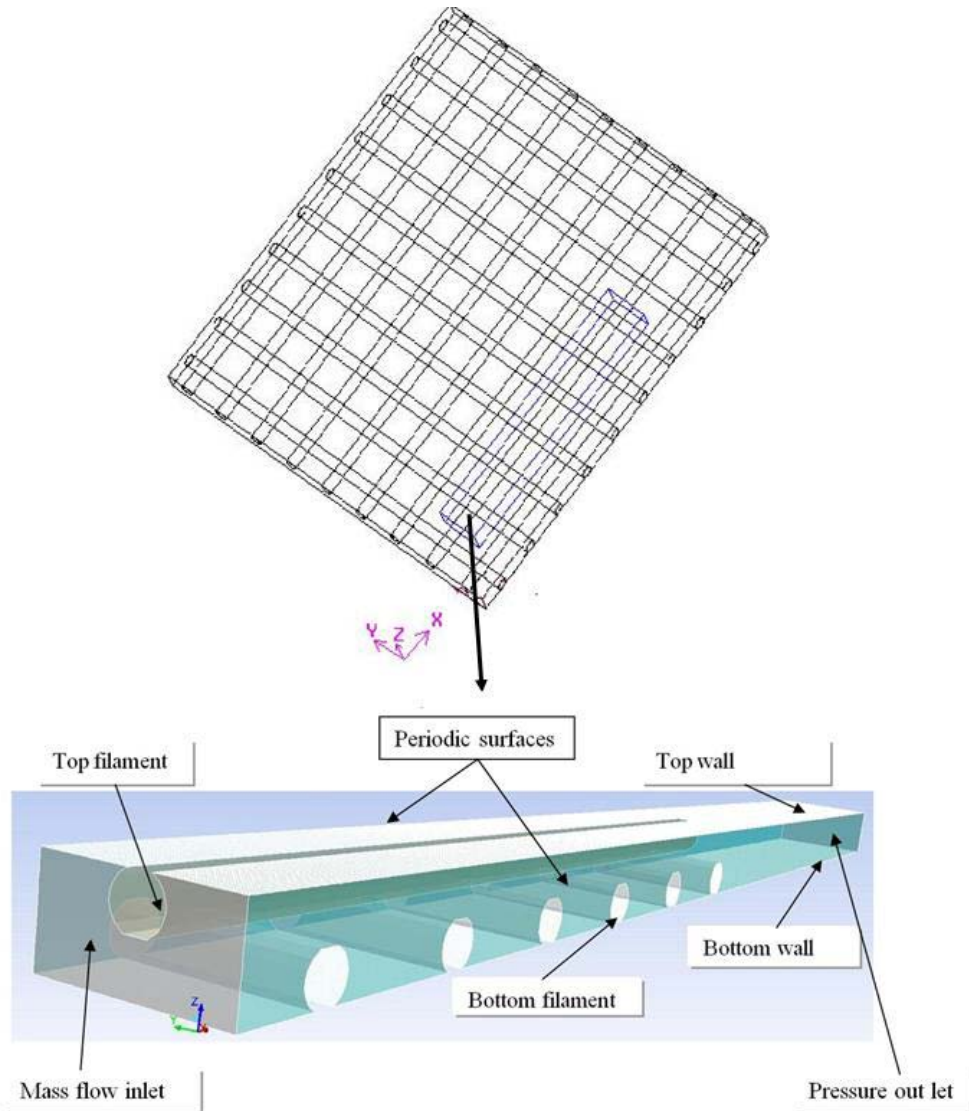


**Figure 5.1: Schematic of feed channel spacer and selected computational domain.**

## 5.2 Hydraulic diameter and porosity of spacer filled channel

The porosity of the feed channel, described in the previous chapter, is defined by the following equation:

$$\varepsilon = 1 - \frac{V_{sp}}{V_T} \quad (5.2 - 1)$$

In the above equation  $V_T$  represents the total volume of the channel,  $V_{sp}$  represents the spacer volume and  $\varepsilon$  represents porosity.

Similarly the general definition of hydraulic diameter, already described in chapter 4 in detail, is used here due to slight change in the geometry to have refined mesh near

the top and bottom membrane walls in order to capture mass transport of the solute away from the membrane walls. The hydraulic diameter is defined by the following equation:

$$d_h = \frac{4(V_T - V_{sp})}{S_{fc} + S_{sp}} \quad (5.2 - 2)$$

In the above equation  $S_{fc}$  represents the wetted surface of the flat channel and  $S_{sp}$  represents wetted surface of the spacer and  $d_h$  represents the hydraulic diameter.

## 5.3 Modelling Procedure

### 5.3.1 Computational domain and boundary conditions

The computational domain comprises of six bottom and one top filament with sufficient exit length provided to avoid the interference of the outlet conditions with the recirculation regions after the last bottom filament. It has been established in chapter 4 that the flow gets fully developed after passing few filaments (3-4) in the flow direction. So the cell between the last two filaments will be a true representative of the flow and concentration patterns generated in a SWM. Moreover it will be shown later in the chapter that the contours of wall shear stress and mass transfer coefficient are identical between the 4<sup>th</sup> & 5<sup>th</sup> and 5<sup>th</sup> & 6<sup>th</sup> filaments.

The computational domain considered for a specific spacer arrangement, having bottom filaments in transverse and top filament in axial direction to the normal flow direction respectively, is shown in Figure 5.1. The flow direction is chosen to be along the x-axis and the spacer thickness (sum of the top and bottom filament diameter) is along the z-axis. The boundary conditions used for the model are shown in Figure 5.1 and are discussed below:

- The two opposite vertical faces perpendicular to the flow direction (x-direction) are defined as Mass flow inlet and pressure outlet. Mass flow rate is specified in flow direction (x-direction) and varied to get the desired hydraulic Reynolds number ( $Re_h$ ). The solute mass fraction is zero at the inlet.

- The working fluid is assumed to be a binary mixture of water and monovalent salt, such as sodium chloride having a mass diffusivity of  $1.54 \times 10^{-9} \text{ m}^2/\text{s}$  [172]. Working fluid is further assumed to be isothermal and incompressible and having constant density ( $998.2 \text{ Kg/m}^3$ ), viscosity ( $0.001 \text{ Kg/(m s)}$ ) and solute diffusivity.
- Translational periodic boundary conditions are defined for the two vertical surfaces parallel to top filaments.
- The filament surfaces are defined as walls.
- Both top and bottom membrane walls or surfaces are assumed to be impermeable walls with no slip conditions assigned to them and have a constant higher value of solute mass fraction than that defined for the inlet condition. In all the simulations the solute mass fraction at the walls were assigned a value of 1, where as the particular mass fraction of the solute is defined as zero at the inlet. Since cross flow filtration processes tend to recover only 10 to 15 % of the feed as product and also have large surface area, therefore large surface area coupled with low recovery rates yields very low permeation velocities compared with feed velocity, hence the assumption of impermeable walls for both top and bottom membrane surfaces of the computational domain is justified [164, 165]. Moreover, although there is an increase in the solute mass fraction at the membrane surfaces in the flow direction as a result of separation process but the due to low permeation rate through the membrane surfaces the variation of local concentration on the membrane walls along the flow direction is negligible and hence top and bottom membrane walls are set to be at higher fixed values of concentration than at the inlet [165]. This assumption of assigning a constant higher mass fraction values to the membrane walls is further justified by comparing the results of the present study with the experimental studies considering wall permeation effects and numerical studies using dissolving wall assumption [20, 128, 135, 164, 165]. It has also been established that the choice of mass fraction values at the membrane surface and at the inlet does not have impact on the mass transfer results obtained, provided they are not set approximately equal. In that case this would lead to numerical round-off error [173].

The hydraulic Reynolds number, which considers effective velocity and hydraulic diameter as characteristic velocity and length respectively, is defined by the following equation:

$$Re_h = \frac{d_h u_{eff}}{\nu} \quad (5.3.1 - 1)$$

In the above equation  $u_{eff}$ ,  $d_h$  and  $\nu$  represents the effective velocity (or average) in the computational domain, hydraulic diameter of the channel and kinematic viscosity respectively. The hydraulic diameter is calculated using equation 5.2-2.

The effective velocity is calculated at a particular hydraulic Reynolds number and then the following equation is used to calculate the mass flow rate ( $m$ ) which is defined as the inlet boundary condition for the computational domain.

$$m = u_{eff} A_{eff} \rho \quad (5.3.1 - 2)$$

In the above equation  $A_{eff}$  and  $\rho$  represents the effective cross-sectional area and density respectively. For a channel filled with spacer having width  $b$  (along  $y$ -direction), channel height  $h_{ch}$  and porosity  $\varepsilon$ ,  $A_{eff}$  is defined by the following equation:

$$A_{eff} = h_{ch} b \varepsilon \quad (5.3.1 - 3)$$

For a specific feed spacer case (SP22) at  $Re_h=100$ , input provided to the CFD code is presented in Appendix-I. Sample calculation to determine mass flow rate for SP22 at  $Re_h=100$  is provided in Appendix-II.

In membrane systems, cost associated with pumping the fluid is one of the most important factors. Power number, which relates resistance force to inertia force, is evaluated to compare the results of the present study with the data available in literature. Earlier Li et al. [135] defined dimensionless power number ( $P_n$ ) to compare energy consumption of different spacer, used later by Skakaib et al. [164] in their study. The same definition is used for the present study and represented by the following equation:-

$$P_n = \text{SPC} \left( \frac{\rho^2 h_{ch}^4}{\mu^3} \right) \quad (5.3.1 - 4)$$

In the above equation SPC is the specific power consumption. Pressure drop cannot be avoided in spacer filled channels and it reduces the overall transmembrane pressure acting on the membrane surface. To compensate for the pressure loss higher pumping energy is required. The term SPC reflects the mechanical power consumption dissipated per unit volume of the flow channel [163]. Degree of SPC in spiral wound membrane channels depends on the spacer configuration and on  $Re_n$ . Specific power consumption (SPC) is given by the following relation

$$\text{SPC} = \frac{u_{eff} \Delta P A}{L_c A_c} = \frac{\Delta P}{L_c} u_{eff} \quad (5.3.1 - 5)$$

In the above expressions,  $L_c$  and  $\Delta P$  are the channel length and pressure drop over the channel respectively, whereas  $u_{eff}$ ,  $\mu$ ,  $\rho$  and  $A_c$  are the effective velocity, dynamic viscosity, density and channel cross-section area respectively.

For spacer filled narrow channels Sherwood number using the hydraulic diameter of the channel is defined by the following equation:

$$Sh = \frac{k_{av} d_h}{D} \quad (5.3.1 - 6)$$

Efficacy of spacer configuration is evaluated by the ratio between the Sherwood number and Power number. Higher value of the ratio means that the particular spacer configuration tend to promote the mass transport of the solute away from the membrane wall into the bulk of the solution at moderate energy loss. Spacer Configuration Efficacy (SCE) is defined by the following ratio:

$$SCE = \frac{Sh}{Pn} \quad (5.3.1 - 7)$$

To validate the present model friction factor values for some spacers are calculated by equation 5.3.1-8 and compared with those presented by Gerald et al. [20]. Following equation is employed for the calculation of friction factor[20]:

$$f = \frac{\Delta P}{L_c} \frac{h_{ch}}{\rho u_{eff}^2} \quad (5.3.1 - 8)$$

Da Costa et al. [128] in their research work showed that Grober equation predicts Sherwood number for spacer filled narrow channels within  $\pm 30\%$  error. For the spacers, having filament oriented along axial and transverse direction to the fluid flow, Grober equation is presented as [128]:

$$Sh_{Grober} = 0.664 Re_h^{0.5} Sc^{0.33} \left[ \frac{d_h}{l} \right]^{0.5} \quad (5.3.1 - 9)$$

For the validation of the current model, computationally determined Sherwood number (obtained from equation 5.3.1-6) for different spacer arrangements are also compared with those obtained from equation 5.3.1-9. In the above equation  $Sc$  is Schmidt number defined as the ratio of momentum and mass diffusivity ( $Sc = \nu/D$ ).

### 5.3.2 Grid refinement and independence

The computational domain was constructed and meshed in geometry construction and grid generation pre-processor software Gambit<sup>®</sup>. The grid generated consisted of a number of finite hexahedral volumes. The number of cells used were enough to cater the steep velocity gradients near the filament walls and the mesh was refined near the membrane walls to cater for the very steep concentration gradients in that area. For example in case of spacer SP22, having  $L_1=L_2=2$  and  $D_1=D_2=0.5$  with bottom filaments transverse to the flow direction and the top filament axial to the flow direction, it was concluded by a comprehensive successive grid refinement study that approximately 717,000 cells were adequate to have mass transfer coefficient results independent of the grid density at  $Re_h=100$ . The following figures (Figure 5.2-5.4) show the top wall shear stress, pressure drop and mass transfer coefficient verses number of meshed cells. Considering only the wall shear stress and pressure drop results variation with an increase in number of meshed cells, it can be seen from the Figure 5.2 and Figure 5.3 that a grid size of 311,850 is sufficient for the study. On the contrary, if the variation of mass transfer coefficient is also taken into account then this grid size appears to be insufficient for a grid independent solution as evident from Figure 5.4. This can be attributed to the steep concentration gradients in the vicinity of the membrane walls.

It can be seen from Figure 5.2- 5.4 that the change in average shear stress values on the top wall, pressure drop and mass transfer coefficient is around 0.07%, 0.05% and 3.9% respectively when the number of cells is increased from 716,880 to 878,976. Considering the degree of accuracy of the results needed, computational time required and available computational capabilities a grid size of 716,880 was chosen as an adequate grid size for that specific spacer arrangement. Similarly adequate grid sizes for different spacer arrangements were determined to ensure that the reported numerical values for different parameters in this thesis do not vary significantly with further grid density enhancement. For instance approximately 1.4 and 6 Million cells were found sufficient for spacers SP33 and SP66 respectively.

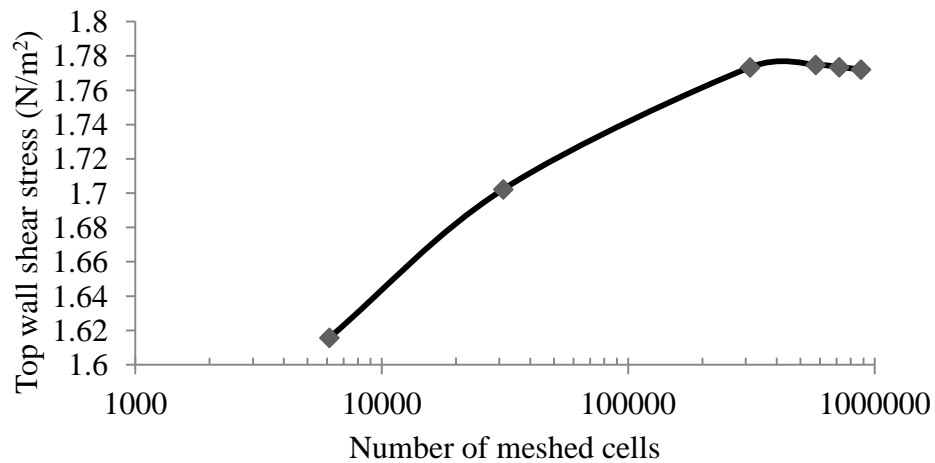


Figure 5.2: Top wall shear stress vs number of meshed cells for SP22 at  $Re_h=100$ .

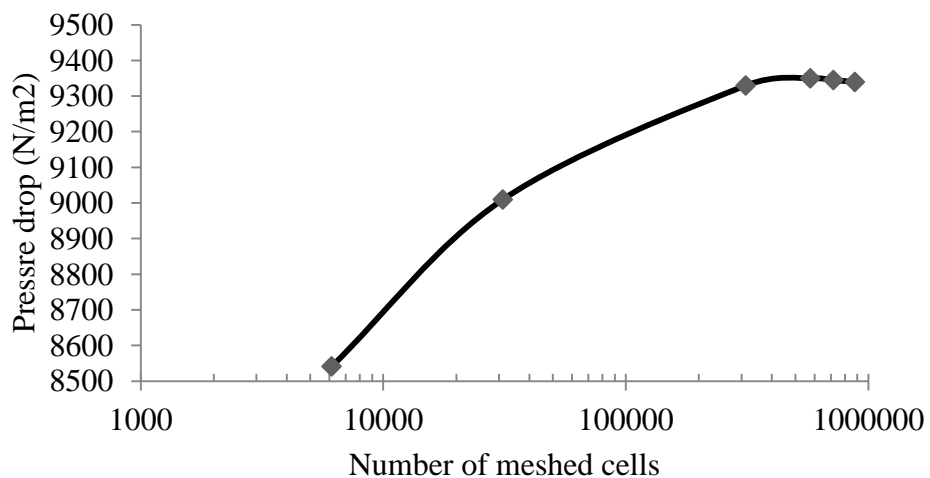


Figure 5.3: Pressure drop vs number of meshed cells for SP22 at  $Re_h=100$ .

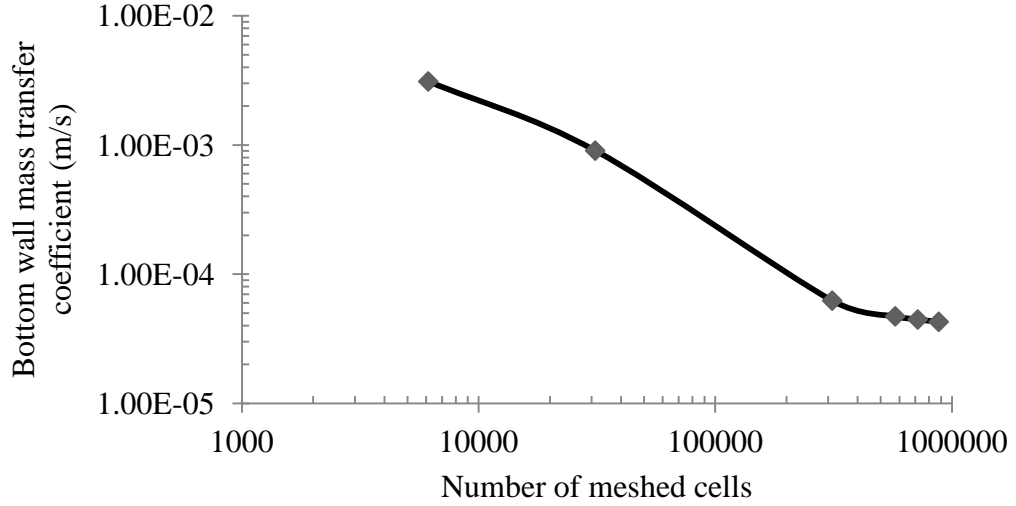


Figure 5.4: Mass transfer coefficient vs number of meshed cells for SP22 at  $Re_h=100$ .

### 5.3.3 Governing equations, solution methods & controls

Continuity, three momentum equations (x, y and z momentum) and concentration equations are the five governing equations (Navier-Stokes equations) which are represented below for steady, laminar and incompressible flow in three-dimensional form [55, 165] and are discussed in chapter 3 of this thesis:

$$\frac{\partial u}{\partial x} + \frac{\partial v}{\partial y} + \frac{\partial w}{\partial z} = 0 \quad (5.3.3 - 1)$$

$$u \frac{\partial u}{\partial x} + v \frac{\partial u}{\partial y} + w \frac{\partial u}{\partial z} = -\frac{1}{\rho} \frac{\partial P}{\partial x} + \nu \left[ \frac{\partial^2 u}{\partial x^2} + \frac{\partial^2 u}{\partial y^2} + \frac{\partial^2 u}{\partial z^2} \right] \quad (5.3.3 - 2)$$

$$u \frac{\partial v}{\partial x} + v \frac{\partial v}{\partial y} + w \frac{\partial v}{\partial z} = -\frac{1}{\rho} \frac{\partial P}{\partial y} + \nu \left[ \frac{\partial^2 v}{\partial x^2} + \frac{\partial^2 v}{\partial y^2} + \frac{\partial^2 v}{\partial z^2} \right] \quad (5.3.3 - 3)$$

$$u \frac{\partial w}{\partial x} + v \frac{\partial w}{\partial y} + w \frac{\partial w}{\partial z} = -\frac{1}{\rho} \frac{\partial P}{\partial z} + \nu \left[ \frac{\partial^2 w}{\partial x^2} + \frac{\partial^2 w}{\partial y^2} + \frac{\partial^2 w}{\partial z^2} \right] \quad (5.3.3 - 4)$$

$$u \frac{\partial Y}{\partial x} + v \frac{\partial Y}{\partial y} + w \frac{\partial Y}{\partial z} = D \left[ \frac{\partial^2 Y}{\partial x^2} + \frac{\partial^2 Y}{\partial y^2} + \frac{\partial^2 Y}{\partial z^2} \right] \quad (5.3.3 - 5)$$

ANSYS FLUENT is used to solve the governing equations and pressure based segregated solver was employed for the solution like in chapter 4 of this thesis. QUICK (Quadratic Upstream Interpolation for convective Kinetics) scheme is used for discretising momentum equations, whereas SIMPLEC (Semi-Implicit Method for

Pressure linked Equations, Consistent) algorithm is used for pressure velocity coupling [35, 165, 167]. For solution control values of 0.3 and 0.7 were set respectively as under-relaxation factors for pressure and momentum. The details of QUICK scheme and SIMPLEC algorithm are discussed already in chapter 4 of this thesis. However for the discretization of concentration equation power law scheme is employed.

Power law difference scheme yields very accurate results for one dimensional problems because it attempts to generate the exact solution more closely [35]. The face value of a variable is interpolated using exact solution to a one dimensional convection-diffusion equation [167]. In this scheme when the Peclet number (Pe) exceeds 10 the diffusion is set to zero. However, for Pe greater than zero and less than 10, the flux is calculated by using a polynomial expression. For instance, following expression is used to evaluate net flux per unit area at the west control volume face ( $q_w$ ) [35]:

$$q_w = F_w [\phi_w - \beta_w(\phi_p - \phi_w)] \quad \text{for } 0 < Pe < 10 \quad (5.3.3 - 6)$$

$$q_w = F_w \phi_w \quad \text{for } Pe > 10 \quad (5.3.3 - 7)$$

Where  $\beta_w$  in equation 5.3.3-6 is defined as [35]:

$$\beta_w = (1 - 0.1Pe_w)^5 / Pe_w \quad (5.3.3 - 8)$$

In the above expressions  $F_w$ ,  $\phi_p$  and  $\phi_w$  represents convective flux at west face, value of a property at a particular computational cell and value of a property at the west of that particular computational cell respectively. Peclet number  $Pe$ , being a ratio of convective ( $\rho u$ ) and diffusive ( $\Gamma/\delta x$ ) fluxes, is defined by the following expression for the west face of the computational cell [35]:

$$Pe_w = \frac{(\rho u)_w}{\Gamma_w / \delta x_{wp}} \quad (5.3.3 - 9)$$

The convergence criterion for the scaled residuals of continuity, x, y and z components of velocity and solute mass fraction were set at 1e-06. Moreover the convergence was further confirmed by stable values of velocity and solute mass fraction at different monitoring points defined in the computational domain. Figure

5.5 represents the monitoring of the residuals for continuity, components of velocity and solute mass fraction versus number of iteration for SP22 at  $Re_h=100$ . Figure 5.6 represents the monitoring points (MP1 & MP2) selected within the specific area of interest in the computational domain. Figure 5.7 (a & b) represents velocity and solute mass fraction at MP1 and MP2 respectively versus number of iterations.

It can be seen from Figure 5.5 and Figure 5.7 that the convergence of the solution was insured by selecting the residuals of continuity, velocity components and solute mass fraction to a very smaller value. It was also ensured that the numerical values of velocity magnitude and mass fraction are also stabilized at defined monitoring points in the computational domain in the area of interest (between the last two bottom filaments in the flow direction).

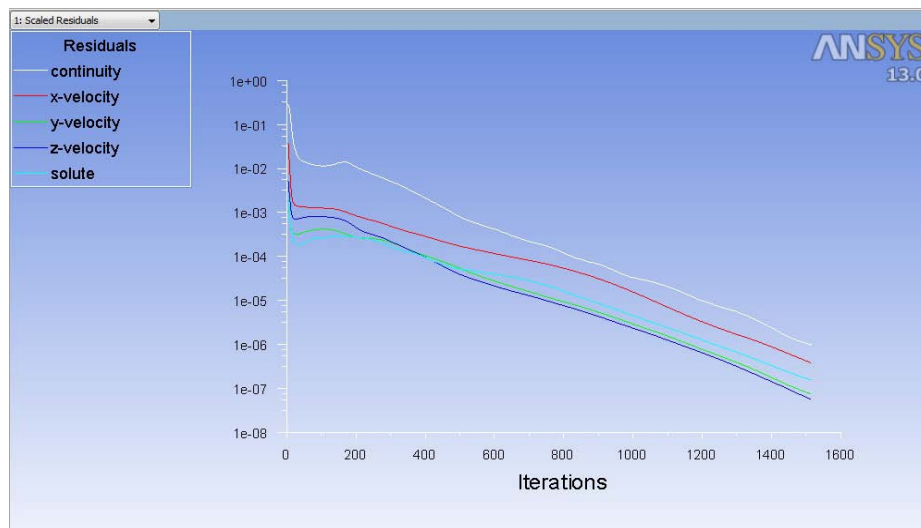


**Figure 5.5: Residuals of continuity, velocity components and solute mass fraction.**

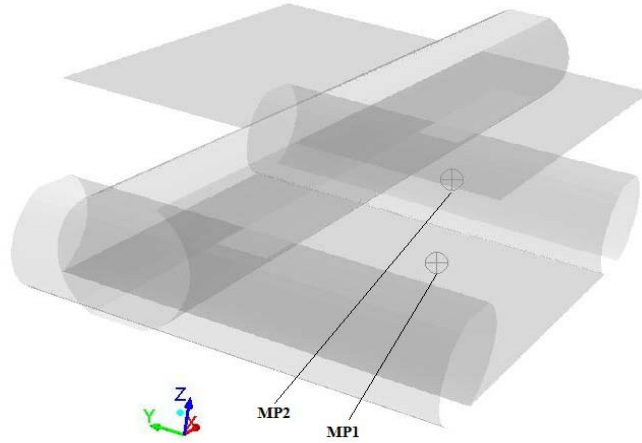


**Figure 5.6: Monitoring points (MP1 & MP2) in computational domain.**

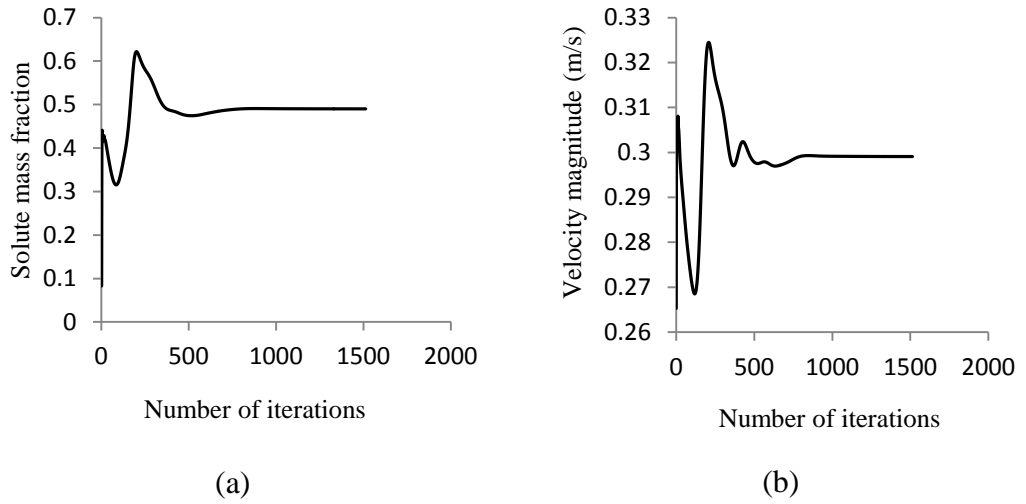


**Figure 5.7: Number of iterations vs (a) solute mass fraction at MP2 (b) velocity magnitude at MP1.**

### 5.3.4 Incorporation of mass transfer coefficient in the model

Mass transfer coefficient correlates concentration difference, contact area and mass transfer rate as explained in detail in section 2.4.8 of this thesis. In case of spacer filled narrow channels having impermeable membrane walls, the local and average mass transfer coefficients can be defined respectively by the following equations [32, 165, 174]:

$$k_l = \frac{D}{Y_w - Y_b} \left[ \frac{\partial Y}{\partial z} \right]_w \quad (5.3.4 - 1)$$

$$k_{av} = \frac{1}{A} \sum_{i=1}^n k_l A_i \quad (5.3.4 - 2)$$

In the above equations  $k_l, k_{av}$  are the local and average mass transfer coefficients. The terms  $Y_w, Y_b$  and  $\left[\frac{\partial Y}{\partial z}\right]_w$  represents mass fraction of the solute at the membrane wall, mass fraction of solute in the bulk and gradient of mass fraction at the membrane wall respectively. The terms  $A$  and  $A_i$  represents the membrane surface area and face area of any computational cell respectively. The above mentioned pair of equations is used often by researchers, simulating mass transport of solute for impermeable membrane walls scenarios, for CFD simulations [32, 165, 174]. However, to incorporate the mass transport equations in the model there is a need to write down a program in C language which is commonly referred to as the User Defined Function (UDF).

#### **5.3.4.1 Details of the User Defined Function (UDF)**

ANSYS FLUENT does not have the facility to calculate mass transfer coefficient by default. To enable this purpose a user defined function (UDF) was written in C language and was later hooked with ANSYS FLUENT to calculate the bulk mass fraction of the solute and mass transfer coefficient. The detail of the UDF is presented in Appendix- III.

The main objective behind the UDF is to calculate local mass transfer coefficient based on equation 5.3.4-1. The mass diffusivity and solute mass fraction at the membrane wall was defined in the model setup and were kept constant, so we need to have solute mass fraction in the bulk and gradient of solute mass fraction along the channel height (in Z direction). For this purpose total mass of solute and water was calculated by adding the respective values for all the cells and later used to calculate the bulk mass fraction of the solute. ANSYS FLUENT does not provide the facility to calculate the gradient of a variable by default, but at the same time it provides the flexibility to calculate the gradient of a scalar using a macro. The value of solute mass fraction was stored in a scalar and its differential along the Z direction was obtained by using this macro, and stored in user defined memory (UDMI 1). At

this stage we have all the values of the variables present in equation 5.3.4-1 to calculate local mass transfer coefficient. So  $k_1$  values for each cell is stored in a user defined memory (UDMI 2) to make it accessible during post processing.

During post processing mass transfer coefficient values at the membrane walls are obtained by taking the area weighted average of local mass transfer coefficients calculated at the wall. These local mass transfer coefficients use the values of gradient (of mass fraction) for each cell taken at the wall i.e  $(\partial Y/\partial z)_w$ .

Figure 5.8 represents the logic followed by the UDF written to calculate mass transfer coefficient at the top and bottom membrane walls.

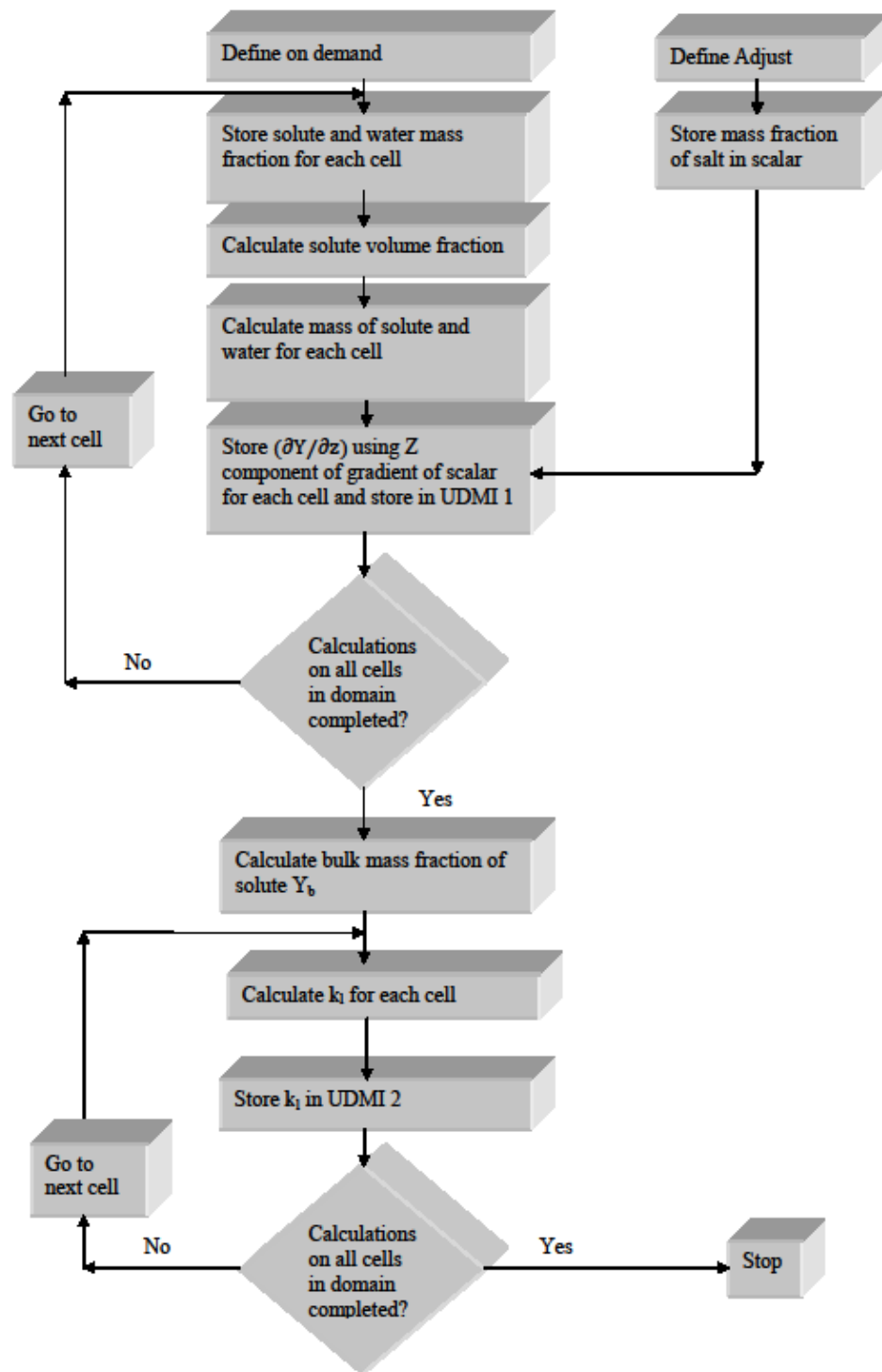
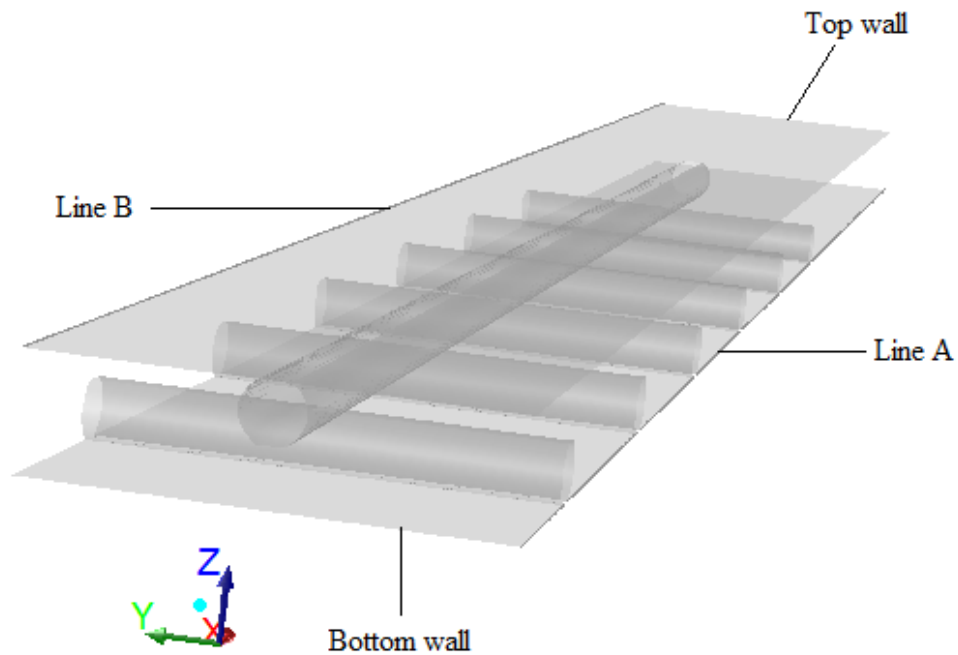


Figure 5.8: Logic behind the User Defined Function (UDF).

## 5.4 Part of the computational domain representing the SWM module

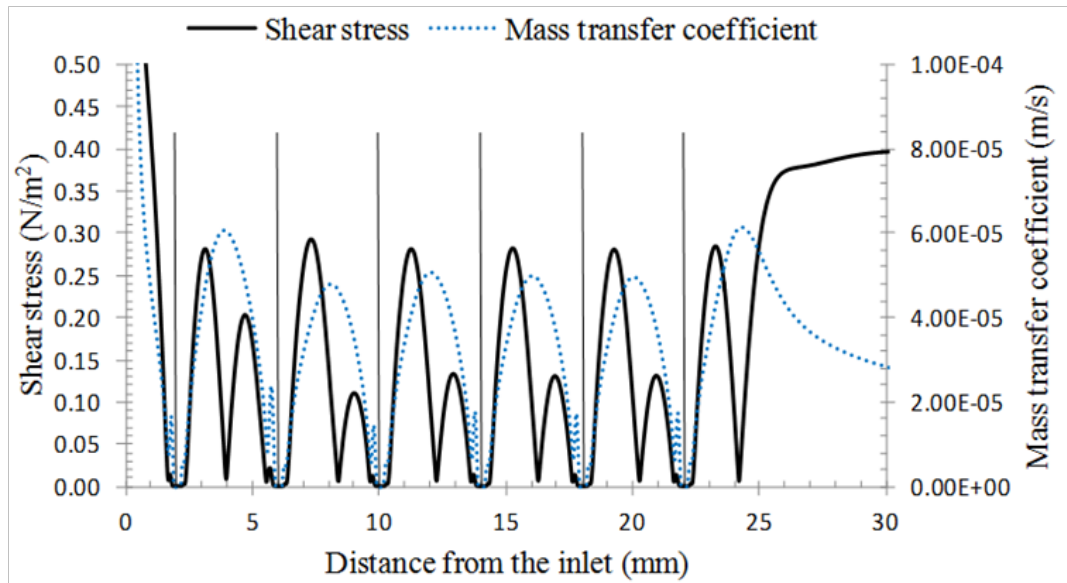
As described in the earlier sections the computational domain for all spacer arrangements consist of six bottom and one top filament to provide sufficient entrance region to make sure that the flow and the concentration patterns are stabilized within the computational domain before exit. Moreover, sufficient exit length is incorporated in the computational domain to eliminate any exit effects that could impact the upstream flow and concentration patterns.

In order to investigate which part of the flow domain is true representative of the whole Spiral Wound Membrane module, top and bottom wall shear stresses and mass transfer coefficients are plotted along flow direction on bottom and top membrane walls (along line A and B respectively) as shown in Figure 5.9.



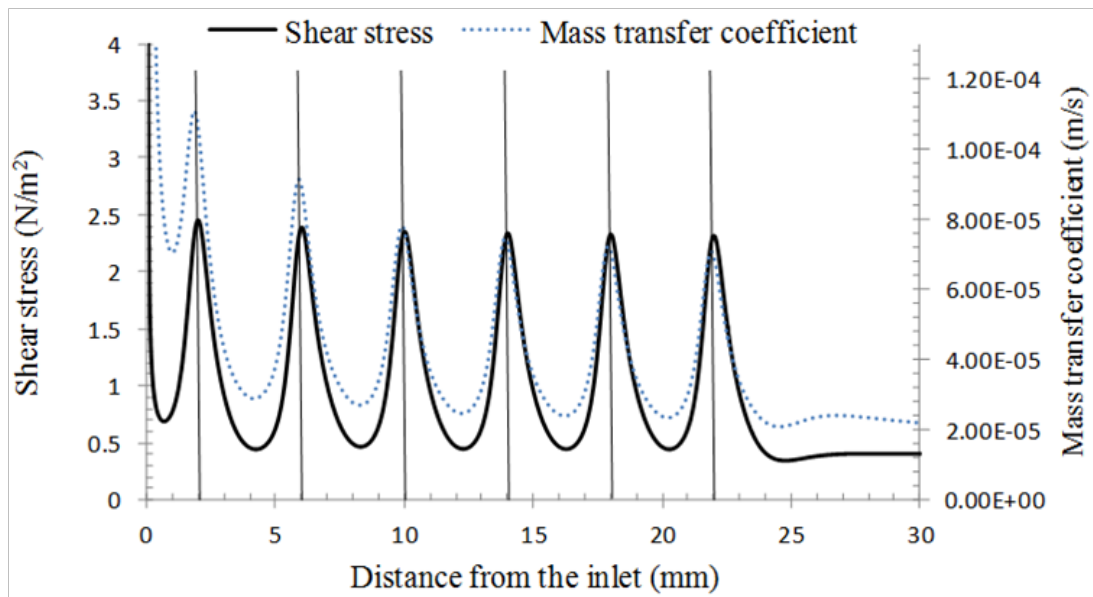
**Figure 5.9:** Total computational domain with Lines A & B on bottom and top wall respectively.

Variation in local values of mass transfer coefficient and shear stress at bottom and top membrane walls along lines A & B are shown in Figure 5.10 and Figure 5.11 respectively.



(Note: Vertical lines indicate the centre line of bottom filaments)

**Figure 5.10: Shear stress and Mass transfer coefficient distribution on bottom wall for SP44 at  $Re_h=100$ .**



(Note: Vertical lines indicate the centre line of bottom filaments)

**Figure 5.11: Shear stress and Mass transfer coefficient distribution on top wall for SP44 at  $Re_h=100$ .**

It can be seen from the Figure 5.10 and Figure 5.11 that the shear stress variation along the flow direction is not identical in the entrance region (first two filaments). However at the third and fourth bottom filament those variations appear to become identical ensuring that the flow has been fully developed and periodic at the third bottom filament. The plot for mass transfer coefficient for the two walls starts with a

very high value for mass transfer coefficient at the inlet due to larger concentration difference between the entering fluid and membrane walls. For the first two filaments the local variations for mass transfer coefficient is also not identical but somewhere near the third bottom filament the local values for mass transfer coefficient tend to get stabilised and repeat in a periodic manner along the flow direction. The trends showing the local variation of mass transfer coefficient and wall shear stress along the flow direction for both the walls are found similar to earlier two dimensional [136, 145, 147] and three dimensional CFD studies [165].

In real life, there are thousands of filaments present at the feed side channel of a spiral wound membrane module and the first two filaments of the selected computational domain cannot be the true representative for an entire real life membrane module assembly. Similarly, the region between the last bottom filament and the exit do not represent the actual mass transfer and shear stress variations in the major portion of a spiral wound module. However, in the region between 5<sup>th</sup> and 6<sup>th</sup> bottom filament the flow and concentration patterns are fully developed and are identical to the patterns developed in the region between 4<sup>th</sup> and 5<sup>th</sup> bottom filament. Hence, it can be concluded that the region between the 5<sup>th</sup> and 6<sup>th</sup> bottom filament may be selected as true representative of the flow and concentration patterns prevailing in the major portion of a real life spiral wound membrane module. Selection of this region is further strengthened by comparing the contours of mass transfer coefficient and wall shear stress for the region between 4<sup>th</sup> & 5<sup>th</sup> and 5<sup>th</sup> and 6<sup>th</sup> bottom filament.

In the following figures (Figure 5.12 to Figure 5.15) mass transfer coefficient and wall shear stress contours for the selected region (between 5<sup>th</sup> and 6<sup>th</sup> bottom filament) and adjacent region (between 4<sup>th</sup> and 5<sup>th</sup> bottom filament) are presented for only few spacer arrangements considered. These contours for the stated regions are also identical for all the spacers considered in the thesis.

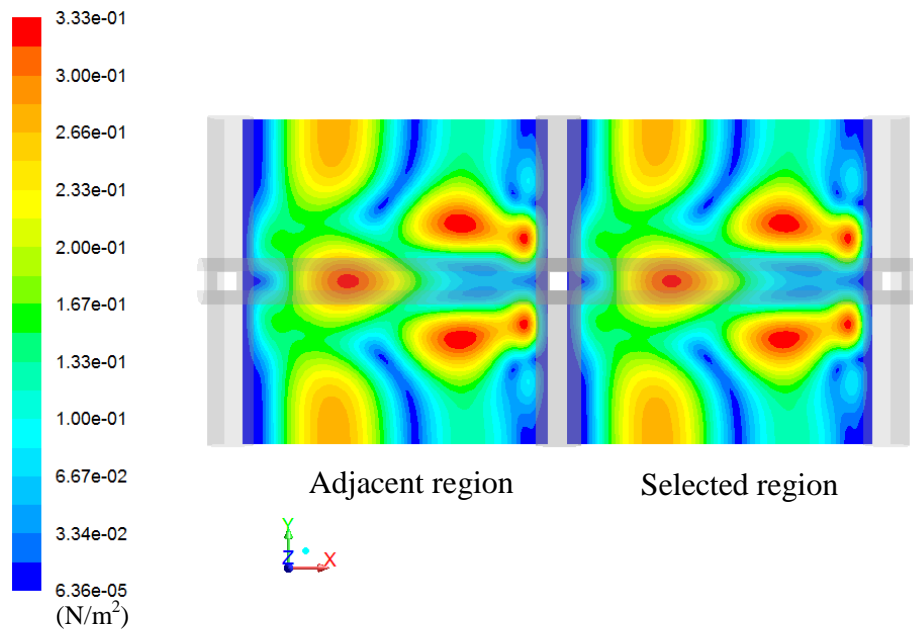


**Figure 5.12: Contours of bottom wall shear stress for SP44 at  $Re_h=100$  between the selected and adjacent region of the computational domain.**

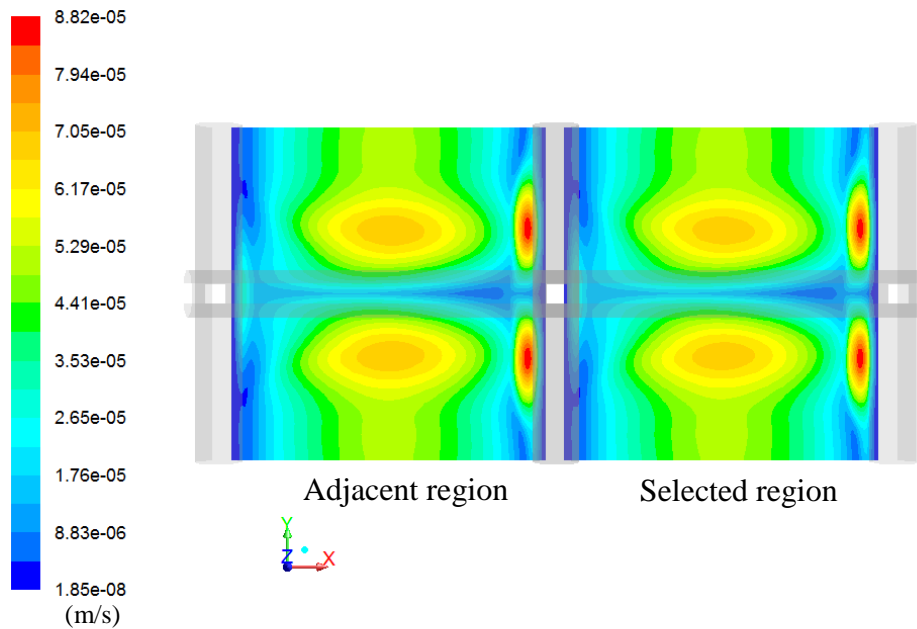
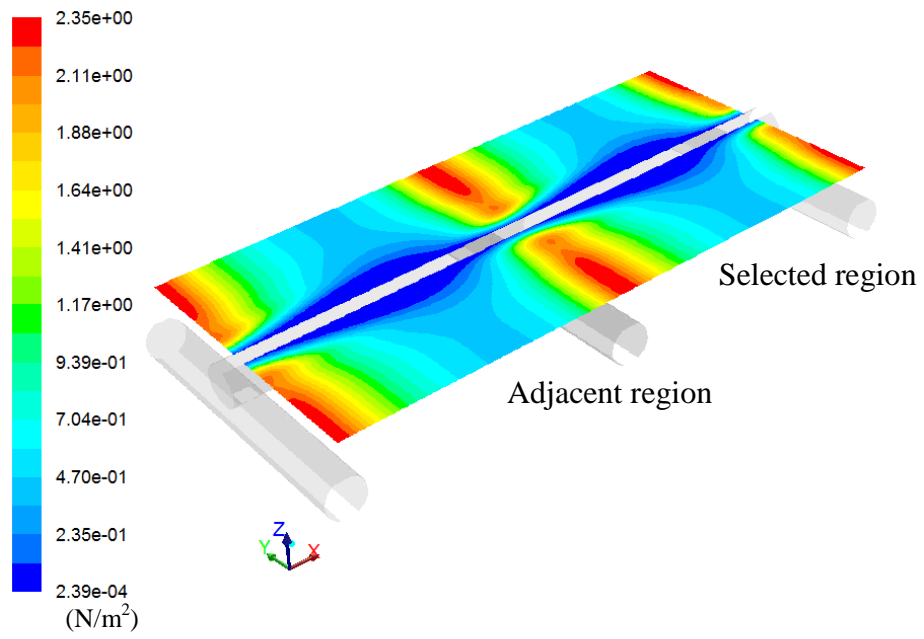
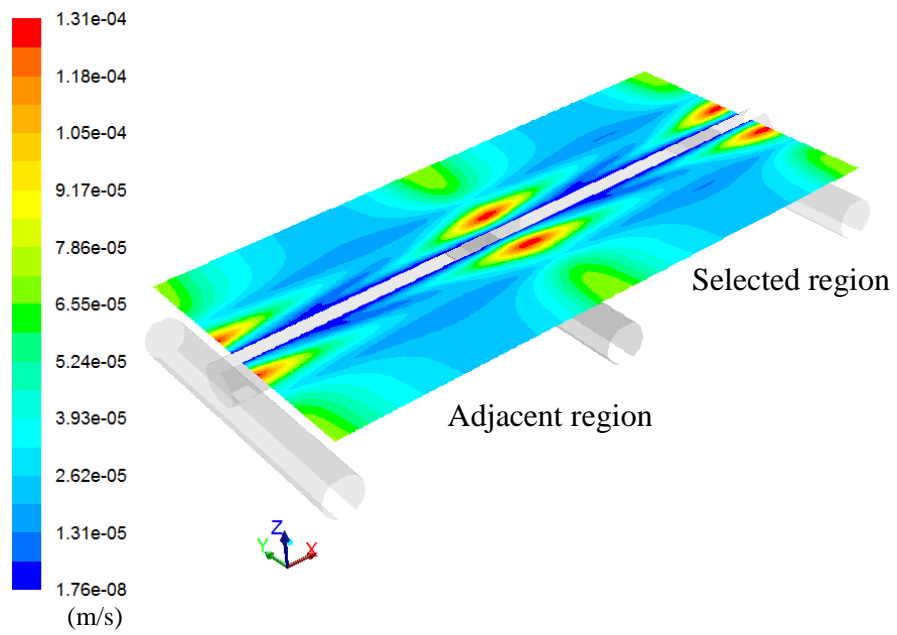


**Figure 5.13: Contours of mass transfer coefficient at bottom wall for SP44 at  $Re_h=100$  between the selected and adjacent region of the computational domain.**



(a)



(b)

**Figure 5.14: Contours of (a) top wall shear stress (b) mass transfer coefficient at top wall for SP44 at  $Re_n=100$  between the selected and adjacent region of the computational domain.**

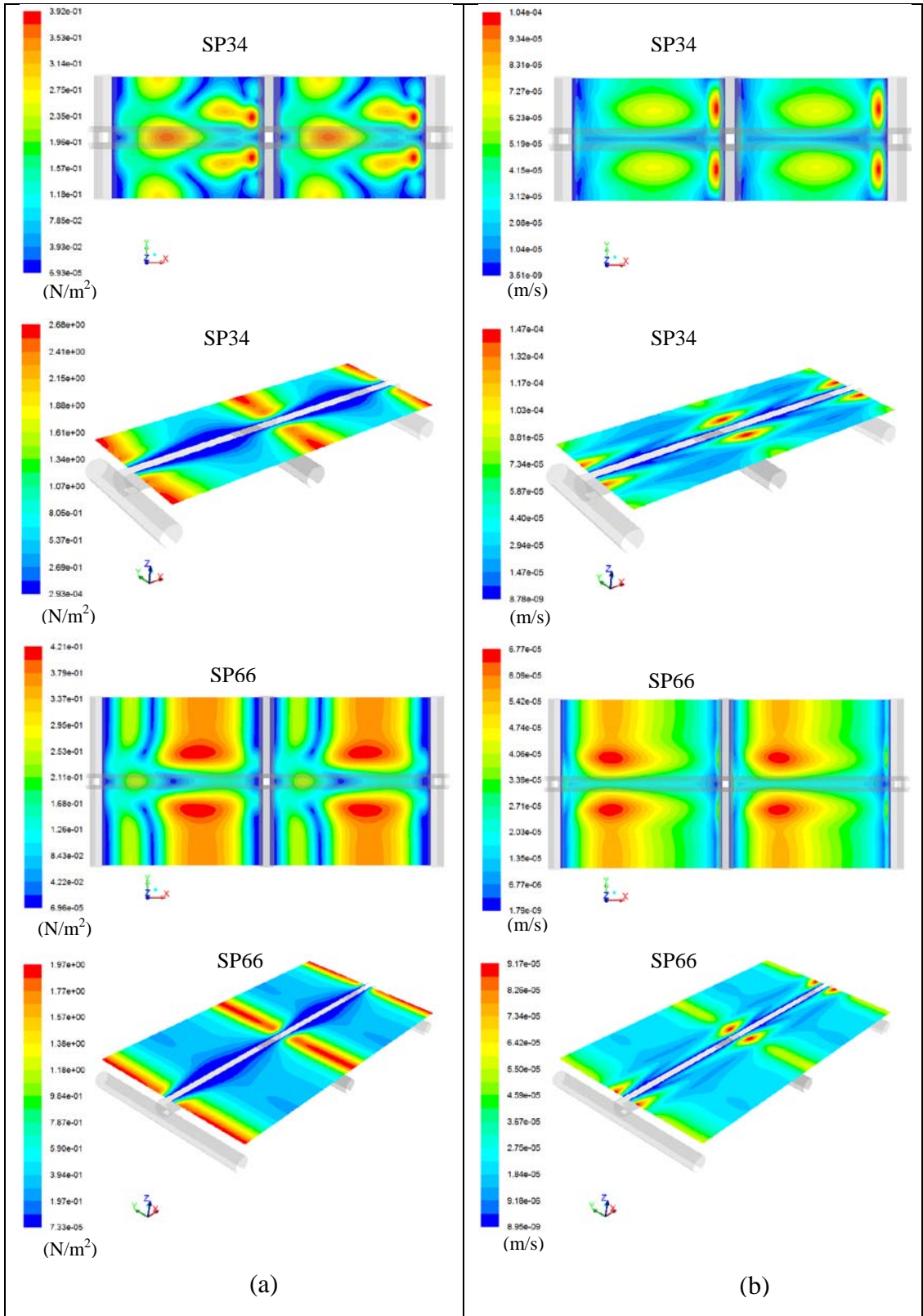


**Figure 5.15: Contours of (a) wall shear stress and (b) mass transfer coefficient for different spacers at  $Re_h=100$  between the selected and adjacent region of the computational domain.**

From the figures (Figure 5.10 to Figure 5.15) it can be concluded that the contours of mass transfer coefficient and wall shear stress are identical for the selected region

(between 5<sup>th</sup> and 6<sup>th</sup> bottom filament) and the adjacent region (between 4<sup>th</sup> and 5<sup>th</sup> bottom filament) for different spacers. Based on the above discussion we can safely say that the region between the last two filaments (in the flow direction i.e. between 5<sup>th</sup> and 6<sup>th</sup> filament) may be taken as a true representative for the flow and concentration patterns generated in major portion of a spiral wound membrane module. In this thesis all the reported values and comparisons are made based on numerical values and trends for the selected portion of the computational domain.

## 5.5 Discussion on results for Spacer SP44

In case of spacer filled membrane modules there are two important factors that have a direct impact on the wall shear stress and mass transport pattern developed in the module:

- There is a reduction in cross sectional flow area due to the presence of bottom (transverse) filament and the fluid tends to accelerate when crossing over the bottom filament. This phenomenon induces a nozzle like effect which results in higher local wall shear stress and mass transfer coefficient values at the top membrane wall directly above the bottom filaments. This fact is quite evident in Figure 5.11, Figure 5.14 and Figure 5.15.
- Fluid after passing over the bottom filament tends to reattach, somewhere in the middle of the two consecutive bottom filaments, with the bottom membrane surface and further undergoes flow reversal and recirculation. This recirculation induces a scouring action on major portion of the bottom membrane and hence results in higher values of mass transfer coefficient for major part of the bottom membrane. However, there are also some stagnant fluid regions very close to the bottom filaments in the vicinity of the bottom membrane which results in lower values of local wall shear stress and mass transfer coefficient. These facts are evident from Figure 5.10, Figure 5.12 and Figure 5.13. The flow recirculation in the vicinity of bottom membrane is captured in Figure 5.16 which represent contours of solute mass fraction and contours of velocity magnitude overlaid by the velocity vectors (fixed length) at different vertical planes for SP44 at  $Re_h=100$ .

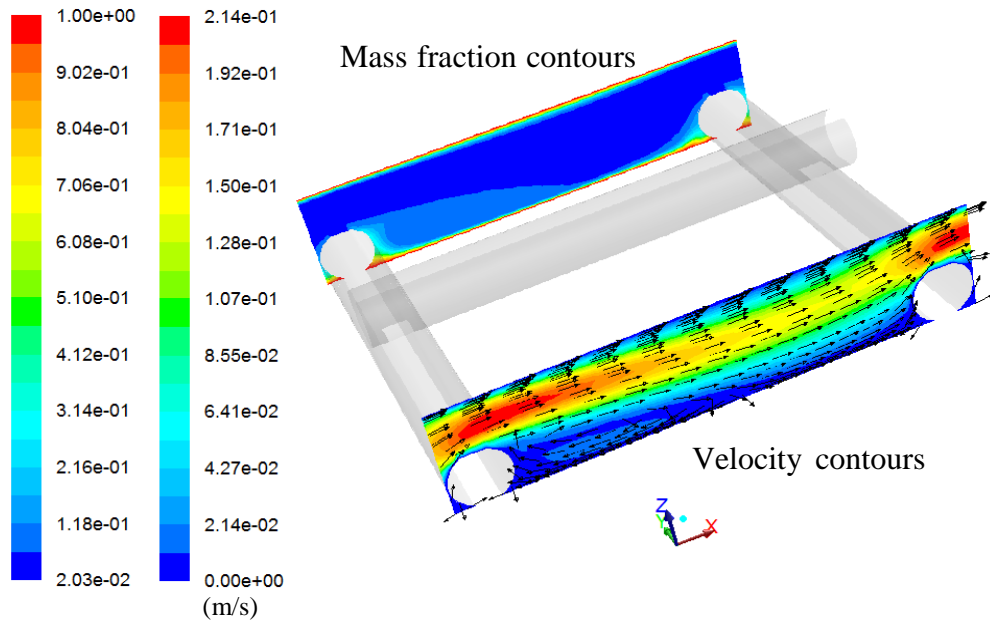


**Figure 5.16: Contours of solute mass fraction and contours of velocity magnitude overlaid by the velocity vectors (fixed length) at different vertical planes for SP44 at  $Re_h=100$ .**

### 5.5.1 Top membrane surface

Since the shear stress distribution at a surface depends on the velocity field in the vicinity of that surface therefore in order to have an insight into the shear stress and mass transfer coefficient distribution on the top membrane surface, velocity vectors (fixed length) coloured by velocity magnitude are shown on a plane in the proximity of the top membrane surface (at  $z = 0.95\text{mm}$ ) in Figure 5.17.

Due to the presence of bottom transverse filament the area available for flow (just above the bottom filaments) is reduced resulting in acceleration of the fluid in that particular region which eventually leads to higher wall shear stress at the top membrane surface just above the bottom filament location. Moreover, in the vicinity of the top membrane surface, somewhere midway between two consecutive bottom filaments the flow tends to deviate from the normal flow direction (x-direction) and undergoes directional changes. Flow separates from the top filament and also reverses its direction. Close to the intersection of top and bottom filament the flow tends to reattach itself to the top filament. These two distinct regions (separation and reattachment) are shown in the Figure 5.17.

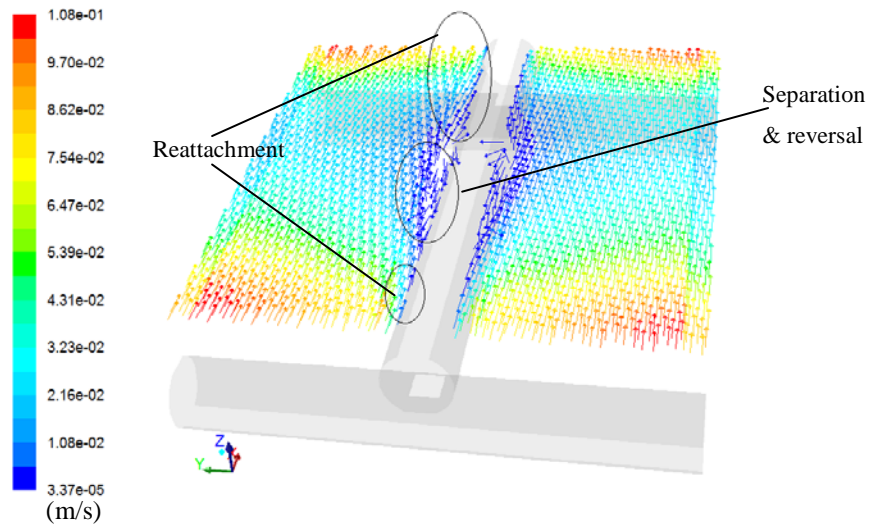


**Figure 5.17: Velocity vectors coloured by velocity magnitude (fixed length) at a plane very close to top membrane ( $Z=0.95\text{mm}$ ) for SP44 at  $Re_h=100$ .**

To have a further insight into the shear stress and mass transfer coefficient patterns generated at the top membrane surface a few virtual lines were drawn on the top membrane surface and the mass transfer coefficient along with the shear stress distribution is shown in Figure 5.18. Figure 5.18 (a) represents the selected portion of the computation domain which is a true representative of the whole SWM (between 5<sup>th</sup> and 6<sup>th</sup> bottom filament). The virtual lines b, c and d are drawn along the normal flow direction at specific distances from the top filament. Whereas, the virtual line e is drawn in y direction midway between the two transverse filaments. Figure 5.18 (b-e) shows the mass transfer coefficient and shear stress distribution on top membrane surface along lines b-e respectively.

It is quite clear from the shear stress and mass transfer coefficient distributions for Figure 5.18 (b-d) that the local values of mass transfer coefficient are higher in the region where the wall shear stress values are higher and vice versa. In Figure 5.18 (e) the variation of shear stress and mass transfer coefficient is shown in y direction. It can be seen that for the major portion of the top membrane surface, local mass transfer coefficient and wall shear stress values show the same trend. At the surface of the top filament the fluid velocity and hence the shear stress is zero which results in the minimum value for the mass transfer coefficient. In the region adjacent to the top filament where the flow is reversed the mass transfer coefficients shows the first peak despite the low local values of velocities and hence shear stress. The second

peak for the mass transfer coefficient on the figure is observed due to the higher local velocities in that region which also results in higher local shear stress.

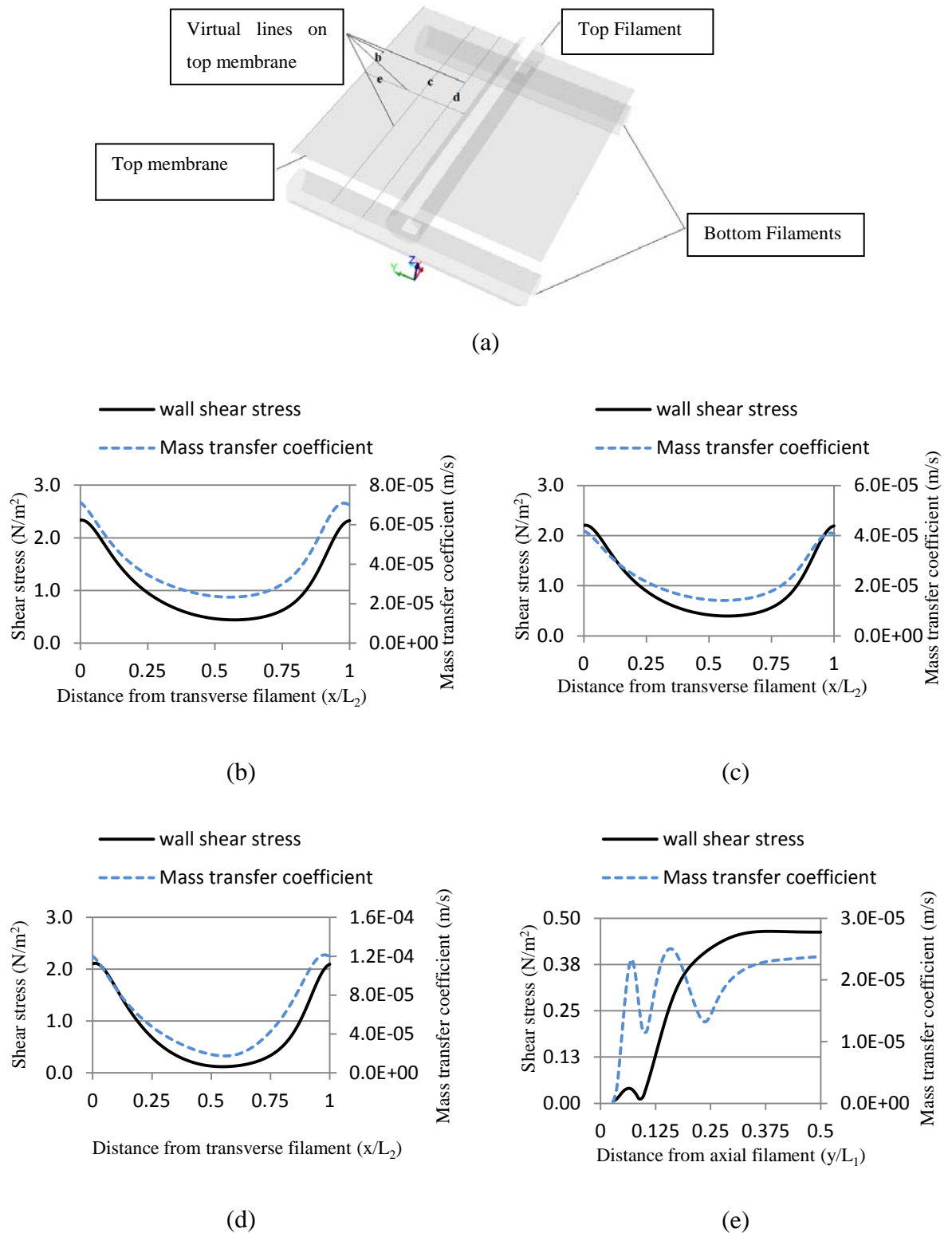


**Figure 5.18: (a) Selected computational domain with virtual lines on top membrane wall. (b-e) Mass transfer coefficient and shear stress distribution on top wall along virtual lines b-e respectively for SP44 at  $Re_h=100$ .**

## 5.5.2 Bottom membrane surface

In order to have an insight of the flow pattern generated in the vicinity of the bottom wall the velocity vectors at a plane close to the bottom wall (at  $Z=0.05$  mm) are shown in Figure 5.19. Two distinct flow regions are evident in the following figure. The regions termed as “Reattachment” shows the area where the flow reattaches its self to the plane. Flow recirculation is evident to the left hand side of this region. Whereas the flow proceeds in the normal flow direction downstream that region. Another region termed as “Separation” is shown in the figure where the fluid tends to detach itself from the plane due to presence of transverse filament. The flow separation region can be seen near both the upstream and downstream transverse filament. In both the regions the fluid velocity is minimum which results in lower values for wall shear stress and fluid undergo directional changes enhancing the mass transfer coefficient. Comparing Figure 5.17 and Figure 5.19 it can be seen that the fluid flow in the vicinity of bottom membrane surface is quite complex compared to the flow in the vicinity of the top membrane wall.

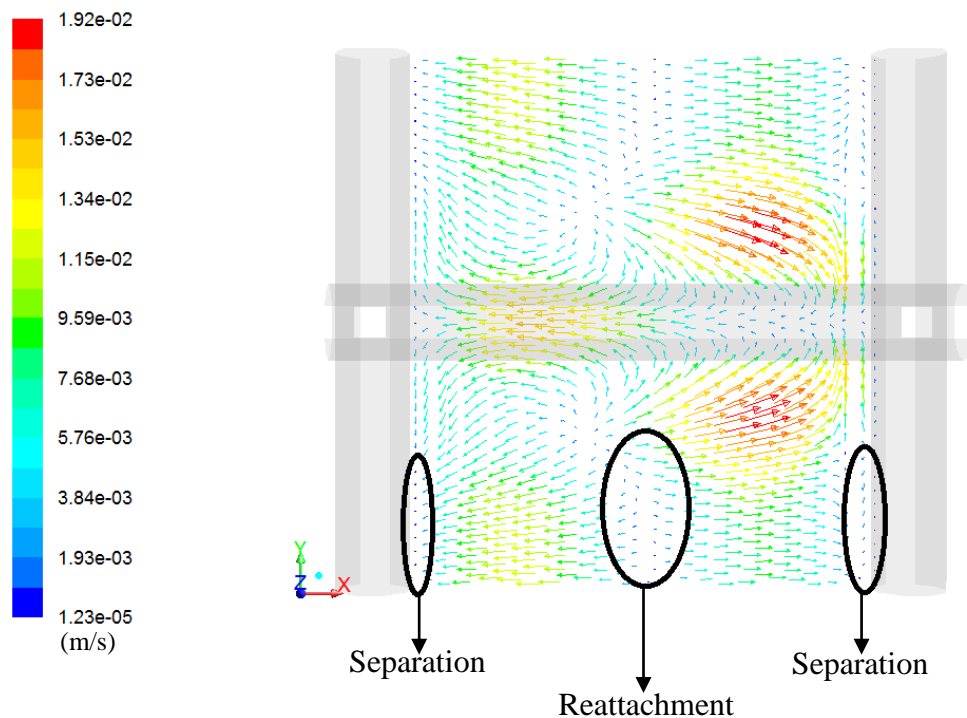


**Figure 5.19: Velocity vectors coloured by velocity magnitude at a plane in the vicinity of bottom membrane wall ( $Z=0.05$ mm), showing flow reattachment and separation.**

In Figure 5.20 (a) velocity magnitude contours overlaid by the velocity vectors (fixed length) are shown at a vertical plane ( $y=0$ mm). In Figure 5.20 (b) the local

wall shear stress along with the mass transfer coefficient at the bottom wall along the flow direction are shown. Flow separation regions near the bottom transverse filaments and flow reattachment region somewhere in the middle of the two bottom filaments are quite evident in the figure.

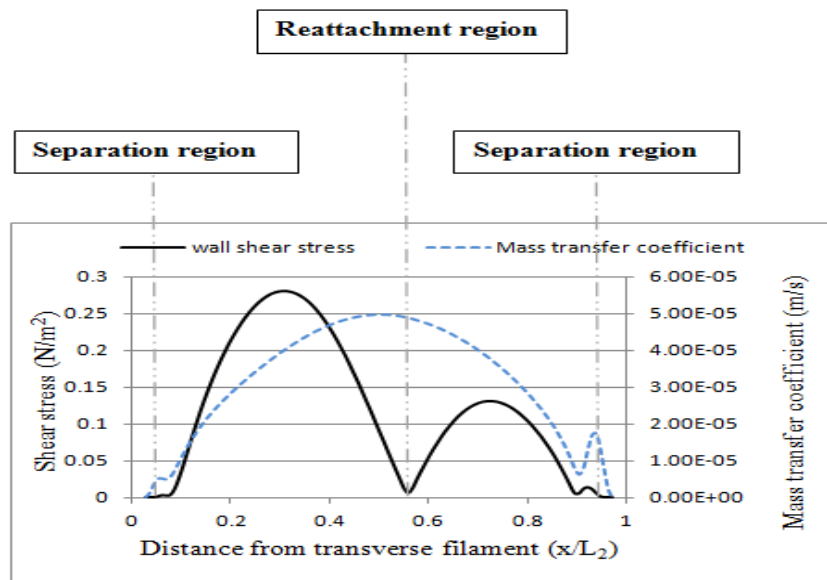
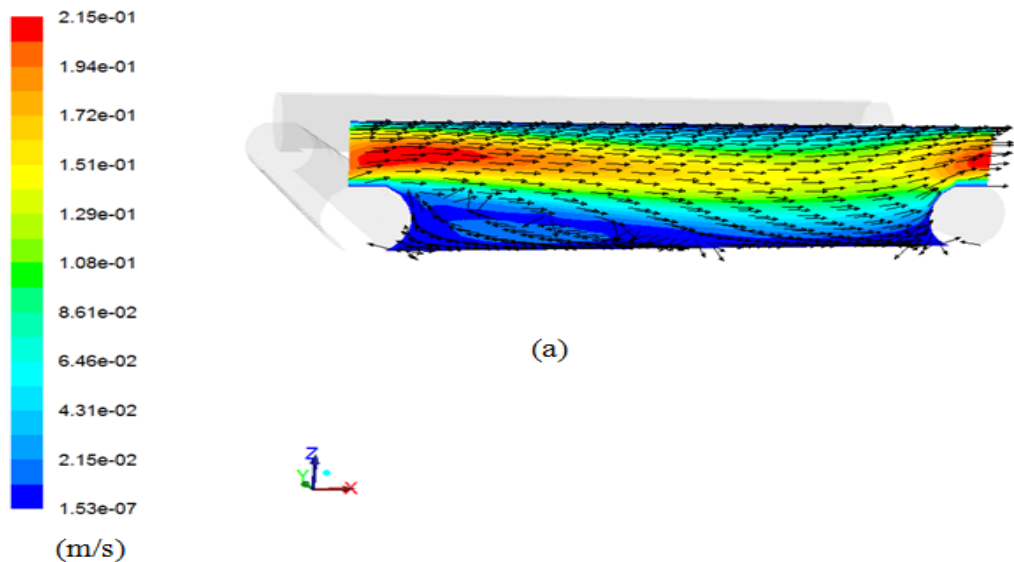


Figure 5.20: (a) Contours of velocity magnitude overlaid by the velocity vectors (fixed length) at vertical plane ( $y=0$  mm). (b) Shear stress and mass transfer coefficient distribution at plane  $y=0$ mm, for SP44 at  $Re_h=100$ .

Based on the discussion regarding the flow patterns prevailing in the vicinity of the bottom membrane surface, it is now convenient to explain the local mass transfer coefficient and wall shear stress patterns generated on the bottom membrane surface. Figure 5.21 (a) represents the selected portion of the computational domain (between 5<sup>th</sup> and 6<sup>th</sup> bottom filaments). The virtual lines b-e are drawn along the normal flow direction and the line f is drawn along y-direction. The variation of local wall shear stress and mass transfer coefficient along virtual lines b-f are shown in Figure 5.21 (b-f) respectively.

In Figure 5.21 (b-d) there are three regions where the wall shear stress shows almost zero values but the mass transfer coefficient are higher. Out of the three regions, two regions represent the area just after and just before the transverse upstream and downstream filament. It can be seen from Figure 5.19 that the fluid in those areas tends to separate from the bottom filaments (labelled as “Separation” in Figure 5.19) and as a result of associated directional changes enhance the local mass transfer coefficient. Moreover the fluid velocity in those areas are very small which leads to minimum wall shear stress in those regions.

The third region where the mass transfer coefficient curve shows local peak despite minimum value of local wall shear stress resides somewhere in the middle of the two bottom transverse filaments. It can be seen from Figure 5.19, this region is particularly that very area where the flow reattaches its self, somewhere in the middle of the two consecutive bottom filaments, to the bottom surface after crossing over the upstream bottom filament and undergoes strong directional changes leading to enhanced local mass transfer coefficient in this region despite very low local velocity and wall shear stress.

Figure 5.21 (e) represents the local variation of wall shear stress and mass transfer coefficient for the virtual line e, drawn on the bottom membrane surface exactly below the top filament. To understand the flow pattern generated just beneath the top filament in the vicinity of the bottom membrane surface, we have to take into account the flow behaviour in the vicinity of that particular region on both sides of the top filament. It can be seen from Figure 5.19 that flow, on both sides of the top axial filament, after reattaching to the bottom membrane surface, diverge in an accelerating manner and meet just below the top filament and accelerate in the

direction opposite to the bulk flow and undergo flow separation on reaching the upstream filament. A small portion of the fluid also undergoes flow separation in the vicinity of the downstream bottom filament. This phenomenon can be seen in Figure 5.19 and yields the two local peaks on the mass transfer coefficient curve in the regions adjacent to the two bottom filaments where the local velocities and hence the wall shear stress are at the minimum values. Since there is no flow reattachment region present just beneath the top filament (on the bottom membrane surface) that is the reason the third local peak for the mass transfer coefficient is absent along the virtual line e. Apart from these two regions the local values of mass transfer coefficient are higher where the local values of the shear stress are higher and vice versa. Up to best of the Author's knowledge the local wall shear stress and mass transfer coefficient on the bottom wall just under the top filament was never discussed previously in any study and is purely the outcome of this current study.

Figure 5.21 (f) represents the local variation of mass transfer coefficient and wall shear stress on the bottom wall along line f drawn in y-direction. The local mass transfer coefficient shows higher values either at the regions of higher local velocities or at the regions where the flow reattaches itself with the bottom membrane surface.

Comparing the fluid flow patterns in the vicinity of top and bottom membrane surface, it can be seen from the Figure 5.17 that near the region of top membrane surface, major portion of the fluid follows the main flow direction (x-direction). However in the vicinity of bottom membrane surface complex flow patterns are generated which, apart from involving the fluid flowing in the normal flow direction, also includes flow reattachment and recirculation regions where the fluid undergoes drastic directional changes. Due to this complexity of the flow the local mass transfer coefficient and the local wall shear stress on the bottom membrane surface varies significantly at different distances from the top and bottom filaments. Moreover, unlike the simple trends for local mass transfer coefficient and local wall shear stress on the top membrane where both either increase or decrease simultaneously, those trends are different for the bottom membrane surface. For instance, at the point of flow separation near the bottom filament region and at the point of flow reattachment with the membrane bottom wall, mass transfer coefficient shows the local peaks due

to strong directional changes in the flow direction despite the minimum local velocities and shear stress values.

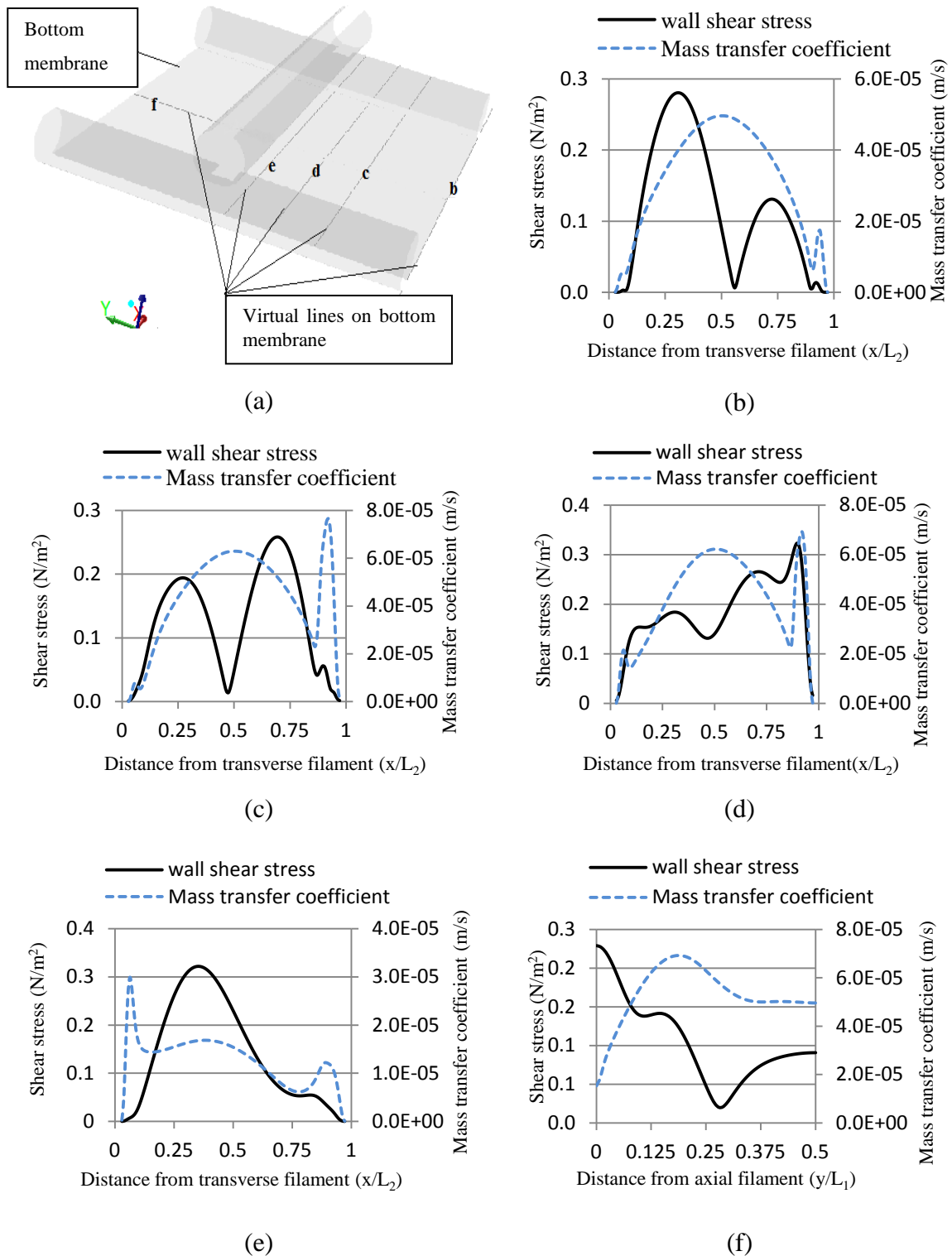


**Figure 5.21: (a) Selected computational domain with virtual lines on bottom membrane wall.(b-f) Mass transfer coefficient and shear stress distribution on bottom wall along virtual lines b-f respectively for SP44 at  $Re_h=100$ .**

## 5.6 Effect of filament spacing

It has been established in the previous section that the fluid flow patterns are quite complex in the vicinity of the bottom membrane surface as compared to region in the vicinity of the top membrane wall when the bottom filaments are oriented in transverse direction and top filament are present in the axial direction to the normal flow. This is because the bulk of the fluid, in the vicinity of the top membrane wall, follows the main flow direction and hence for the major portion of the top membrane wall shear stress and mass transfer coefficient local values follows the same trend i.e. they increase or decrease simultaneously at different locations with the exception of very small regions where the flow separates and reattaches from and to the top filament. However, there are strong three dimensional effects seen in the vicinity of the bottom membrane wall due to flow reattachment and separation phenomena covering a larger portion of the bottom membrane. As a result the local wall shear stress and mass transfer coefficient do not follow same trend as in case of top membrane wall.

Further, it has been seen that the dimensionless bottom filament mesh length ( $L_2$ ) has an important role to define the flow patterns near the bottom membrane surface. On investigating different spacers it is concluded that when  $L_2$  is up to 3 the flow after colliding the downstream transverse bottom filament reverses its direction and region of reattachment is absent for those spacers. However, flow reattachment region appears for the spacers having  $L_2 \geq 4$ . This conclusion is in line with the previous investigations by the author of this thesis [175] and other three dimensional CFD studies involving flow through spacer obstructed narrow feed channels when the top and bottom feed channel side spacers are oriented in axial and transverse direction to the main flow [164, 165].

Figure 5.22 presents velocity vectors (fixed length) coloured by velocity magnitude at a plane in the vicinity of the bottom membrane surface ( $Z=0.05\text{mm}$ ) for different spacers. In the figure four different spacers arrangement are considered. Dimensionless top filament spacing is same for the four cases (i.e  $L_1=4$ ) and the effect on flow patterns is investigated by increasing  $L_2$  from 2 to 6. It is quite evident that for the spacer arrangements SP42 and SP43 the velocity vectors after colliding with the downstream transverse filament reverse their direction and the flow

reattachment cannot be seen for those spacers. However, for the spacer arrangements SP44 and SP46, apart from the flow attachment regions in the vicinity of the two transverse filaments, flow reattachment region is also present which shifts further to the upstream bottom filament when  $L_2$  is increased from 4 to 6 resulting in the extension of the high velocity region (in the normal flow direction) and shrinkage of the flow reversal region.

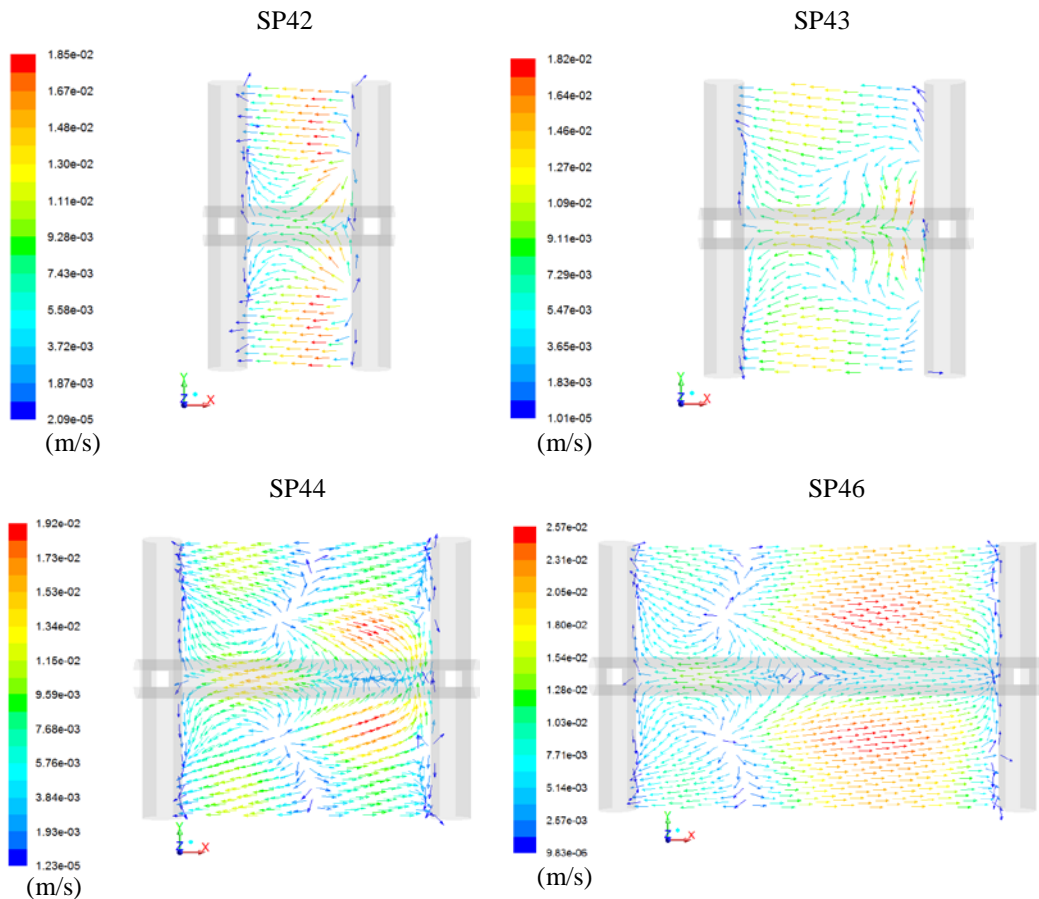


**Figure 5.22: Velocity vectors coloured by velocity magnitude (fixed length) for different spacers at  $Z=0.05h_{ch}$  and  $Re_h=100$ .**

Due to this reason the region of higher mass transfer coefficient in case of SP66 at the bottom wall shift towards the upstream transverse filament and stretches in length when compared to SP44. But, due to increased mesh spacing for the bottom filaments the region of high velocity in the vicinity of the top membrane wall shrinks and lead to lower area weighted mass transfer coefficient for the top membrane wall. Although area weighted mass transfer coefficient at the bottom membrane surface increases when we compare SP66 with SP44, but at the top membrane surface the area weighted mass transfer coefficient reduces significantly giving an impression

that for SP66 the top membrane surface would be fouled more rapidly as compared to the bottom membrane surface which is not desirable at all for any membrane operations. Figure 5.23 shows the mass transfer coefficient contours for top and bottom membrane walls for SP44 and SP66.

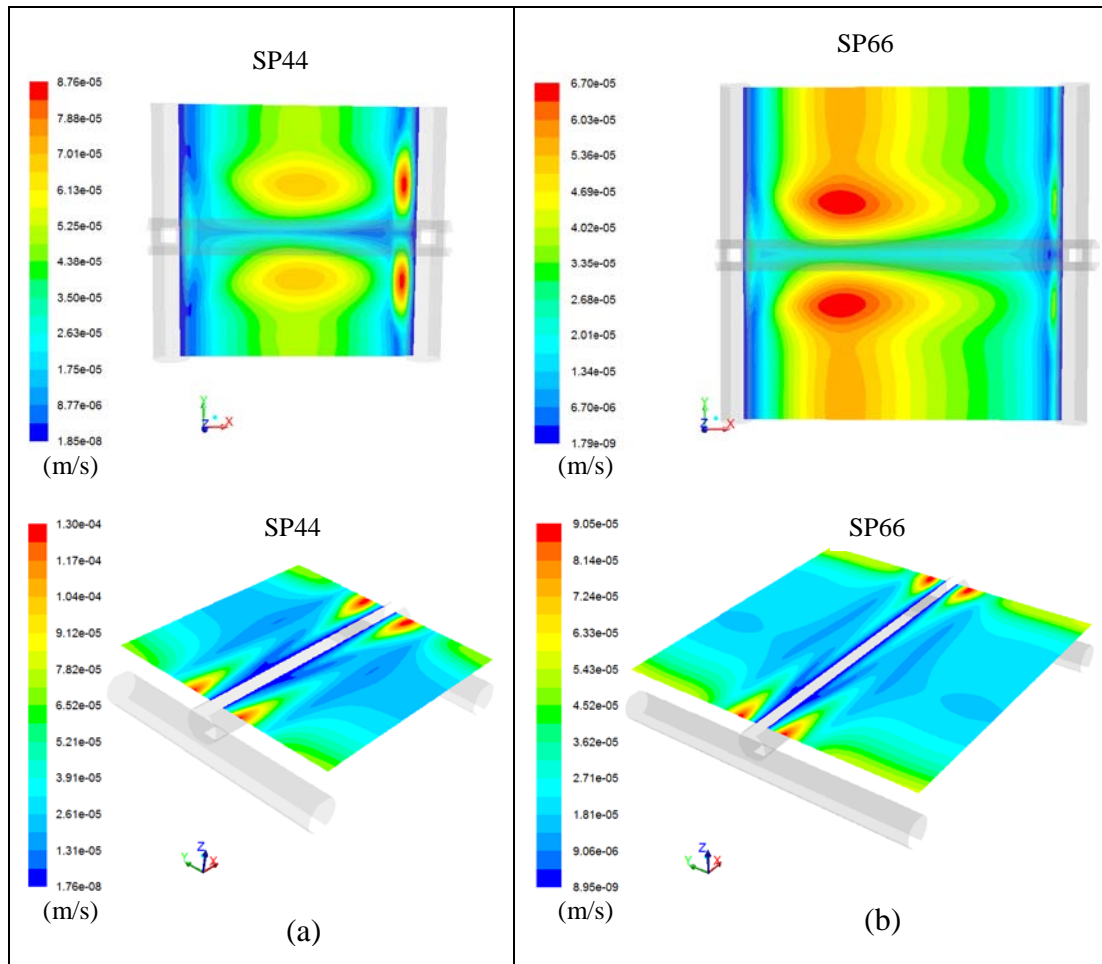


**Figure 5.23: Contours of mass transfer coefficient for (a) SP44 and (b) SP66 at  $Re_h=100$  at bottom and top membrane surfaces.**

Previous studies [164, 165, 175] report the existence of flow reattachment region at the bottom membrane surface for spacers having  $L_2 \geq 4$ , but the shift of this region with change in the bottom filaments mesh length and the resulting impact on the mass transfer coefficient for the two membrane surfaces is the outcome of the present study.

Figure 5.24 presents the velocity vectors overlaid by mass transfer coefficient contours at top and bottom membrane surfaces for different spacer arrangements at  $Re_h=100$ . There are four important regions each on the top and bottom membrane

surfaces in terms of variation in mass transfer coefficient and are marked as A-D & E-H for top and bottom membranes respectively for SP44 in Figure 5.24.

At top membrane surface, the fluid tends to shift away from the top axial filament in the region “A” and leads to lower values of mass transfer coefficient. The fluid while proceeding in the normal flow direction tends to reattach to the top filament in the region where the top filament crosses over the bottom filament and yields higher local values for mass transfer coefficient in region “B”. Mass transfer coefficient is also observed to be higher in the region “C” when high velocity fluid flows over the bottom filament and when the flow detaches from the top membrane in region “D” the mass transfer coefficient drops down. Sizes of the mentioned regions depend widely on the axial and transverse dimensionless filament spacing ( $L_1$  and  $L_2$ ) as can be seen from the Figure 5.24. For instance, the size of region “A” decrease with an increase in axial filament spacing as can be seen in Figure 5.24 for spacers SP24, SP44 and SP64. However, the size of this zone increases with an increase in transverse filament spacing and is evident from Figure 5.24 for SP42, SP44 and SP46. It is observed that local values of mass transfer coefficient in region “B” are largely dependent on the bottom transverse filament spacing. For spacers having moderate to larger transverse filament spacing (SP44, SP46), the fluid while flowing over the bottom filament accelerates due to reduction in available area and after passing over the bottom filament tends to slow down considerably due to increase in the available flow area (to satisfy continuity) hence would yield a higher shear stress at top wall just above the bottom filament and considerably lower wall shear stress somewhere between the two consecutive bottom filaments. This acceleration and retardation above the bottom filament and between the two consecutive bottom filament respectively, results in higher local values for mass transfer coefficient in region “B” when compared to rest of the top membrane surface for the spacers having higher transverse filament spacing. On the other hand for the spacers having lower values for transverse filament spacing (SP42) the local rise in the mass transfer coefficient in region “B” is not that significant and the mass transfer coefficient distribution is seen to be of more even nature for the entire top membrane surface.

Further, it has been seen that the dimensionless bottom filament mesh length ( $L_2$ ) has an important role to define the flow patterns near the bottom membrane surface. On investigating different spacers it is concluded that when  $L_2$  is up to 3 the flow after

colliding the downstream transverse bottom filament reverses its direction and region of reattachment is absent for those spacers. However, flow reattachment region appears for the spacers having  $L_2 > 3$ . This conclusion is in line with our earlier observations [175] and other modelling studies involving flow through spacer obstructed narrow feed channels when the top and bottom feed channel side spacers are oriented in axial and transverse direction to the main flow [164, 165].

It is quite evident from Figure 5.24 that spacers having  $L_2 \leq 3$  show only flow reversal and when it is increased to 4 and above both flow reattachment and reversal regions are seen. There are four important regions bottom membrane surfaces in terms of variation in mass transfer coefficient and are marked E-H for bottom membranes for SP44 in Figure 5.24. On the bottom membrane surface, mass transfer coefficient exhibits higher local values in region E where the fluid reattaches to the surface. It is interesting to notice that flow reattachment region is absent for SP22 and SP33 because the fluid does not reattach to the bottom membrane surface and undergoes recirculation after hitting the downstream bottom filament.

In region F just after the upstream filament a stagnant fluid zone is created which leads to lower values of mass transfer coefficient. The size of this stagnant region reduces with the increase in the transverse filament spacing ( $L_2$ ) as seen in Figure 5.24 for SPP 42, SP44 & SP46 and is highly desirable for efficient process. Low values of mass transfer coefficient are observed just below the top filament on the bottom membrane surface in region G. In the vicinity of the downstream bottom filament (region H) fluid undergoes strong directional changes (in Y direction) due to the presence of bottom filament and results in higher value for the mass transfer coefficient. It can be seen from the Figure 5.24 that the relative size of the zone H and local values of mass transfer coefficient in that zone reduces when either of the transversal ( $L_2$ ) or axial filament ( $L_1$ ) spacing is increased.

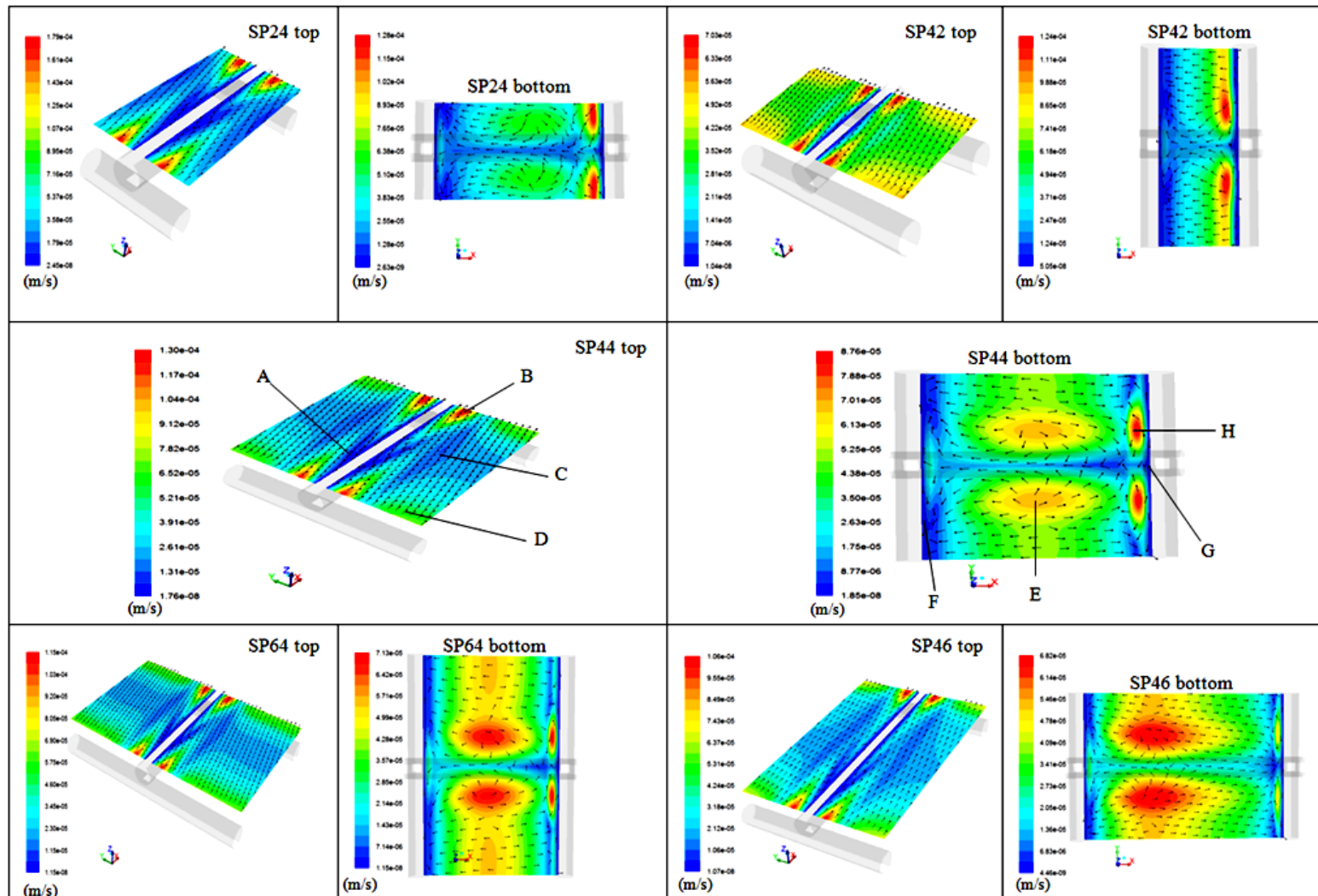


Figure 5.24: Velocity vectors (fixed length) overlaid by mass transfer coefficient contours at top & bottom membrane surfaces for different spacers at  $Re_h=100$ .

The effect of dimensionless filament spacing ( $L_1$  and  $L_2$ ) on average pressure drop and top & bottom wall average shear stress is presented in Figure 5.25 – 5.27. Figure 5.28 - 5.29 represents the effect of the filament dimensionless spacing on the average mass transfer coefficient for top and bottom membrane surfaces respectively and combined in the Figure 5.30 for relative comparison.

Previous studies [28, 152-155] investigating hydrodynamics and mass transport through spacer filled narrow channels concluded that an ideal spacer configuration should lead to moderate pressure drop across the membrane channel with higher mass transport of the solute away from the membrane surface. Additionally, major contribution of the pressure drop should come from the viscous drag not from the form drag. This is because viscous drag increases the shear rates at the membrane wall, whereas form drag leads to power dissipation without any beneficial impact on the membrane performance.

It is evident from Figure 5.25 that with an increase in bottom filament dimensionless spacing ( $L_2$ ) the pressure drop decreases due to presence of lesser number of filaments per unit length and therefore decrease the form drag. For example, with an increase of  $L_2$  from 2 to 6 the pressure drop decreases to approximately one-half. Similar trend can be observed for top wall shear stress values as they decrease by almost the same ratio with an increase of  $L_2$  from 2 to 6 and can be seen in Figure 5.26. However, for the bottom wall shear stress values the trend is different and can be attributed mainly due to complex flow patterns generated within the vicinity of the bottom membrane surface and is presented in Figure 5.27. As mentioned earlier, for the spacer configuration having  $L_2 \leq 3$  there is complete flow reversal in the vicinity of the bottom membrane surface and this phenomena result in higher average value of shear stress at the bottom membrane surface. For spacer configurations having  $L_2=4$ , the fluid reattaches to the bottom membrane surface somewhere in the middle of the two consecutive bottom filament and results in partial recirculation. This leads to lower average values of bottom wall shear stress for those configurations. But when  $L_2$  is further increased to 6 the reattachment point is shifted further towards the upstream filament. The resulting impact of this shift enables sufficient length for the fluid to accelerate in the normal flow direction before it strikes the downstream bottom filament and eventually results in increased average wall shear stress value for the bottom membrane surface. Total flow

reversal, partial recirculation and shift of the reattachment point for SP43, SP44 and SP46 respectively are quite evident in Figure 5.22.

The impact of top filament dimensionless spacing on pressure drop and wall shear stress is also evident from the Figure 5.25 to 5.27. It can be noted that when  $L_1$  is reduced from 4 to 2, there is a significant increase in pressure drop (59 to 79 % for the spacer arrangement studied) compared to the associated increase in top and bottom wall shear stress (13 to 30% for the spacer arrangement studied). It can be stated safely that the increase in pressure drop by reducing the top filament mesh spacing will lead to higher form drag compared to the viscous drag and is not required for efficient membrane processes. It can be concluded that the larger top or axial filament dimensionless spacing tend to reduce the portion of pressure drop contributing towards form drag and would result in significant portion of the energy loss contributing towards the viscous drag which is highly desired for an efficient membrane process.

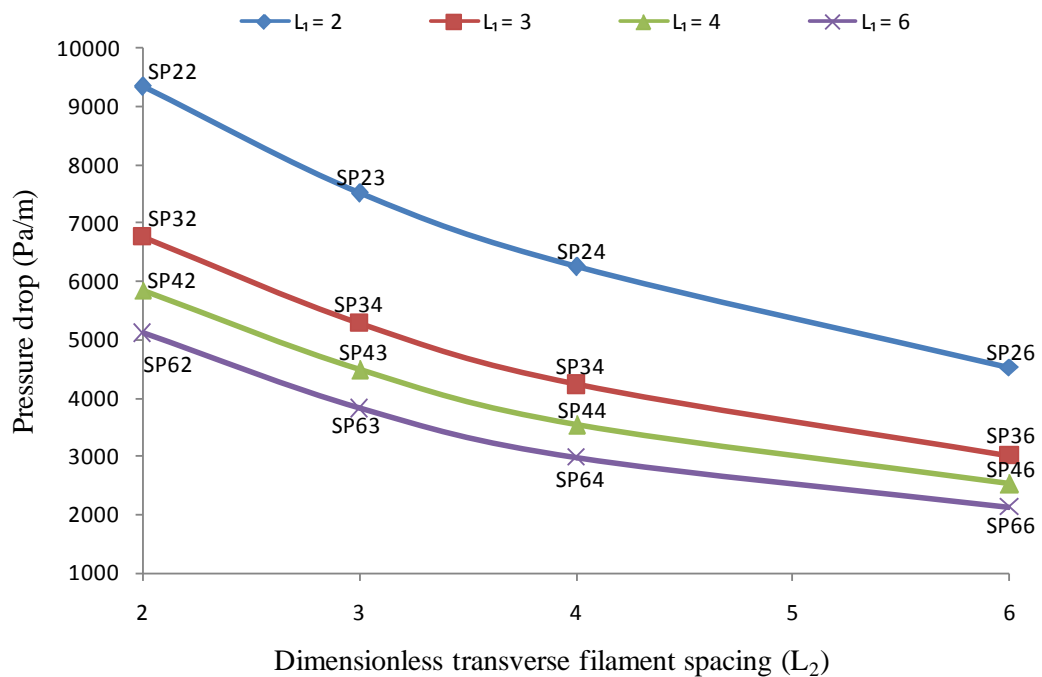


Figure 5.25: Dimensionless filament spacing effect on pressure drop at  $Re_h=100$ .

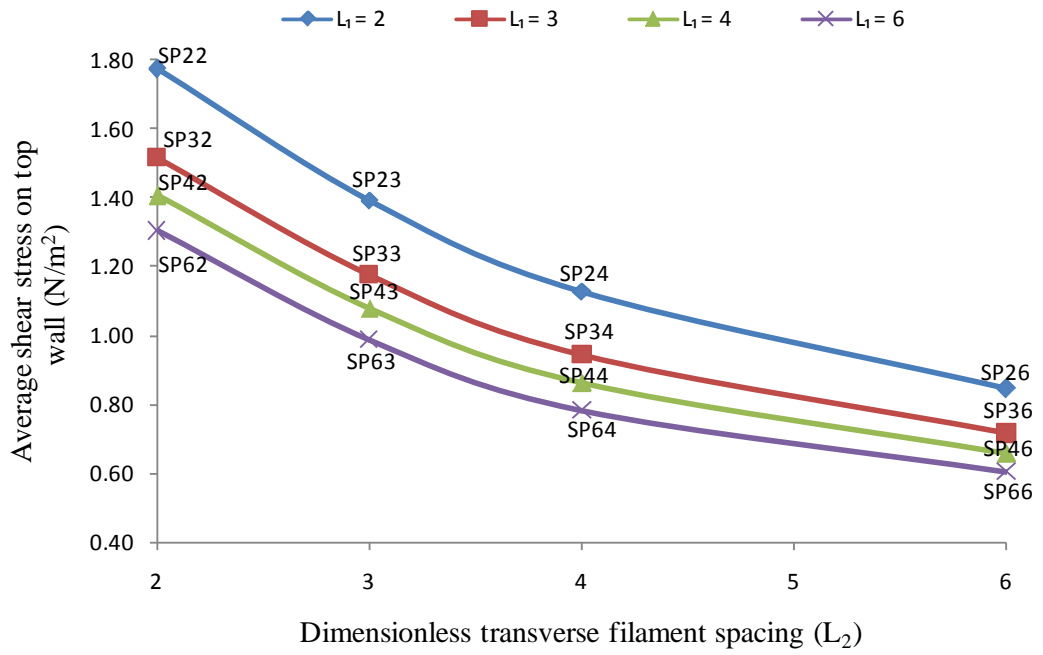


Figure 5.26: Dimensionless filament spacing effect on top wall average shear stress at  $Re_h=100$ .

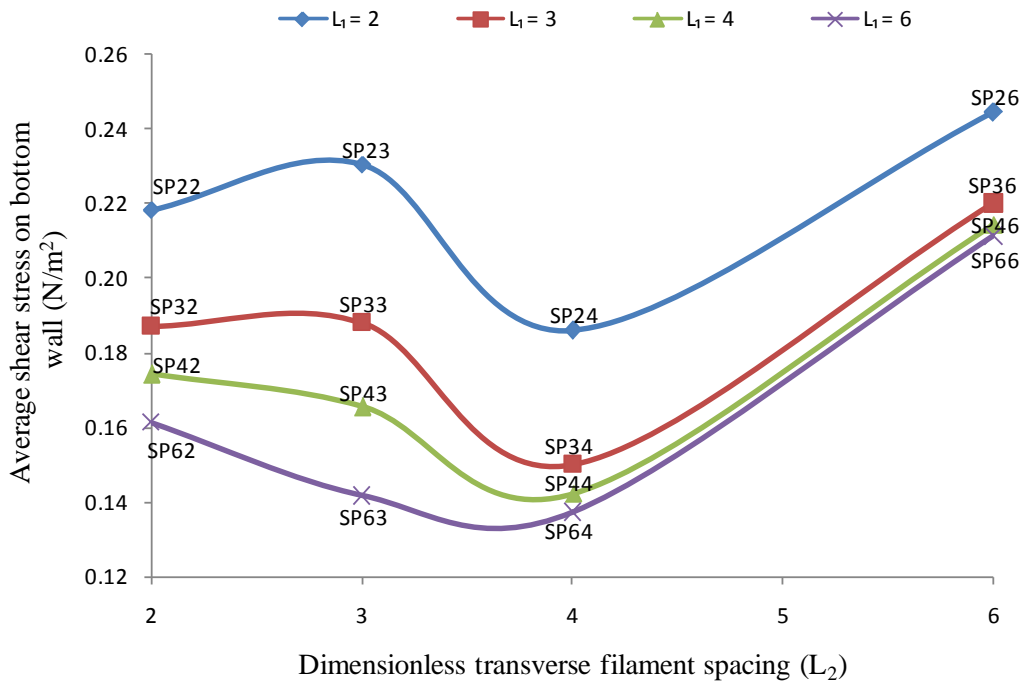


Figure 5.27: Dimensionless filament spacing effect on bottom wall average shear stress at  $Re_h=100$ .

Figure 5.28 – 5.30 represents the impact of dimensionless filament spacing on top and bottom wall mass transfer coefficients. It can be seen from the figures that for all the spacer configurations considered in this work when  $L_2=4$  there is a dip in the average bottom wall shear stress which is due to the fluid flow reattaching somewhere in the middle of the two consecutive bottom filament and partly been recirculated. But at the same time the induced directional changes to the flow are responsible for moderately higher average mass transfer coefficient values. However when  $L_2 < 4$  the average mass transfer coefficient values at the bottom membrane surface have higher values but at the same time the pressure drop is also significantly higher as shown in Figure 5.25. When  $L_2$  is increase from 4 to 6 the reattachment point is shifted closer to the upstream bottom filament and provides sufficient length for the flowing fluid to accelerate in the normal flow direction and results in higher average bottom wall shear stress, but the impact of this increase in  $L_2$  has no significant increase in the bottom wall mass transfer coefficient and adversely effects the top wall mass transfer coefficient as can be seen from Figure 5.28. This can be attributed to the fact that for spacer configurations having  $L_2 = 6$  the relative region of high velocity in the vicinity of the top membrane wall shrinks and lead to lower area weighted mass transfer coefficient for the top membrane wall. Although area weighted mass transfer coefficient at the bottom membrane surface is higher when we compare spacers configurations having  $L_2= 6$  with those having  $L_2=4$ , but at the top membrane surface the area weighted mass transfer coefficient reduces significantly giving an impression that for spacers having  $L_2=6$  the top membrane surface would be fouled more rapidly as compared to the bottom membrane surface which is not desirable at all for any membrane operations. The relative comparison of the two surfaces mass transfer coefficients are shown in Figure 5.30.

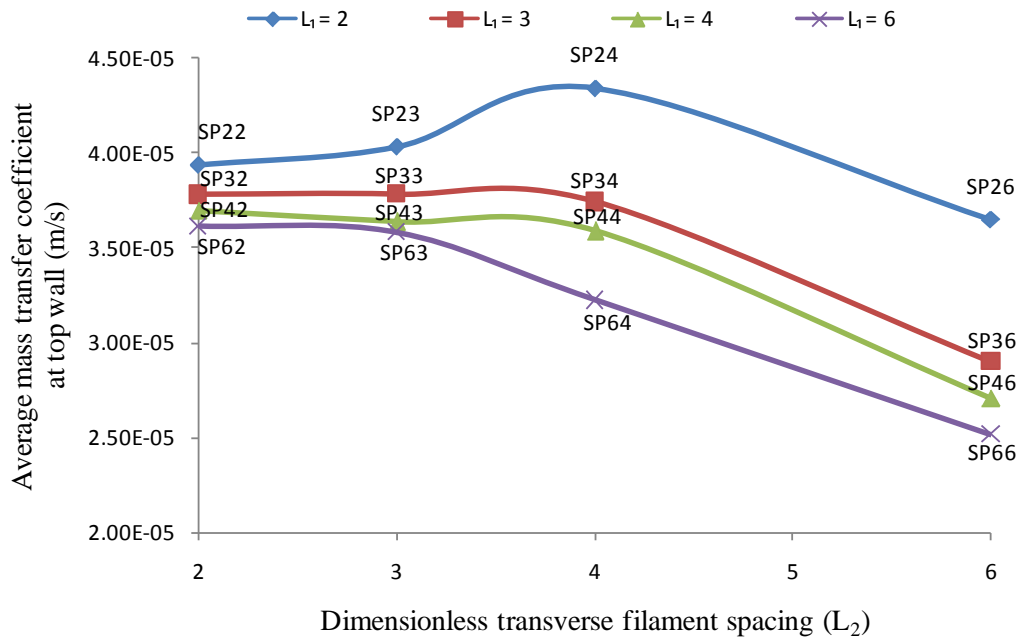


Figure 5.28: Dimensionless filament spacing effect on top wall average mass transfer coefficient at  $Re_h=100$ .

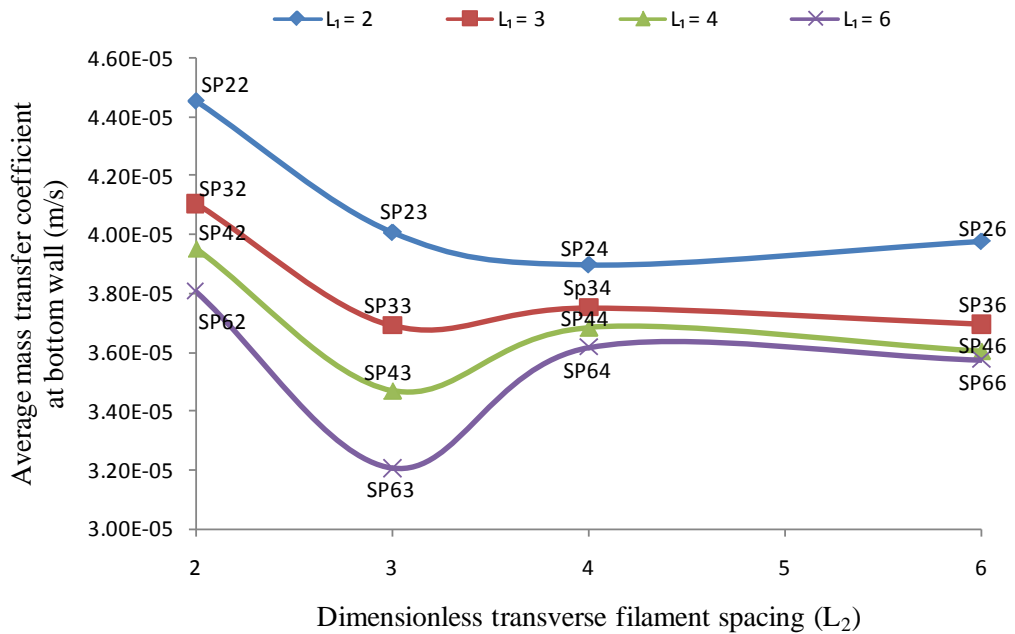
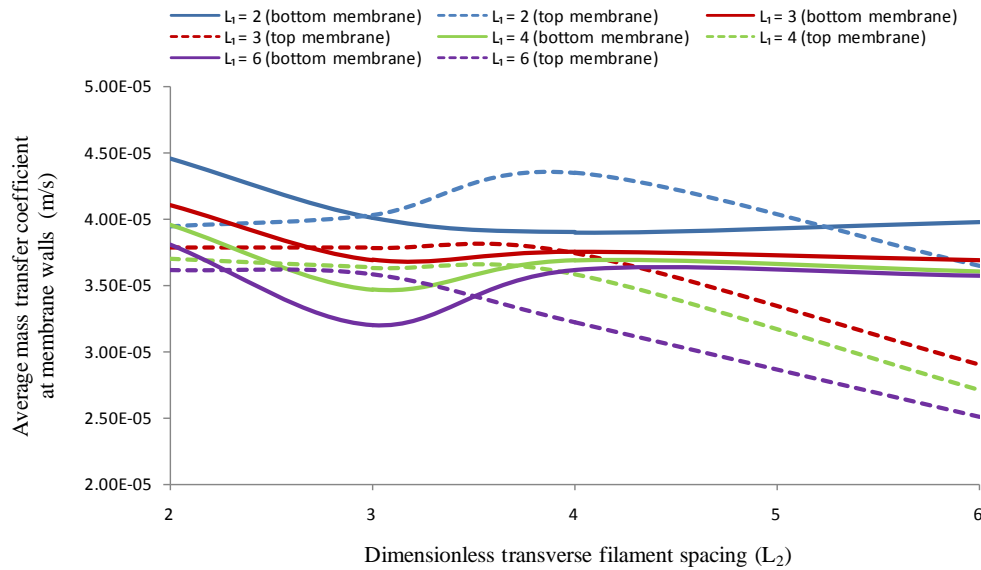


Figure 5.29: Dimensionless filament spacing effect on bottom wall average mass transfer coefficient at  $Re_h=100$ .



**Figure 5.30: Dimensionless filament spacing effect on top & bottom wall average mass transfer coefficient at  $Re_h=100$ .**

Table 5.1 presents the different spacer configurations studied in this work and the corresponding results for average wall shear stress, mass transfer coefficient and pressure drop. It can be seen that for the spacer configurations having  $L_2 = 6$  yields lower values for the top wall mass transfer coefficient compared to the bottom wall and hence would lead to relatively quick fouling of the top membrane wall than the bottom. For this reason they are not at all suitable at all for any efficient membrane separation process. In addition to that, SP22 and SP64 also have a lower ratio of the top to bottom mass transfer coefficient and would increase the fouling propensity of top membrane surface compared to the bottom surface and are not suitable to be used in efficient membrane separation processes. It is also evident from the table that area weighted wall shear stress on the bottom membrane surface first decrease when  $L_2$  is decreased from 6 to 4 (due to shift of the flow reattachment region towards the downstream bottom filament and hence providing less length for the reattaching fluid to accelerate in the main flow direction) then increase when  $L_2$  is further decreased from 4 to 2, due to complete flow reversal or recirculation. Whereas area weighted wall shear stress on the top wall and pressure drop increase on reducing  $L_1$  and/or  $L_2$ .

**Table 5.1: Spacer configurations considered in this section and corresponding results at  $Re_h=100$ .**

Spacer configuration	Top filament dimensionless spacing ( $L_1$ )	Bottom filament dimensionless spacing ( $L_2$ )	Bottom wall shear stress N/m <sup>2</sup>	Top wall shear stress N/m <sup>2</sup>	Wall shear stress ratio	Pressure drop Pa/m	Bottom wall mass transfer coefficient m/s	Top wall mass transfer coefficient m/s	Mass transfer coefficient ratio
SP22	2	2	0.22	1.77	8.13	9344.74	4.46E-05	3.94E-05	0.88
SP23	2	3	0.23	1.39	6.05	7509.98	4.01E-05	4.04E-05	1.01
SP24	2	4	0.19	1.13	6.06	6250.16	3.90E-05	4.34E-05	1.11
SP26	2	6	0.24	0.84	3.46	4517.87	3.98E-05	3.65E-05	0.92
SP32	3	2	0.19	1.52	8.10	6775.23	4.10E-05	3.78E-05	0.92
SP33	2	3	0.19	1.18	6.26	5285.31	3.69E-05	3.78E-05	1.02
SP34	2	4	0.15	0.94	6.30	4232.24	3.75E-05	3.74E-05	1.00
SP36	2	6	0.22	0.72	3.25	3019.78	3.69E-05	2.90E-05	0.79
SP42	4	2	0.17	1.41	8.07	5859.32	3.95E-05	3.70E-05	0.94
SP43	4	3	0.17	1.08	6.53	4479.46	3.47E-05	3.64E-05	1.05
SP44	4	4	0.14	0.86	6.06	3536.12	3.69E-05	3.59E-05	0.97
SP46	4	6	0.21	0.66	3.07	2526.83	3.60E-05	2.71E-05	0.75
SP62	6	2	0.16	1.30	8.09	5109.48	3.81E-05	3.61E-05	0.95
Sp63	6	3	0.14	0.99	6.98	3816.73	3.20E-05	3.48E-05	1.09
Sp64	6	4	0.14	0.78	5.71	2975.04	3.62E-05	3.22E-05	0.89
Sp66	6	6	0.21	0.60	2.86	2131.75	3.58E-05	2.52E-05	0.70

Table 5.2 represents the selected spacer configurations that have the two average mass transfer coefficients values quite close to each other and would result in almost the same fouling tendency of the two membrane surfaces and could be suitable for membrane operations in real life. The average mass transfer coefficient in this table is taken as arithmetic average of the two mass transfer coefficients for the two membrane walls.

**Table 5.2: Comparison of selected spacer configurations at  $Re_h=100$ .**

Spacer configuration	Average mass transfer coefficient	Hydraulic diameter	Sherwood number	Power number	SCE * $10^5$
	m/s	m			
SP23	4.02E-05	1.06E-03	28	698545	3.97
SP24	4.12E-05	1.13E-03	30	548403	5.49
SP32	3.94E-05	1.06E-03	27	630202	4.31
SP33	3.74E-05	1.19E-03	29	437135	6.63
SP34	3.75E-05	1.27E-03	31	329673	9.36
SP42	3.83E-05	1.13E-03	28	514111	5.44
SP43	3.55E-05	1.27E-03	29	348931	8.38
SP44	3.64E-05	1.35E-03	31	259170	12.11
SP62	3.71E-05	1.19E-03	29	422593	6.81
SP63	3.34E-05	1.35E-03	29	279737	10.45

Spacer arrangements presented in Table 5.2 are further compared on the basis of Sherwood number to Power number ratio. As already mentioned before, the optimal spacer arrangement will yield to higher mass transport of the solute away from the membrane walls with moderate energy losses. Based on this argument SP44 is seen to have the highest Spacer Configuration Efficacy (SCE) and can be regarded as the best performing spacer arrangement and this fact is quite evident from Figure 5.31.

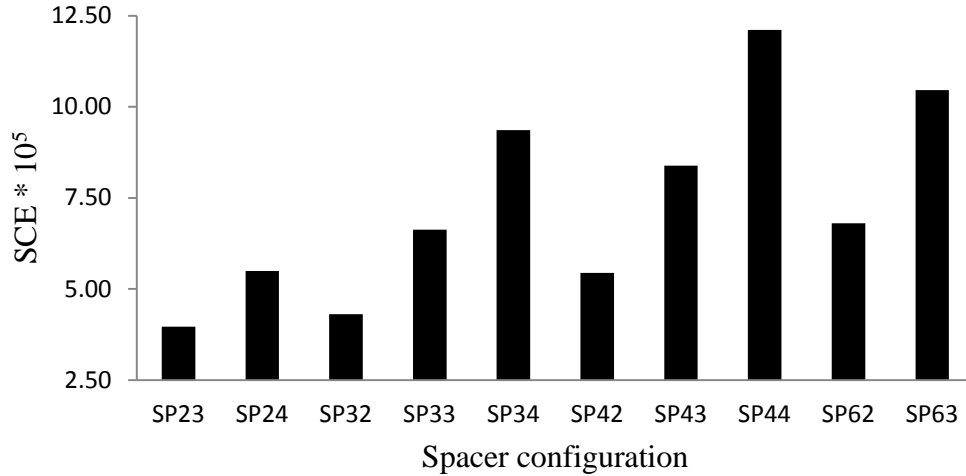
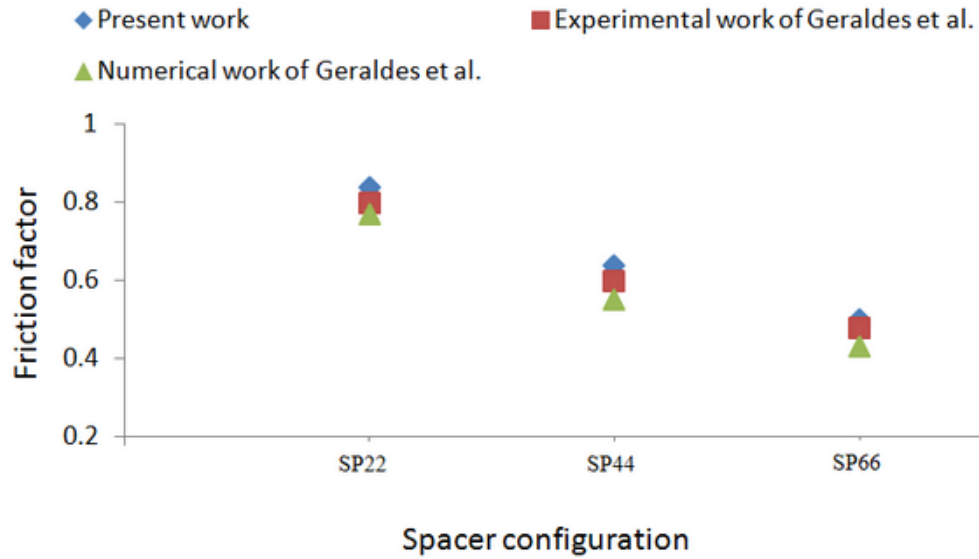


Figure 5.31: Comparison of different spacer configurations at  $Re_h=100$ .

## 5.7 Comparison of present study with previous experimental and numerical studies

For validation of the current model used in this work, results for some spacer configurations are compared with some previous experimental and numerical studies. For instance, friction factor values calculated by equation 5.3.1-8 for SP22, SP44 and SP66 are compared with experimental and numerical values presented by Geraldès et al. [20] for spacer configuration termed as S1, S2 and S3 respectively having transverse dimensionless filament spacing of 1.9, 3.8 and 5.7. The comparison is shown in Figure 5.32.

It can be seen from Figure 5.32 that the friction factor values obtained by the present numerical study have excellent agreement (within 4% deviation) with those obtained experimentally and numerically by Geraldès et al. [20].



**Figure 5.32: Comparison of some spacer configurations with experimental and numerical study of Geraldles et al. [20] at  $Re_h=100$ .**

Figure 5.33 and Figure 5.34 respectively show the comparison of wall shear stress and pressure drop respectively for some spacer configurations with the numerical work of Shakaib et al. [164]. The Pressure drop and wall shear stress values obtained by the present model are in excellent agreement ( $\pm 1.8\%$  and  $\pm 4\%$  deviation respectively) with those reported by Shakaib et al. [164] and hence further validates our model. For some spacer arrangements the simulations were carried out at  $Re_h=125$  to compare the mass transfer coefficient values reported by Shakaib et al. [165] and the comparison is present in Figure 5.35. It is quite evident that the numerically obtained mass transfer coefficient in the present study (by means of a UDF) has an excellent agreement (within 5% difference) with those reported by Shakaib et al. [165] and validate our model further.

To compare Sherwood number obtained by the present work with experimental work of Li et al. [135] simulations were carried out for few spacers at Schmidt number of 1350 (as used by Li et al. [135]). Sherwood number obtained for SP22, SP33 and SP44 are compared with spacer configurations studied by Li et al. [135] having  $L=2.2, 2.8$  and  $4$  respectively and also compared with the values obtained by using Grober equation defined by Da Costa et al. [128] for ladder type spacers arrangement. Figure 5.36 presents the comparison of the Sherwood number obtained by the present study with experimental work of Li et al. [135], numerical study of

Shakaib et al. [165] and Grober equation suggested by De Costa et al. [128] for ladder type spacers. It can be seen from Figure 5.36 that Sherwood number obtained by the present study for different spacer arrangement is in fair accordance with previous experimental and numerical studies. Grober equation suggested by De Costa et al. [128] for ladder type spacers however presents a relatively higher value for SP22 (approximately 30% higher). This is due to fact that Grober equation presented by De Costa et al. [128] for ladder type space arrangement predicts the mass transfer rate with  $\pm 30\%$  error as mentioned in their manuscript [128].

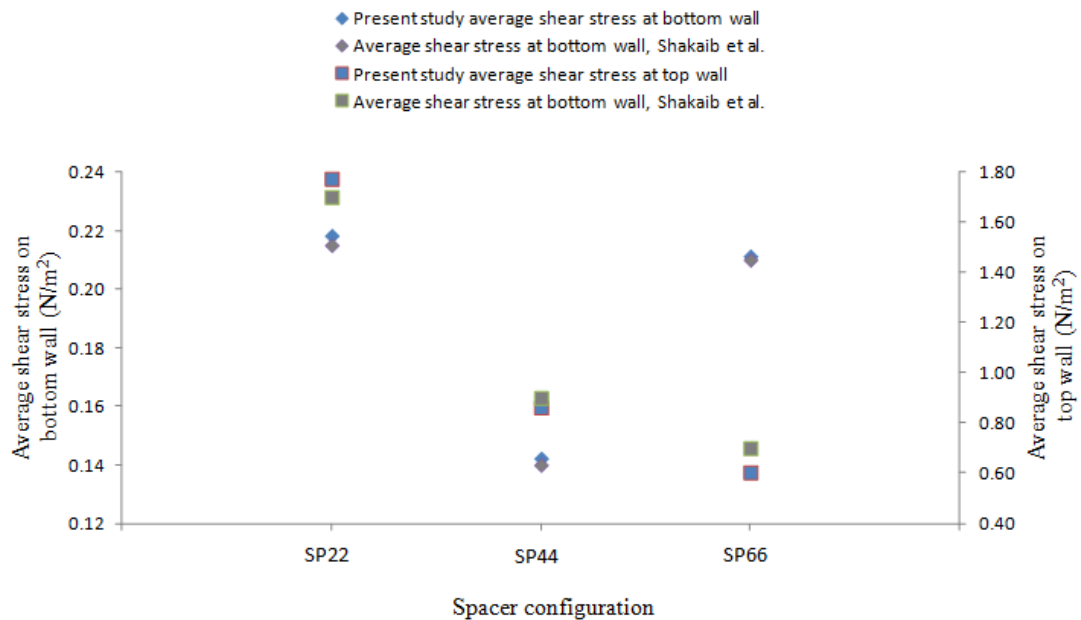


**Figure 5.33: Comparison of wall shear stress for different spacer arrangements with Shakaib et al. [164] at  $Re_h=100$ .**

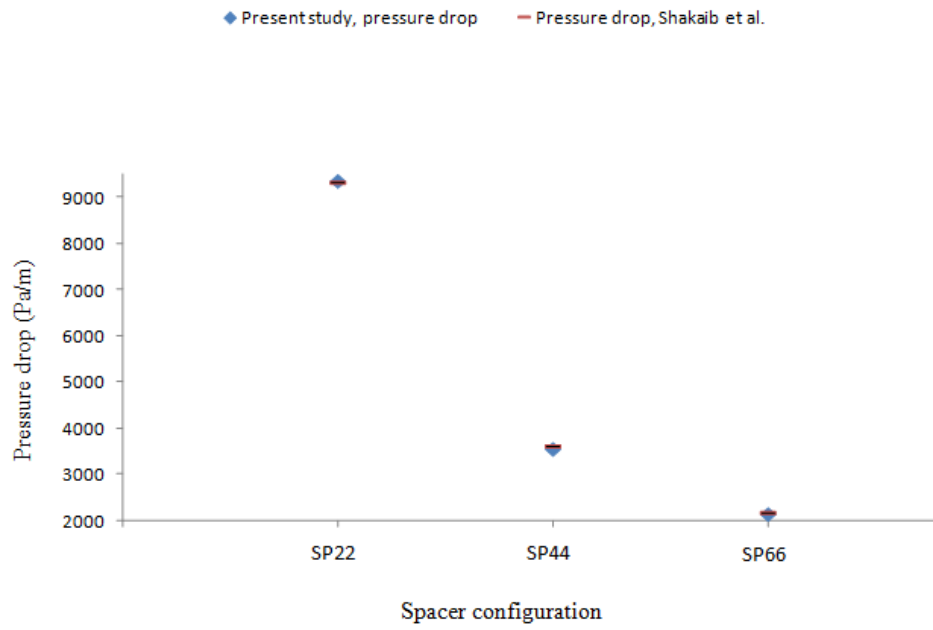


Figure 5.34: Comparison of pressure drop for different spacer arrangements with Shakaib et al. [164] at  $Re_h=100$ .

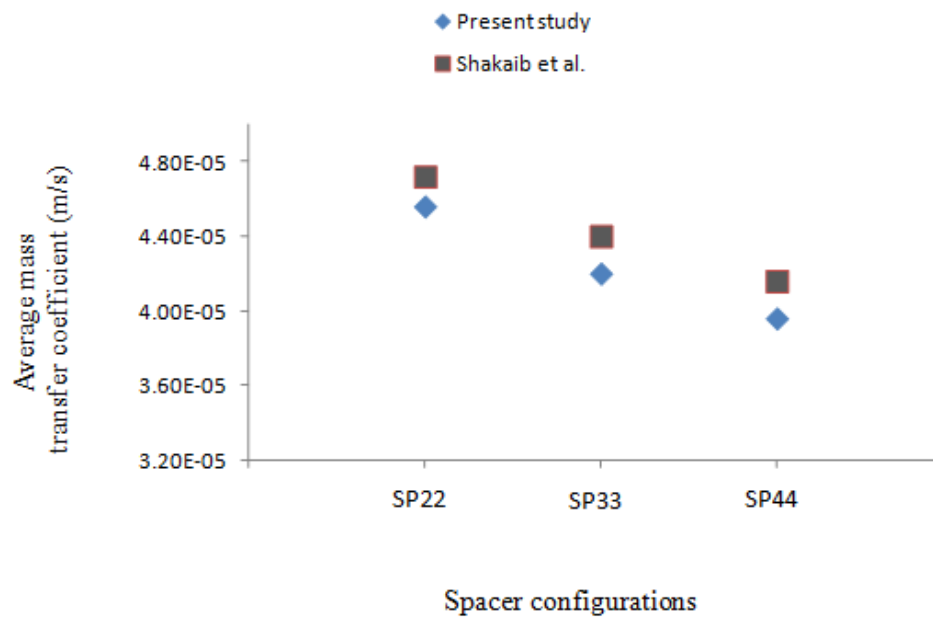
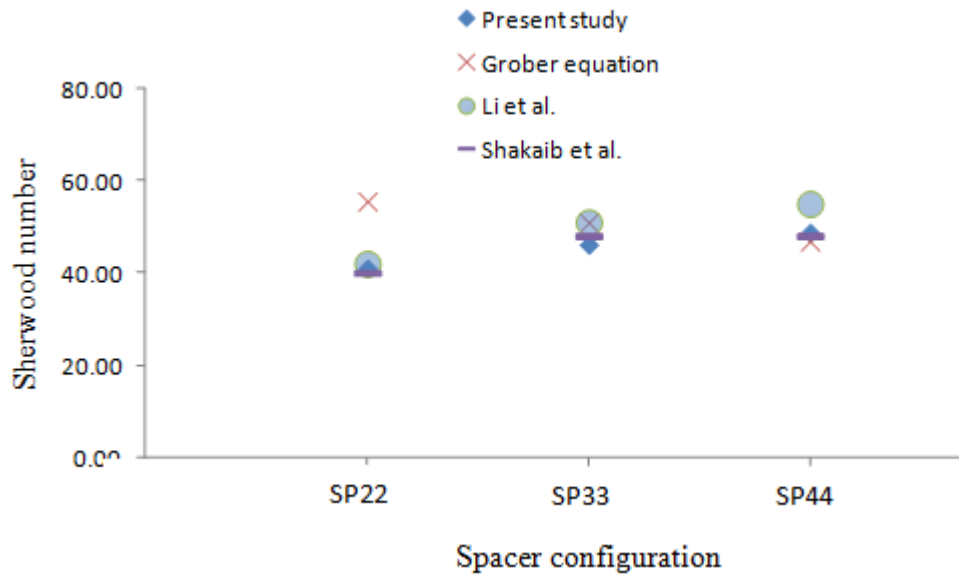


Figure 5.35: Comparison average mass transfer coefficient values for different spacer arrangements with Shakaib et al. [165] at  $Re_h=125$ .



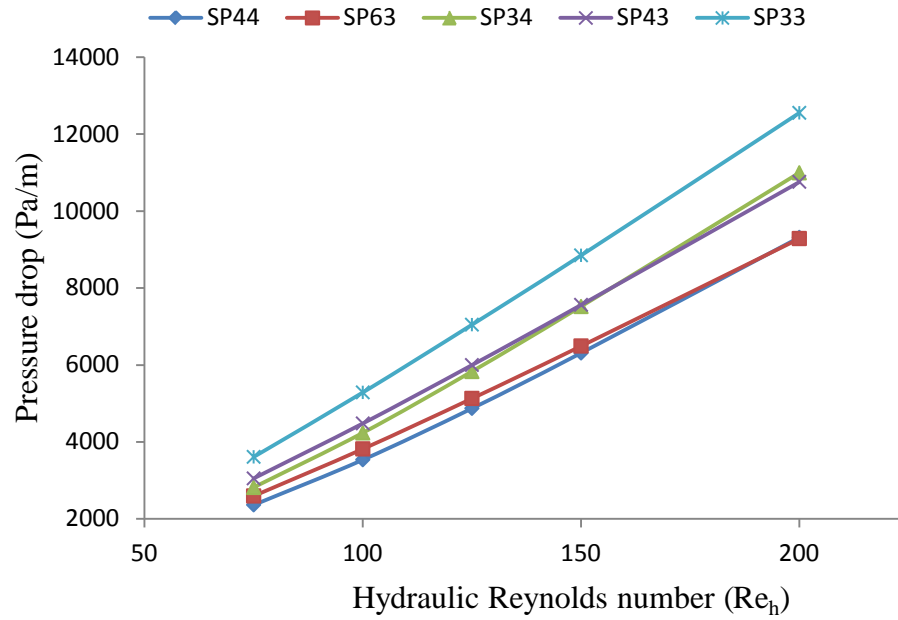
**Figure 5.36: Comparison of Sherwood number for different spacer arrangement with previous experimental and numerical studies at  $Sc=1350$ .**

### 5.8 Comparison of spacers at different Reynolds number

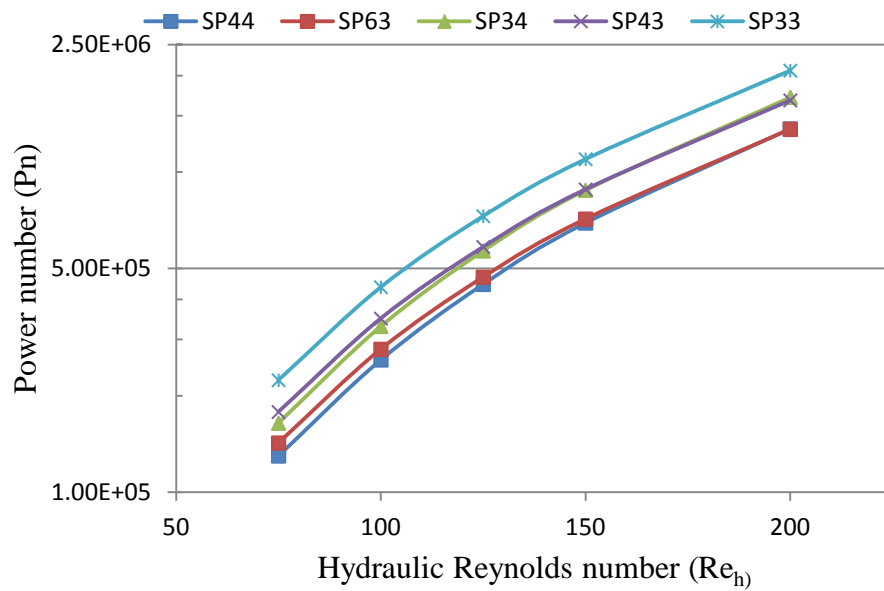
Spiral wound membrane modules normally operate at Reynolds number range below the transition to turbulent flow regime [28, 166, 173]. In this section few spacer arrangements having higher SCE values (refer to Figure 5.31) are compared at  $Re_h=75$  to 200.

Figure 5.37 (a & b) respective presents the hydraulic Reynolds number versus pressure drop and Power number for a few spacer arrangements having higher SCE values. It can be seen that SP44 presents the least pressure drop and lowest power number throughout the range of Reynolds number considered in this work. On the other hand SP33 can be seen to have highest Power number and pressure drop values throughout the Reynolds number range considered. It is interesting to note that for the pair of spacer arrangement having approximately the same hydraulic diameter (SP44 and SP63 & SP34 and SP43) the pressure drop and Power number are very close for the entire range of Reynolds number covered in this thesis. This is because for those pairs effective velocity of fluid within the computational domain is very close at the same Reynolds number in addition to closely matching porosity and hydraulic diameter. On the other hand for SP33 the spacer filaments are close to one another compared to the above mentioned two pairs and results in lower hydraulic diameter for the feed channel which increase the effective fluid velocity in the

computational domain and hence results in higher pressure drop and Power number values at the same Reynolds number.



(a)



(b)

**Figure 5.37: Hydraulic Reynolds number vs (a) Pressure drop and (b) Power number for few spacer arrangements.**

Figure 5.38 represents the comparison of different spacer arrangement in terms of Reynolds number versus SCE. It can be seen that for SP44 at the same Reynolds number the values of SCE is higher compared to the rest of the spacer arrangements from  $Re_h=75$  to 125. However, at  $Re_h \geq 150$  SP44 and SP63 yields almost the same SCE.

As already established in current study, for spacers having  $L_2 \geq 4$  there is flow reattachment and reversal seen in the vicinity of the bottom membrane surface which enhances the mass transfer coefficient at the membrane walls. Due to this reason SP44 performs better than SP63 and SP34 performs better than SP43 as indicated by higher values of SCE for those spacers compared to their counterparts for the range of Reynolds number  $Re=75$  to 125. For instance at  $Re_h=100$ , pressure drop for SP63 is about 9% higher than that for SP44 indicating more energy consumption but the SCE for SP44 is approximately 15% higher than that for SP63. This comparison leads to the conclusion that for SP63 the portion of form drag contributing to the total pressure drop is higher as compared to that for SP44 at those flow conditions and hence confirms the superiority of SP44 over SP63.

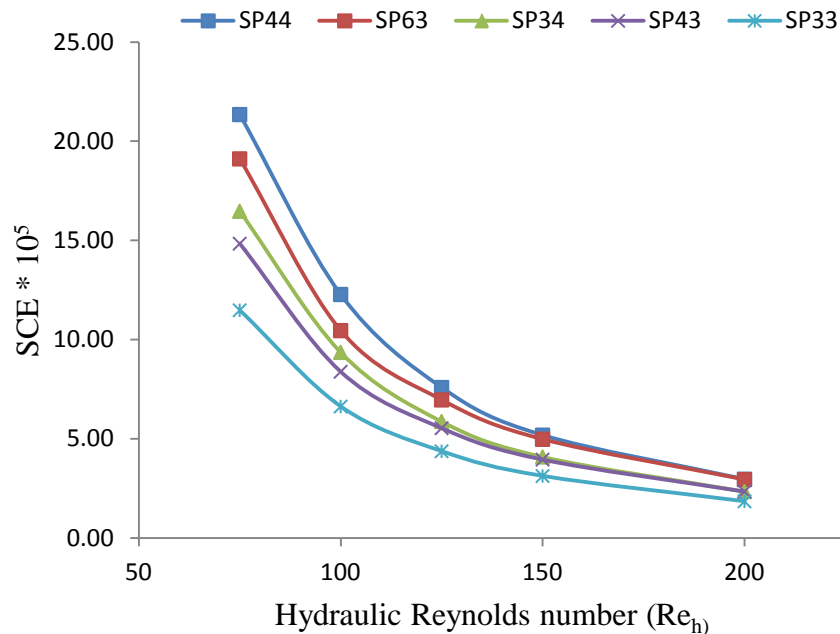
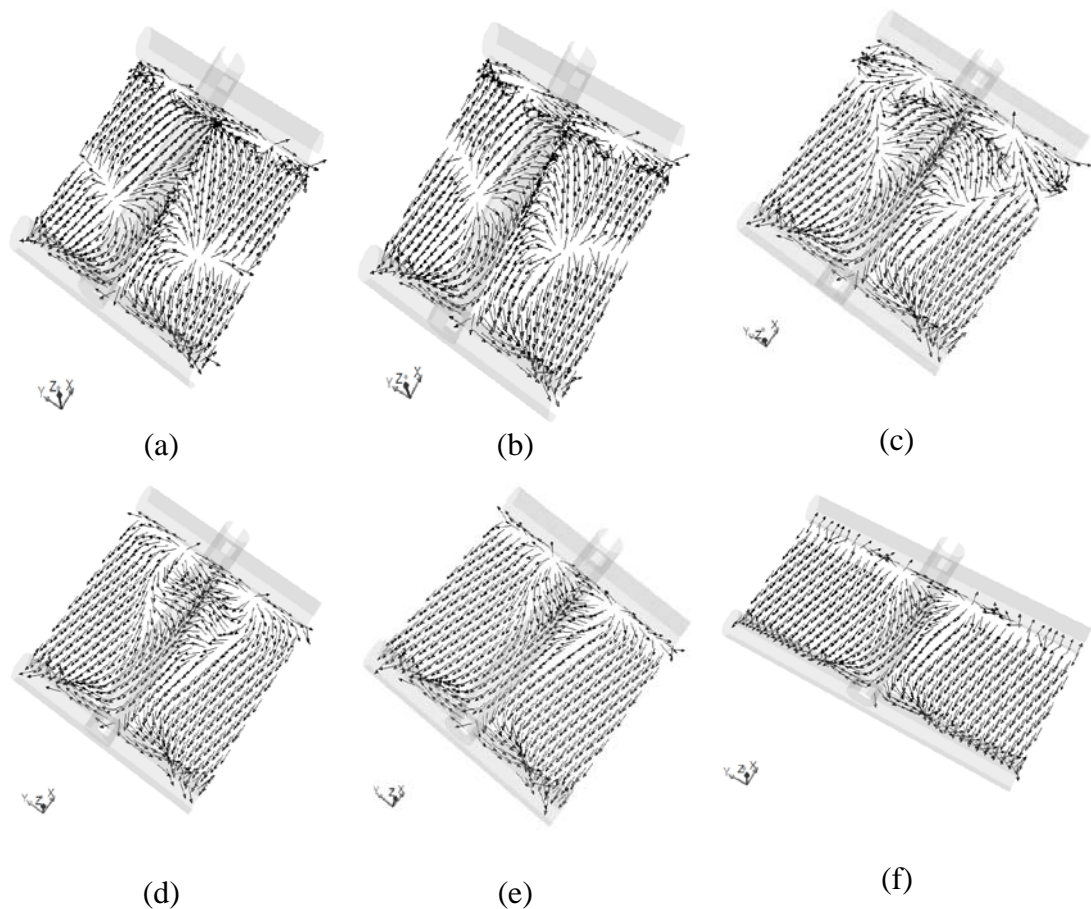


Figure 5.38: Hydraulic Reynolds number vs SCE for few spacer arrangements.

At higher Reynolds number ( $Re_h \geq 150$ ) both the pressure drop and SCE for the two spacers (SP44 and SP63) are seen to be almost the same. This is due to the fact that for SP44 with the increase in hydraulic Reynolds number the reattachment point at the bottom membrane surface shifts towards the downstream bottom filament and on further increase the reattachment phenomenon is not seen at all and only the flow reversal is evident like SP63. Shifting of reattachment point towards downstream bottom filament with an increase of hydraulic Reynolds number and eventually vanishing at  $Re_h \geq 150$  is shown in Figure 5.39.



**Figure 5.39: Velocity vectors in the vicinity of bottom membrane surface for SP44 at (a)  $Re_h=75$  (b)  $Re_h=100$  (c)  $Re_h=125$  (d)  $Re_h=150$  (e)  $Re_h=200$  and for (f) SP63 at  $Re_h=200$ .**

It can be seen that the nature of the flow is quite similar in SP44 and SP63 at  $Re_h=200$  and thus yields similar pressure drop and SCE

This shift of reattachment point at the bottom membrane surface with an increase in hydraulic Reynolds number and eventually vanishing is never described before in any study and it is an outcome of this study.

Comparison of SP44 and SP63 is shown in Table 5.3 at  $Re_h=200$ . It is quite evident that pressure drop for SP44 is marginally higher (0.31%) than that for SP63, but at the same time the ratio of area weighted mass transfer coefficient for top and bottom membrane surfaces is approximately unity (1.04) for SP44 as compared to SP63 (0.89). This would lead to almost the same fouling propensity for the two membrane surfaces in case of SP44, where as for SP63 top membrane is expected to be fouled at a quicker rate compared to the bottom wall surface as evident from the lower ratio of top to bottom membrane mass transfer coefficient and indeed not desirable in normal cross flow separation processes.

This finding further confirms that even at higher hydraulic Reynolds number SP44 is expected to perform better than SP63. It may be concluded from the discussion that for the entire hydraulic Reynolds number range considered ( $Re_h=75$  to 200) in this thesis (at which mostly real life membrane operations are carried out) SP44 performs better than SP63 and all other considered spacers.

**Table 5.3: Comparison of SP44 and SP63 at  $Re_h=200$ .**

Parameters	SP44	SP63
Pressure drop (Pa/m)	9313	9284
Top wall mass transfer coefficient (m/s)	4.71E-05	4.32E-05
Bottom wall mass transfer coefficient (m/s)	4.53E-05	4.83E-05
Top to bottom mass transfer coefficient ratio	1.04	0.89
SCE*10 <sup>5</sup>	2.96	2.94

It is evident from Figure 5.37 (b) that at the same hydraulic Reynolds number different spacer arrangements tend to have different energy losses. It therefore appears to be more reasonable to compare Sherwood number for different spacer arrangement at the same Power number. In Figure 5.40 different spacer arrangement are compared at the same Power number in terms of Sherwood number. It can be

seen from the figure that SP44 spacer arrangement tend to have higher values of Sherwood number for the Range of Power number considered in this work and tend to assure greater mass transport of solute away from the membrane surfacer compared to the rest of the arrangements considered in this thesis.

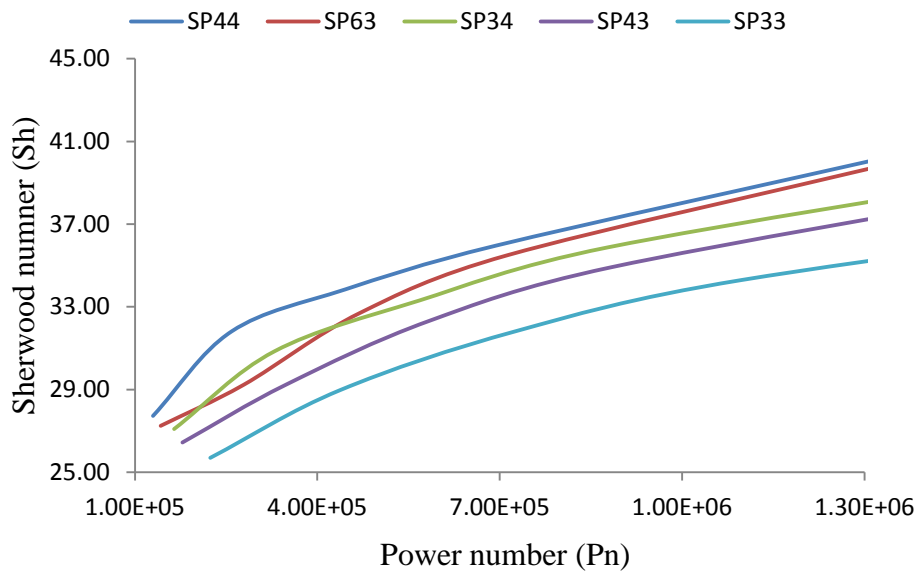


**Figure 5.40: Power number versus Sherwood number for different spacer arrangements.**

Figure 5.37 to Figure 5.40 lead to the conclusion that among all the spacer arrangement considered in this work SP44 tend to have greater mass transport of the solute away from the membrane surface to the bulk of the solution at moderate energy loss for the flow conditions expected in real life spiral wound membrane module.

## 5.9 Conclusions

This chapter deals with flow patterns generated within feed channel of spacer obstructed modules and their resulting impact on shear stress, Power number, mass transfer coefficient and relative fouling propensity of the two membrane surfaces, by altering the filament mesh spacing of ladder type feed spacers. Flow visualizations carried out in this study clearly indicate that the fluid flow patterns, mass transfer coefficient and wall shear stress distribution along with the pressure drop are largely dependent on the filament mesh spacing.

Some of the key conclusions drawn by the post processing of the simulations carried out in this chapter are as follows:

- In case of spacer filled narrow obstructed channels mass transfer coefficient stabilizes after first 3-4 filaments in the main flow direction and the flow becomes fully developed and periodic approximately at the same distance from the inlet for hydraulic Reynolds number up to 200.
- Fluid flow is of complex nature near the bottom membrane surface as compared to that at the top surface. Bulk of the fluid follows in the main flow direction in the vicinity of the top membrane surface and therefore local values of wall shear stress and mass transfer coefficient either increases or decreases simultaneously. For the spacer arrangement having  $L_2 \leq 3$  complete flow recirculation is observed in the vicinity of the bottom membrane surface, but for spacers with  $L_2 \geq 4$  ( $Re_h \leq 150$ ) reattachment and separation regions are also quite evident in addition to flow recirculation which may lead scouring action on the major portion of the bottom membrane surface. The reattachment point location shifts towards the downstream bottom filament with an increase of hydraulic Reynolds number and eventually vanishes with further increase in hydraulic Reynolds number. For instance, In case of SP44, the flow reattachment point appears to be somewhere in the middle of the two consecutive bottom filaments at  $Re_h=100$ , it shifts towards the downstream bottom filament ( $75 < Re_h \leq 150$ ) and eventually vanishes ( $Re_h \geq 150$ ). As a result at  $Re_h = 200$ , SP44 SCE is almost same as its counterpart SP63. The shift in the flow reattachment point with change in Reynolds number has never been investigated in the previous studies and is an important outcome of the present study.
- There are certain regions on the bottom membrane surface where despite very low values of wall shear stress, local mass transfer coefficient values are found to be higher. This suggests that lower values of wall shear stress do not necessarily mean lower local values of mass transfer coefficient.
- Although the wall shear stress at the top membrane surface is always higher (approximately 3 to 8 times for the spacer arrangements considered in the study) than that for the bottom wall, but interestingly the mass transfer coefficient values for the two walls are not significantly different for the

ladder type spacer arrangement having low to moderate bottom filament spacing ( $L_2 = 2$  to 4). However, when the bottom filament spacing is further increased ( $L_2 = 6$ ), there is a sharp decline in the pressure drop but the area weighted mass transfer coefficient for the top membrane wall showed a sharp reduction compared to the bottom membrane wall suggesting high fouling propensity of the top membrane wall which is not a desirable feature in membrane operations.

- Among all the spacer arrangement considered in this chapter, SP44 is found to be the best spacer arrangement (for the range  $Re_h=75$  to 200) having higher SCE values throughout the Reynolds number range considered in this thesis and would result in yielding moderate pressure drop with nearly equal and higher area weighted values of mass transfer coefficient for the two walls and would lead to lower and equal fouling tendency for top and bottom membrane surfaces.

## Nomenclature

Symbol	Description	Units
$A$	Membrane surface area	$m^2$
$A_c$	Channel cross sectional area	$m^2$
$A_{eff}$	Effective area	$m^2$
$A_i$	Face area of any computational cell	$m^2$
$b$	Channel width (in y-direction)	m
$D$	Mass diffusivity	$m^2/s$
$D_1$ and $D_2$	Top and bottom dimensionless filament thickness	-
$d_h$	Hydraulic diameter	m
$d_1$ and $d_2$	Top and bottom filament thickness	m
$f$	Friction factor	-
$h_{ch}$	Channel height	m
$k_{av}$	Average mass transfer coefficient	m/s
$k_l$	Local mass transfer coefficient	m/s
$L_c$	Channel length	m
$L_1$ and $L_2$	Top and bottom dimensionless filament spacing	-
$l_1$ and $l_2$	Top and bottom filament spacing	m

$m$	Mass flow rate	Kg/s
$P$	Pressure	Pa
$Pe$	Peclet number	-
$Pn$	Power number	-
$\Delta P$	Pressure drop	Pa
$Re_h$	Hydraulic Reynolds number	-
$SCE$	Spacer Configuration Efficacy	-
$Sh$	Sherwood number	-
$Sh_{Grober}$	Sherwood number calculated by equation 5.3.1- 9	-
$SPC$	Specific Power Consumption	Pa/s
$S_{fc}$	Wetted surface of flat channel	m <sup>2</sup>
$S_{sp}$	Wetted surface of spacer	m <sup>2</sup>
$u$	x-component of velocity	m/s
$u_{av}$	Average feed velocity or superficial velocity	m/s
$u_{eff} = u_{av}/\varepsilon$	Effective velocity or average velocity in domain	m/s
$V_{sp}$	Spacer volume	m <sup>3</sup>
$V_T$	Total volume	m <sup>3</sup>
$v$	y-component of velocity	m/s
$w$	z-component of velocity	m/s
$x$	x-coordinate	m
$Y$	Solute mass fraction	-
$Y_w$	Solute mass fraction at membrane surface or wall	-
$Y_b$	Solute mass fraction in the bulk	-
$\left[\frac{\partial Y}{\partial z}\right]_w$	Gradient of mass fraction at the membrane wall	1/m
$y$	y-coordinate	m
$z$	z-coordinate	m
$\varepsilon$	Porosity	-
$\nu$	kinematic viscosity	m <sup>2</sup> /s
$\rho$	Density	kg/m <sup>3</sup>
$\mu$	Dynamic viscosity	Pa s

# Chapter 6. Conclusions and future work

## 6.1 Conclusions

In this thesis the impact of feed spacer filament geometric parameters on performance of a spiral wound module was investigated. To enable flow visualization ANSYS FLUENT was used as the working tool and the predicted results showed excellent agreement with the previous experimental and other numerical studies. It reveals that CFD predicts hydrodynamics and mass transport within feed channel of spacer obstructed membranes quite accurately.

This thesis can be broadly divided into two parts. The first part deals with fluid flow modelling within spacer filled narrow channels without incorporating the mass transfer aspect. Fluid flow modelling can provide deep insight into the flow patterns generated within the spacer filled module and their resulting impact on the wall shear stress at the membrane surface, which may indirectly indicate the areas having higher or lower fouling propensities. But those simulations cannot provide deep understanding of the concentrations patterns generated within the module. Therefore in the second part of the thesis mass transport aspect of the spacer filled narrow channels was also taken into account by hooking a User Defined Function (UDF) with ANSYS FLUENT, in addition to fluid flow modelling. Post processing of the results revealed that spacer geometry has a large impact on flow patterns generated within the module which directly affects the power consumption, mass transport and fouling propensity of the membrane surfaces.

The conclusions drawn from the thesis are summarized as follows:

- Local values for shear stress and mass transfer coefficient varies considerably for first few filaments and flow tend to become fully developed and periodic and the mass transfer coefficient tend to stabilize after 3 to 4 filaments for all the spacer arrangement considered in this work up to  $Re_h=200$ . It may be concluded safely that for that range of  $Re_h$  the entrance effects may be eliminated after 3 to 4 filaments.

- Post processing revealed that the alignment of the feed spacers with the flow direction have great influence on the generation of secondary flow patterns through the spacer filled channels. Pressure drop in spacer filled SWM appears to depend largely on the filament orientation based on current investigations. Pressure drop and power number will be higher if the filaments are inclined more towards the channel axis and vice versa. To arrive at this conclusion simulation was carried out for a spacer arrangement having  $\theta_1$ ,  $\theta_2$  and  $\alpha$  set as  $135^\circ$ ,  $0^\circ$  and  $45^\circ$  respectively which had never been investigated in previous studies and no results are available in the literature apart from the outcomes of current work.
- The fluid flow modelling provided a deep insight to the complex flow patterns generated within membrane modules and their resulting impact on the wall shear stress at the two membrane surface. Post processing of the results revealed two distinct regions, in terms of fluid flow. The first region was of higher fluid velocity zone appearing just above the bottom wall filament in the vicinity of the top membrane surface and second region was the zone where the fluid velocity was lower and flow reattachment and recirculation was seen in the vicinity of bottom membrane surface. Due to the co-existence of these two distinct regions shear stress distribution was different from one another at the two membrane surfaces. The position of the reattachment point (dictating the size of the recirculation region), size of the high velocity region and area weighted average values for the wall shear stress on top and bottom wall depend largely on the filament dimensionless spacing. While decreasing the bottom filament dimensionless spacing (from 6 to 4) shear stress exerted on the bottom membrane surface first decreases due to shift in the reattachment point towards the downstream bottom filament which inturns reduces the available length for the reattaching fluid to accelerate before striking the downstream bottom filament in the normal flow direction. On further decreasing the bottom filament dimensionless mesh spacing (from 4 to 2) the shear stress exerted on the bottom membrane surface tend to increase as the reattachment phenomenon disappears (where the shear stress is expected to be minimal) and the fluid shows total flow reversal after striking the downstream

bottom transverse filament. The pressure drop and shear stress exerted on the top membrane surface increases with decrease in top/or bottom filament dimensionless spacing.

- The phenomena of flow reversal and recirculation in the vicinity of bottom membrane surface depends on the bottom filament dimensionless spacing ( $L_2$ ). For spacer arrangements having  $L_2 \leq 3$  flow reattachment phenomenon is not seen and fluid tends to recirculate only after striking the downstream bottom filament. For spacer arrangements having  $L_2 \geq 4$  fluid tend to reattach with the bottom membrane surface somewhere in the middle of the two consecutive bottom filaments (at  $Re_h=100$ ). The position of the reattachment point is seen to be dependent on bottom filament mesh spacing ( $L_2$ ) and hydraulic Reynolds number ( $Re_h$ ). The reattachment zone tend to shift towards the upstream bottom filament when  $L_2$  is increased and tend to move towards the downstream bottom filament with an increase in  $Re_h$  and on further increase, eventually disappears. Although, previous studies mention the existence of fluid reattachment phenomena, but the shift of the reattachment zone towards downstream bottom filament and eventual disappearance with further increase in  $Re_h$  is outcome of the present study.
- Wall shear stress at the top membrane surface is always higher (approximately 3 to 8 times for the spacer arrangements considered in the study at  $Re_h=100$ ) than that for the bottom wall, but interestingly the mass transfer coefficient values for the two walls are not significantly different for the ladder type spacer arrangement having low to moderate bottom filament spacing ( $L_2 = 2$  to 4). However, when the bottom filament spacing is further increased ( $L_2 = 6$ ), there is a sharp decline in the pressure drop but the area weighted mass transfer coefficient for the top membrane wall showed a sharp reduction compared to the bottom membrane wall suggesting high fouling propensity of the top membrane wall which is not a desirable feature in membrane operations.
- For the spacer configurations having  $L_2=4$  (at  $Re_h=100$ ) there is a dip in the average bottom wall shear stress which is due to the fluid flow reattaching somewhere in the middle of the two consecutive bottom filament and partly been recirculated. But at the same time the induced directional changes to the

flow are responsible for moderately higher average mass transfer coefficient values. However when  $L_2 < 4$  the average mass transfer coefficient values at the bottom membrane surface have higher values but at the same time the pressure drop is also significantly higher and those arrangements lead to lower SCE values. When  $L_2$  is increase from 4 to 6 the reattachment point is shifted closer to the upstream bottom filament and provides sufficient length for the flowing fluid to accelerate in the normal flow direction and results in higher average bottom wall shear stress, but the impact of this increase in  $L_2$  do not result in significant increase in the bottom wall mass transfer coefficient and adversely effects the top wall mass transfer coefficient. This can be attributed to the fact that for spacer configurations having  $L_2 = 6$  the relative region of high velocity in the vicinity of the top membrane wall shrinks and lead to lower area weighted mass transfer coefficient for the top membrane wall. Although area weighted mass transfer coefficient at the bottom membrane surface is higher when we compare spacers configurations having  $L_2=6$  with those having  $L_2=4$ , but at the top membrane surface the area weighted mass transfer coefficient reduces significantly giving an impression that for spacers having  $L_2=6$  the top membrane surface would be fouled more rapidly as compared to the bottom membrane surface which is not desirable at all for any membrane operations.

- There are certain regions on the bottom membrane surface where despite very low values of wall shear stress, local mass transfer coefficient values are found to be higher (flow reattachment and separation regions). This suggests that lower values of wall shear stress do not necessarily mean lower local values of mass transfer coefficient.
- All the spacers arrangements considered in this work were compared on the basis of Spacer Configuration Efficacy (SCE), which in this thesis is defined as the ratio of Sherwood number to Power number. Spacer having higher SEC values would lead to higher mass transport of the solute away from the membrane walls to the bulk of the solution at moderate pressure losses. It has been concluded by carrying out mass transfer simulations for different spacer arrangements that the spacer arrangement having top and bottom filament

dimensionless ratio equal to 4 perform better than all the other arrangements for  $Re_h$  up to 200.

The results emanated out of the current study are considered to be of significant value and could potentially lead to the development of efficient membrane modules with optimum spacer arrangements for RO operations.

## 6.2 Recommendations for future research

- In this thesis, only 2-layered cylindrical feed spacers were considered. Some of the experimental studies utilizing multi-layered novel spacer arrangements have better performance than the conventional 2-layerd arrangements. CFD may be utilized to check their claims and can provide better insight into the flow patterns generated by their use in the feed channel. Based on the findings from the current work novel spacer arrangements can be suggested which may lead to higher mass transport with moderate energy loss.
- In most of the real life cross flow Reverse Osmosis membrane operations, the permeation velocity is quite lower than the feed velocity and recovers only 10 to 15 % of the feed as product. This fact justifies the dissolving wall assumption used for simulations involving mass transfer in this thesis. However, in future there will be need for membrane operations having higher recovery rates. As a follow-up to the current studies a new model may be developed to investigate mass transport of the solute at higher recovery rates treating the membrane as porous surfaces.
- In this thesis, only one set of translational periodic boundary conditions was used to limit the extent of computational domain (in y direction) but along the flow direction the computational domain was extended to 6 bottom filaments which was found adequate to eliminate the entrance effects for the range of  $Re_h$  up to 200 for the spacers considered in this work. However, for further higher Reynolds number this entry length appears to be insufficient. Instead of increasing the domain extent along the flow direction, which would demand higher computational time and capabilities, it is suggested to apply another set of periodic boundary conditions at the two corresponding faces (inlet and outlet) which indeed would require another User Defined Function (UDF) to define the velocity profile.

- Current study deals with the mass transport of a single solute dissolved in water and can be extended to investigate the sensitivity of the current approach for different electrolytes.
- The concept of SEC can be utilized to optimize filaments flow attack angle. To validate the findings of the present research work with the experimental work, autopsy of a used membrane housing same spacer configuration should be carried out. Contours of wall shear stress and mass transfer coefficient can be compared with the areas of high, low and moderate fouling to validate CFD results emanated out of the present research work.

## References

1. H.K. L., *The growth of membrane technology*. Journal of Membrane Science, 1982. **10**(2-3): p. 81-181.
2. Khawaji, A.D., I.K. Kutubkhanah, and J.M. Wie. *Advances in seawater desalination technologies*. 2007: Elsevier Science Bv.
3. Wang, L.K., J.P. Chen, and N.K. Shamma, *Membrane and Desalination Technologies*. Vol. 13. 2008: Humana Pr Inc.
4. Sourirajan, S., *Reverse osmosis*. 1970: London, UK: Logos Press Ltd.
5. Neal, P.R., et al., *The effect of filament orientation on critical flux and particle deposition in spacer-filled channels*. Journal of Membrane Science, 2003. **214**(2): p. 165-178.
6. Schwinge, J., et al., *Spiral wound modules and spacers: Review and analysis*. Journal of Membrane Science, 2004. **242**(1-2): p. 129-153.
7. Fritzmann, C., et al., *State-of-the-art of reverse osmosis desalination*. Desalination, 2007. **216**(1-3): p. 1-76.
8. Drioli, E., A. Criscuoli, and E. Curcio, *Integrated membrane operations for seawater desalination*. Desalination, 2002. **147**(1-3): p. 77-81.
9. Guohua, C., et al., *Treatment of textile desizing wastewater by pilot scale nanofiltration membrane separation*. Journal of Membrane Science, 1997. **127**(1): p. 93-99.
10. Jean-Pierre, D.W., *Surface water potabilisation by means of a novel nanofiltration element*. Desalination, 1997. **108**(1-3): p. 153-157.
11. M, G.K., *Development of reverse osmosis desalination membranes composition and configuration: Future prospects*. Desalination, 2003. **153**(1-3): p. 295-304.
12. Flemming, H.C., et al., *Biofouling—the Achilles heel of membrane processes*. Desalination, 1997. **113**(2-3): p. 215-225.
13. Hong, S. and M. Elimelech, *Chemical and physical aspects of natural organic matter (NOM) fouling of nanofiltration membranes*. Journal of Membrane Science, 1997. **132**(2): p. 159-181.
14. Le Gouellec, Y.A. and M. Elimelech, *Calcium sulfate (gypsum) scaling in nanofiltration of agricultural drainage water*. Journal of Membrane Science, 2002. **205**(1-2): p. 279-291.
15. Potts, D.E., R.C. Ahlert, and S.S. Wang, *A critical review of fouling of reverse osmosis membranes*. Desalination, 1981. **36**(3): p. 235-264.
16. Hoek, E.M.V., et al., *Modeling the effects of fouling on full-scale reverse osmosis processes*. Journal of Membrane Science, 2008. **314**(1-2): p. 33-49.
17. Howell, J.A., V. Sanchez, and R. Field, *Membranes in bioprocessing: theory and applications*. 1993: Chapman & Hall.
18. Redondo, J.A. and I. Lomax, *Experiences with the pre-treatment of raw water with high fouling potential for reverse osmosis plant using FILMTEC membranes*. Desalination, 1997. **110**(1-2): p. 167-182.
19. Fárková, J., *The pressure drop in membrane module with spacers*. Journal of Membrane Science, 1991. **64**(1-2): p. 103-111.
20. Geraldes, V., V. Semião, and M.N. de Pinho, *Flow management in nanofiltration spiral wound modules with ladder-type spacers*. Journal of Membrane Science, 2002. **203**(1-2): p. 87-102.
21. Geraldes, V., V. Semião, and M.N. de Pinho, *The effect of the ladder-type spacers configuration in NF spiral-wound modules on the concentration boundary layers disruption*. Desalination, 2002. **146**(1-3): p. 187-194.

22. Geraldes, V., V. Semião, and M. Norberta Pinho, *Hydrodynamics and concentration polarization in NF/RO spiral-wound modules with ladder-type spacers*. Desalination, 2003. **157**(1-3): p. 395-402.
23. Zimmerer, C.C. and V. Kottke, *Effects of spacer geometry on pressure drop, mass transfer, mixing behavior, and residence time distribution*. Desalination, 1996. **104**(1-2): p. 129-134.
24. G. Chatterjee, S. and G. Belfort, *Fluid flow in an idealized spiral wound membrane module*. Journal of Membrane Science, 1986. **28**(2): p. 191-208.
25. Da Costa, A.R., et al., *Optimal channel spacer design for ultrafiltration*. Journal of Membrane Science, 1991. **62**(3): p. 275-291.
26. Fane, A., P. Beatson, and H. Li, *Membrane fouling and its control in environmental applications*. Water science and technology, 2000: p. 303-308.
27. Da Costa, A.R. and A.G. Fane, *Net-type spacers: effect of configuration on fluid flow path and ultrafiltration flux*. Industrial & engineering chemistry research, 1994. **33**(7): p. 1845-1851.
28. Fimbres-Weihs, G.A. and D.E. Wiley, *Numerical study of mass transfer in three-dimensional spacer-filled narrow channels with steady flow*. Journal of Membrane Science, 2007. **306**(1-2): p. 228-243.
29. Li, Y.-L. and K.-L. Tung, *CFD simulation of fluid flow through spacer-filled membrane module: selecting suitable cell types for periodic boundary conditions*. Desalination, 2008. **233**(1-3): p. 351-358.
30. Thomas, D.G., W.L. Griffith, and R.M. Keller, *The role of turbulence promoters in hyperfiltration plant optimization*. Desalination, 1971. **9**(1): p. 33-50.
31. Fimbres-Weihs, G., D. Wiley, and D. Fletcher, *Unsteady flows with mass transfer in narrow zigzag spacer-filled channels: a numerical study*. Industrial & engineering chemistry research, 2006. **45**(19): p. 6594-6603.
32. Kang, I.S. and H.N. Chang, *The effect of turbulence promoters on mass transfer—numerical analysis and flow visualization*. Int. J. Heat Mass Transfer, 1982. **25**(8): p. 1167-1181.
33. Gimmelshtein, M.M. and R. Semiat, *Investigation of flow next to membrane walls*. Journal of Membrane Science, 2005. **264**(1-2): p. 137-150.
34. Li, H., et al., *Direct observation of particle deposition on the membrane surface during crossflow microfiltration*. Journal of Membrane Science, 1998. **149**(1): p. 83-97.
35. Versteeg, H.K. and W. Malalasekera, *An introduction to computational fluid dynamics: the finite volume method*. 2007: Prentice Hall.
36. Ghidossi, R., D. Veyret, and P. Moulin, *Computational fluid dynamics applied to membranes: State of the art and opportunities*. Chemical Engineering and Processing, 2006. **45**(6): p. 437-454.
37. Cath, T.Y., A.E. Childress, and M. Elimelech, *Forward osmosis: Principles, applications, and recent developments*. Journal of Membrane Science, 2006. **281**(1-2): p. 70-87.
38. Baker, R.W., *Membrane separation systems: recent developments and future directions*. 1991: William Andrew Publishing.
39. Schäfer, A.I., A.G. Fane, and T.D. Waite, *Nanofiltration: principles and applications*. 2005: Elsevier Science.
40. Amjad, Z., *Reverse osmosis: membrane technology, water chemistry & industrial applications*. 1993: Chapman & Hall.
41. Lien, L.A., *Spiral-wound membrane with improved permeate carrier*. 1989, Google Patents.

42. Kucera, J., *Reverse Osmosis: Design, Processes, and Applications for Engineers*. Vol. 35. 2010: Wiley-Scrivener.
43. Bartels, C., M. Hirose, and H. Fujioka, *Performance advancement in the spiral wound RO/NF element design*. *Desalination*, 2008. **221**(1-3): p. 207-214.
44. Rautenbach, R. and R. Albrecht, *Membrane processes*. 1989: John Wiley & Sons Inc.
45. Mulder, M., *Basic principles of membrane technology*. 1996: Springer.
46. Cheryan, M., *Ultrafiltration and microfiltration handbook*. 1998: CRC press.
47. Evangelista, F. and G. Jonsson, *OPTIMAL DESIGN AND PERFORMANCE OF SPIRAL WOUND MODULES II: ANALYTICAL METHOD*. *Chemical Engineering Communications*, 1988. **72**(1): p. 83-94.
48. Evangelista, F. and G. Jonsson, *Optimal Design and Performance of Spiral Wound Modules I: Numerical Method*. *Chemical Engineering Communications*, 1988. **72**(1): p. 69-81.
49. Hwang, S.T. and K. Kammermeyer, *Membranes in separations*. Vol. 8. 1984.
50. Sherwood, T., et al., *Salt concentration at phase boundaries in desalination by reverse osmosis*. *Industrial & Engineering Chemistry Fundamentals*, 1965. **4**(2): p. 113-118.
51. Sablani, S., et al., *Concentration polarization in ultrafiltration and reverse osmosis: a critical review*. *Desalination*, 2001. **141**(3): p. 269-289.
52. Porter, M., *Concentration polarization with membrane ultrafiltration*. *Industrial & Engineering Chemistry Product Research and Development*, 1972. **11**(3): p. 234-248.
53. Brian, P.L.T., *Concentration Polarization in Reverse Osmosis Desalination with Variable Flux and Incomplete Salt Rejection*. *Industrial & Engineering Chemistry Fundamentals*, 1965. **4**(4): p. 439-445.
54. Matthiasson, E. and B. Sivik, *Concentration polarization and fouling*. *Desalination*, 1980. **35**: p. 59-103.
55. Bird, R.B., W.E. Stewart, and Lightfoot, *Transport Phenomena*. John & Sons, New York. 1960.
56. Deissler, R.G., *Analysis of turbulent heat transfer, mass transfer, and friction in smooth tubes at high Prandtl and Schmidt numbers*. 1954, NATIONAL AERONAUTICS AND SPACE ADMINISTRATION CLEVELAND OH GLENN RESEARCH CENTER.
57. Skelland, A.H.P., *Diffusional mass transfer*. 1974: Wiley New York.
58. Mason, E., R.P. Wendt, and E. Bresler, *Test of the Onsager relation for ideal gas transport in membranes*. *J. Chem. Soc., Faraday Trans. 2*, 1972. **68**: p. 1938-1950.
59. Kozinski, A. and E. Lightfoot, *Protein ultrafiltration: a general example of boundary layer filtration*. *AIChE Journal*, 1972. **18**(5): p. 1030-1040.
60. McCabe, W.L., J.C. Smith, and P. Harriott, *Unit operations of chemical engineering*. 2005: McGraw-Hill.
61. Schock, G. and A. Miquel, *Mass transfer and pressure loss in spiral wound modules*. *Desalination*, 1987. **64**: p. 339-352.
62. HUANG, H.Z. and W.E.N.Q. TAO, *An experimental study on heat/mass transfer and pressure drop characteristics for arrays of nonuniform plate length positioned obliquely to the flow direction*. *Journal of heat transfer*, 1993. **115**(3): p. 568-575.
63. Li, F., et al., *Optimization of commercial net spacers in spiral wound membrane modules*. *Journal of Membrane Science*, 2002. **208**(1-2): p. 289-302.
64. Isaacson, M. and A.A. Sonin, *Sherwood number and friction factor correlations for electro dialysis systems, with application to process optimization*. *Industrial & Engineering Chemistry Process Design and Development*, 1976. **15**(2): p. 313-321.

65. Koutsou, C., S. Yiantsios, and A. Karabelas, *Numerical simulation of the flow in a plane-channel containing a periodic array of cylindrical turbulence promoters*. Journal of Membrane Science, 2004. **231**(1-2): p. 81-90.
66. Koutsou, C.P., S.G. Yiantsios, and A.J. Karabelas, *Direct numerical simulation of flow in spacer-filled channels: Effect of spacer geometrical characteristics*. Journal of Membrane Science, 2007. **291**(1-2): p. 53-69.
67. Al-Bastaki, N. and A. Abbas, *Use of fluid instabilities to enhance membrane performance: a review*. Desalination, 2001. **136**(1-3): p. 255-262.
68. Li, Q.Y., Z.F. Cui, and D.S. Pepper, *Effect of bubble size and frequency on the permeate flux of gas sparged ultrafiltration with tubular membranes*. Chemical Engineering Journal, 1997. **67**(1): p. 71-75.
69. Kyllönen, H.M., P. Pirkonen, and M. Nyström, *Membrane filtration enhanced by ultrasound: a review*. Desalination, 2005. **181**(1-3): p. 319-335.
70. Muthukumaran, S., et al., *Mechanisms for the ultrasonic enhancement of dairy whey ultrafiltration*. Journal of Membrane Science, 2005. **258**(1-2): p. 106-114.
71. Muthukumaran, S., et al., *The optimisation of ultrasonic cleaning procedures for dairy fouled ultrafiltration membranes*. Ultrasonics Sonochemistry, 2005. **12**(1-2): p. 29-35.
72. Ng, H.Y., et al., *Novel 16-inch spiral-wound RO systems for water reclamation — a quantum leap in water reclamation technology*. Desalination, 2008. **225**(1-3): p. 274-287.
73. Li, J., et al., *Quantitative study of the effect of electromagnetic field on scale deposition on nanofiltration membranes via UTDR*. Water Research, 2007. **41**(20): p. 4595-4610.
74. Saxena, A., et al., *Membrane-based techniques for the separation and purification of proteins: An overview*. Advances in Colloid and Interface Science, 2009. **145**(1-2): p. 1-22.
75. Al-Bastaki, N.M. and A. Abbas, *Improving the permeate flux by unsteady operation of a RO desalination unit*. Desalination, 1999. **123**(2-3): p. 173-176.
76. Kim, S. and E. Hoek, *Modeling concentration polarization in reverse osmosis processes*. Desalination, 2005. **186**(1-3): p. 111-128.
77. Murthy, Z.V.P. and S.K. Gupta, *Estimation of mass transfer coefficient using a combined nonlinear membrane transport and film theory model*. Desalination, 1997. **109**(1): p. 39-49.
78. Nilsson, J.L., *Protein fouling of UF membranes: causes and consequences*. Journal of Membrane Science, 1990. **52**(2): p. 121-142.
79. Shu-Sen, W., *Effect of solution viscosity on ultrafiltration flux*. Journal of Membrane Science, 1988. **39**(2): p. 187-194.
80. Song, L. and M. Elimelech, *Theory of concentration polarization in crossflow filtration*. J. Chem. Soc., Faraday Trans., 1995. **91**(19): p. 3389-3398.
81. Wijmans, J.G., et al., *Hydrodynamic resistance of concentration polarization boundary layers in ultrafiltration*. Journal of Membrane Science, 1985. **22**(1): p. 117-135.
82. De, S. and P.K. Bhattacharya, *Prediction of mass-transfer coefficient with suction in the applications of reverse osmosis and ultrafiltration*. Journal of Membrane Science, 1997. **128**(2): p. 119-131.
83. Bhattacharya, S. and S.-T. Hwang, *Concentration polarization, separation factor, and Peclet number in membrane processes*. Journal of Membrane Science, 1997. **132**(1): p. 73-90.

84. Miranda, J.M. and J.B.L.M. Campos, *Mass transport regimes in a laminar boundary layer with suction—parallel flow and high Peclet number*. International Journal of Heat and Mass Transfer, 2004. **47**(4): p. 775-785.
85. Jonsson, G., *Boundary layer phenomena during ultrafiltration of dextran and whey protein solutions*. Desalination, 1984. **51**(1): p. 61-77.
86. Van Oers, C., et al., *Unsteady-state flux behaviour in relation to the presence of a gel layer*. Journal of Membrane Science, 1992. **73**(2-3): p. 231-246.
87. Rautenbach, R. and F.P. Helmus, *Some considerations on mass-transfer resistances in solution—diffusion-type membrane processes*. Journal of Membrane Science, 1994. **87**(1-2): p. 171-180.
88. Mc Donogh, R.M., et al., *Experimental in situ measurement of concentration polarisation during ultra- and micro-filtration of bovine serum albumin and Dextran Blue solutions*. Journal of Membrane Science, 1995. **104**(1-2): p. 51-63.
89. Sandeep K, K., *Unsteady state flux response: a method to determine the nature of the solute and gel layer in membrane filtration*. Journal of Membrane Science, 2001. **188**(1): p. 9-20.
90. Baker, R. and H. Strathmann, *Ultrafiltration of macromolecular solutions with high-flux membranes*. Journal of Applied Polymer Science, 1970. **14**(5): p. 1197-1214.
91. Gupta, V.K., et al., *Characterization of nanofiltration and reverse osmosis membrane performance for aqueous salt solutions using irreversible thermodynamics*. Desalination, 2007. **208**(1-3): p. 1-18.
92. Khayet, M. and J. Mengual, *Effect of salt type on mass transfer in reverse osmosis thin film composite membranes\**. Desalination, 2004. **168**: p. 383-390.
93. Sutzkover, I., D. Hasson, and R. Semiat, *Simple technique for measuring the concentration polarization level in a reverse osmosis system*. Desalination, 2000. **131**(1-3): p. 117-127.
94. Song, L. and S. Yu, *Concentration polarization in crossflow reverse osmosis*. AIChE Journal, 1999. **45**(5): p. 921-928.
95. Song, L., *A new model for the calculation of the limiting flux in ultrafiltration*. Journal of Membrane Science, 1998. **144**(1-2): p. 173-185.
96. Song, L., et al., *Performance limitation of the full-scale reverse osmosis process*. Journal of Membrane Science, 2003. **214**(2): p. 239-244.
97. Song, L., et al., *Emergence of thermodynamic restriction and its implications for full-scale reverse osmosis processes*. Desalination, 2003. **155**(3): p. 213-228.
98. Boudinar, M.B., W.T. Hanbury, and S. Avlonitis, *Numerical simulation and optimisation of spiral-wound modules*. Desalination, 1992. **86**(3): p. 273-290.
99. Van der Meer, W. and J. Van Dijk, *Theoretical optimization of spiral-wound and capillary nanofiltration modules*. Desalination, 1997. **113**(2-3): p. 129-146.
100. Avlonitis, S., W. Hanbury, and M.B. Boudinar, *Spiral wound modules performance. An analytical solution, part I*. Desalination, 1991. **81**(1-3): p. 191-208.
101. Avlonitis, S., W. Hanbury, and M.B. Boudinar, *Spiral wound modules performance an analytical solution: Part II*. Desalination, 1993. **89**(3): p. 227-246.
102. Rautenbach, R. and W. Dahm, *Design and optimization of spiral-wound and hollow fiber RO-modules*. Desalination, 1987. **65**(0): p. 259-275.
103. Sablani, S.S., et al., *Influence of spacer thickness on permeate flux in spiral-wound seawater reverse osmosis systems*. Desalination, 2002. **146**(1-3): p. 225-230.
104. Schwinge, J., et al., *Estimation of foulant deposition across the leaf of a spiral-wound module*. Desalination, 2002. **146**(1-3): p. 203-208.

105. Zhou, W., L. Song, and T.K. Guan, *A numerical study on concentration polarization and system performance of spiral wound RO membrane modules*. Journal of Membrane Science, 2006. **271**(1-2): p. 38-46.
106. Pellerin, E., et al., *Turbulent transport in membrane modules by CFD simulation in two dimensions*. Journal of Membrane Science, 1995. **100**(2): p. 139-153.
107. Geraldes, V.M., V.A. Semião, and M.N. de Pinho, *Nanofiltration mass transfer at the entrance region of a slit laminar flow*. Industrial & engineering chemistry research, 1998. **37**(12): p. 4792-4800.
108. Geraldes, V., V. Semiao, and M. Norberta de Pinho, *The effect on mass transfer of momentum and concentration boundary layers at the entrance region of a slit with a nanofiltration membrane wall*. Chemical engineering science, 2002. **57**(5): p. 735-748.
109. Geraldes, V., V. Semiao, and M.N. de Pinho, *Flow and mass transfer modelling of nanofiltration*. Journal of Membrane Science, 2001. **191**(1-2): p. 109-128.
110. Geraldes, V., V. Semião, and M.N. Pinho, *Numerical modelling of mass transfer in slits with semi-permeable membrane walls*. Engineering Computations: Int J for Computer-Aided Engineering, 2000. **17**(3): p. 192-218.
111. Darcovich, K., et al., *CFD-assisted thin channel membrane characterization module design*. Journal of Membrane Science, 1997. **124**(2): p. 181-193.
112. Ahmad, A., et al., *Integrated CFD simulation of concentration polarization in narrow membrane channel*. Computers & chemical engineering, 2005. **29**(10): p. 2087-2095.
113. Ahmad, A. and K. Lau, *Modeling, simulation, and experimental validation for aqueous solutions flowing in nanofiltration membrane channel*. Industrial & engineering chemistry research, 2007. **46**(4): p. 1316-1325.
114. Karode, S.K., *Laminar flow in channels with porous walls, revisited*. Journal of Membrane Science, 2001. **191**(1-2): p. 237-241.
115. Alexiadis, A., et al., *Dynamic response of a high-pressure reverse osmosis membrane simulation to time dependent disturbances*. Desalination, 2006. **191**(1-3): p. 397-403.
116. Alexiadis, A., et al., *CFD modelling of reverse osmosis membrane flow and validation with experimental results*. Desalination, 2007. **217**(1-3): p. 242-250.
117. de Pinho, M.N., V. Semião, and V. Geraldes, *Integrated modeling of transport processes in fluid/nanofiltration membrane systems*. Journal of Membrane Science, 2002. **206**(1-2): p. 189-200.
118. Magueijo, V., M.N. de Pinho, and V. Geraldes, *Numerical and experimental study of mass transfer in lysozyme ultrafiltration*. Desalination, 2002. **145**(1-3): p. 193-199.
119. Lyster, E. and Y. Cohen, *Numerical study of concentration polarization in a rectangular reverse osmosis membrane channel: Permeate flux variation and hydrodynamic end effects*. Journal of Membrane Science, 2007. **303**(1-2): p. 140-153.
120. Rahardianto, A., et al., *Diagnostic characterization of gypsum scale formation and control in RO membrane desalination of brackish water*. Journal of Membrane Science, 2006. **279**(1-2): p. 655-668.
121. Wiley, D.E. and D.F. Fletcher, *Techniques for computational fluid dynamics modelling of flow in membrane channels*. Journal of Membrane Science, 2003. **211**(1): p. 127-137.
122. Wiley, D.E. and D.F. Fletcher, *Computational fluid dynamics modelling of flow and permeation for pressure-driven membrane processes*. Desalination, 2002. **145**(1-3): p. 183-186.

123. Fletcher, D. and D. Wiley, *A computational fluids dynamics study of buoyancy effects in reverse osmosis*. Journal of Membrane Science, 2004. **245**(1-2): p. 175-181.
124. Levy, P.F. and R.S. Earle, *The effect of channel height and channel spacers on flux and energy requirements in crossflow filtration*. Journal of Membrane Science, 1994. **91**(1-2): p. 135-143.
125. Polyakov, S. and F. Karelin, *Turbulence promoter geometry: its influence on salt rejection and pressure losses of a composite-membrane spiral wound module*. Journal of Membrane Science, 1992. **75**(3): p. 205-211.
126. Winograd, Y., A. Solan, and M. Toren, *Mass transfer in narrow channels in the presence of turbulence promoters*. Desalination, 1973. **13**(2): p. 171-186.
127. Da Costa, A., A. Fane, and D. Wiley, *Ultrafiltration of whey protein solutions in spacer-filled flat channels*. Journal of Membrane Science, 1993. **76**(2-3): p. 245-254.
128. Da Costa, A., A. Fane, and D. Wiley, *Spacer characterization and pressure drop modelling in spacer-filled channels for ultrafiltration*. Journal of Membrane Science, 1994. **87**(1-2): p. 79-98.
129. Eriksson, P. and C. Escondido, *New Design Feed Channel Spacer in Spiral Wound Elements for Pretreatment Cost Reduction, Report No. 45, Desalination Research and Development Program, 1998*.
130. Li, H., et al., *An assessment of depolarisation models of crossflow microfiltration by direct observation through the membrane*. Journal of Membrane Science, 2000. **172**(1-2): p. 135-147.
131. Schwinge, J., et al., *Characterization of a zigzag spacer for ultrafiltration*. Journal of Membrane Science, 2000. **172**(1-2): p. 19-31.
132. Schwinge, J., D. Wiley, and A. Fane. *Novel spacer design improves spiral wound module performance*. in, *6th World Congress of Chemical Engineering 2001*. Melbourne.
133. Schwinge, J., D. Wiley, and A. Fane, *Novel spacer design improves observed flux*. Journal of Membrane Science, 2004. **229**(1-2): p. 53-61.
134. Yang, G., W. Xing, and N. Xu, *Concentration polarization in spiral-wound nanofiltration membrane elements*. Desalination, 2003. **154**(1): p. 89-99.
135. Li, F., et al., *Experimental validation of CFD mass transfer simulations in flat channels with non-woven net spacers*. Journal of Membrane Science, 2004. **232**(1-2): p. 19-30.
136. Cao, Z., D.E. Wiley, and A.G. Fane, *CFD simulations of net-type turbulence promoters in a narrow channel*. Journal of Membrane Science, 2001. **185**(2): p. 157-176.
137. Schwinge, J., D. Wiley, and D. Fletcher, *Simulation of the flow around spacer filaments between channel walls. 2. Mass-transfer enhancement*. Industrial & engineering chemistry research, 2002. **41**(19): p. 4879-4888.
138. Schwinge, J., D. Wiley, and D. Fletcher, *A CFD study of unsteady flow in narrow spacer-filled channels for spiral-wound membrane modules*. Desalination, 2002. **146**(1-3): p. 195-201.
139. Schwinge, J., D.E. Wiley, and D.F. Fletcher, *Simulation of the flow around spacer filaments between narrow channel walls. 1. Hydrodynamics*. Industrial & engineering chemistry research, 2002. **41**(12): p. 2977-2987.
140. Schwinge, J., D.E. Wiley, and D.F. Fletcher, *Simulation of unsteady flow and vortex shedding for narrow spacer-filled channels*. Industrial & engineering chemistry research, 2003. **42**(20): p. 4962-4977.

141. Geraldes, V., V. Semiao, and M. Norberta de Pinho, *Concentration polarisation and flow structure within nanofiltration spiral-wound modules with ladder-type spacers*. Computers & structures, 2004. **82**(17): p. 1561-1568.
142. Ahmad, A., K. Lau, and M. Abu Bakar, *Impact of different spacer filament geometries on concentration polarization control in narrow membrane channel*. Journal of Membrane Science, 2005. **262**(1-2): p. 138-152.
143. Ahmad, A. and K. Lau, *Impact of different spacer filaments geometries on 2D unsteady hydrodynamics and concentration polarization in spiral wound membrane channel*. Journal of Membrane Science, 2006. **286**(1-2): p. 77-92.
144. Ma, S., S. Kassinos, and D. Fatta, *Assessing the accuracy of wall concentration estimation based on averaged permeate velocity in spacer-filled reverse osmosis (RO) membrane systems*. Industrial & engineering chemistry research, 2006. **45**(24): p. 8134-8144.
145. Ma, S. and L. Song, *Numerical study on permeate flux enhancement by spacers in a crossflow reverse osmosis channel*. Journal of Membrane Science, 2006. **284**(1-2): p. 102-109.
146. Ma, S., et al., *A 2-D streamline upwind Petrov/Galerkin finite element model for concentration polarization in spiral wound reverse osmosis modules*. Journal of Membrane Science, 2004. **244**(1-2): p. 129-139.
147. Song, L. and S. Ma, *Numerical studies of the impact of spacer geometry on concentration polarization in spiral wound membrane modules*. Industrial & engineering chemistry research, 2005. **44**(20): p. 7638-7645.
148. Subramani, A., S. Kim, and E. Hoek, *Pressure, flow, and concentration profiles in open and spacer-filled membrane channels*. Journal of Membrane Science, 2006. **277**(1-2): p. 7-17.
149. Modek, M. and R. Semiat, *Experimental study of the flow between two membranes*. Desalination, 2006. **199**(1-3): p. 108-110.
150. Santos, J.L.C., et al., *Modelling of flow and concentration patterns in spiral wound membrane modules with ladder-type spacers*. Desalination, 2006. **200**(1-3): p. 395-396.
151. Li, Y.L. and K.L. Tung, *The effect of curvature of a spacer-filled channel on fluid flow in spiral-wound membrane modules*. Journal of Membrane Science, 2008. **319**(1-2): p. 286-297.
152. Karode, S.K. and A. Kumar, *Flow visualization through spacer filled channels by computational fluid dynamics I.: Pressure drop and shear rate calculations for flat sheet geometry*. Journal of Membrane Science, 2001. **193**(1): p. 69-84.
153. Dendukuri, D., S.K. Karode, and A. Kumar, *Flow visualization through spacer filled channels by computational fluid dynamics-II: improved feed spacer designs*. Journal of Membrane Science, 2005. **249**(1-2): p. 41-49.
154. Ranade, V.V. and A. Kumar, *Fluid dynamics of spacer filled rectangular and curvilinear channels*. Journal of Membrane Science, 2006. **271**(1-2): p. 1-15.
155. Ranade, V.V. and A. Kumar, *Comparison of flow structures in spacer-filled flat and annular channels*. Desalination, 2006. **191**(1-3): p. 236-244.
156. Moll, R., et al., *Dean vortices applied to membrane process: Part II: Numerical approach*. Journal of Membrane Science, 2007. **288**(1-2): p. 321-335.
157. Moll, R., et al., *Dean vortices applied to membrane process: Part I. Experimental approach*. Journal of Membrane Science, 2007. **288**(1-2): p. 307-320.
158. Chung, K.Y., M.E. Brewster, and G. Belfort, *Dean vortices with wall flux in a curved channel membrane system: 3. Concentration polarization in a spiral reverse osmosis slit*. Journal of chemical engineering of Japan, 1998. **31**(5): p. 683-693.

159. Li, F., et al., *Optimization of non-woven spacers by CFD and validation by experiments*. Desalination, 2002. **146**(1-3): p. 209-212.
160. Li, F., et al., *Novel spacers for mass transfer enhancement in membrane separations*. Journal of Membrane Science, 2005. **253**(1-2): p. 1-12.
161. Koutsou, C., S. Yiantsios, and A. Karabelas, *A numerical and experimental study of mass transfer in spacer-filled channels: effects of spacer geometrical characteristics and Schmidt number*. Journal of Membrane Science, 2009. **326**(1): p. 234-251.
162. Santos, J., et al., *Investigation of flow patterns and mass transfer in membrane module channels filled with flow-aligned spacers using computational fluid dynamics (CFD)*. Journal of Membrane Science, 2007. **305**(1-2): p. 103-117.
163. Lau, K.K., et al., *Feed spacer mesh angle: 3D modeling, simulation and optimization based on unsteady hydrodynamic in spiral wound membrane channel*. Journal of Membrane Science, 2009. **343**(1-2): p. 16-33.
164. Shakaib, M., S.M.F. Hasani, and M. Mahmood, *Study on the effects of spacer geometry in membrane feed channels using three-dimensional computational flow modeling*. Journal of Membrane Science, 2007. **297**(1-2): p. 74-89.
165. Shakaib, M., S.M.F. Hasani, and M. Mahmood, *CFD modeling for flow and mass transfer in spacer-obstructed membrane feed channels*. Journal of Membrane Science, 2009. **326**(2): p. 270-284.
166. Thomas, D.G., *Forced convection mass transfer: Part II. Effect of wires located near the edge of the laminar boundary layer on the rate of forced convection from a flat plate*. AIChE Journal, 1965. **11**(5): p. 848-852.
167. FLUENT, A., *12.0/12.1 Documentation*. Users Guide Manual, Ansys Inc, 2009.
168. Chen, W., D. De Kee, and P.N. Kaloni, *Advanced mathematics for engineering and science*. 2003: World Scientific Pub Co Inc.
169. Rhie, C. and W. Chow, *Numerical study of the turbulent flow past an airfoil with trailing edge separation*. AIAA journal, 1983. **21**(11): p. 1525-1532.
170. Peters, T., *Membrane Technology for Water Treatment*. Chemical Engineering & Technology, 2010. **33**(8): p. 1233-1240.
171. Yuan, Z.-X., W.-Q. Tao, and Q.-W. Wang, *Numerical prediction for laminar forced convection heat transfer in parallel-plate channels with streamwise-periodic rod disturbances*. International Journal for Numerical Methods in Fluids, 1998. **28**(9): p. 1371-1387.
172. Capobianchi, M., et al., *A new technique for measuring the Fickian diffusion coefficient in binary liquid solutions*. Experimental thermal and fluid science, 1998. **18**(1): p. 33-47.
173. Fimbres-Weihs, G. and D. Wiley, *Review of 3D CFD modeling of flow and mass transfer in narrow spacer-filled channels in membrane modules*. Chemical Engineering and Processing, 2010. **49**(7): p. 759-781.
174. Fletcher, D., S. Maskell, and M. Patrick, *Heat and mass transfer computations for laminar flow in an axisymmetric sudden expansion*. Computers & fluids, 1985. **13**(2): p. 207-221.
175. Saeed, A., et al., *Effect of feed spacer arrangement on flow dynamics through spacer filled membranes*. Desalination, 2012. **285**(0): p. 163-169.

*“Every reasonable effort has been made to acknowledge the owners of copyright material. I would be pleased to hear from any copyright owner who has been omitted or incorrectly acknowledged.”*

# Appendix

## A. Appendix-I

Appendix-1 incorporates the details of CFD code used in this thesis (ANSYS FLUENT 13.0). For a specific feed spacer case SP22 at  $Re_h=100$ , the figures in this appendix summarizes the domain extents, material properties, boundary conditions, solution methods, solution controls, solution limits, equations solved, monitoring points used to ensure convergence and residuals monitors .

### A.1. ANSYS FLUENT 13.0

3d, dp, pbns, spe, lam (3D, double precision, pressure-based, species, laminar)

Space	3D
Time	Steady state
Viscous	Laminar
Model	Species Transport (without chemical reaction)
Number of volumetric species	2

### A.2. Boundary conditions

Name	id	Type
fluid	2	fluid
Top filament	3	Wall (top filament surface)
Bottom filaments	4	Wall (bottom filament surface)

Bottom wall	5	Wall (solute mass fraction=1)
Top wall	6	Wall (solute mass fraction=1)
Side wall 1&2	7, 8	Translational periodic
Pressure_outlet	9	Pressure outlet (gauge pressure=0 Pa)
Mass_flow_inlet	10	Mass-flow-inlet (0.0001625 kg/s)
Default-interior	11	interior

### A.3. Equations solved

- Flow
- Species

### A.4. Executed on demand

Mass fraction of solute in the bulk, which is later used to calculate mass transfer coefficient at the top and bottom membrane walls.

### A.5. Under-Relaxation Factors

Pressure	0.3
Density	1
Body forces	1
Momentum	0.7
Solute	1

## A.6. Pressure-Velocity coupling

Scheme used	SIMPLEC
Skewness correction	0

## A.7. Spatial discretization Schemes

Pressure	standard
Momentum	QUICK
Solute	Power Law

## A.8. Solution limits

Minimum absolute pressure (Pascal)	1
Maximum absolute pressure (Pascal)	5e+10

## A.9. Material Properties

Material type	Mixture (Binary mixture)
Mixture Species	h2o<1> and solute

Property	Units	Method	Value
Density	Kg/m <sup>3</sup>	Constant	998.2
Viscosity	Kg/m-s	Constant	0.001003
Mass Diffusivity	m <sup>2</sup> /s	Constant	1.54e-09

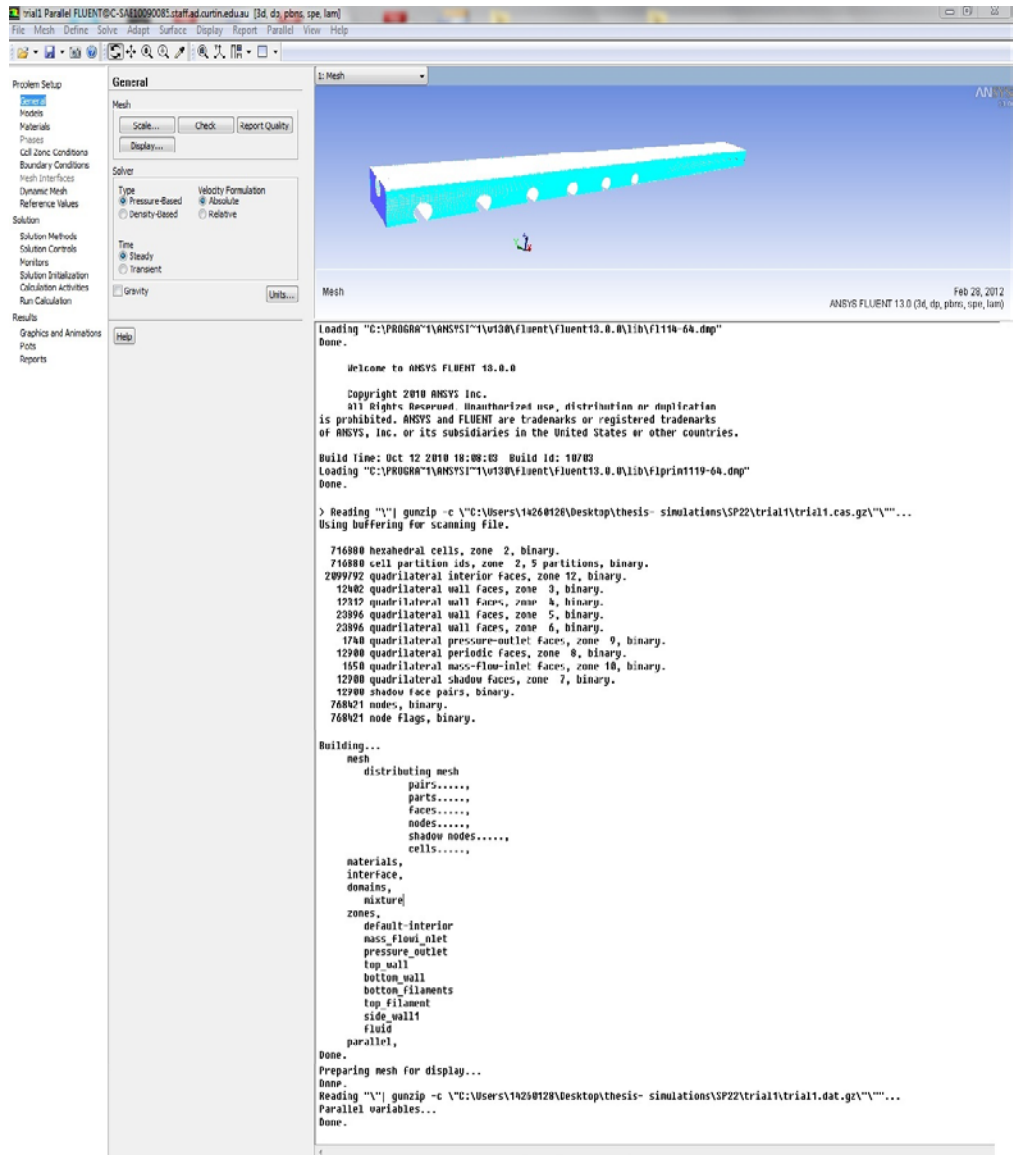


Figure A.1: Computational grid and console window of ANSYS FLUENT 13.0

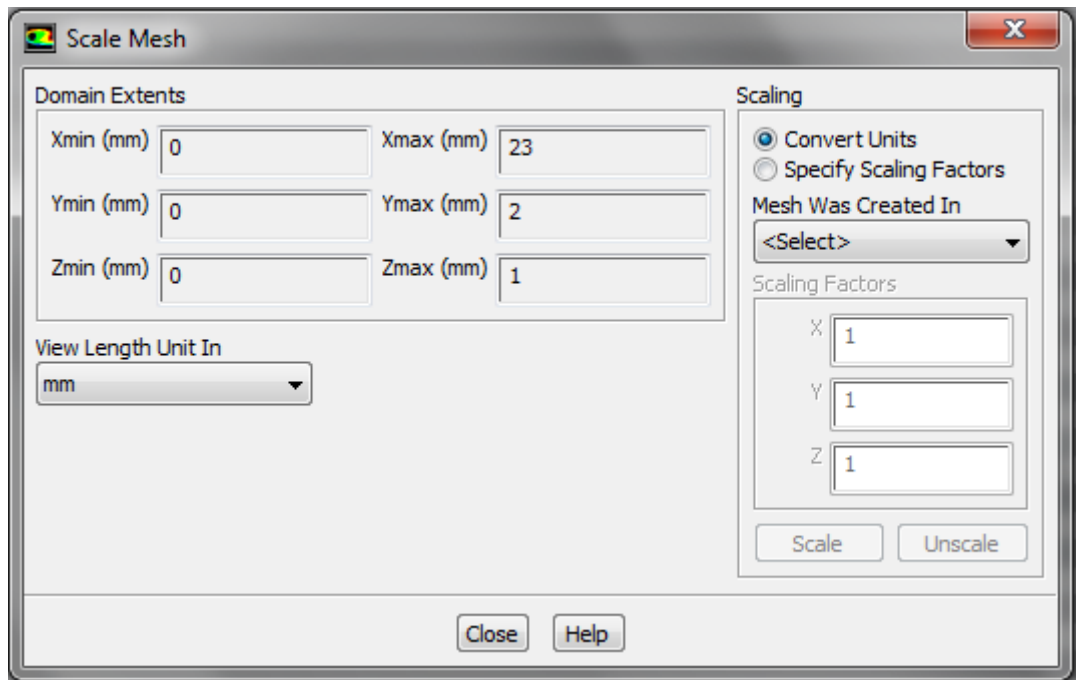


Figure A.2: Domain extents.

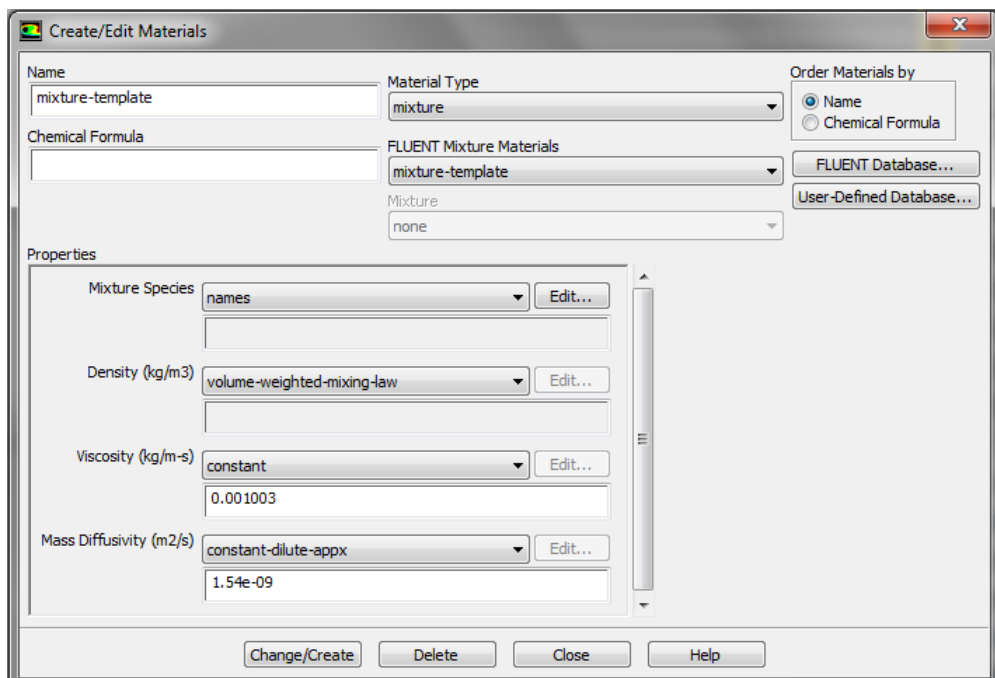


Figure A.3: Setting properties of the mixture.

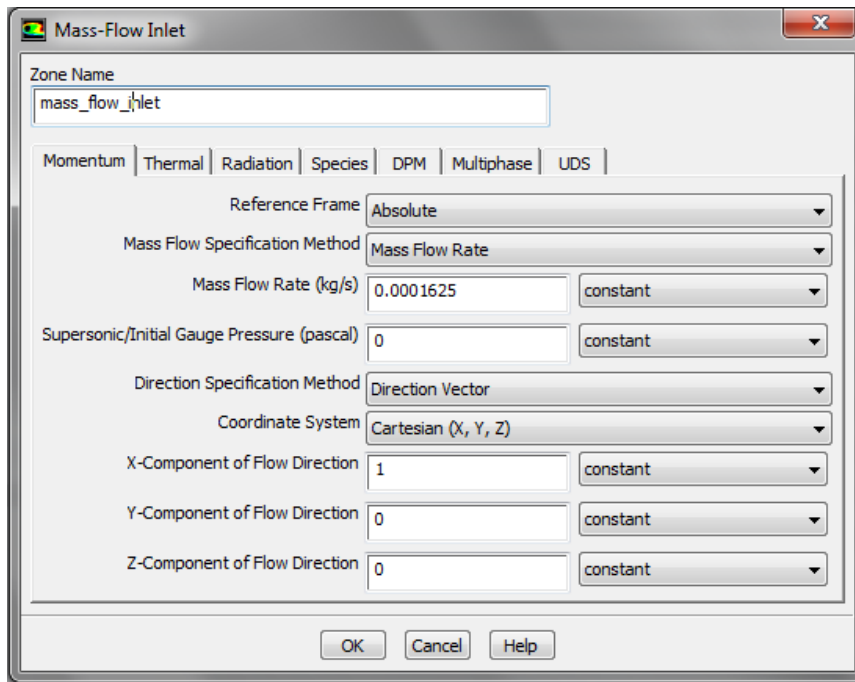


Figure A.4: Setting mass flow rate at inlet for SP22 to achieve  $Re_h=100$ .

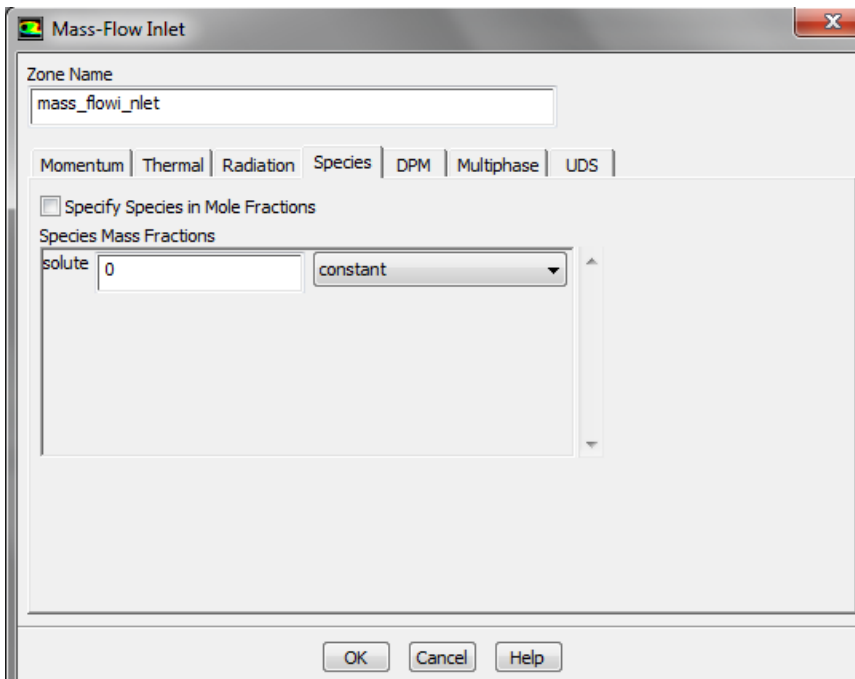
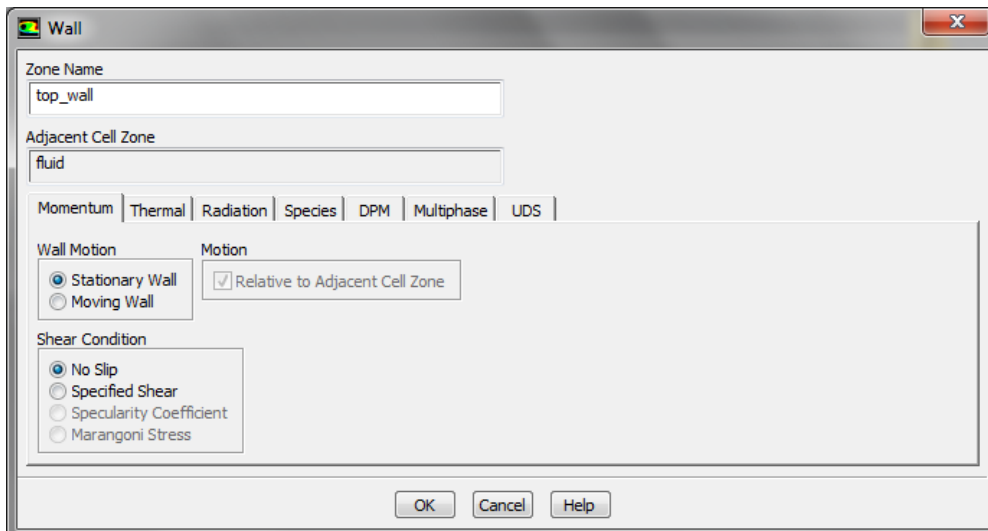
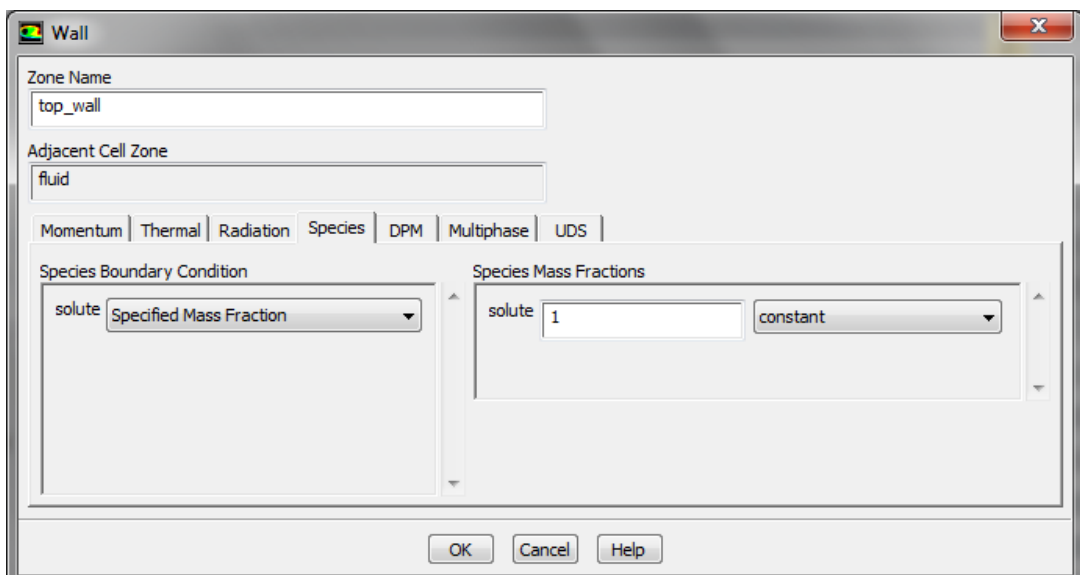


Figure A.5: Setting solute mass fraction at inlet.



**Figure A.6: Setting Boundary conditions at top (and bottom) membrane surface.**



**Figure A.7: Defining solute mass fraction at top (and bottom) membrane surface.**

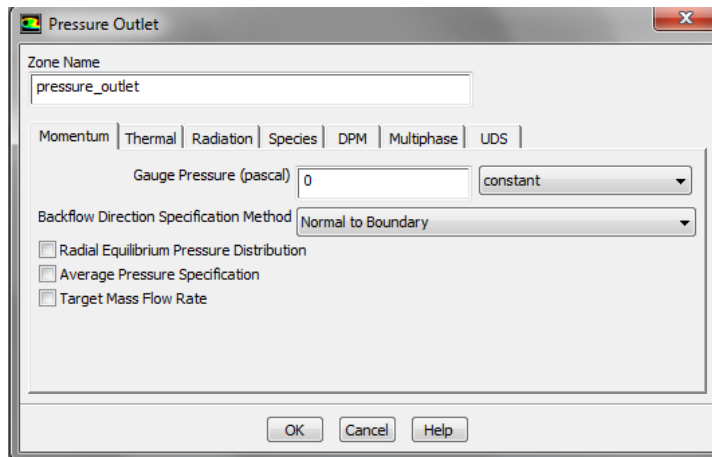


Figure A.8: Boundary conditions at outlet.

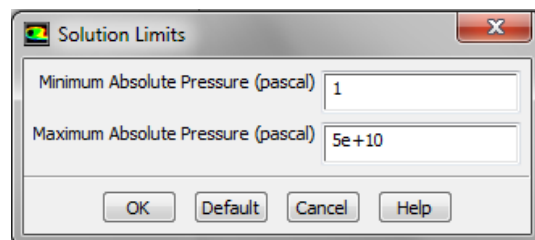
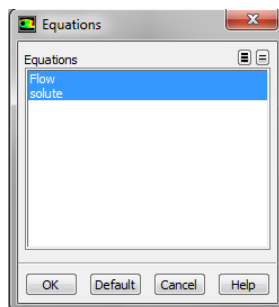
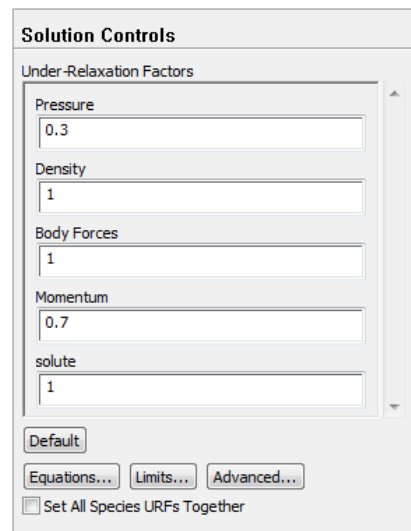
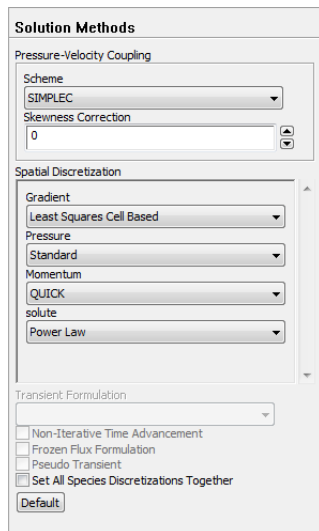


Figure A.9: Solution methods, control, limits and equations.

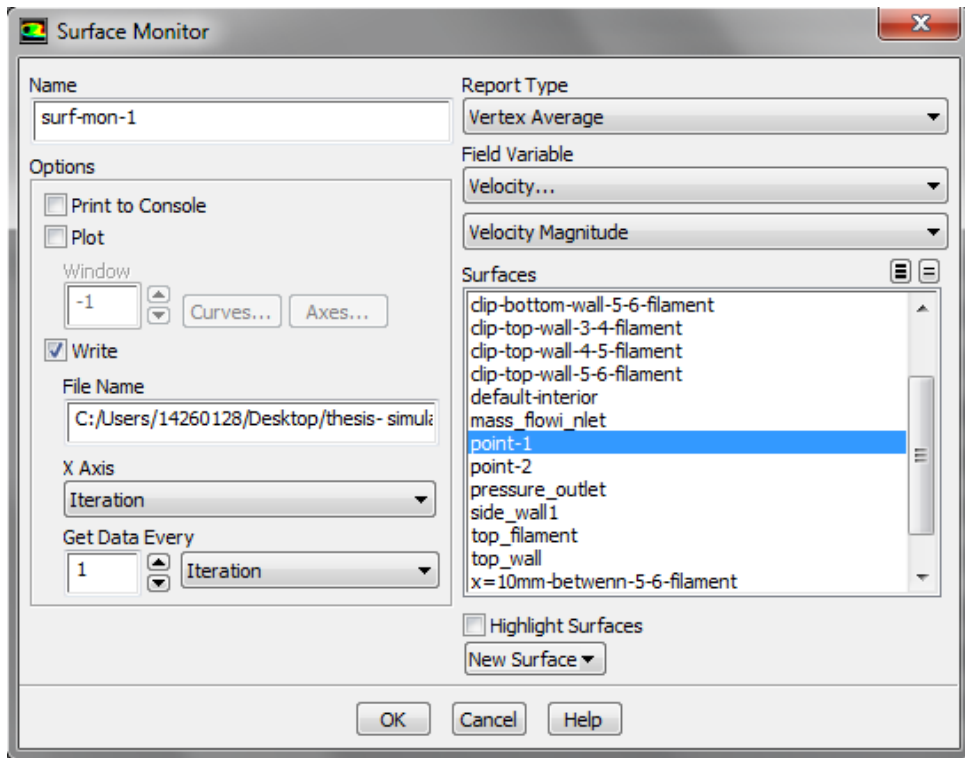


Figure A.10: Defining Monitoring point in the domain.

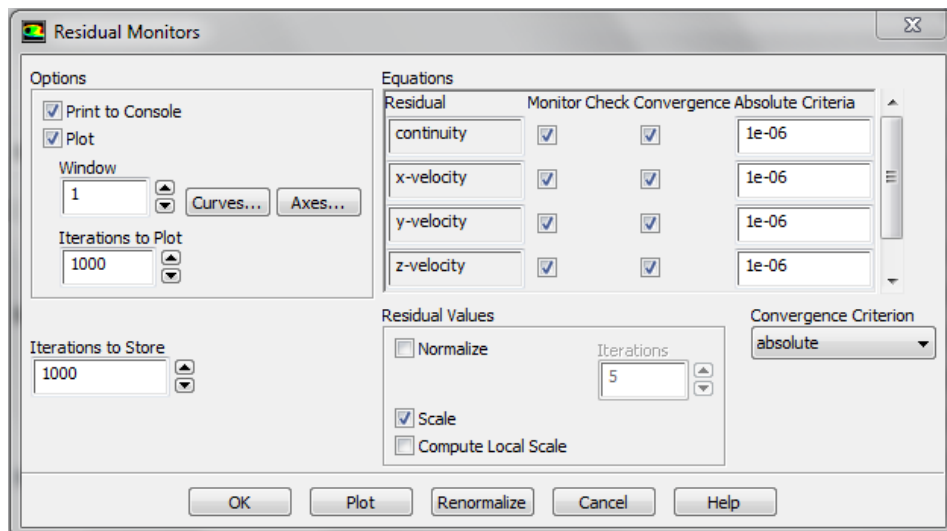
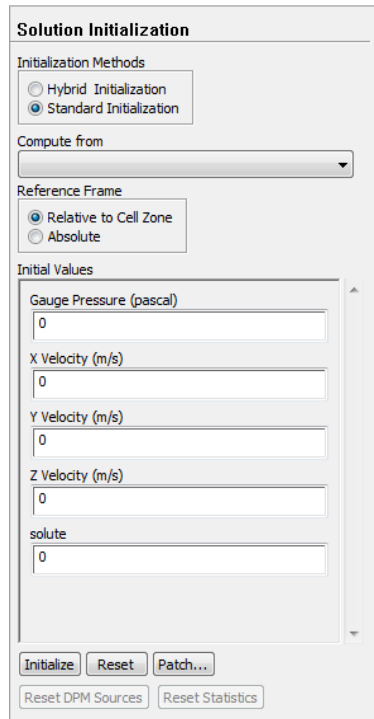
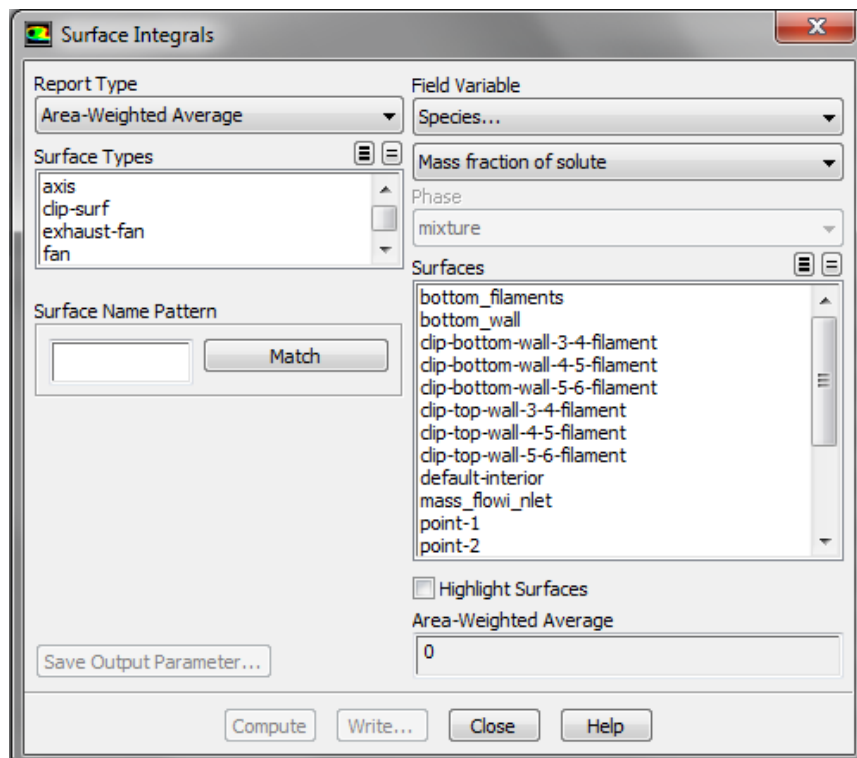


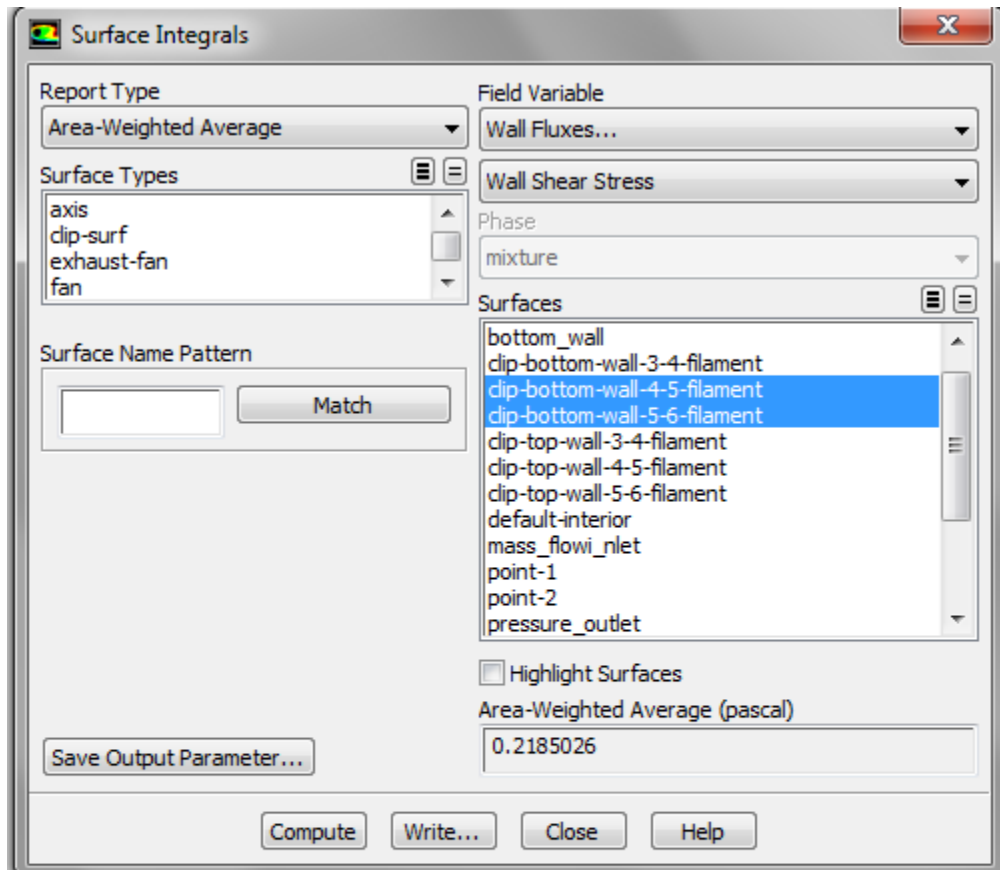
Figure A.11: Selecting residuals of continuity, velocity components and solute mass fraction.



**Figure A.12: Solution initialization.**



**Figure A.13: Reporting average values of the variables.**



Area-Weighted Average Wall Shear Stress	(pascal)
clip-bottom-wall-4-5-filament	0.21874633
clip-bottom-wall-5-6-filament	0.21825877
Net	0.21850255

Figure A.14: Reporting average values of bottom wall shear stress for SP22 at  $Re_h=100$ .

## B. Appendix-II

Appendix-2 incorporates the calculation of mass flow rate at  $Re_h=100$ , for spacer SP22 which is used as boundary condition at the inlet.

For  $Re_h=100$ , effective velocity ( $u_{eff}$ ) is calculated by the following equation:

$$u_{eff} = \frac{Re_h \mathbf{v}}{d_h} \quad (\text{AII} - 1)$$

The values used for kinematic viscosity is  $1e-06 \text{ m}^2/\text{s}$ . The hydraulic diameter is calculated for the SP22 based on the following equation:

$$d_h = \frac{4(V_T - V_{sp})}{S_{fc} + S_{sp}} \quad (\text{AII} - 2)$$

For the particular spacer SP22, based on the above equation the hydraulic diameter  $d_h = 9.463e-04 \text{ m}$

Equation AII-1 is used to calculate the effective velocity ( $u_{eff}$ ):

$$u_{eff} = \frac{100 \times 10^{-6}}{9.463 \times 10^{-4}} = 0.1056 \text{ m/s}$$

The porosity for SP22 is calculated by the following formula:

$$\varepsilon = 1 - \frac{V_{sp}}{V_T} \quad (\text{AII} - 3)$$

$$\varepsilon = 0.7701$$

The effective area ( $A_{eff}$ ) is calculated by the following formula

$$A_{eff} = h_{ch} b \varepsilon \quad (\text{AII} - 4)$$

Where,

$$h_{ch} = 1 \times 10^{-3} \text{ m}$$

$$b = 2 \times 10^{-3} \text{ m}$$

From equation AII-4:

$$A_{eff} = (1 \times 10^{-3})(2 \times 10^{-3})(0.7701) = 1.54 \times 10^{-6} \text{ m}^2$$

Mass flow rate is calculated by the following relation:

$$m = u_{eff} A_{eff} \rho \quad (\text{AII} - 5)$$

Where the density ( $\rho$ ) is  $998.2 \text{ kg/m}^3$

Using the above equation with known values for effective velocity, effective area and density, the mass flow rate based on equation AII-5 is calculated as:

$$m = 0.1056 \times 1.54 \times 10^{-6} \times 998.2 = 0.0001625 \text{ kg/s}$$

This value for mass flow rate is used as the boundary condition at the inlet, as can be seen in figure A.4.

## C. Appendix-III

Appendix-III incorporates the details of UDF (Used Defined Function) used to calculate the bulk solute mass fraction and eventually the mass transfer coefficient. The logic followed by the UDF is described in detail in section 5.3.4.1 of this thesis. The UDF is written in C language and hooked to ANSYS FLUENT. Details of the UDF are as follows:

```
#include "udf.h"

#include "mem.h"

#include "math.h"

#define SALT 0

#define H2O 1

#define R0_SALT 2165

#define R0_WATER 998.2

DEFINE_ADJUST(ADJUST_SCALAR, domain)

{

    real salt_m, water_m, vol_frac, cell_volume, bulk_mass_frac,
    mass_coeff;
```

```

Thread *t;

cell_t c;

face_t f;

/* Loop over all cell threads in the domain */
thread_loop_c(t, domain)
{
    /* Loop over all cells */
    begin_c_loop(c, t)
    {
        salt_m = C_YI(c, t, SALT);
        C_UDSI(c, t, 0) = salt_m;
    }
    end_c_loop(c, t)
}
thread_loop_f(t, domain)
{
    if (THREAD_STORAGE(t, SV_UDS_I(0)) != NULL)
        begin_f_loop(f, t)
        {
            F_UDSI(f, t, 0) = F_YI(f, t, SALT);
        }
        end_f_loop(f, t)
    }
}

```

```

DEFINE_ON_DEMAND(mass_transfer_coeff)
{
    Domain *d; /* declare domain pointer since it is not passed as an
                argument to the DEFINE macro */

    real salt_m, water_m, vol_frac, cell_volume, bulk_mass_frac,
mass_coeff;

    real mass_salt=0.0;

    real mass_water = 0.0;

    Thread *t;

    cell_t c;

    d = Get_Domain(1); /* Get the domain using Fluent utility */

    /* Loop over all cell threads in the domain */
    thread_loop_c(t, d)
    {
        /* Loop over all cells */
        begin_cell_loop(c, t)
        {
            cell_volume = C_VOLUME(c, t);

            salt_m = C_YI(c, t, SALT);

            water_m = C_YI(c, t, H2O);

            C_UDMI(c, t, 0) = abs(C_UDSI_G(c, t, 0)[2]);

            /*volume fraction of salt*/
            vol_frac =

                (salt_m/RO_SALT)/((salt_m/RO_SALT)+(water_m/RO_WATER));

            mass_salt =

                mass_salt + vol_frac*RO_SALT*cell_volume;

            mass_water =

```

```

        mass_water+ (1.0-vol_frac)*RO_WATER*cell_volume;
    }

    end_c_loop(c, t)
}

bulk_mass_frac= mass_salt/(mass_salt+mass_water);

Message( "\nSalt Mass = %f \t Water Mass = %f \tBulk mass
fraction = %f", mass_salt, mass_water, bulk_mass_frac);

thread_loop_c(t, d)
{
    /* Loop over all cells */
    begin_c_loop(c, t)
    {
        salt_m = C_YI(c, t, 0);

        mass_coeff =
            1.54*pow(10, -9)*C_UDMI(c, t, 0)/(salt_m-bulk_mass_frac);

        C_UDMI(c, t, 2)=mass_coeff;
    }
    end_c_loop(c, t)
}
}

```